ON THE IDENTIFIABILITY, PARAMETER IDENTIFICATION AND FAULT DIAGNOSIS OF INDUCTION MACHINES

Ahmed Mohamed Alturas
BSc., M.Sc.

School of Electrical and Electronic Engineering
Newcastle University

A thesis submitted for the degree of
Doctor of Philosophy

March, 2016

Abstract

Due to their reliability and low cost, induction machines have been widely utilized in a large variety of industrial applications. Although these machines are rugged and reliable, they are subjected to various stresses that might result in some unavoidable parameter changes and modes of failures. A common practice in induction machine parameter identification and fault diagnosis techniques is to employ a machine model and use the external measurements of voltage, current, speed, and/or torque in model solution. With this approach, it might be possible to get an infinite number of mathematical solutions representing the machine parameters, depending on the employed machine model. It is therefore crucial to investigate such possibility of obtaining incorrect parameter sets, i.e. to test the identifiability of the model before being used for parameter identification and fault diagnosis purposes. This project focuses on the identifiability of induction machine models and their use in parameter identification and fault diagnosis.

Two commonly used steady-states induction machine models namely T-model and inverse Γ-model have been considered in this thesis. The classical transfer function and bond graph identifiability analysis approaches, which have been previously employed for the T-model, are applied in this thesis to investigate the identifiability of the inverse Γ-model. A novel algorithm, the Alternating Conditional Expectation, is employed here for the first time to study the identifiability of both the T- and inverse Γ-models of the induction machine. The results obtained from the proposed algorithm show that the parameters of the commonly utilised T-model are non-identifiable while those of the inverse Γ-model are uniquely identifiable when using external measurements. The identifiability analysis results are experimentally verified by the particle swarm optimization and Levenberg-Marquardt model-based parameter identification approaches developed in this thesis.

To overcome the non-identifiability problem of the T-model, a new technique for induction machine parameter estimation from external measurements based on a combination of the induction machine's T- and inverse Γ-models is proposed. Results for both supply-fed and inverter-fed operations show the success of the technique in identifying the parameters of the machine using only readily available measurements of steady-state machine current, voltage and speed, without the need for extra hardware.

A diagnosis scheme to detect stator winding faults in induction machines is also proposed in this thesis. The scheme uses time domain features derived from 3-phase stator currents in conjunction with particle swarm optimization algorithm to check characteristic parameters of the machine and detect the fault accordingly. The validity and effectiveness of the proposed technique has been evaluated for different common faults including interturn short-circuit, stator winding asymmetry (increased resistance in one or more stator phases) and combined faults, i.e. a mixture of stator winding asymmetry and interturn short-circuit. Results show the accuracy of the proposed technique and it is ability to detect the presence of the fault and provide information about its type and location.

Extensive simulations using Matlab/SIMULINK and experimental tests have been carried out to verify the identifiability analysis and show the effectiveness of the proposed parameter identification and fault diagnoses schemes. The constructed test rig includes a 1.1 kW three-phase test induction machine coupled to a dynamometer loading unit and driven by a variable frequency inverter that allows operation at different speeds. All the experiment analyses provided in the thesis are based on terminal voltages, stator currents and rotor speed that are usually measured and used in machine control.

Acknowledgment

First of all, my deepest thanks are always due to Allah, the most gracious, the most merciful, for his unlimited blessings and giving me the power and the patience to complete this work.

I would like to state my deep gratitude to my supervisors, Dr Shady Gadoue, Dr Mohammed Elgendy and Dr Bashar Zahawi for their guidance which made it possible for me to complete my dissertation. I appreciate their help and their ability to import a lot of knowledge and critical thinking and also for their genuine friendship. I also appreciate their encouragement and support especially during writing for publications.

Most importantly, I give huge thanks to my beloved parents, brothers, sisters, my wife, and my kids for always being there when I need them. Words are not profound enough to express how grateful I am for their support to see me through my educational life; my endeavours in life to date have been possible due to their presence.

The financial support of my government, Libya, through the Engineering Faculty of Misurata-Misurata University, is gratefully acknowledged.

Finally, I would like to show gratitude to all my colleagues and friends, here and in my home country, for their support.

List of Contents

List of Tables

List of Figures

Notation

IM	induction machine
d.c.	Direct current
ω_e	Synchronous speed
ω_r	Rotor speed
f	Stator or field frequency
s	Slip
R_s	stator winding resistances
R_r	rotor winding resistances
l_{ls}	Stator leakage inductances
l_{lr}	Rotor leakage inductances
L_m	Magnetising inductance
L_s	Stator self-inductances
L_r	Rotor self-inductances
MMF	megnetomotive force
ACE	Alternating Conditional Expectation
PSO	Particle Swarm Optimization
L-M	Levenberg-Marquardt
AC	Alternating Current
i_s	Stator current
i_r	Rotor current
$i_{A,B,C}$	Three phase stator currents
$i_{a,b,c}$	Three phase rotor currents
i_m	Magnetising current
Ψ	flux-linkage
Ψ_s^s, Ψ_r^s	Stator flux linkage
Ψ_r^s	Rotor flux linkage
θ_r	Electrical rotor position
$\mathbf{P}$	Parameter vector
$\mathrm{G}(\mathbf{P})$	Transfer function
SE	Effort source

SF	Flow source
UMP	unbalanced magnetic pull
SNR	Signal-to-noise ratio
AI	Artificial intelligence
X_s	Stator leakage impedance
X_r	Rotor leakage impedance
X_m	Magnetising impedance
Z_{eq}	Impedance
EKF	Extended Kalman Filter
MRAS	Model reference adaptive system
MCSA	Motor current signature analysis
FFT	Fast Fourier transform
ZFFT	Zoom fast Fourier transform
CZT	chirp Z transform
MUSIC	multiple signal classification
ESPRIT	Estimation of signal parameters via rotational invariance techniques
STFT	Short-time Fourier transform
WFM	winding function methods

CHAPTER 1

Introduction

1.1 Motivations

Due to their simple structure, low cost and high performance, induction machines (IMs) have been intensively utilized and they are considered as the “workhorse” in many industrial and automation applications [1]. These machines can be supplied from constant-frequency sinusoidal power supplies (supply-fed) or from adjustable-frequency ac drives (inverter-fed). Although IMs are rugged and reliable, they are subjected to various stresses that might lead to some unavoidable modes of failures/faults, especially when supplied by ac drives where the winding insulation experiences higher stresses due to the voltages with high harmonic contents [2]. Due to the critical integration of IMs in a massive number of industrial applications, fault diagnoses have a great importance in enhancing the reliability of the machine and consequently the industrial process. Accurate identification of IM parameters is required for fault diagnosis [3] and is also a prerequisite to many applications such as sensorless control [4] and model predictive control [5].

A variety of IM parameter identification methods have been proposed [8-11]. Most of these methods try to estimate the parameters of an IM model based on external measurements of voltage, current, speed and/or torque while the machine is running [6-8]. These model-based techniques are relatively easy to implement, do not require any additional hardware circuitry and are applicable to different types of machines under different operating conditions.

When developing a model-based approach for parameter estimation and fault diagnosis of IM, it is essential to start with an appropriate and accurate model that sufficiently describes the measured data. It is also important to assess how well the actual parameters of the model are estimated from the measurements. Any mismatch between the real and estimated model parameter values may result in a wrong assessment of the machine performance [6, 9, 10]. Therefore, before using a machine model in a parameter estimation technique, it is important to test the identifiability of the model to make sure that its parameters are uniquely identifiable.

Different IM models have been derived to represent the machine’s dynamic and steady-state behaviour [11-13]. Some of these models have been used in parameter identification and fault diagnosis of the machine [10, 14-16]. However, there still a lot more work needs to be done in this area. This includes a comprehensive study on the identifiability of IM models and choice and development of models suitable for parameter identification and fault diagnosis. More research is also required on the parameter identification and fault diagnosis methods of the IM in order to increase the accuracy and reduce the implementation cost of these methods. This research is a trial to cover these important topics. For the parameter identification and fault diagnosis of induction machines, only model-based techniques that make use of external measurements are considered in this study.

1.2 Induction machine structure and principle

Induction machines are the most widely used electrical machines due to their simple structure, robustness, low cost and reliability [12]. The name of the IMs derived from the fact that the torque producing currents in the rotor of the IMs are induced by electromagnetic action. The stator windings of the IMs not only produce the magnetic field (the excitation), but also supply the energy that is converted to mechanical output. The absence of any sliding mechanical parts, like the commutator in the dc machines, and the consequent saving in terms of maintenance is a main advantage of the cage IMs.

The IM is composed of stator, rotor, bearing and frame, as shown in figure 1.1. Depending on rotor type, they are divided into two main types; squirrel-cage and wound-rotor IMs. In both types, the rotor consists of a stack of laminations, to prevent the eddy currents from flowing in the iron, with evenly spaced slots punched around the rotor circumference. In the cage rotor, each slot contains a solid conductor bar and all the bars are connected electrically and physically by conducting end-rings.

In wound-rotor (also called slipring) type, the rotor is provided with insulated windings similar to the stator. The windings are connected with three outputs brought out to three sliprings. In slipring machines, the rotor circuit is open and a connection via brushes on the sliprings can be made. Unlike the cage machines; the resistance of each rotor phase is not fixed and can be increased by adding external resistance, which can be beneficial in terms of speed control. Even though all these advantages, wound-rotor machines are still more expensive than cage machines because of the extra cost of the wound rotor and the associated control system, especially for low-power machines [17]. Recently, due to the continuous improvements of variable-frequency inverter suppliers, cage machines have begun to replace wound-rotor machines and still few wound-rotor machines used only in large sizes [17]. The induction machine used as a test machine in the thesis (Figure 1.1) is of the squirrel-cage type.

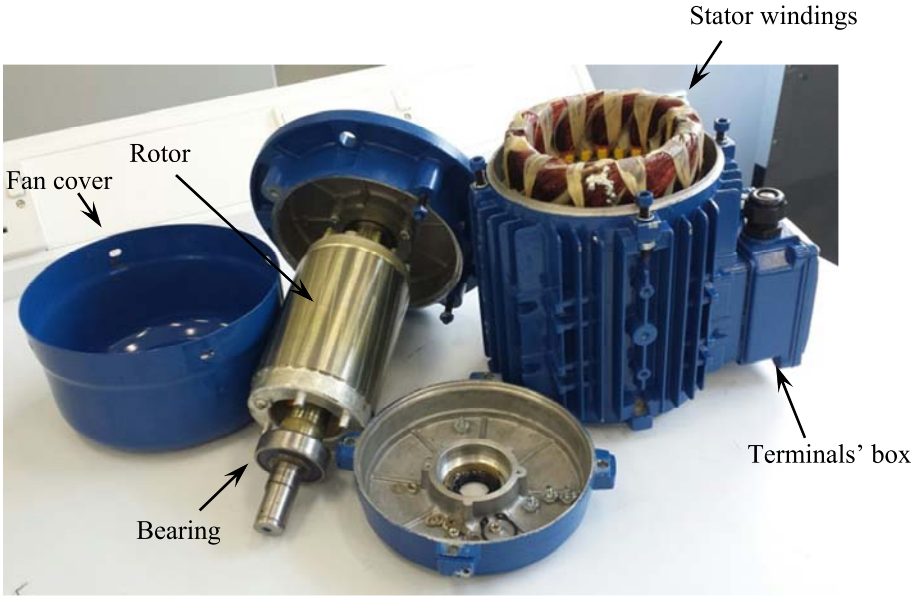

Figure 1.1 The structure of induction motor.

The fundamental principle of the IM is the creation of a sinusoidally distributed rotating magnetic field in the air-gap. When a sinusoidal three-phase electrical power supply with a frequency f is connected to the stator, the stator currents create a synchronously rotating magnetic field in the air-gap of the machine. The rotational speed (ω_e) of the field is directly proportional to the supply frequency (f) and inversely proportional to the pole number (P) of the winding, and is given by:

$$\omega_e = \frac{120f}{P} \tag{1.1}$$

According to the principles of magnetic induction theory, as long as there is a relative motion between a conductor and a magnetic field, induced current will start to flow in the rotor conductors and an alternating flux which lags behind the stator flux is introduced.

The interaction between the axial currents in the rotor conductors and the radial magnetic flux waves produces the driving torque of the motor. In order to produce a torque, the rotor speed

(ω_r) should be different from the synchronous speed (ω_e). At any speed, the difference between the rotor speed N_r and the synchronous speed N_e is called the slip speed (N_{sl}) which induces rotor current and develop the torque. The slip s is given by:

$$s = \frac{N_e - N_r}{N_e} = \frac{\omega_e - \omega_r}{\omega_e} \tag{1.2}$$

1.3 Induction machine modelling

In the literature, many mathematical models have been developed to describe the dynamic and steady-state behaviour of IMs [11-13]. Although this thesis considers only steady-state IM models, a brief review of the most used dynamic models is also provided in the appendix A for information.

Due to their simplicity and shorter computation time, steady-state models have gained more acceptances in many applications including parameter identification [10, 18] and fault diagnosis [14]. One of the most commonly utilized steady-state models is the standard per-phase induction motor T-equivalent circuit model shown in figure. 1.2. This model includes five electrical parameters: R_s, R_r, l_{ls}, l_{lr}, and L_m, where R_s is the stator resistance, R_r is the rotor resistance (referred to the stator), l_{ls} is the stator leakage inductance, l_{lr} is the rotor leakage inductance (referred to the stator), L_m is the magnetizing inductance and s is the slip.

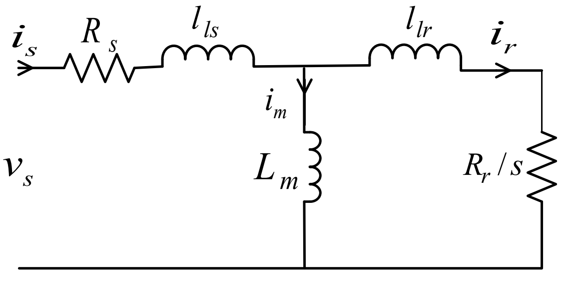

Figure 1.2 Induction motor T-equivalent circuit.

For the T-model shown in figure 1.2, the relationship between the flux linkages (Ψ_s^s, Ψ_r^s), and the winding currents (i_s^s, i_r^s) is given by [12, 18]:

$$\begin{bmatrix} \psi_s^s \\ \psi_r^s \end{bmatrix} = \begin{bmatrix} l_{ls} + L_m & L_m \\ L_m & l_{lr} + L_m \end{bmatrix} \begin{bmatrix} i_s^s \\ i_r^s \end{bmatrix} \tag{1.3}$$

The total per phase resistance (R_{eq}), reactance (X_{eq}), and impedance (Z_{eq}) at the stator side are given by [6]:

$$\begin{aligned} R_{eq} &= R_s + (X_m^2 R_r / s)/((R_r / s)^2 + (X_m + X_r)^2) \\ X_{eq} &= X_s + X_m - (X_m^2 (X_m + X_r))/((R_r / s)^2 + (X_m + X_r)^2) \\ Z_{eq} &= R_{eq} + jX_{eq} \end{aligned} \tag{1.4}$$

A simple change to obtain two mathematically equivalent circuits with only two inductances that give the same performance as the T-equivalent circuit have been proposed [12]. As long as the input voltage is the same, the two models have the same input impedance and produce the same torque as the T-model. The first equivalent circuit is known as the inverse Γ-model and is shown in figure 1.3.

The relationship between the flux linkages (Ψ_s^s, $\Psi_r^{s\prime}$) and the winding currents ($i_s^s, i_r^{s\prime}$) of inverse Γ-model is given by [12, 18]:

$$\begin{bmatrix} \psi_s^s \\ \psi_r^{s'} \end{bmatrix} = \begin{bmatrix} l_{ls}' + L_m' & L_m' \\ L_m' & L_m' \end{bmatrix} \begin{bmatrix} i_s^s \\ i_r^{s'} \end{bmatrix} \tag{1.5}$$

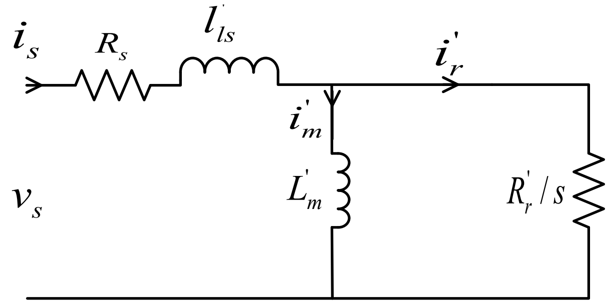

Figure 1.3 Induction motor Inverse Γ-equivalent circuit.

In this model, the stator resistance is equal to that of the T-model while the other parameters' values are transferred based on the value of the transformation constant *α*. The relations between the parameters of the T-model and the inverse Γ-model are as follow [10, 12, 18]:

$$\begin{aligned} l'_{ls} &= L_s - \alpha L_m, \\ L'_m &= \alpha L_m, \\ R'_r &= \alpha^2 R_r \end{aligned} \tag{1.6}$$

where $\alpha = L_m/L_r$, L_s and L_r are the self-inductances of the stator and rotor given by $L_s = L_m + l_{ls}$ and $L_r = L_m + l_{lr}$, respectively.

The second equivalent circuit is known as the Γ-model and shown in figure 1.4. The relationship between the flux linkages and the winding currents of Γ-model is given by [12, 18]:

$$\begin{bmatrix} \psi_s^s \\ \psi_r^{s''} \end{bmatrix} = \begin{bmatrix} L''_m & L''_m \\ L''_m & l''_{lr} + L''_m \end{bmatrix} \begin{bmatrix} i_s^s \\ i_r^{s''} \end{bmatrix} \tag{1.7}$$

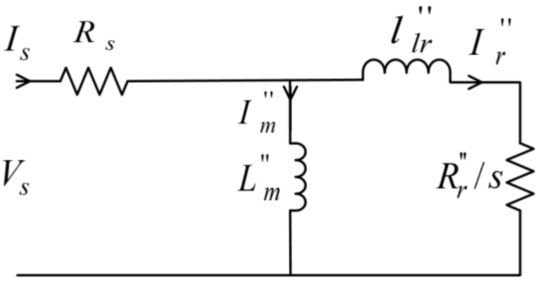

Figure 1.4 Induction motor Γ-equivalent circuit.

The stator resistance in this Γ-model is similar to that of the T-model while the other parameters' values are transformed based on *α'*. The relations between the parameters of the T-model and the Γ- model are given by [10, 12, 18]:

$$\begin{aligned} l''_{lr} &= \alpha'^2 L_r - \alpha L_m, \\ L''_m &= \alpha' L_m, \\ R''_r &= \alpha'^2 R_r \end{aligned} \tag{1.8}$$

where $\alpha' = L_s/L_m$, L_s and L_r are the self-inductances of the stator and rotor, respectively.

1.4 Thesis objectives

The main objectives of this thesis are:

- To do a comprehensive study that contributes to the research on identifiability analysis, parameter identification, and fault diagnosis of induction machines.
- To develop techniques to assess model identifiability and apply them on the two commonly used steady-state IM models; the T-model and inverse Γ-model.
- To develop a technique for IM parameter identification.
- To develop a tool for IM fault diagnosis and detection of IM stator faults.
- To develop a laboratory test facility to permit the detailed investigation of IM identifiability, parameter identification and fault diagnosis.
- To validate the proposed and considered approaches for IM parameter identification and fault diagnosis using the test facility.

1.5 Assumptions

A number of assumptions and simplifications have been made throughout the thesis in order to reduce the IM model complexity and time of calculations. Due to these simplifications, some differences between the measured and simulated data are expected. However, these assumptions are in line with previous publications in this area [10, 11, 19]. They can be summarised as follows:

- Only three-phase induction motors at steady-state operating condition are considered.
- The machine parameters which are most mentioned in this thesis are the electrical parameters including the stator and rotor resistances (R_s and R_r), the stator and rotor leakage inductances (l_{ls} and l_{lr}), and the magnetising inductance (L_m).
- Space magnetomotive force (MMF) and flux profile are considered to be sinusoidally distributed and higher order harmonics are negligible.
- Iron losses, saturation and skin effect were assumed to be negligible.
- The self- and mutual-inductances between stator and rotor phases are constant. Dependency of the leakage inductances on the rotor position, caused be slots, is neglected.

- For parameter identifications, it is assumed that the three phases are identical and as a result only one phase can be used for this purpose. For condition monitoring, the three phase measurements are collected and used.
- All time varying parameters, such as the rotor resistance which may vary due to the rotor heating, are assumed to vary so slow that they can be treated as constants during the test course.
- Different cases of supply-fed and inverter-fed operation are investigated and, thus the applied voltages (and currents) are not necessary of constant frequency and/or amplitude and, therefore different impedances may result.

1.6 Methodology and outlines

Due to the wide use of IM steady-state models in many applications including IM parameter identification and condition monitoring, two commonly used IM models, the conventional per phase equivalent circuit (T-model) and the inverse Γ-model are considered in this thesis. One of the most important points when designing an approach for IM parameter identification and condition monitoring is to choose the proper IM model and the method that will be used for data analysis. To enable a clear understanding of IM identifiability analysis, parameter identification, and fault diagnosis, previous research related to these topics is firstly reviewed. However, the review showed that the study of identifiability of the IM models and its approaches has not been received high attention.

The parameters of the T-model (the familiar equivalent circuit of the machine) may be identified by performing the standard no-load, dc and locked rotor tests as detailed in IEEE Standard 112-2004. This requires the ratio of stator leakage inductance to rotor leakage inductance (l_{ls}/l_{lr}) to be known. When this ratio is unavailable or when the machine in question is in operation and it is not possible to carry out the standard tests, an alternative parameter identification approach is required.

One such approach recently proposed in the literature [6, 8, 10], is to try to estimate the induction machine parameters based on external measurements at stator terminal while the machine is running. Before using a machine model in such a parameter estimation technique, however, it is important to test the identifiability of the model to make sure that its parameters are uniquely identifiable. As a result, the identifiability of the two aforementioned models (T-and inverse Γ-) is extensively investigated in this thesis using the transfer function, bond graph, and Alternating Conditional Expectation (ACE) identifiability test techniques. The obtained results from these three techniques are then verified by using the Levenberg-Marquardt (L-M) and particle swarm optimization (PSO) parameter estimation algorithms that use the external measurements of motor's voltage, current and speed.

The research also concerns the way in which the two IM models (T- and inverse Γ-) are combined together for the sake of eliminating the T-model redundancy and estimating its parameters uniquely from the external measurements of stator current and voltage and rotor speed. To close the loop and to show that the proposed integrated model has the ability to effectively resolve the identifiability issues of the T-model, its (integrated model) identifiability is firstly assessed. This is achieved by testing the structural identifiability of the model using the transfer function identifiability test approach.

A diagnosis scheme to detect stator winding faults in induction machines is also proposed in this thesis. According to the review, model-based methods were used in this thesis due to their advantages including their simplicity, easy to implement, they are non-intrusive methods, and the cost of implementation tends to be low.

Matlab/Simulink is used to analyze and simulate the induction motor under both healthy and faulty conditions. The M-file is then run along with the simulation to apply the proposed approaches and find the situation of the machine. All the obtained results are experimentally verified using the test rig described in chapter 4.

In order to achieve the objectives of the thesis and validate the obtained results, the thesis is organized as follows.

Chapter-2 discusses the identifiability concept and provides a detailed theoretical background on the identifiability approaches presented in this thesis.

Chapter-3 presents a literature review on IM parameter identification. It also describes the symptoms and mechanism of common electrical/mechanical faults and reviews previous research on fault diagnosis of IMs.

Chapter-4 gives a detailed description of the experimental setup used in the project. Steady-state experimental measurements of stator voltages and currents for healthy and faulty IM are provided to be used in chapters 5-7. The mathematical models of the IM are implemented in Matlab/Simulink program environment.

In Chapter-5, the identifiability of the T-equivalent circuit and inverse Γ-equivalent circuit of the induction motor is investigated in details, using the five approaches provided in Chapter 3. The transfer function and bond graph a priori (structural) identifiability analysis approaches are utilised. The Alternating Conditional Expectation (ACE) approach is used for the first time to assess the identifiability of IM models. Steady-state measurements of stator voltage and current and rotor speed of the IM obtained in Chapter 4 are utilized by the Levenberg-Marquardt (L-M) and Particle Swarm Optimization (PSO) techniques in parameter identification of both IM equivalent circuits.

Chapter-6 proposes a novel method for IM parameter identification using an integrated steady-state model. By analysing the identifiability of T- and inverse Γ-models, a new model is suggested to solve the non-identifiability problem of the T-model based on a combination of the two models (T- and inverse Γ-).

Chapter-7 presents a new model-based technique for the detection of stator winding faults of IMs. The proposed method is based on the use of the inverse Γ-model in conjunction with external measurement of terminal waveforms.

Chapter-8 includes conclusions of the thesis and recommendations for future work.

1.7 Contributions and publications

The research reported in this thesis considers the problem of IM identifiability analysis and parameter identification under different operating conditions (healthy and faulty). The completion of the thesis objectives is supported by the main contribution of the project that can be summarized as follows:

- A novel identifiability analysis approach is proposed in which the Alternating Conditional Expectation (ACE) algorithm is used for the first time to address steady-state IM models identifiability issues. The analysis is employed to examine the identifiability of both the T- and inverse Γ-models.
- An experimental approach based on the use of the Levenberg-Marquardt (L-M) and Particle Swarm Optimization (PSO) algorithms in conjunction with measured steady-state machine stator currents, voltages and rotor speed is developed for identifiability analysis and parameter identification of IMs.

- A novel approach for IM parameter identification based on an integrated steady-state model is proposed. The technique is performed at steady state using only the terminal quantities without any additional hardware or any changes in motor connections and, therefore, is fit for running machines.
- An induction machine fault diagnosis technique is developed using model-based approach based on the use of the PSO.

In addition to these main contributions, several minor contributions are as follows:

- Developing a comprehensive understanding of the identifiability analysis, parameter identification and electrical faults of IMs.
- Comprehensive discussions and evaluation of electrical parameter of induction motors and the effects of different electrical faults including short-circuited and open-circuited faults on them.
- Developing comprehensive modelling, simulation and evaluation tools for assessing the proposed identifiability, parameter identification and fault diagnosis algorithms developed in this thesis.

The following papers have been extracted from this research:

1. **A. M. Alturas**, S. M. Gadoue, B. Zahawi, and M. A. Elgendy, "On the Identifiability of Steady-State Induction Machine Models Using External Measurements," IEEE Transactions on Energy Conversion, Early Access, Digital Object Identifier: 10.1109/TEC.2015.2460456, 2015.
2. **A. M. Alturas**, S. M. Gadoue, M. A. Elgendy, B. Zahawi, and Y. Zbede, "An Integrated Steady-State Model to Estimate the Parameters of the Induction Machine," submitted to IEEE Transactions on Industrial Electronics, 15-TIE-4063, 2015.
3. **A. M. Alturas**, S. M. Gadoue, M. A. Elgendy, B. Zahawi, and A. S. Abdel-Khalik, "Structural Identifiability Analysis of Steady-State Induction Machine Models," IEEE 4th International Conference on Electrical Power and Energy Conversion Systems EPECS 2015, Sharjah, UAE, 24-26 November, 2015.

CHAPTER 2

Identifiability Test Approaches

The identifiability of induction machine models investigates the uniqueness of the solution for the unknown parameters of the model and is, therefore, a prerequisite for IM parameter identification. In this chapter, the identifiability concept, definitions and the used approaches in this thesis are presented.

2.1 Identifiability concept

Since the publication of Bellman and Astrom paper in 1970 [20], the identifiability issue has received considerable attention in a number of fields including statics, economics, system engineering, and mathematical biology [21-24]. The identifiability of induction machine (IM) model parameters is concerned with the unique association of the solution (identified model parameters) with the measured characteristics of the machine. If some parameters of a system model are not uniquely identifiable, there will be always several combinations of parameters that satisfy the solution.

The concept of identifiability can be explained by comparing the two functions shown in figure 2.1. In figure 2.1.a, there is only one combination of parameter values that results in the function having a global minimum. In contrast, an infinite number of combinations of parameter values can result in the same minimum value of the function shown in figure 2.1.b. The system represented in figure 2.1.a is identifiable whereas that represented in figure 2.1.b is non-identifiable.

The identifiability term means whether it is possible to recover the parameter vector **P** uniquely from input/output measurements or not. In other words, the parameter vector **P** is identifiable if and only if any change in the values of the parameters results in a change in the measured quantities **Y**(t).

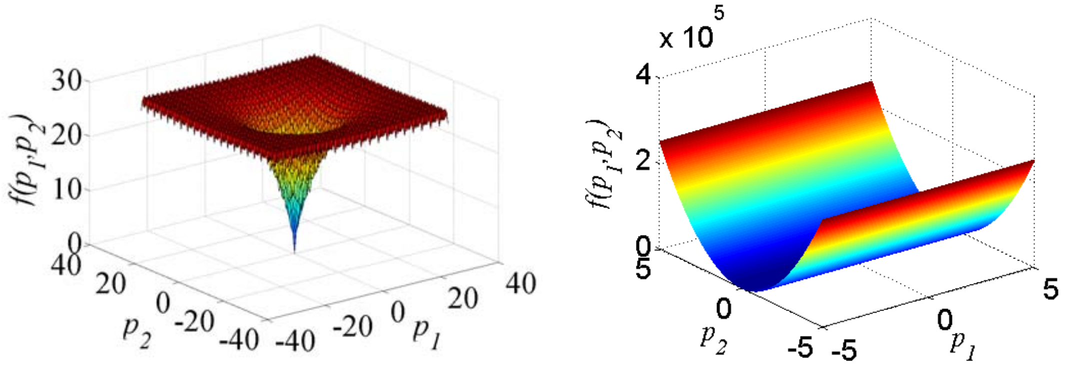

(a) (b)

Figure 2.1 Estimation of hypothetical parameters p_1 and p_2, (a) Identifiable system, (b) non-identifiable system.

Models describing dynamic properties of systems are usually defined by differential equations and can be written in the form of state-space. The dynamic model of any system depending on a parameter vector **P** ∈ R_m is described by:

$$\begin{aligned}\dot{\mathbf{X}}(t) &= \mathbf{A}(\mathbf{P})\mathbf{X}(t) + \mathbf{B}(\mathbf{P})\mathbf{U}(t)\\ \mathbf{Y}(t) &= \mathbf{C}(\mathbf{P})\mathbf{X}(t)\end{aligned} \tag{2.1}$$

where $\mathbf{X} = [x_1\, x_2 \ldots\, x_{nx}]^T$ is the state vector, $\mathbf{U} = [u_1\, u_2 \ldots\, u_{nu}]^T$ is the input, $\mathbf{Y} = [y_1\, y_2 \ldots.\, y_{ny}]^T$ is the output (measurements), $\mathbf{P} = [p_1\, p_2 \ldots\, p_{np}]^T$ is the unknown parameter vector, **A**, **B** and **C** are matrices of proper dimensions and each of them consisting of some or all of unknown parameters.

The vector **P** is said to be globally identifiable if [25]:

$$\mathbf{C}(\mathbf{P})e^{\mathbf{A}(\mathbf{P})t}\mathbf{B}(\mathbf{P}) = \mathbf{C}\left(\tilde{\mathbf{P}}\right)e^{\mathbf{A}\left(\tilde{\mathbf{P}}\right)t}\mathbf{B}\left(\tilde{\mathbf{P}}\right) \tag{2.2}$$

Implies that $\mathbf{P} = \tilde{\mathbf{P}}\ \forall\ \mathbf{P},\ \tilde{\mathbf{P}} \in Rm$.

Since the IM drives became widely used in different applications, a lot of efforts for improving their performance and reliability have been taken off. A major factor affecting the machine performance is the accuracy of its electrical parameters which is related to many applications including condition monitoring [3], Model Predictive Control [5] and sensorless control [4]. Before using any IM model for parameter identification, it is important to assess its identifiability.

Several approaches for identifiability analysis have been proposed in the literature [10, 18, 26, 27]. In general, identifiability analysis can be done either structurally or practically. In structural (a priori) analysis, the model structure is considered and no attention is paid to any restrictions related to the model operation. A structural non-identifiability arises when there are redundant parameters in model structure. The most obvious case of non-identifiability is over-parameterisation in the sense that the model can be rewritten in terms of smaller sets of parameters. This kind of non-identifiability is known as parameter redundancy, where it is not possible to uniquely estimate all the parameters in the model [28]. If such a non-identifiability occurs, it is essential to be removed analytically by introducing new restrictions, e.g. an identifiable combination of some non-identifiable parameters [29].

In practical (posteriori) identifiability analysis, identifiability is tested by finding out if the measured information is enough to estimate the parameter reliably or not. The idea of practical identifiability approaches is to test model identifiability using simulated or measured data [22]. Practical identifiability is mainly dependant on the accuracy of the available experimental data and therefore, a model that is structurally identifiable may still be practically unidentifiable if the experimental data are not sufficient [30].

In this investigation, the two methods will be applied to assess the identifiability of IM. The obtained results from the practical identifiability analysis should agree with the outcomes obtained from structural methods.

2.2 Theoretical background of the employed approaches

This section gives a theoretical background on the five identifiability test methods used in this thesis. The first three approaches, the transfer function, the bond-graph and the alternating conditional expectation (ACE) are used only for identifiability analysis in chapter (5). The other two approaches, Levenberg-Marquardt (L-M) and particle swarm optimization (PSO) in conjunction with measured time-domain data are used for identifiability analysis in chapter 5, parameter identification in chapters 5 and 6, and condition monitoring in chapter 7.

2.2.1 The transfer function approach

Recently, some work has been carried out to obtain general criteria for a priori identifiability analysis based on the transfer function of the system [31]. This is a simple approach that can be used if the transfer function of the model is known.

The complete dynamic model with parameter vector **P c**an be described as:

$$\begin{aligned} \dot{\mathbf{X}}(t) &= \mathbf{A}(\mathbf{P})\mathbf{X}(t) + \mathbf{B}(\mathbf{P})\mathbf{U}(t) \\ \mathbf{Y}(t) &= \mathbf{C}(\mathbf{P})\mathbf{X}(t) + \mathbf{D}(\mathbf{P})\mathbf{U}(t) \end{aligned} \tag{2.3}$$

where **X** is the state vector, **U** is the input vector, **Y** is the output vector, **A** is the state matrix, **B** is the input matrix, **C** is the output matrix, and **D** is the feed forward matrix. Any dynamical system can be completely characterized by its transfer matrix $\mathbf{G}(\mathbf{P})$. The transfer function for this model is:

$$\mathbf{G}(\mathrm{S},\mathbf{P}) = \mathbf{C}(\mathbf{P})(\mathrm{S}\mathbf{I}-\mathbf{A})^{-1}\mathbf{B}(\mathbf{P}) + \mathbf{D}(\mathbf{P}) \qquad (2.4)$$

In this approach, the transfer functions are written in a canonical form, common factors in numerator and denominator are cancelled and the transfer function is simplified so that the coefficients of the higher power of S in the denominator is always one. After this simplification, all the transfer function's coefficients are often referred to as moment invariants. The identifiable parameters are the parameters that can be uniquely deduced from the coefficients of the transfer function matrix [32]. If it is not possible to uniquely determine the parameters from the transfer function coefficients, it is essential to re-arrange the model or to use another model [33, 34].

2.2.2 *Bond graph approach*

Bond-graph modelling is a graphical representation that can be used to describe various systems including electrical, mechanical, hydraulic and chemical systems [35]. The graphical nature of the bond graph enables the characteristics of the model to be easily visualized and determines whether or not the model is appropriate for the task in hand [36]. In this approach, the system can be represented by lines and symbols identifying the power flow paths of the system by a combination of efforts and flows.

The bond graph has five types of elements; two active and three passive. The two active elements are the bond graph sources i.e. effort source *SE* (voltage) and flow source *SF* (current). The remaining three are represented by an *R*, *L* and *C* for resistive, inductive and capacitive elements, respectively. Each of these elements has a single power bond attached (line with the element at the end of the bond) showing the exchange of the power at one location. Any interface between two elements in the bond graph is known as a port. In electrical domain, port variables of the bond graph are the voltage over the element port and the current through the element port.

A simple example to clarify the concept of the bond graph is to derive the bond graph of the series RLC shown in figure 2.2. For this circuit, the effort source *SE* is the voltage *v* and the flow source *SF* is the current *i*. The different bond graph elements in this circuit are shown in figure 2.3 (a).

Power bond may join in one of two types of junctions called 1-junction and 0-junction. 1-junction represents locations in the circuit with common current flow, where 0-junction represents nodes of the circuit where voltages are same. Consequently, series connected elements are connected at 1-junction while parallel branches are connect at 0-junction. A power flow diagram is created by connecting the elements in an energy conserving mode by means of junctions and nodes. Figure 2.3 (b) shows the bond graph of the RLC circuit where the common current in the bond graph becomes a 1-junction.

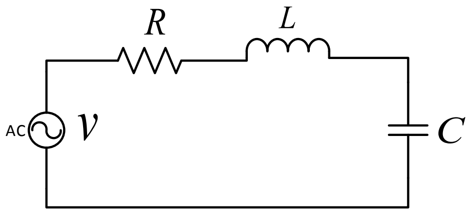

Figure 2.2 The RLC circuit.

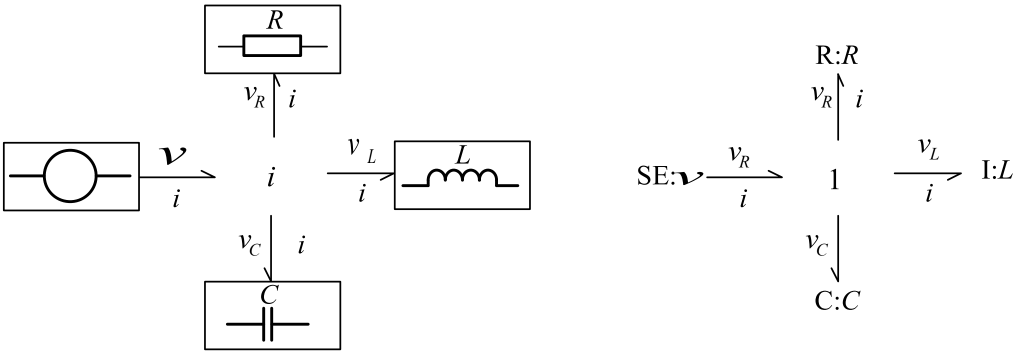

(a) **(b)**

Figure 2.3 Bond graph of the RLC circuit, (a) with electrical symbols, (b) with standard symbols.

Bond graphs have a concept called causality that indicates the direction of the effort and flow for each bond of the power flow diagram and identifies the causal relationships between all variables. For each bond, causality is identified by the causal stroke (end-bar) which is independent of the power flow direction. The causality chooses which one of the two elements linked by a bond sets the effort and which one sets the flow. The effort information moves toward the causal stroke and the flow information moves away from it as shown in figure 2.4 (a).

The R-element dissipates energy and, therefore the energy flows towards the resistor is always positive. It does not matter which of the port variables is the output and which one is the input. Therefore, causal stroke for R-element can go on both directions in such a way to satisfy the junction at the other end of the bond. For the energy storing elements, L-element and C-element, the L–element has a flow out causality and C–element has an effort out causality. Figure 2.4 (b) shows the causal stroke assignment for the R-, L-, and C- elements [35].

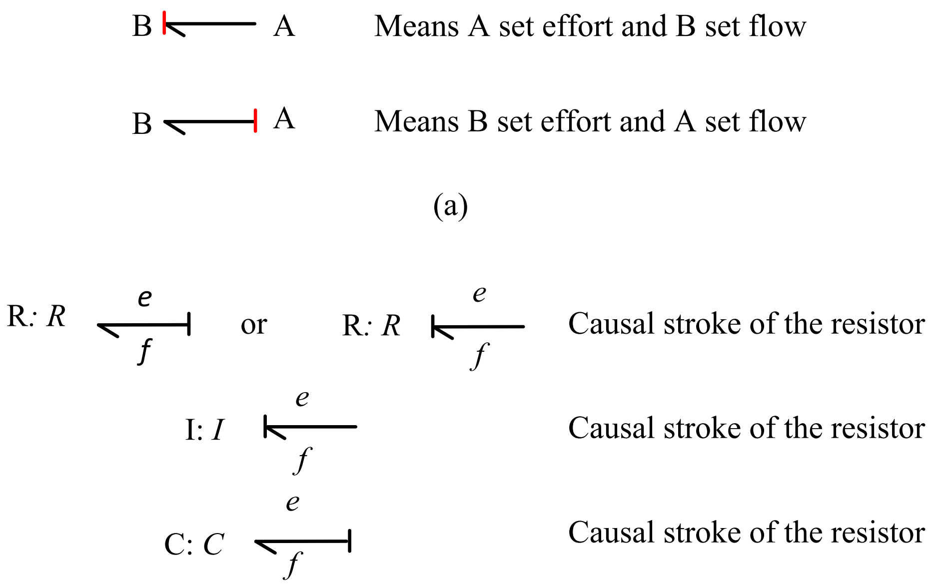

(a)

(b)

Figure 2.4 (a) Causal stroke assignment procedure, (b) causal stroke of R-, I- and C-elements.

At 0-junction, one of the bonds sets the effort for the others. Consequently, only one causal stroke is on the 0-junction, while the others are away from it. At 1-junction, one bond sets the flow; indicates that only one bond has the causal stroke away from the 1-junction, while the others are on it [18, 35]. Figure 2.5 shows the bond-graph of the RLC circuit. The causal strokes are set in accordance with the procedure discussed above. At 1-junction, the effort (v) of source *SE* moves towards its causal stroke while the flow (i) moves away from its causal stroke. The inductor element imposes flow, hence can be modelled as a source with a causal stroke at the element side. The capacitor element has effort-out, hence can be modelled as a source with a causal stroke far from the element side.

For a resistive element, causal stroke can go on both directions in such a way to satisfy the junction at the other end of the bond. For a proper causal completion, the causal strokes for R is set near to 1-junctions. Figure 2.6 shows how to generate the bond-graph from a physical model.

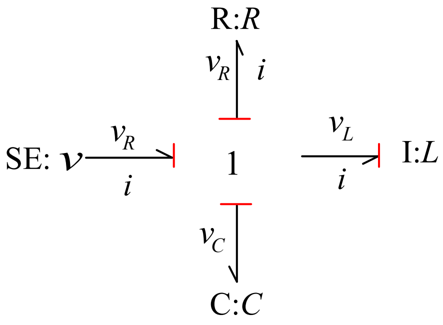

Figure 2.5 RLC circuit causal bond graph.

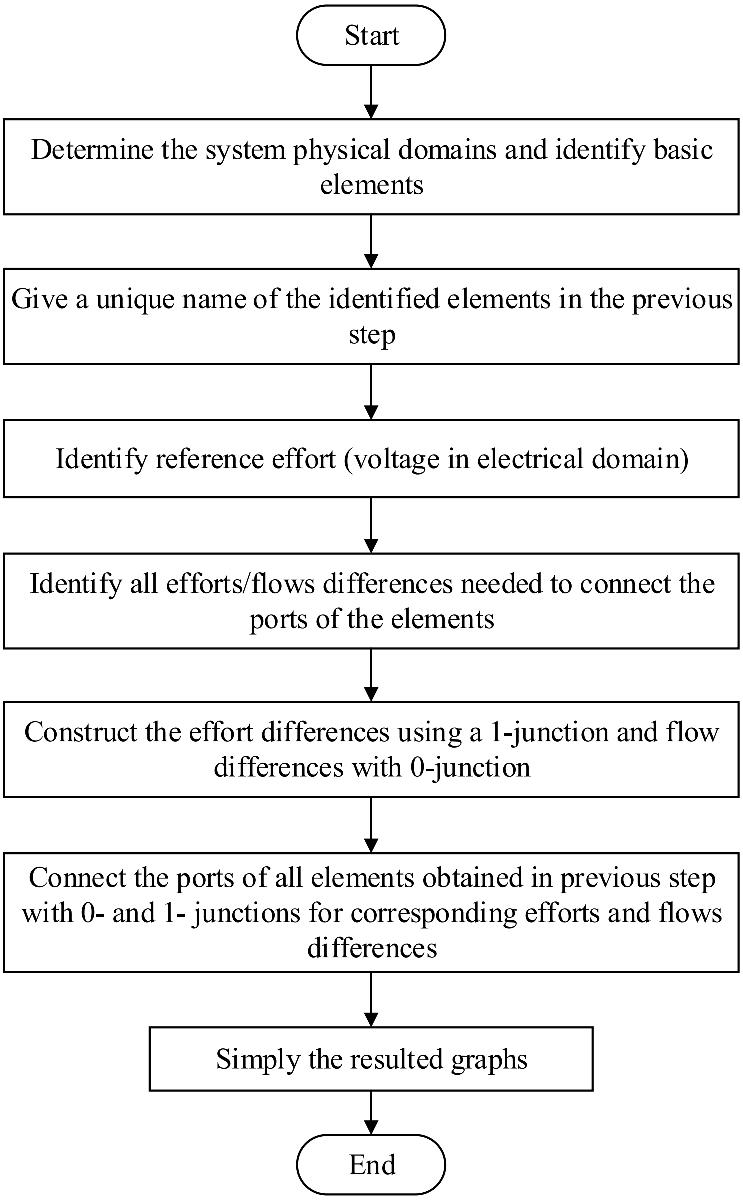

Figure 2.6 How to generate a bond-graph model from a physical model.

2.2.3 Alternating Conditional Expectation

The Alternating Conditional Expectation (ACE) algorithm was initially developed in 1985 for the purpose of regression analysis to estimate the relationship between variables [37]. It is a simulation-based approach that can be used to determine whether the model is identifiable or not. The power and usefulness of this algorithm lie in its ability to identify the effect of one or more independent variables (predictors) on a dependent variable (response) and reveal accurate relationships between them. In addition, ACE is a non-parametric approach that does not require any assumptions about the functional relationship between the dependent and independent variables [10].

In the ACE approach, the problem of estimating a linear function of n-dimensional predictors **P**= $(p_1, p_2, \ldots, p_n)$ and a response Y is replaced by estimating n separate one-dimensional functions of the predictors and a function of the response [38] as expressed by:

$$\theta(Y) = \sum_{i=1}^{n} \phi_i(p_i) + \varepsilon \tag{2.5}$$

where θ is a function of the response variable Y, $\emptyset_i$ is a function of the predictor p_i and ε is an independent normal random variable. These transformations are achieved through minimizing the variance of a linear relationship between the transformed response variable and the summation of transformed predictor variables. The normalized error variance (e^2) (for $\|\theta\|^2 = 1$) is given by:

$$e^2(\theta, \phi_1, \ldots, \phi_n) = E\{[\theta(Y) - \sum_{i=1}^{n} \phi_i(p_i)]\}^2 \tag{2.6}$$

The minimization of the error is carried out through a series of individual function minimizations that result in the following expressions:

$$\phi_i(x_i) = E[\theta(Y) - \sum_{j \neq i} \phi_i(p_j) \big| p_i] \tag{2.7}$$

$$\theta(Y) = \frac{E[\sum_{i=1}^{n} \phi_i(p_i) \big| Y]}{\left\| E[\sum_{i=1}^{n} \phi_i(p_i) \big| Y] \right\|} \tag{2.8}$$

These two equations represent iterative minimization and conditional expectation (E), from which the name of Alternating Conditional Expectation is derived. Figure 2.7 shows the operational steps of the ACE algorithm.

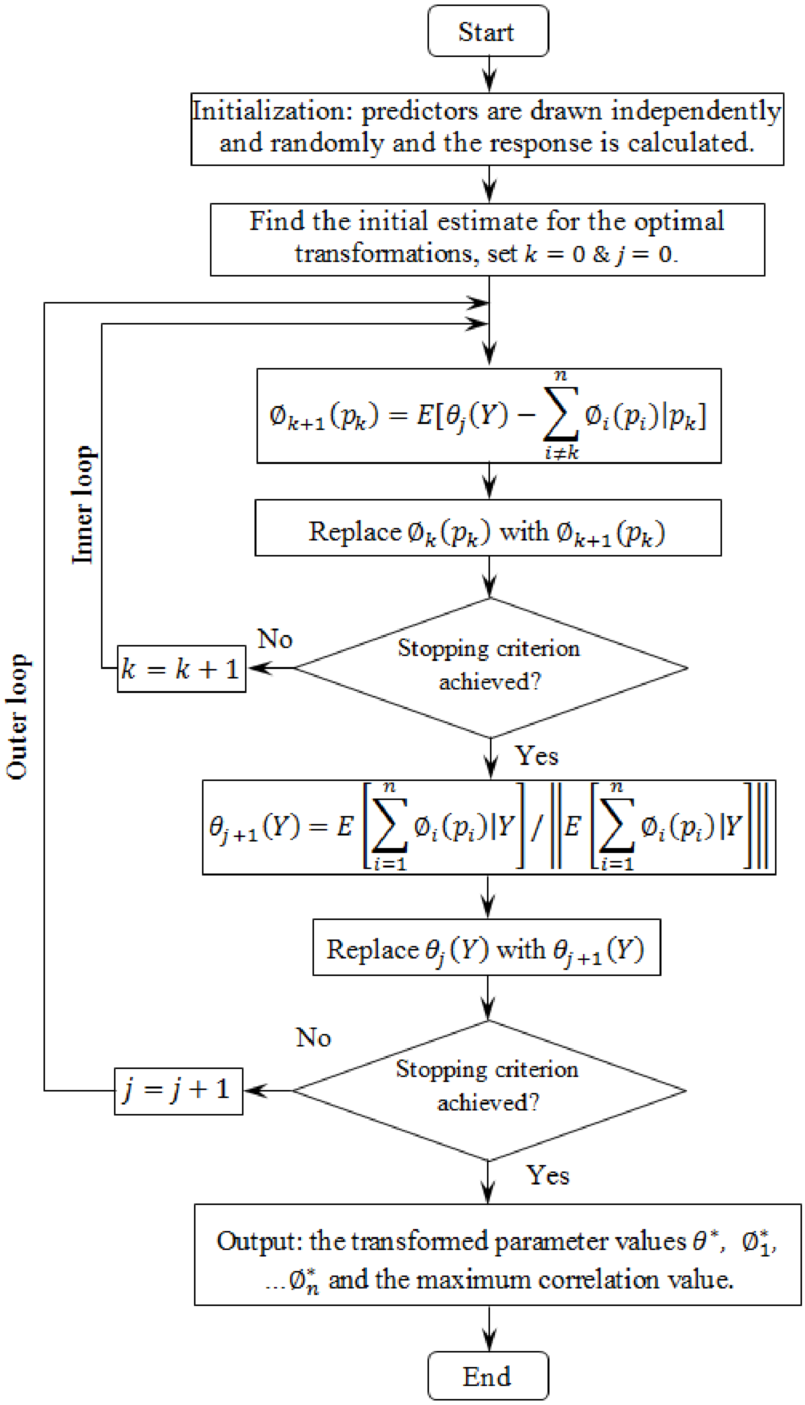

Figure 2.7 ACE Algorithm description.

For a simple two dimensional case, considering two random variables p and y with zero expectation $E[p] = E[y] = 0$, the functions $\theta(y)$ and $\phi(p)$ are called optimal transformations if they satisfy:

$$\frac{E[\theta(y) - \phi(p)]}{E[\theta^2(y)]} = \min \tag{2.9}$$

This is equivalent to the maximization of the correlation coefficients between the transformed variables $\theta(y)$ and $\phi(p)$. ACE estimates the optimal transformations $\hat{\theta}(y)$ and $\hat{\phi}(p)$ which maximize the linear correlation R between $\hat{\theta}(y)$ and $\hat{\phi}(p)$ [39] non-parametrically (i.e. based on classification and ranking, not actual numbers):

$$\{\hat{\theta}, \hat{\phi}\}_{y,p} = \sup_{\hat{\theta},\hat{\phi}} \left| R(\hat{\theta}(y), \hat{\phi}(p)) \right| \tag{2.10}$$

with a correlation coefficient:

$$R(p, y) = \frac{E[py] - E[p]E[y]}{\sqrt{E[p^2]E[y^2]}} \tag{2.11}$$

where the goal is to minimize $\|\theta(y) - \phi(p)\|^2$ with $\|\theta\|^2$=1.

The maximum correlation coefficient R ($-1 \leq R \leq 1$) is used as a measure of the relationship between two variables p and y. R=0 if and only if p and y are independent. A large correlation coefficient, such as ±0.8, would suggest a strong relationship between parameters which may make a model not-identifiable. On the other hand, a small correlation coefficient, such as ±0.3, suggests weaker parameter dependence and an identifiable model.

This concept can be extended to higher-dimensional problems with more than one predictor variable, i.e.

$$\frac{E[(\theta(y) - \sum_{i=0}^{n} \phi_i(p_i))^2]}{E[\theta^2(y)]} = \min \tag{2.12}$$

The calculation of (2.12) is carried out iteratively by the algorithm where new estimates of the transformation of the response serve as an inputs to new estimates of the transformation of the predictors and vice versa.

A simple example to demonstrate the use of the ACE is to consider a multivariate (multi-dimensional) case with three predictors (p_1, p_2, p_3) and a response y. Five hundred tuples of predictors are drawn independently and randomly from the interval $[0, 1]$ and the response is calculated for each tuple from (2.13), imitating 500 different observations.

$$y = 0.5p_1^3 + \tan^{-1}(p_2) \tag{2.13}$$

This was repeated three different times and, accordingly, three different matrices $\mathbf{k}_i = [y\ p_1\ \ p_2\ \ p_3]$ (i=1, 2 and 3) with dimension of 500×4 are obtained and serve as inputs for the ACE algorithm. Functionally related parameters provide quite stable optimal transformations from one sample to another and from the one matrix to another. If there is a relation between parameter, all matrices ($\mathbf{k_1}$, $\mathbf{k_2}$ and $\mathbf{k_3}$) render the same optimal transformations from one sample to another and vice versa. Figure 2.8 shows a scatterplot of these data sets after applying ACE three times, where the three different colours illustrate the three estimates ($\mathbf{k_1}$, $\mathbf{k_2}$ and $\mathbf{k_3}$).

As shown in the figure, for each estimate (a row of the matrix k), only the first three columns (y, p_1 and p_2) are functionally related (based on Equation 2.13) and the forth (p_3) is independent and, thus nearly linear transformations for all variables except p_3 exist. The transformations of the first three parameters (y, p_1 and p_2) remain stable from one sample to another and from one estimate to another, while the transformation of the fourth parameter (p_3) looks different. The estimated regression model of (2.13) from ACE transformed variables has a maximum correlation value of 0.99986 which is almost equal to 1. Such a high correlation coefficient between the parameters means that the model is non-identifiable.

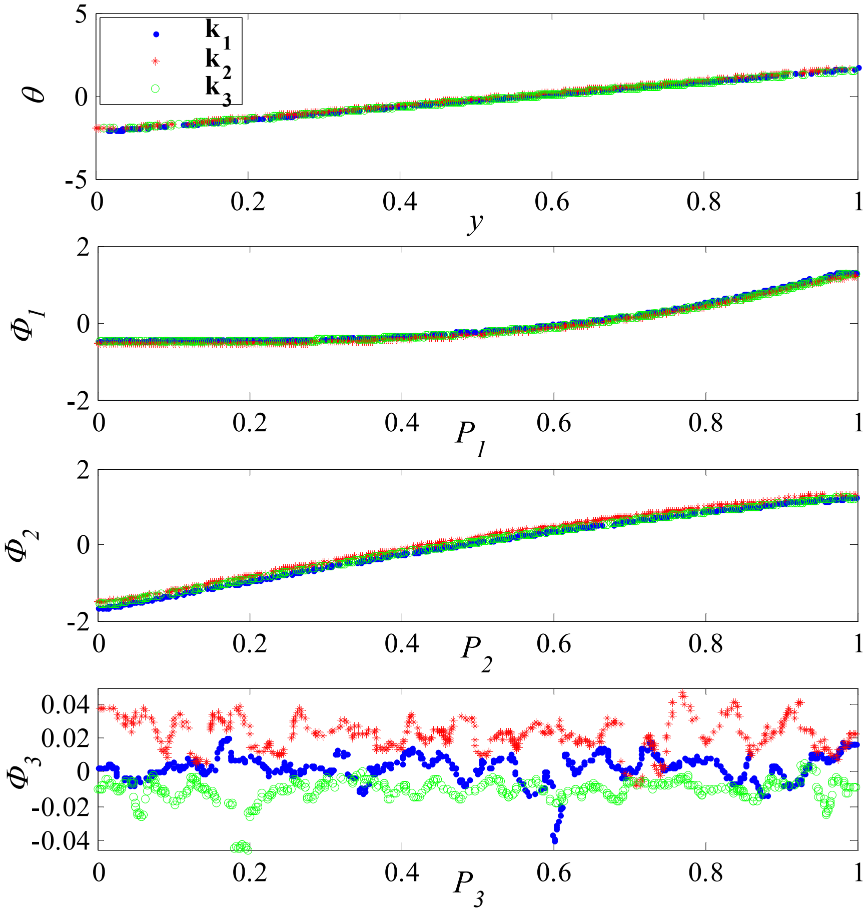

Figure 2.8 ACE optimal transformation of equation (2.13) data.

2.2.4 Particle Swarm Optimization

Particle Swarm Optimization (PSO) is a population based stochastic optimization technique inspired by the social behaviour of large animal swarms such as birds flocking or fish schooling. PSO was originally designed and developed by Eberhart and Kennedy [40]. Each potential solution, called particle, is interpreted as a solution to the problem being investigated and allowed to fly through the search space. During the process, each member (particle) cooperates with the others trying to find a global optimum (global best) in a partially random way. As soon as a new better solution (objective function) is obtained, the global best will be updated with this new best solution [41]. A member with low fitness will not be discarded, it is still surviving and it is possible to be potentially the future successful member of the swarm.

With the PSO, the system is initialized randomly and searching for optima by updating generations, similar to many other computation techniques. However, it is much simpler and each particle has its own memory that allows it to remember the best position and fitness that has been achieved so far. In addition, each particle shares the information with its neighbours and adjusts its behaviour according to the best experiences of the swarm. In N-dimensional space, the main steps of PSO can be summarized in the flowchart shown in figure 2.9.

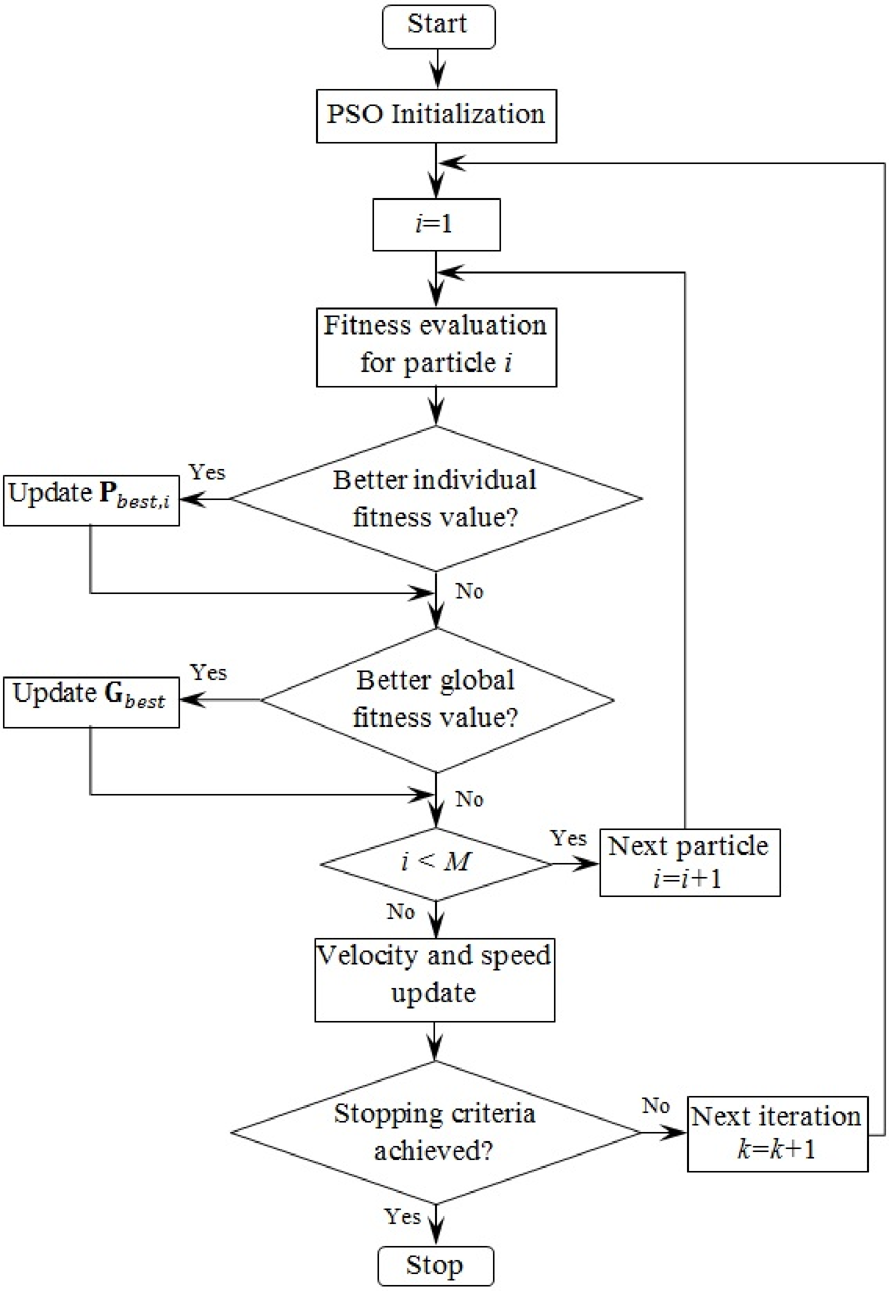

Figure 2.9 The flowchart of Particle Swarm Optimization.

Each member in the swarm keeps tracking three main variables; the objective function, the global best (that indicates which particle is close to the best optima) and the stopping criteria that is used to stop the swarm if the optima has not been found. Each particle i has a position $\mathbf{X}_i$ and treated as a point in N-dimensional space representing the optimization problem, so that: $\mathbf{X}_\mathrm{i} = (x_{i1}, x_{i2}, \ldots, x_{iN})$ for $i = 1, 2, \ldots, M$, where N is the dimension (the number of variables) and M is the number of particles that form the population.

PSO assumes all the particles to fly in the search space with velocity $\mathbf{V}_i$ that is continuously adjusted according with the flying history of the particle and other members in the population, so that: $\mathbf{V}_\mathbf{i} = (v_{i1}, v_{i2}, v_{i3}, \ldots, v_{iN})$, for $i = 1, 2, \ldots, M$, where the velocity is the rate of change of the position per unit iteration.

Considerable research has been done in order to improve the performance of the PSO. In this thesis, an improved version of the PSO described in [42] has been used. This version of the PSO introduces an inertia weight variable to control the exploitation and impact of the previous and current velocities. This variable significantly affects the exploration and the speed of convergence of the PSO algorithm.

The motion for each particle can be determined by the following equations:

$$\mathbf{V}_{in}^{k+1} = \omega \mathbf{V}_{in}^{k} + c_1 r_1 \left(\mathbf{P}_{in}^{k} - \mathbf{X}_{in}^{k}\right) + c_2 r_2 \left(\mathbf{G}_{Jn}^{k} - \mathbf{X}_{in}^{k}\right) \tag{2.14}$$

$$\mathbf{X}_{in}^{k+1} = \mathbf{X}_{in}^{k} + \mathbf{V}_{in}^{k+1} \tag{2.15}$$

where k is the iteration number, ω is the inertia weight, $n = (1, 2, \ldots, N)$, r_1 and r_2 are random numbers between 0 and 1 standing for the weight that particle gives to its own best position and that for its best neighbour's position, $P_{in} = (p_{i1}, p_{i2}, \ldots, p_{iN})$ is the previous best position of the i^{th} particle (that gives the best fitness value), and $\mathbf{G}_{Jn} = (g_{J1}, g_{J2}, .., g_{JN})$ is the global best position of the best particles (J) in the swarm. c_1 and c_2 are accelerating coefficients that determine the maximum position step size of the particle in a single iteration [43].

Figure 2.10 shows the main three fundamental displacement of each particle according to the current velocity, its own best performance and performance of the best particle in the swarm.

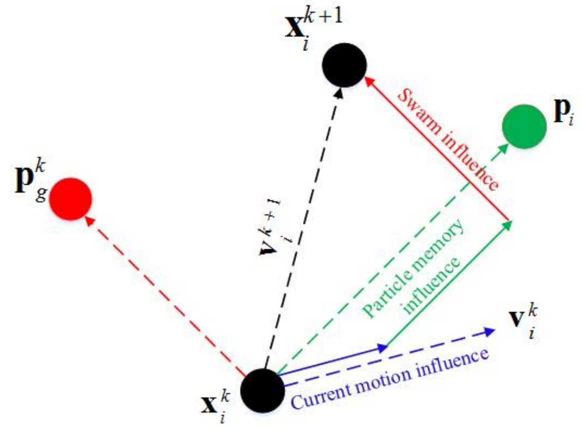

Figure 2.10 Schematic representation of the motion of particle in PSO.

For each iteration *k* (time step), the position vector in Equation (2.15) is updated with the velocity vector obtained from Equation (2.14) and the process is repeated until the stopping criteria are achieved. As can be seen from equations (2.14) and (2.15), the main parameters of the PSO model are the inertia ω, the accelerating coefficients c_1, c_2, and the swarm size *M*. It is important to choose the correct parameters in order to get reasonable results to the optimization problem. As a result, it is important to have knowledge of the effects of choosing different setting of parameters from one problem to another, so that it will be possible to pick to most appropriate setting for a specific problem.

The inertia weight ω plays an important role in controlling the momentum of the particles. Depending on the value of ω the momentum will be changed. The original PSO velocity update equation can be obtained by setting ω=1. If ω was zero ($\omega=0$), then the concept of velocity will be totally lost and the particle will move in each step without any knowledge of the previous velocity. For $\omega \ll 1$, the momentum preserved from the previous step will be little and quick changes of direction will be possible with this setting. For $\omega > 1$, the particles can change their direction hardly and as a result a large exploration area will be required and there will be difficulties to converge towards optimum.

Large number of particles reduces the speed and increases the number of function evolutions in order to converge to an error limit. The population size has a slight improvement on the optimal value and a smaller population sizes are usually more appropriate with the PSO method [44]. It is very common to limit the number of the particles between 20 and 60 [45]. In the literature, many efforts have been made in order to find the optimal values for c_1 and c_2 in equation (2.14) and many values have been suggested to these parameters in different applications. In this work, the values of c_1 and c_2 are chosen to be equal [45].

In many applications it is important to confine the search space in order to avoid a particle leaving the search space. A simple confinement mechanism that is used in this work is described by the following operator [46]:

$$x_n^k \notin [x_{\min}, x_{\max}] \rightarrow \begin{cases} v_n^k = 0 \\ x_n^k < x_{\min} \rightarrow x_n^k = x_{\min} \\ x_n^k > x_{\max} \rightarrow x_n^k = x_{\max} \end{cases} \qquad (2.16)$$

where x_{max} is the upper limit and x_{min} is the lower limit.

Herein, the PSO algorithm is used to find the best-fit and to locate the minimum value of one of the most commonly used test functions called the Griewank function which is given by:

$$f(t) = \frac{(p_1 - 100)^2 + (p_2 - 100)^2}{4000} - \cos\left(\frac{p_1 - 100}{\sqrt{1}}\right) \times \cos\left(\frac{p_2 - 100}{\sqrt{2}}\right) + 1 \qquad (2.17)$$

This is a two dimensional 2-D function has one global minimum of zero value at point (100,100). As shown in figure 2.11, the global minimum of this function is almost indistinguishable from many other local minima that closely surround it, which increases the difficulty of the problem.

The PSO was initialized with 8 particles that generated and distributed randomly in the search space. Values of ω= 1.414 and c_1= c_2= 1.2 were used in this test. Each particle is interpreted as a solution to the Griewank function and has been allowed to fly through the search space. The task of the PSO is to update the particles (parameters' values) to minimize the objective function. As soon as better optimum is discovered the best optimum will be changed. Figures 2.12 and 2.13 show the convergence history of the estimated parameters (p_1 and p_2) and the error function, respectively. It can be observed that the PSO algorithm success the find the global optimum at (99.5355, 100.3194) with a small error of 0.0429.

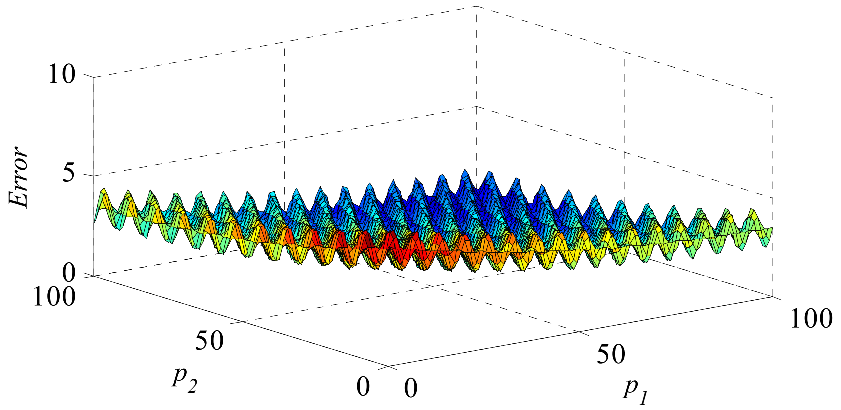

Figure 2.11 Griewank function, Minimum 0 at point (100, 100).

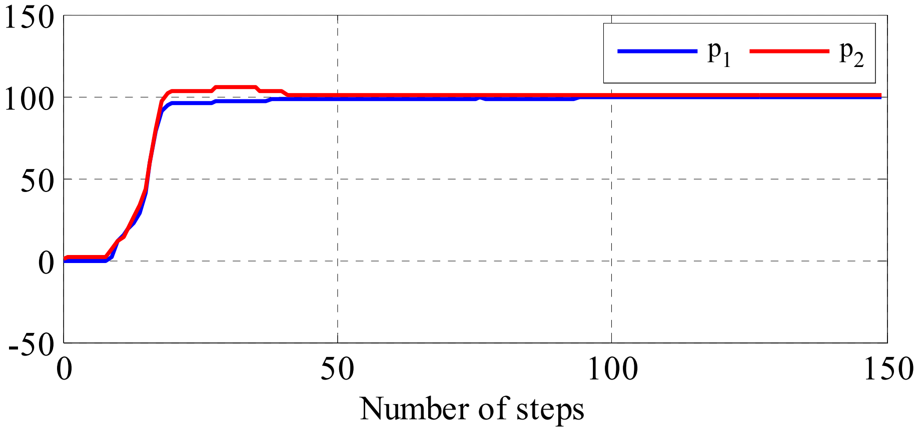

Figure 2.12 Convergence of the estimated parameters of the Griewank function.

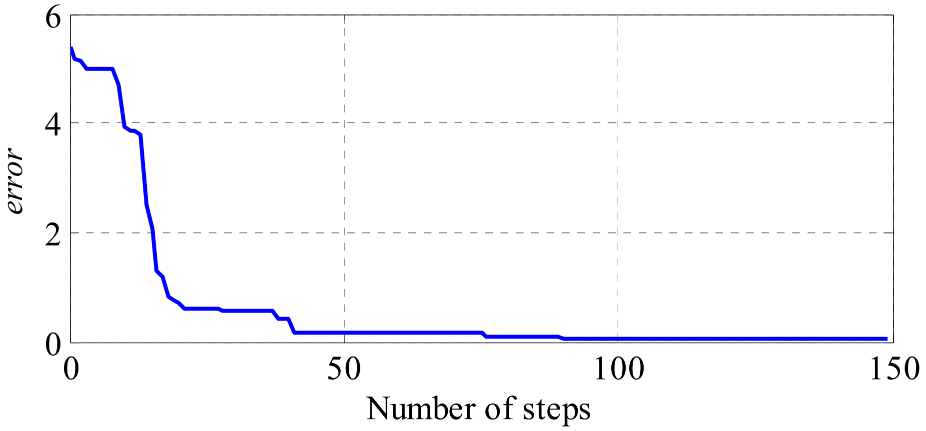

Figure 2.13 Error function convergence of the estimated parameters of the Griewank function.

2.2.5 *Levenberg-Marquardt Algorithm*

The Levenberg-Marquardt (L-M) [10, 47] optimization tool is developed and employed in this project to estimate the parameters of the T- and Inverse Γ-models of the IM. The L-M algorithm is an optimization technique that uses a combination of two methods; the Gauss-Newton method and the Gradient Descent method [47]. The parameter values are updated in the opposite direction to the gradient of the objective function (error) and the error is reduced by assuming that the objective function is approximately quadratic near to the optimal solution.

Like many parameter estimation algorithms, especially for nonlinear models, the L-M algorithm is based on the minimization of an index (usually an error). The most commonly applied procedure is to search the best parameters set $\mathbf{P}^*$ in the search space that minimize the error function *err*,

$$err* = \min(E(\mathbf{P})) \tag{2.18}$$

Herein, the L-M algorithm is used to find the best-fit model parameters by minimizing an objective function, the weighted square errors between the measured data vector $\mathbf{Y}_\mathrm{m}(\mathrm{t})$ and the calculated data vector $\mathbf{Y}_\mathrm{c}(\mathrm{t})$. This is known as a chi-squared error criterion, given by:

$$\begin{aligned}\chi^2(\mathbf{P}) &= \sum_{i=1}^{q}\left[\frac{\mathbf{Y}_\mathrm{m}(t_i)-\mathbf{Y}_c(t_i,\mathbf{P})}{\omega_i}\right]^2 \\ &= (\mathbf{Y}_\mathrm{m}(t_i)-\mathbf{Y}_C(t_i,\mathbf{P}))^T\mathbf{W}(\mathbf{Y}_\mathrm{m}(t_i)-\mathbf{Y}_c(t_i,\mathbf{P})) \\ &= \mathbf{Y}_\mathrm{m}{}^T\mathbf{W}\mathbf{Y}_\mathrm{m}-2\mathbf{Y}_\mathrm{m}{}^T\mathbf{W}\mathbf{Y}_c+\mathbf{Y}_c{}^T\mathbf{W}\mathbf{Y}_c\end{aligned} \tag{2.19}$$

where q is the number of data points, ω_i is a measure of the error in the measurement, W is a weighting matrix with $\mathbf{W}_\mathrm{ii} = 1/\omega_i^2$. The goal is to minimize χ^2 with respect to the parameters by finding the perturbation h to the parameters $\mathbf{P}$.

The update relationships are given by [47]:

$$h = \alpha\mathbf{J}^T\mathbf{W}(\mathbf{Y}_\mathrm{m}-\mathbf{Y}_\mathrm{c}) \tag{2.20}$$

$$[\mathbf{J}^T\mathbf{W}\mathbf{J}+\lambda diag(\mathbf{J}^T\mathbf{W}\mathbf{J})]h = \mathbf{J}^T\mathbf{W}(\mathbf{Y}_\mathrm{m}-\mathbf{Y}_\mathrm{c}) \tag{2.21}$$

where α is a positive scalar which determines the length of the step in the steepest-descent direction, $\mathbf{J}$ is an $q \times n$ Jacobian matrix $[\partial \mathbf{Y_c}/\partial \mathrm{p}]$ represents the local sensitivity of $\mathbf{Y_c}$ to variation in parameters, h is the perturbation that moves the parameters in the direction of the steepest descent, and λ is the damping parameter.

For each step (iteration), if the present λ produces a smaller error, then the step is applied and λ is divided by a constant σ. In contrast, if the present λ produces a higher error, the step is discarded and λ is multiplied by σ. L-M acts in a similar way to the Gauss-Newton method when parameters are close to their optimum values (small values of λ) and similar to the Gradient Descent method at large values of λ. Figure 2.14 shows the operational steps of L-M algorithm.

A simple example is given here where the L-M approach is used as an optimization algorithm to fit the following function (find the minima) to a set of measured data.

$$f(t) = p_1 \exp(-t / p_2) + p_3 \exp(-t / p_4) \tag{2.22}$$

Table 2.1 shows the real parameter values and the estimated solution based on the use of the L-M. It is obvious that the L-M algorithm can successfully estimate the parameters within an acceptable error. Figures 2.15 and 2.16 show the convergence history of the estimated parameters and the error, respectively. Figure 2.17 shows the real data points and the curve fit. As shown, a very good agreement between the two curves is realized. The squared error (χ^2) as a function of the two parameters (p_3 and p_4) is shown in figure 2.18.

Par.	Real par.	Estimated par.
p_1	20.00	19.918
p_2	10.00	10.159
p_3	1.00	0.9958
p_4	50.00	50.136

Table 2.1 Parameter Estimation of Equation (2.22).

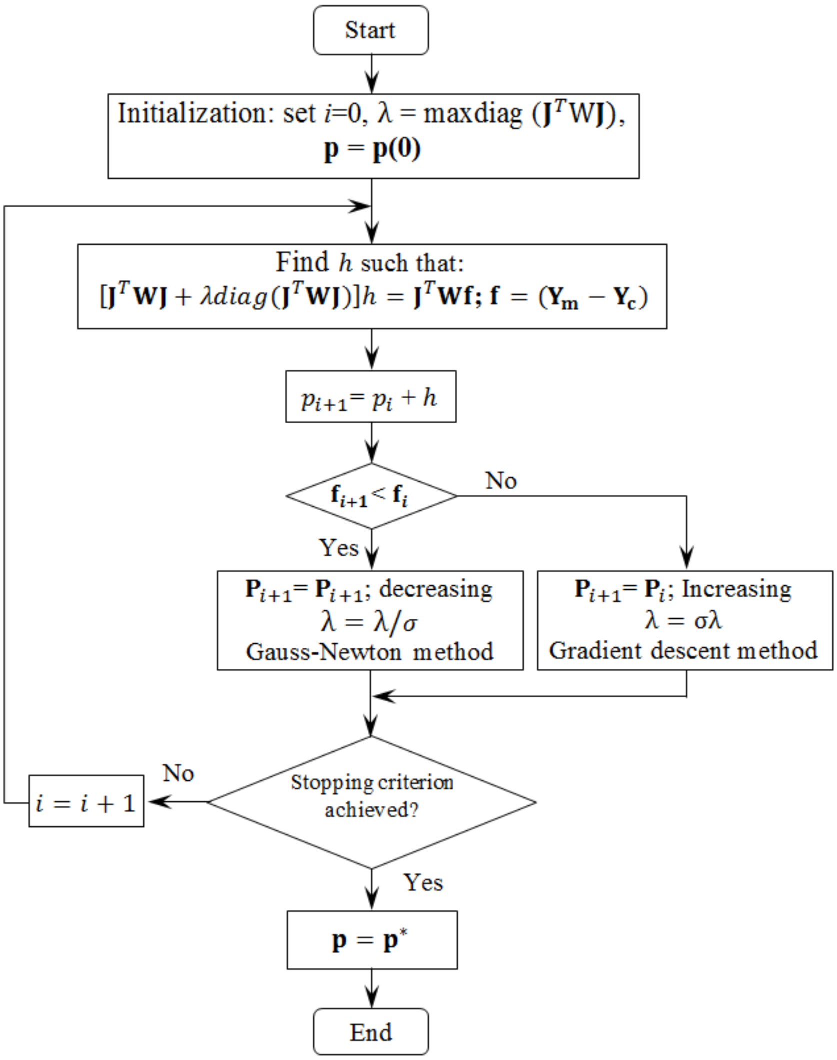

Figure 2. 14 Levenberg-Marquardt (L-M) Algorithm Description.

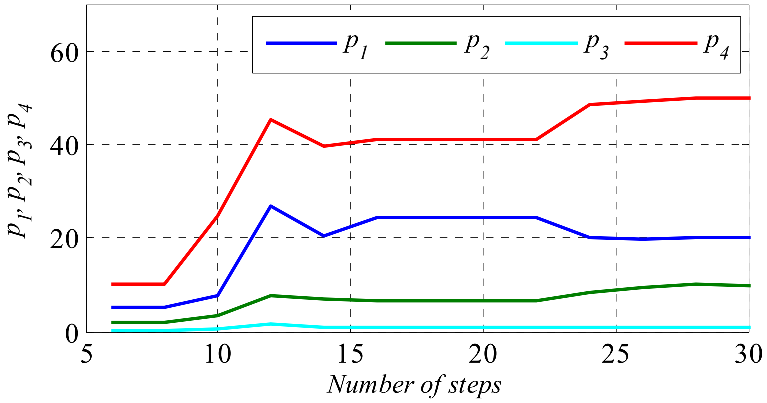

Figure 2.15 Convergence of the estimated parameters of the model (2.22).

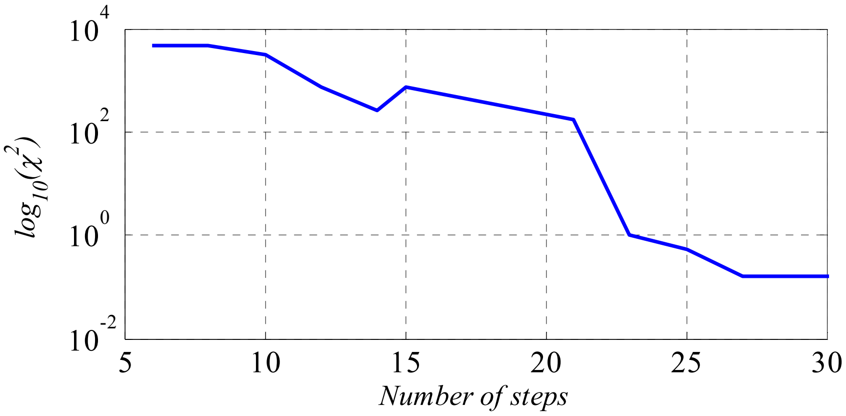

Figure 2.16 Error function convergence for the estimated (χ^2).

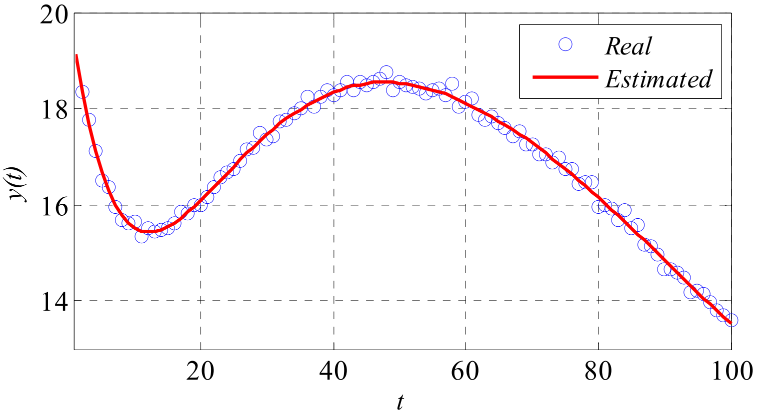

Figure 2.17 The real data points and the curve fit.

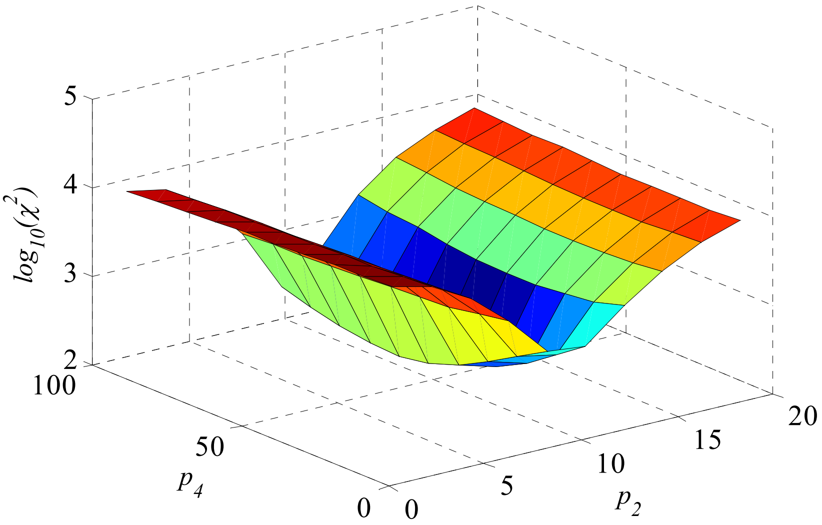

Figure 2.18 The sum of the squared errors as a function of p_3 and p_4.

2.3 Conclusion

The identifiability problem has been discussed and an example to help readers unfamiliar with this concept is introduced. The five employed methods in this thesis including the transfer function, bond-graph, alternating conditional expectation, particle swarm optimization and Levenberg-Marquardt are discussed. For the sake of clarification, mathematical examples for these methods have been given. In Chapter 5, the first three methods (transfer function, bond-graph and alternating conditional expectation) will be used only for identifiability assessment of IM steady-state models, while the other methods (particle swarm optimization and Levenberg-Marquardt) will be used for the identifiability, parameter identification and fault diagnosis purposes in Chapters 5-7.

CHAPTER 3

Induction machine parameter identification and fault diagnosis

Concepts of parameter identification and condition monitoring of induction machines are discussed in this chapter. An up-to-date survey of the current research state on both topics is introduced. The symptoms and mechanisms of the most common electrical/mechanical faults are presented.

3.1 Induction machine parameter identification

Parameter identification is the process of fitting parameters to an existing model of a system from external input-output measurements. The knowledge of the IM parameters allows estimating what the machine dynamics would be if the operating conditions have been changed. Parameter identification of IMs is important and very useful for many applications including sensorless control [4], Model Predictive Control (MPC) [5], and fault diagnosis [3].

In practice, IM parameters have been identified based on the data measured from the motor. Tests of no-load, dc and locked rotor, during which the rotor has to be disconnected from the load or kept mechanically locked, are performed and measurements of the current and voltage at the stator terminals are taken, as detailed in IEEE Standard 112-2004 [48]. However, those tests become impractical when the motor has been coupled to a load [49]. Importantly, it is not possible to determine the stator and rotor leakage inductances (l_{ls} and l_{lr}) separately from the measurements at the stator terminals using these tests. One way to determine them separately is to assume that $l_{ls} = l_{lr}$, which is not always true (e.g. for a faulty machine) and might lead to a wrong parameter estimation [10]. When the ratio (l_{ls}/l_{lr}) is unavailable or when the machine in question is in operation and it is not possible to carry out the standard tests, an alternative parameter identification approach is required.

A variety of IM parameter identification methods based on external measurements of stator voltages, stator currents, speed and/or torque have been proposed in the literature [6, 9, 10, 50, 51]. Most of these methods use many assumptions and require prerequisite information about the investigated model. For example, some methods may limit the number of estimated parameters (assuming constant values for the other parameters of the model) in order to reduce the complexity and increase the accuracy of the estimation process [52]. The majority of those approaches can be categorized into two main groups: 1) signal-based [53, 54]; 2) model-based [6, 8, 55-57].

A. signal-based induction machines' parameter identification

Signal-based techniques are usually system specific and require more computational power and extra hardware to be implemented. This type is based on the analysis of characteristic frequencies in the voltage and/or current spectrum components by using algorithms such as the fast Fourier transform (FFT) [58]. These components are based on the measurement response to deliberately injected test signals or to existing characteristic harmonics [59]. An example of signal-based IM parameter identification approaches is to inject negative sequence current and detecting the negative sequence voltage and, thus the required parameter can be estimated from the mathematical model [60, 61]. This technique, however, produces a strong second harmonic torque pulsation in the system due to the interaction of the positive and negative rotating components of the Magnetic Motive Force (MMF) [59]. A different approach is based on injecting sinusoidal perturbation into the flux producing stator current [62]. Although this technique can provide a good estimation, the cost is very high due to the need of installation two flux search coils [59]. A different approach is based on injecting a pseudo-random binary signal into the d-axis and correlating with q-axis is used for the estimation. With light load operating condition, however, this techniques does not provide good estimation [59].

Although signal-based methods perform well with some applications, they are more complicated in terms of computations and need more sophisticated components and external hardware to be implemented. In addition, most of these approaches cannot be used during the normal operating conditions while the machine is running and, thus it is hardly been used in industrial applications. Moreover, injecting such signals may cause to disturb the system behaviour and produce losses.

B. Model-based induction machines' parameter identification

Due to their simplicity and low cost of implementation, model-based parameter identification approaches are the most widely used [56]. In general, model-based approaches are based on the construction of a mathematical model of the target system that allows estimating its parameters [63]. The model of the system is fed with the measured inputs of the real system. The model output is then compared with that of the system and the difference between the two outputs (the error) is passed to an optimization algorithm that adjusts the model parameter values until a minimum error value between measured and calculated outputs is achieved. The model parameters identified by the optimization algorithm at this minimum error point are then taken as the correct model parameters.

Model-based techniques can deal with different types of models like ordinary differential equations, intelligent data-driven models, artificial neural network models and fuzzy logic models [64]. The main advantage of model-based techniques is no additional hardware or components needed to realize the parameter identification algorithm [10, 65]. The accuracy of this type is greatly dependent on the used IM model for parameter estimation. A block diagram for model-based parameter identification of the induction machine is shown in figure 3.1.

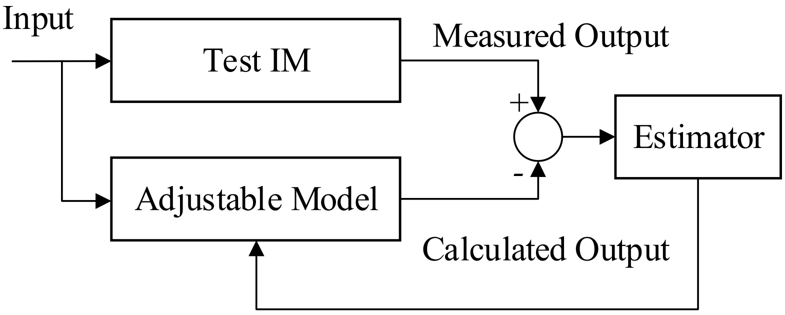

Figure 3.1 A Block diagram of model-based parameter identification scheme.

Various model-based techniques have been proposed in the literature. The main differences between all these techniques are the used machine model and the applied algorithm for error (the difference between the calculated and measured outputs) calculation. Among model-based techniques, observer-based techniques have recently received much attention [66, 67]. These techniques are used to estimate the parameters of the IM during the normal operation. Some of these techniques are based on the use of the extended Kalman filter (EKF) that can be used under noisy condition with a high accuracy of estimation [68, 69]. However, EKF is known as being complex model-based algorithm and computationally very intensive [59, 68]. An extended Luenberger observer (ELO) for state and parameter estimation is presented in [70, 71]. The major disadvantage of this technique is its computational intensity. Other approaches are based on the model reference adaptive system (MRAS) [72-74]. The basic idea of this method is to optimize the model parameters so that the output of the model is close to the output of the reference model. The accuracy of MRAS methods is heavily dependent on the used reference model (which is usually difficult to be determined [75]) and the used optimization technique algorithm for error minimization.

Recently, optimization algorithms have been extensively improved and utilized in many applications and different fields such as finance [76], engineering design [77] and curve fitting-based identification methods [10, 78]. The fundamental principle of such techniques is to search for an optimum solution for the model. These techniques have been motivated by their reliability, availability and ability of dealing with multidimensional and nonlinear problems within a relatively short time [79]. According to the method of the operation, optimization algorithms can be classified into two basic classes; deterministic and stochastic.

Deterministic algorithms take the advantages of the analytical properties of the problem to generate a sequence of steps that finally converge to an optimum solution which might not be the global one, as shown in figure 3.2. They do not include instructions that use random numbers in order to modify the data or to decide what to do next. Such algorithms always produce the same results when giving the same inputs. In the literature, several deterministic techniques exist such as linear programming, nonlinear programming, and mixed-integer nonlinear programming [80]. However, if the problem in hand has a high dimensional space or too complicated, deterministic techniques become impractical and, thus stochastic techniques come into play.

Stochastic optimization algorithms were developed and extensively used in engineering systems since 1950s [81]. They are also known as a probabilistic optimization methods and classified as the most recent and powerful computational products of artificial intelligence techniques [52, 82]. The basic principle of these approaches is based on the use of functions that help to decide which solution set among the available sets could be tested next or how to produce the next solutions [82]. They do not require any assumptions to be made such as continuity, differentiability or unimodality which means they are simple to implement [41].

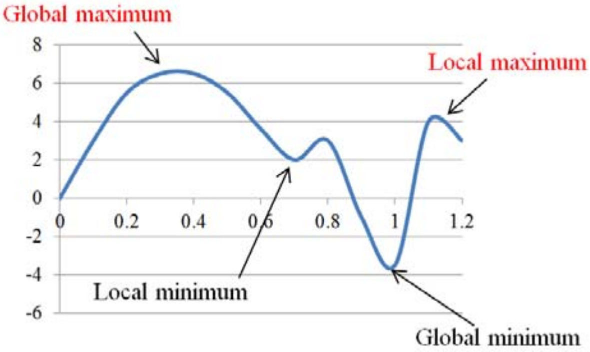

Figure 3.2 Global and local optima.

Compared to deterministic methods, stochastic optimization techniques can deal with more complicated problems and locate the optimal solution relatively quickly. Because of their capability of handling linear and nonlinear problems, multiple objectives and time varying components, stochastic algorithms are considered as a promising alternative to deterministic techniques. However, the results obtained when using these algorithms are always approximate and the accuracy of the solution improves by increasing the number of iterations. In the literature, many stochastic techniques such as evolutionary computation [83], genetic algorithm [84], and simulated annealing [85] are emerging and successfully applied in different fields.

An important class of stochastic techniques is swarm intelligence (SI) such as ant colony optimization algorithms [86], bee colony optimization algorithms [87] and particle swarm optimization algorithms [88]. Swarm algorithms are nature-inspired approaches that work on a population of potential solution in the research space. Throughout the cooperation and competition among particles in the search space, these techniques can often find optima more quickly than other techniques, especially for complex optimization problems.

3.2 Induction machine faults

Induction machines are subjected to many different types of faults especially when they are supplied by ac drives where the windings are stressed by voltage with high harmonic contents [2]. IMs Failures are normally caused by thermal stresses (due to machine overheating as a result of abnormal operating duty or overload and unbalance), magnetic stresses caused by electromagnetic forces, environmental stress such as abrasion, fabrication procedures, vibration, bearing faults, and so on [89]. The history of the electrical machines fault diagnosis dates back to 1924 [90] and since then many developments in the topic have been made [14, 91-94].

Condition monitoring techniques are mainly employed to detect and localize the developments of any fault sufficiently in early stages. Therefore, a proper action can be taken to avoid catastrophic damages and, thus avoiding enormous costs, e.g., motor failures in an offshore oil plant can causes as economical losses as high as $25000/h [95].

Fault diagnosis is the heart of condition monitoring and many techniques are implemented to monitor systems during healthy and abnormal operation conditions [14, 91-94, 96, 97]. The main idea of the fault diagnosis is to correctly detect and locate incipient faults before they propagate and cause irreversible damages. A typical fault diagnosis system can be divided into four phases; collecting data, analysing data, classifying data, and decision making. These four stages are illustrated in figure 3.3.

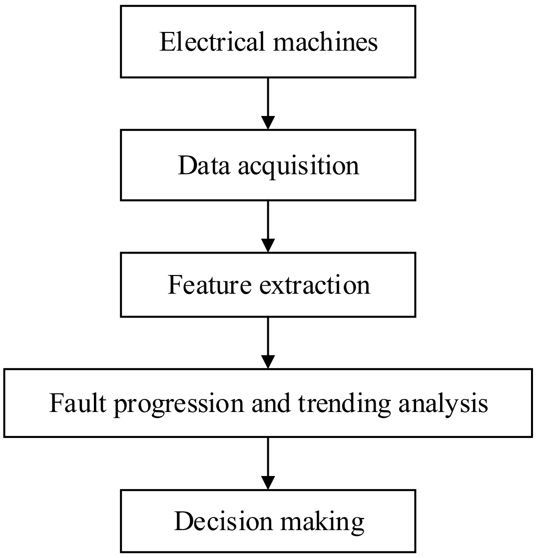

Figure 3.3 Fault diagnosis system's phases.

The main motivations of using fault diagnosis techniques are [98-100]:

- Investigation of the equipment failure.
- Providing an adequate warning of impending failure.
- Decreasing downtimes and increasing productivity.
- Reduction of operational and maintenance costs.
- Improving plants and equipment reliability.
- Optimization of equipment performance.
- Process automation and reduction of labour cost.
- Providing a safe operation environment.

To enable a clear understanding of IM fault diagnosis techniques, a brief description of the most common IMs faults and their diagnosis methods is presented.

3.2.1 Common Induction Motors faults

Induction machines can experience either internal or external faults. These major faults of the IMs can be mainly categorized as [91, 94]:

1) Bearing faults.
2) Stator-related faults, which resulting in shorting or opening in one or more stator phases.
3) Rotor-related faults which includes the open and short circuit faults for wound rotor machine and broken bar(s) or cracked end-rings for cage machines.
4) Eccentricity faults.

A. Bearing faults

Depending on the IM size and the installation type, bearing faults account for a large majority (40% -50%) of the all faults as shown in figure 3.4 [91, 94]. These faults cause increased vibration and lead to torque oscillation which results in amplitude modulation of the stator phase current [101]. These faults are not sudden but progressive and if not detected on time they lead to malfunction, reduce efficiency, loss of performance, and may even cause a severe damage in the machine and a potential injury to nearby personnel.

In general, bearing defects can be categorised as: inner race , outer race, ball, and/or train [91]. Commonly, bearing faults are detected through the shaft vibration frequencies. The vibration frequencies associated with each defect category is given by [91, 94, 102]:

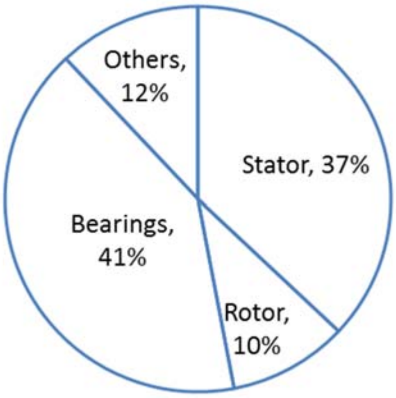

Figure 3.4 Faults in Three phase squirrel-cage induction motor.

$$
\begin{aligned}
F_I &= \frac{N_B}{2} f_r \left[1 + \frac{D_b \cos(\beta)}{D_c} \right] \\
F_O &= \frac{N_B}{2} f_r \left[1 - \frac{D_b \cos(\beta)}{D_c} \right] \\
F_B &= \frac{D_c}{D_b} f_r \left[1 - \left(\frac{D_b \cos(\beta)}{D_c} \right)^2 \right] \\
F_C &= \frac{1}{2} f_r \left[1 - \frac{D_b \cos(\beta)}{D_c} \right]
\end{aligned} \tag{3.1}
$$

where F_I for the inner raceway fault frequency, F_O for the outer raceway fault frequency, F_B for the ball fault frequency, F_C for the cage fault frequency, N_B is the number of rolling elements, D_b and D_c are the ball diameter and the pitch diameter, respectively, and β is the ball contact angle.

However, the vibration signal is mainly affected by the speed and, thus the machine vibration may decrease at low speeds even with faulty machines [94]. In addition, sometimes the vibration signals are not easy to be sensed (e.g. under harsh environments) and, thus the current signal is used as a diagnosis method. In the literature, extensive research work has been conducted to develop bearing faults diagnosis methods based on the current signal [103, 104].

B. Rotor-related faults

In the case of wound-rotor IM, the faults of the rotor windings are similar to the stator winding faults and they result either in open- or short-circuited faults. In the case of squirrel-cage IM around 5%-10% of IM failures are related to the rotor faults including broken bars and cracked end rings, figure 3.4 [91, 94]. These faults result in torque and speed pulsation and lead to the deterioration of steady-state performance of the machine [91]. These faults generate frequency components at $(1 \pm 2ks)f$ around the fundamental component f, where s is the slip and k=1, 2, 3…, in the stator current spectrum that can be used as a fault detector. In the literature, motor current signature analysis (MCSA) has been used extensively to detect rotor faults [105, 106]. Other approaches are based on instantaneous power signal [107], wavelet analysis [108], and so on. As rotor faults are not considered in the thesis, not much attention will be given to their diagnosis methods.

C. Eccentricity faults

The air-gap eccentricity refers to the condition of non-uniform air gap between the stator and the rotor. This fault can be classified as static, dynamic, and mixed eccentricity [109] as shown in figure 3.5. Static eccentricity is characterized by an axis displacement where the rotor is not centred within the stator bore, figure 3.5 (b). As a result, unsymmetrical field distribution in the air-gap occurs and unbalanced radial electromagnetic forces, called unbalanced magnetic pull (UMP), which acts in the direction of minimum air-gap is generated [94]. The dynamic eccentricity, on the other hand, means the rotor is not rotating on its own axis and the minimum air-gap rotates with the rotor, figure 3.5 (c). This causes also a revolving UMP that rotates at the same speed of the motor and acts directly on the rotor [110]. For mixed eccentricity, the rotor and the centre of rotation are displaced from their origin, figure 3.5 (d). Eccentricity faults should be detected in early stages; otherwise they may lead to bending the rotor shaft and cause major damages in the stator and rotor [91]. However, air-gap eccentricity up to 10% is acceptable [94].

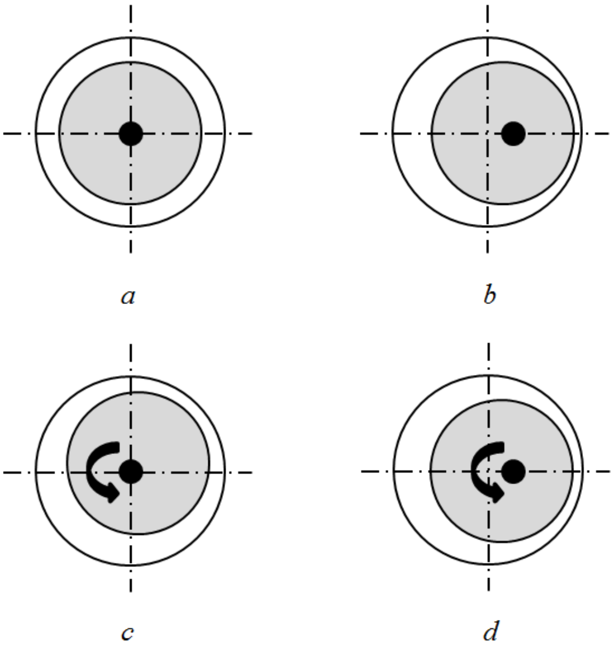

Figure 3.5 Different types of eccentricity, (a) healthy machine, (b) static eccentricity, (c) dynamic eccentricity, (d) mixed eccentricity.

Modelling of eccentricity using both finite element and analytical methods is still under investigation. Many methods are available in the literature to diagnosis the presence of eccentricity faults through different signal such as vibration, current and flux [111-113]. However, due to the high cost and sensitivity of the vibration sensors and the dependence of these signals on the rotor speed, most research work is based on the use of the stator current.

D. Stator-related faults

Usually, electrical faults either within the machine or with supply may cause significant risks including fire, damage to other equipment and possible electrical shocks to people. As shown in figure 3.4, about 30%-40% of motor failures happen because of problems in the stator windings [94]. Stator winding failures can be classified into two main types; an asymmetry in the stator windings (such as an open-phase fault) and short circuit [91]. Open-circuited winding fault occurs when a winding becomes open circuited, preventing the current flow in the faulty machine winding. If an open-circuit winding fault occurs, the machine may stop working or continue to work in either single phase (when star connected) or two phase (when delta connected) operation. Although this fault allows the machine to work with a reduced torque for a period of time, it might ultimately leads to a catastrophic fault, especially for large machines, and results in unexpected interruption in production lines [91].

Compared to open-circuit faults, short-circuited faults are considered as one of the most difficult faults to be detected [91]. These faults often lead to a high current to flow and, thus produce unwanted heat in the shorted turns. If the produced heat exceeding the limit value of the temperature, these faults may result in a complete motor failure that may lead to a serious accident involves loss of a human life. It is believed that the main cause of the stator short circuit winding related faults is the insulation failure in the stator coil turns. Among all these faults, interturn short-circuited fault is the most challenging one and the other short-circuit modes like phase to phase and phase to ground usually come as a result of this fault.

All previous mentioned faults can cause one or more of symptoms including vibration and noise, torque pulsating, excessive heating, unbalanced voltages and currents, leakage flux and other symptoms. Due to the wide integration of IMs in a massive number of industrial applications including nuclear power [114], petrochemical [115] and transportation [116], fault diagnosis has a great importance in enhancing the system reliability.

3.2.2 Induction machine fault diagnosis techniques

In the literature, many methods have been developed to analyse and interpret the machine signals in order to extract the features of useful information for additional diagnosis. Most of these methods are based on the use of the current, vibration, flux and torque signals analysis. Although vibratory signals have higher signal-to-noise ratio (SNR) and enable efficient fault detection, their implementation require expensive sensors that are sensitive to the installation location [92, 97]. The same for the flux and the torque signals that require special and expensive sensors. On the other hand, due to availability and low cost of current sensors that are usually required for control purposes, recent research focuses on the use of current signal analysis in IM fault diagnosis.

Most common IM stator-related fault diagnosis techniques can be broadly categorized into two main categories; signal-based and model-based. The fundamental principles of these two categories are discussed in the previous section and are repeated here from the fault diagnosis perspective.

A. Signal-based IMs diagnosis techniques

Signal-based diagnosis methods do not need a mathematical model of the monitored machine and are based on tracking the frequency signature of each fault type in the stator current [93], air-gap torque profile analysis [117], instantaneous power [118] and so on in time or/and frequency domain. Figure 3.6 shows the basic structure of signal-based fault diagnosis techniques.

The presence of any kind of faults in IMs may cause an asymmetry in the machine magnetic field and generate harmonics in the stator current. Many approaches have been proposed in the literature based on the motor current signature analysis (MCSA) that is based on current monitoring of an induction motor. Some of these techniques are based on the comparison between the current spectrums of the faulty machine with its spectrum when it is healthy. In order to apply such methods and to make the correct interpretation in the spectrum of the different faults, one should be familiar with the spectrum components of the healthy machine [92]. A comprehensive study of spectrum components in stator current signal of a healthy machine is provided in [119].

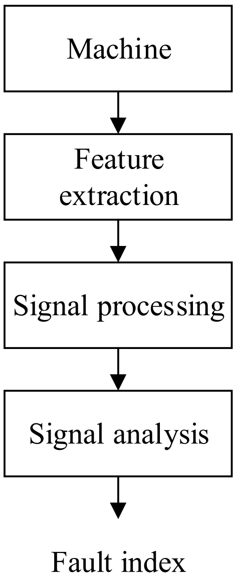

Figure 3.6 Block diagram of signal-based diagnostic procedure.

Signal-based techniques can mainly be classified into three types; spectral analysis, time domain and time-frequency. Spectral analysis techniques are based on detecting characteristic frequencies related to the fault using classical spectral analysis tools like the Fourier transform [92]. The main factors that affect the accuracy of these techniques are the frequency resolution and spectrum leakage [120]. In the literature, some approaches are proposed in order to improve the frequency resolution and to reduce the computation time including zoom-FFT (ZFFT), chirp Z transform (CZT) and zero-padding [120].

Spectral analysis techniques can be divided into three main groups; nonparametric, parametric, and subspace methods. Nonparametric methods are based on classification and ranking, not actual numbers, which include conventional Fourier analysis and its extensions, optimal bandpass filtering analysis and so on. The main drawback of these techniques is their low frequency resolution that eliminates their ability to distinguish between two closely spaced frequency components [121]. Parametric methods are based on the estimation of linear time invariant systems from noise by autoregressive-moving-average model such as covariance, Yule-walker, and Burg [122, 123]. Due to the massive developments in microprocessors and the spectral analysis algorithms, subspace methods have been recently introduced to the IM diagnostic by the application of multiple signal classification (MUSIC) [123, 124] and estimation of signal parameters via rotational invariance techniques (ESPRIT) approaches [125]. These techniques allow detecting fault harmonics and reducing the noise influence [91, 124]. However, most of these techniques require measurements with long data window and known as being computationally demanding [121]. In addition, unsatisfactory results are obtained when these techniques are applied for combined faults or when any transient (e.g. load changing) occurs [14, 92]. For such cases, other signal-based techniques including time domain and time-frequency domain are more accurate for fault detection [126]. These techniques are reviewed in [120, 124]

Time-domain analysis refers to an analysis of data as a function of time and has been introduced as a powerful tool for IM fault diagnosis in terms of low computational cost and reduced time acquisition period. In the literature, many time based approaches for IM fault diagnosis are introduced. One proposed approach is based on the use of the filtering effects to cancel unrelated fault frequencies components such as space and saturation harmonics [127-129]. Different method is based on the use of the maximum covariance matrix which is based on the computation of the covariance between the input signal and the reference signal in the time domain [130]. If a large frequency bandwidth and good frequency resolution are required, this method takes a long computational time [131].

Time-frequency analysis concerns the analysis of signals with time varying frequency contents. One of the most used time-frequency techniques is the short-time Fourier transform (STFT) which is an extension of the Fourier transform. In the STFT the signal is divided into small time windows and each one is analysed using FFT. In order to obtain a good resolution, STFT requires high computational cost and fixed window width, which is a major drawback [132]. To overcome this drawback, the quadratic time-frequency analysis technique is introduced as an alternative to the STFT [120]. This technique is independent of the type and size of the window and it is based on the computation of the energy distributions of the signal over both time and frequency domains [132].

Although signal-based techniques perform well with some applications, they have significant limitations [133]. Most of these techniques require post-processing step using artificial intelligence (AI) techniques to classify different faults [120]. Long-time data with high rate of sampling is required to achieve a good spectral resolution and, thus large memory space to process and store the current spectra is needed [93]. In addition, most of these techniques are based on tracking the frequency signature of each fault type in the recorded signal spectrum, which depends on the machine's slip and must be recomputed for each different operating condition [134]. Moreover, it is common for healthy machines to have various harmonic components due to the machine design, saturation, and the loading variation [119]. If these harmonics are close or overlapped with the fault-related spectrum components, signal-based techniques might fail to differentiate between the faulty and healthy conditions [14]. In large industrial applications, signal-based techniques become more complicated and need more sophisticated components to be implemented. For the inverter-fed IM, the spectral analysis of the stator current signal becomes more difficult [135]. In order to overcome all these shortcoming and improve the signal-based techniques accuracy, advanced signal processing techniques are implemented such as multiple signal classification [136], fraction Fourier transform [137] and maximum covariance methods [131].

B. Model-based IMs diagnosis techniques

Due to the availability of powerful computational platforms, model-based diagnosis techniques have been demonstrated to have superior performance in fault diagnosis and parameter identification processing. Model-based techniques were introduced in 1970s and since then they have been developed dramatically [138]. Today, model-based techniques have been integrated in many applications including robotics, transport systems and power systems [138].

Model-based techniques allow for a deep understanding into the process behaviour [66, 91]. They are based on the construction of a mathematical model of the faults that allows monitoring the characteristic parameters and detecting abnormal situations [14, 139]. External measurements are used with a dynamic process model like state observers [140] and parameter estimation [14] for fault diagnosis. Measured data are used as an input of the machine model to produce the calculated output. The output of the IM model is compared with that of the real machine (real measurements) to produce the error that is used as a faults indicator. If this error is higher than a predefined threshold value, a fault is declared. Figure 3.7 shows a basic structure of model-based fault detection techniques.

One of the great advantages of models-based techniques is that most of them do not require exotic sensors and available sensors are usually used [141]. Due to the assumptions and approximations in the IM model, the fault message might be corrupted by other unknown disturbances. Consequently, it is important to evaluate the error and to extract the needed information about the fault (error evaluation).

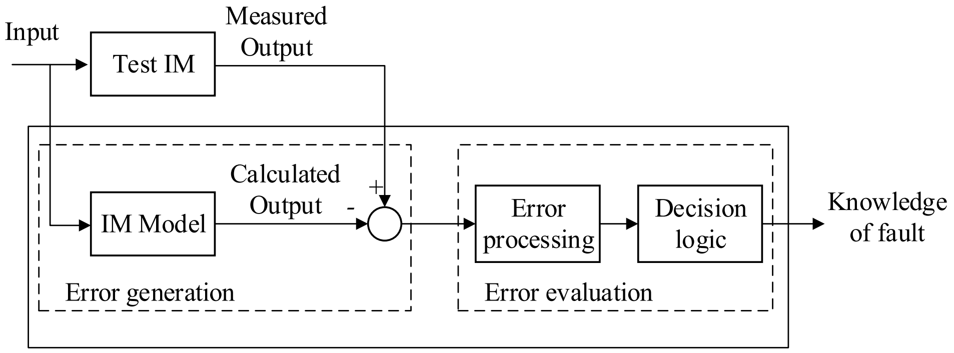

Figure 3.7 Block diagram of model-based diagnostic procedure.

In the literature, many model-based condition monitoring techniques have been proposed. The main difference between them lies in two factors; the adopted process model and the applied algorithm. Among model-based methods, observer-based techniques have received much attention since 1990s [138]. The basic idea of these techniques is to replace the machine model by an observer that will deliver a reliable estimate of the real machine output. Many observer-based approaches are available in the literature including adaptive observer [142] and Extended Kalman Filter (EKF) [143].

Another class of model-based condition monitoring is parameter identification based methods, where the fault decision is performed by online parameter estimation. Parameter identification techniques are structured in a feedback closed-loop in such a way that the error between the actual machine and the model is fed back to the error generator, as shown in figure 3.8. The task is to minimize the objective function, the error between the measured and calculated data, by iteratively adjusting the parameter values and to find a set of characteristic parameters that give the best match between the two sets.

Recently, adaptive observer theory has been developed aiming to combine both observer-based and parameter identification based fault diagnosis methods [144]. The main difference between the regular and adaptive observer-based techniques is the error evaluation [138].

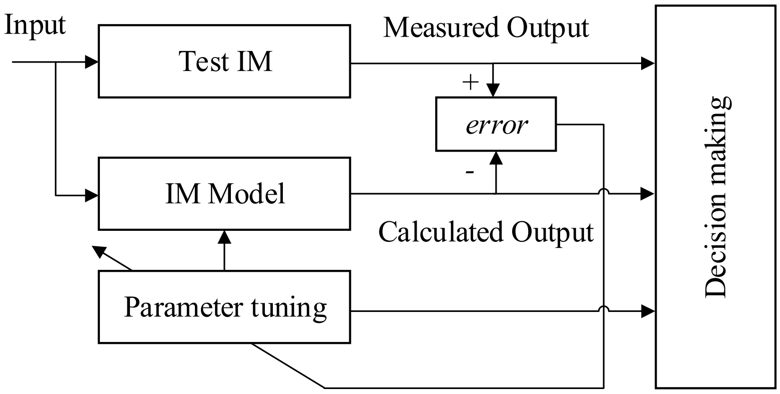

Figure 3.8 Block diagram of parameter identification diagnostic procedure.

Several other model-based techniques for IM fault diagnosis have been introduced in the literature. In [145-147], the winding function method (WFM) is used for modelling interturn short circuits in the IM stator winding. These methods are geometrically based that use functions to model the machine windings and the air gap in order to determine the magnetic field parameters. However, the obtained results from conventional winding function models might not be accurate if the air gap is non-uniform [148]. Many improvements have been proposed to increase the accuracy of the WFM [149, 150]. Although these approaches allow a deep understanding of the process behaviour, they are unsuitable for industrial applications due to their complexity [14].

Another model-based technique is to use the dynamic mesh reluctance approach for winding short-circuit faults [151-153]. The method provides a flexible approach for accurately modelling the equivalent electrical and magnetic circuits of the IMs including different effects like saturation and machine geometry [151]. Although these models provide good results and incorporate other aspects of drive systems like power converters and controllers with an acceptable simulation time, they require a specific knowledge about the machine design parameters that are not usually available from the manufacturer.

Recently, several artificial intelligence (AI) techniques, such as artificial neural networks [154], fuzzy logic systems [65], and support vector machines [155], have been introduced and used for IM fault diagnosis. These diagnoses are based on three steps; choosing the targeted fault, defining the cause-effect relationships and finally computing the diagnostic indices linked to the fault [156].

Unfortunately, most of model-based techniques are designed for a specific fault and the used IM model is different from one fault to another. In addition, these techniques might fail when two faults occur in the same time.

3.3 Conclusion

In this chapter, concepts of parameter identification and condition monitoring of induction machines are reviewed. The IM parameter identification methods are divided into two main categories, model-based and signal-based. The most predominant faults in induction machines have been discussed and the need for the fault diagnosis has been highlighted. An extensive review has been carried out to present the current research state of the parameter identification and fault diagnosis of induction machines. Based on the provided literature on the parameter identification and condition monitoring of IMs, model-based parameter identification and condition monitoring of IMs art adopted and presented in the next chapters of the thesis.

CHAPTER 4

Experimental setup and simulation

This chapter presents the experimental setup used in this thesis. Then a series of experimental investigations that is carried out to validate the proposed schemes is provided. Different operating conditions including heathy and faulty and how the faults were emulated are explained. The tests were performed under steady-state conditions with supply-fed and inverter-fed machine. A description of Matlab/Simulink models constructed and used in the thesis for induction machines identifiability analysis, parameter identification and fault diagnoses is also provided in this chapter.

4.1 Experimental Set up

To allow practical testing of the schemes proposed in this thesis, an experimental platform with a 1.1 kW, 50 Hz, 230/400 V, 4-pole three-phase squirrel cage induction machine is constructed. The test rig includes also a permanent magnet synchronous machine used as a load, and an ac drive. The experimental system is shown in figure 4.1 for supply-fed operation and in figure 4.2 for inverter-fed operation. For supply-fed operation, the IM was connected directly to the 50 Hz mains supply and operated at the rated stator current. The main components of the system are described in details in the following sub-sections.

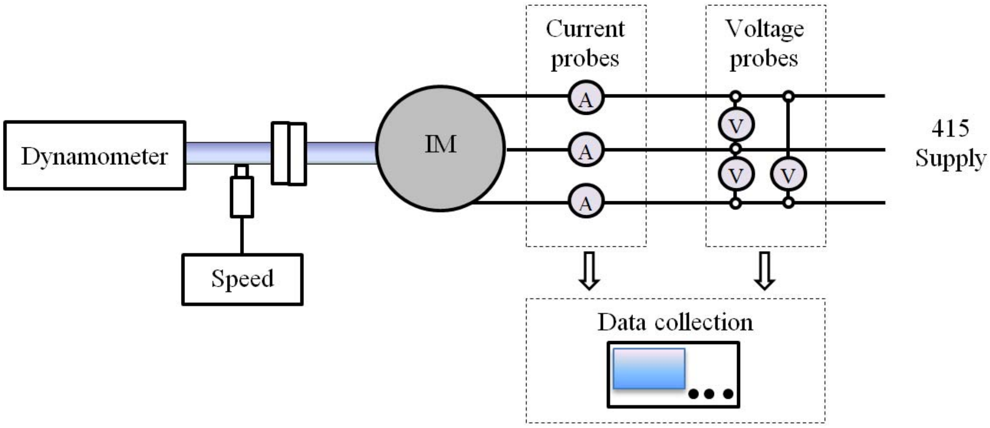

Figure 4.1 Experimental set up for supply-fed IM.

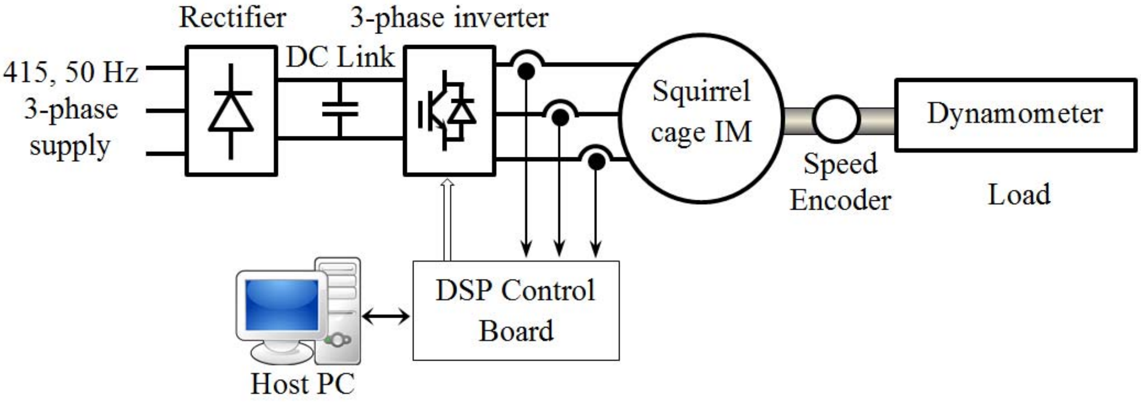

Figure 4.2 Experimental set up for inverter-fed IM.

4.1.1 Test motor

The 1.1 kW, 50 Hz, 230/400 V, 4-pole star connected three-phase squirrel-cage induction machine, manufactured by AmTecs Ltd is used as the test machine, figure 4.3.

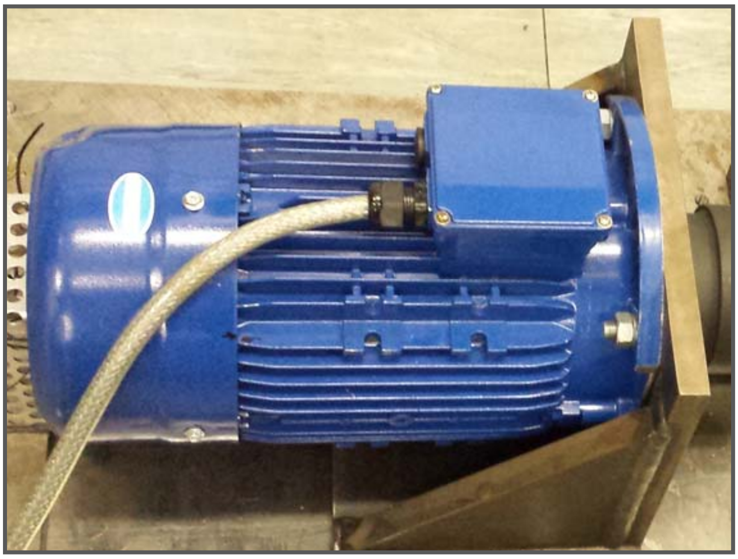

Figure 4.3 The squirrel-cage induction motor.

To obtain the T-equivalent circuit parameters of the machine, the standard tests of no load, locked rotor, and dc tests were performed as described in [48]. The dc test determines the stator resistance (R_s) value, while the no-load test is used to determine the magnetizing inductance (L_m). Finally, the locked rotor test is used to calculate the stator and rotor leakage inductances (l_{ls} and l_{lr}) and the rotor resistance (R_r).

For the motor under consideration, the ratio of l_{ls}/l_{lr} is available (NEMA class B, 40/60) and can be used to calculate the stator and rotor leakage inductances. Table 4.1 gives the parameters of the IM T-model based on these tests.

For the inverse Γ-model, circuit parameters can be independently calculated based on the standard IEEE tests. No assumption is required in this case. The parameters of the inverse Γ-model can also be calculated from those of the T- model (chapter 1) if the l_{ls}/l_{lr} is known. Table 4.2 presents the inverse Γ-model parameters that obtained from the IEEE tests.

Parameter	Value
Stator resistance (R_s)	3.61 Ω
Rotor resistance (R_r)	3.66 Ω
Stator leakage inductance (l_{ls})	0.0395 H
Rotor leakage inductance (l_{lr})	0.056 H
Magnetising inductance (l_m)	0.408 H

Table 4.1 Measured parameters of the T-Model of IM.

Parameter	Value
Stator resistance (R_s)	3.61 Ω
Rotor resistance (R_r')	2.79 Ω
Stator leakage inductance (l_{ls}')	0.0911 H
Magnetising inductance (L_m')	0.3565 H

Table 4.2 Measured parameter of the Inverse Γ–Model of IM.

4.1.2 The load and its drive

A 4.19 kW, 380/480 V, 8-Poles, 2000 r/m permanent magnet synchronous machine (PMSM) (figure 4.4), is used to emulate the mechanical torque on the IM shaft experienced by the load. The PMSM was driven by a Unidrive SP controller (figure 4.5) manufactured by Control Techniques to change the load torque on the shaft.

Figure 4.4 The PMSM machine.

Figure 4.5 The PMSM driver unit.

4.1.3 Test motor ac Drive

The ac drive used in this thesis has been designed and built at Newcastle University. The ac drive of the IM consists mainly of a three-phase diode bridge rectifier, dc link, and an IGBT-based three-phase bridge inverter. The rectifier is Vishay VS-26MT100, 25A, 1000V, 3-phase Diode Bridge which consists of six uncontrolled diodes. The dc link capacitors consisting of two 470 µF capacitors connected in series to smooth the output voltage of the rectifier. Two 150 kΩ resistors each connected across the capacitors to ensure equal voltage sharing between the two capacitors. To monitor the voltage across the dc link, an LV25-P voltage sensor is used. The drive inverter uses six IGBT switches with following specifications: V_{CES}=1200V, $I_{NOMINAL}$=20A, $T_{J(MAX)}$=150ºC, $V_{CE(ON)}$=1.9V. These IGBTs are supplied by International IOR Rectifier.

4.1.4 Control and interface board

For experimental flexibility and ease of programming, a Texas Instruments TMS320F28335 DSP based eZdsp kit was used for control and data acquisition. A general interface board which is designed at Newcastle University is used to interface the microcontroller to the motor drive circuit, shown in figure 4.6. Figure 4.7 shows the experimental circuit.

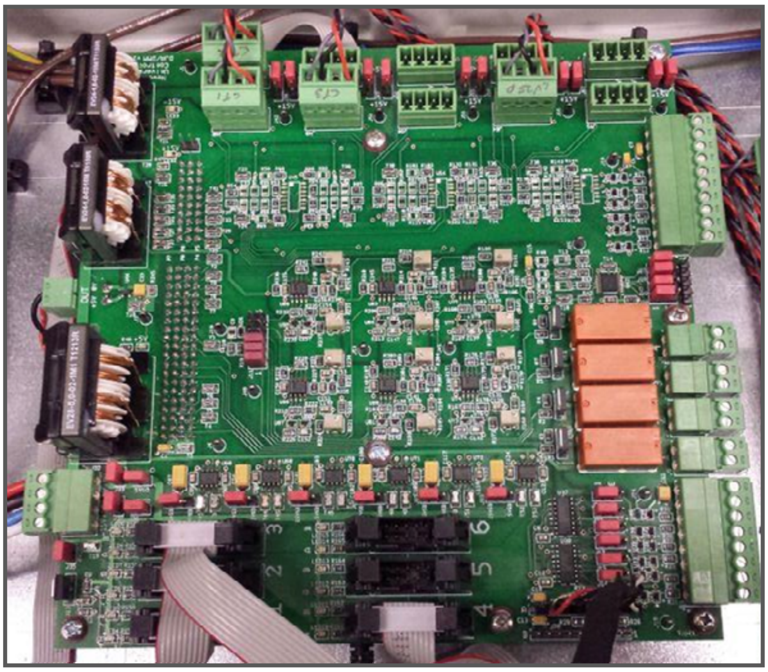

Figure 4.6 The general interface board.

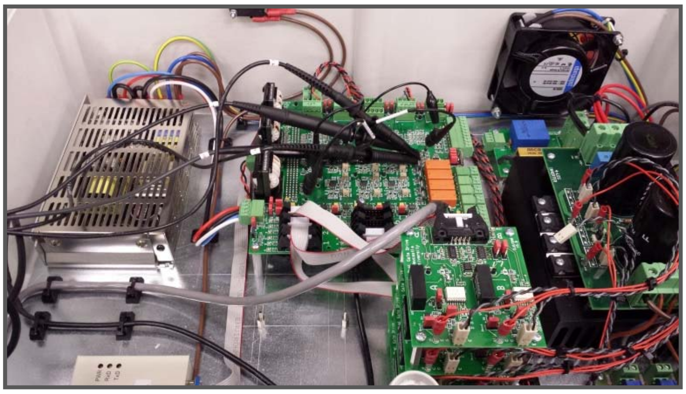

Figure 4.7 The IM drive circuits.

4.2 Induction motor measured data

As this work uses external measurements with IM steady-state models, steady-state measurements of three phase stator voltages (v_{Am}, v_{Bm}, v_{Cm}) and currents (i_{Am}, i_{Bm}, i_{Cm}) were collected over a time window of 0.1 sec with a sampling interval of 1 msec. Motor speed (ω_r) was also measured using an encoder with a digital display unit for each test to calculate the slip required for the model.

All the measurements provided in this thesis are phase measurements taken between the phase terminal and the common point. Therefore, there will be waveforms unbalance in the faulty case due to an asymmetry of the winding.

The test rig is based in a power electronics, machines and drives lab in which different types of nonlinear loads are connected affecting the mains voltage waveform. As a result, a significant amount of harmonics has turned up within the voltage signal. This causes the measured phase voltage to deviate from an ideal sinusoidal, which in turn causes the voltage harmonics and affects the current shape. This problem has been highlighted before in a number of PhD theses such as [157].

The IM was tested under different operating condition (healthy and faulty) for both supply-fed and inverter-fed IM. The measurements of voltages and currents will be shown in the next subsections and will be used in the following chapters.

For supply-fed IM, three Tektronix P5200 high voltage differential probes were used to measure the three phase stator voltages (v_{Am}, v_{Bm}, v_{Cm}), and three Tektronix A622 Current Probes were used to measure the three phase stator currents (i_{Am}, i_{Bm}, i_{Cm}). For inverter-fed IM, phase terminal voltage was calculated from the modulation index of the inverter and the available dc link voltage; hence no stator voltage measurement was needed. Three CAS-15 Hall-effect current sensors were used to measure the phase currents. The sampling frequency of the voltages and currents is 10 kHz and, thus the current signals include 1000 points.

4.2.1 Healthy IM tests

Different no-load and full-load tests with supply-fed and inverter-fed operation were carried out for healthy IM. These tests are then used for identifiability analysis and parameter identification of the IM steady-state models. As mentioned in the first chapter, it is assumed that the three phases are identical and as a result only one phase (phase A) measurements are used in the identifiability analysis and parameter identification.

In order to match the impedance of the supply-fed IM with that obtained in the case of the inverter-fed IM, a variac has been utilized to maintain the level of voltage to be the same as that of the inverter-fed.

Figures 4.8 and 4.9 show phase A measured stator voltage and current obtained from the healthy IM at steady state when the machine was fed from the mains at no load with a speed of 1491 r/m (i.e., a slip of 0.006).

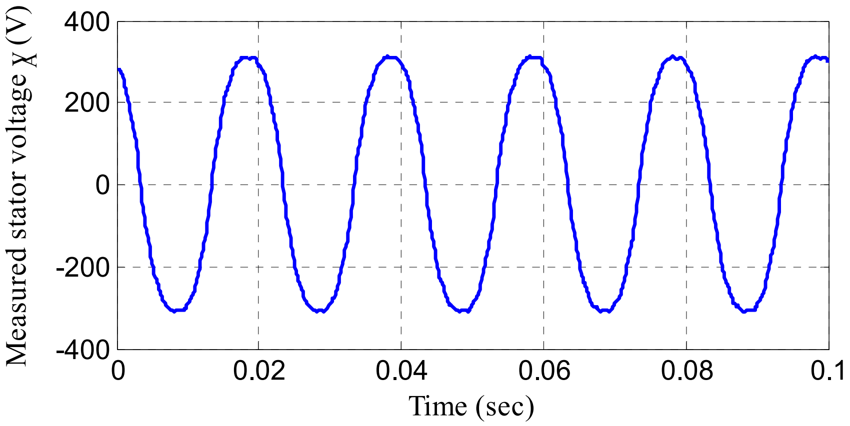

Figure 4.8 Measured stator voltage waveform-phase A; supply-fed, no-load at slip of 0.006.

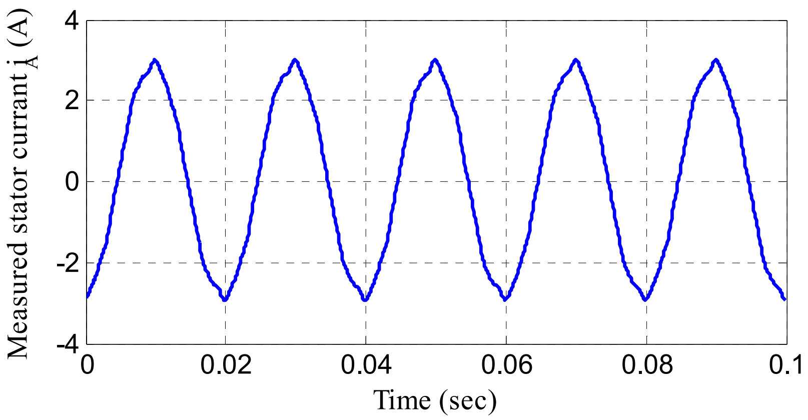

Figure 4.9 Measured stator current waveform-phase A; supply-fed, no-load at slip of 0.006.

The test machine is also tested at a different operating condition by adjusting the ac drive of the synchronous machine loading the IM up to full load. This occurs at a speed of 1418 r/m (i.e. a slip of 0.055), the measured stator voltage and current waveforms are shown in figures 4.10 and 4.11, respectively.

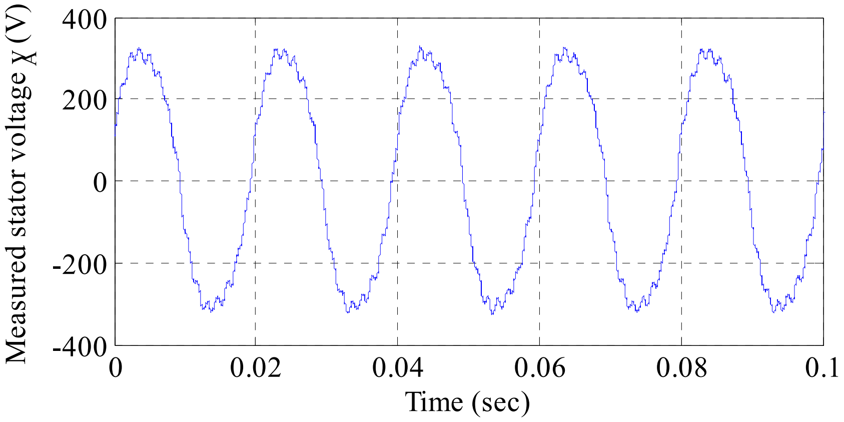

Figure 4.10 Measured stator voltage waveform-phase A; supply-fed, full-load at slip of 0.055.

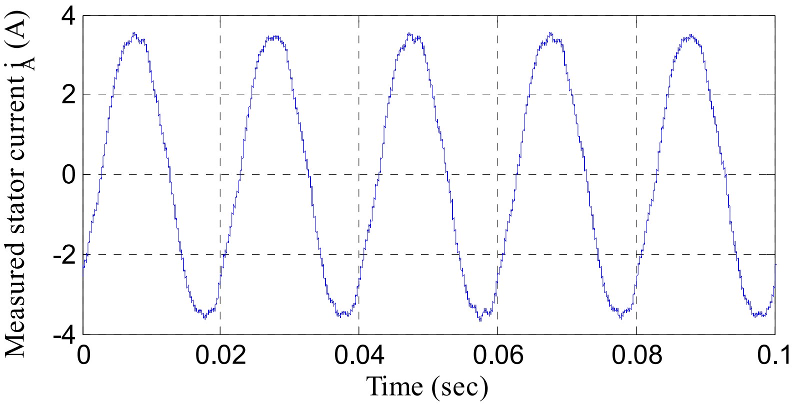

Figure 4.11 Measured stator current waveform-phase A; supply-fed, full-load at slip of 0.055.

For simplicity, V/f control was used for driving the IM. However, any other control technique of an IM drive can also be used. Two different operating frequencies of 50 Hz and 25 Hz were investigated. One phase terminal voltage (v_{Am}) is calculated from the modulation index and the dc link and hence no measurement of that voltage is needed and, thus reducing the cost. As V/f control is an open loop scheme, no current measurements are required for control purpose but current sensors are still needed for protection purpose of the drive.

Similar to the supply-fed case, stator current is adjusted at the full-load value using the ac drive of the synchronous machine load. This occurs at a speed of 1417 r/m (i.e. a slip of 0.055) for the 50 Hz and a speed of 694 r/m (i.e. a slip of 0.075) for the 25 Hz. Figures 4.12 and 4.13 show the measured stator current at 50 Hz and 25 Hz, respectively.

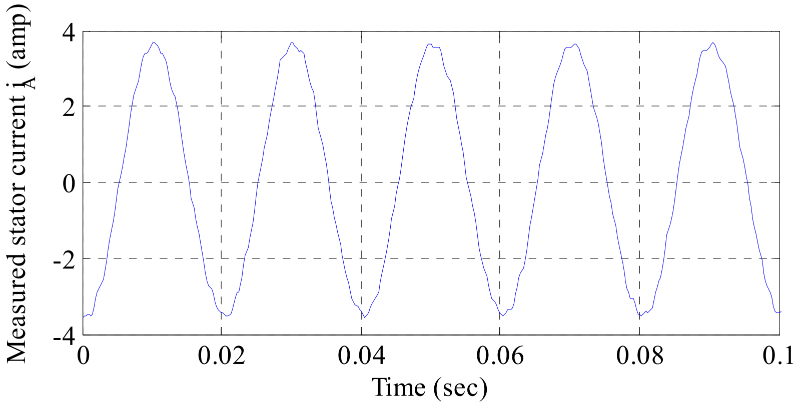

Figure 4.12 Measured stator current waveform-phase A; inverter-fed, 50 Hz, full-load at slip of 0.055.

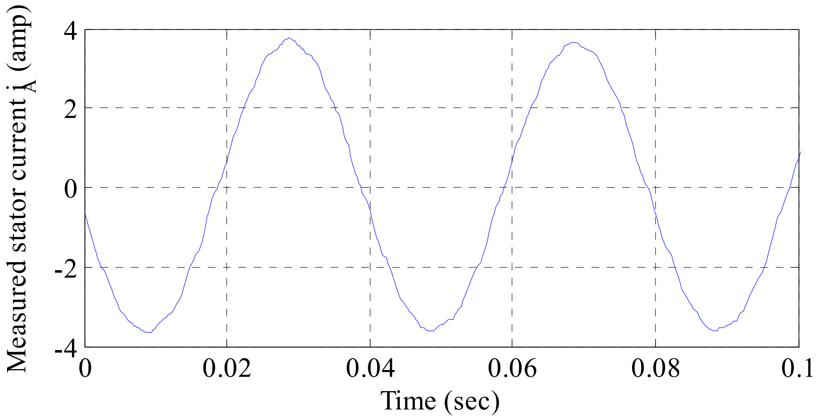

Figure 4.13 Measured stator current waveform-phase A; inverter-fed, 25 Hz, full-load at slip of 0.075.

4.2.2 Faulty IM tests

These tests were carried out to validate the proposed fault diagnosis technique using the test machine. Three fault conditions were implemented using the test facility including stator winding asymmetry (increasing the stator resistance), interturn short-circuited, and combined faults. For safety reasons and to avoid destructive tests, these tests were carried out just when the machine is supplied directly from the mains at no load.

A. Stator Open-circuited winding fault test

Due to the need of the test machine to be used in other tests, it was not possible to make a real open circuit in the stator winding. Stator winding asymmetry fault is simply implemented by increasing the stator resistance towards a very high value (about 10 times) compared to the healthy one [158, 159]. This is done by connecting a 30 Ω resistor in series with one of the stator phases, phase A, imitating an asymmetry fault in one phase. The schematic diagram of the open-circuited fault is shown in figure 4.14.

The measurements were taken at a speed of 1474 r/m (i.e. a slip of 0.017) across the 3-phase terminals (between the phase terminal and the common point). Figures 4.15 and 4.16 show the measured stator voltages and currents waveforms obtained from this test.

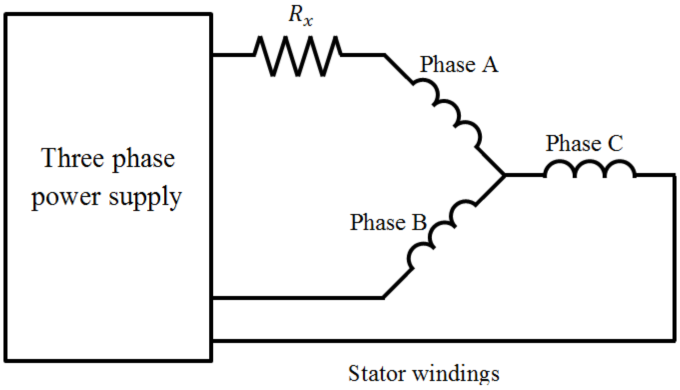

Figure 4.14 Schematic diagram of stator asymmetry.

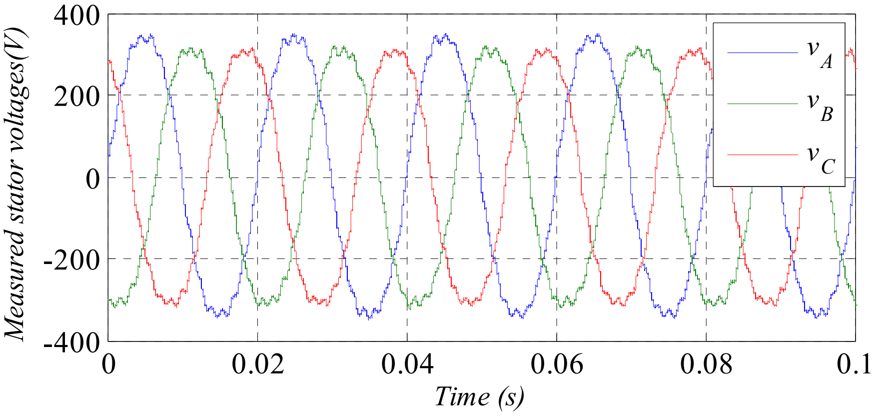

Figure 4.15 Measured stator phase voltage waveforms; developing stator open-circuit winding fault, phase A.

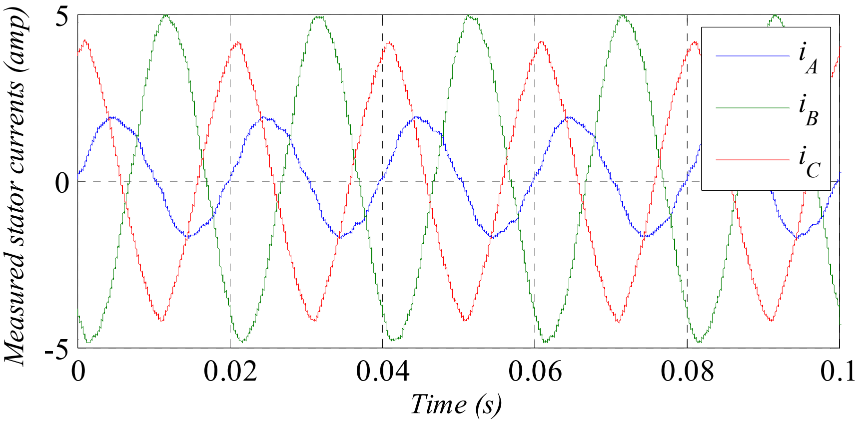

Figure 4.16 Measured stator phase current waveforms; developing stator open-circuit winding fault, phase A.

B. Stator interturn short-circuited winding fault test

The short-circuited stator winding fault was emulated by scraping the insulation layer of windings and soldering them with wires as shown in figure 4.17. The experimental measurements of about 30% interturn short-circuit fault in phase A have been collected at a speed of 1475 r/m (i.e. a slip of 0.016). Figures 4.18 and 4.19 show the measured steady-state stator voltages and currents obtained from faulty induction motor. Again, the measurements in this test have been taken between the 3-phase terminals and the common point.

Figure 4.17 Stator interturn fault.

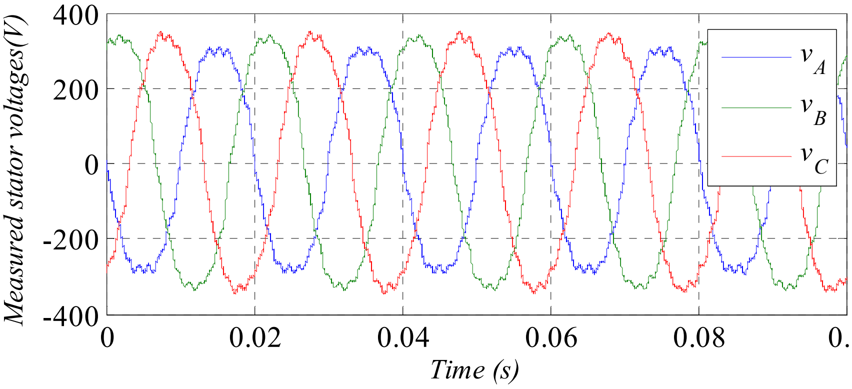

Figure 4.18 Measured stator phase voltage waveforms; developing stator interturn short-circuit fault at no-load, phase A.

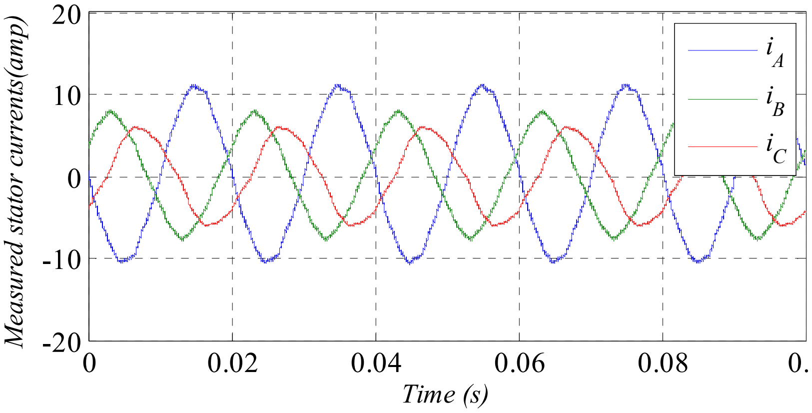

Figure 4.19 Measured stator phase current waveforms; developing stator interturn short-circuit fault, at no-load, phase A.

C. *Stator winding combined fault*

Figure 4.20 shows a schematic diagram of a stator combined fault including an interturn short circuit fault an phase A and an asymmetry winding fault in phase B. Experimental measurements of about 30% stator short-circuited fault in phase A and an open-circuited fault in phase B (by adding 30 Ω) have been collected and used in this test. The experimental measurements have been collected at a speed of 1482 r/m (i.e. a slip of 0.012).). Figure 4.21 and figure 4.22 show the obtained measured steady-state stator voltages and currents.

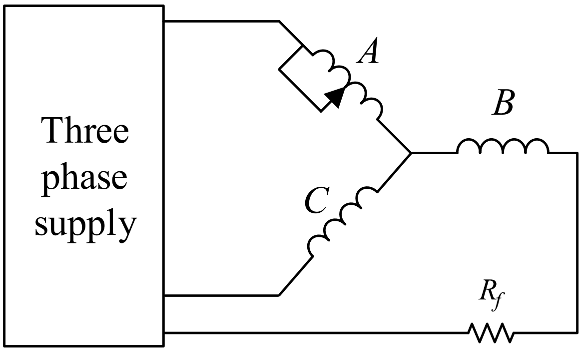

Figure 4.20 Schematic diagram of stator combined fault in two phases, short-circuit fault in phase A and asymmetry winding-fault in phase B.

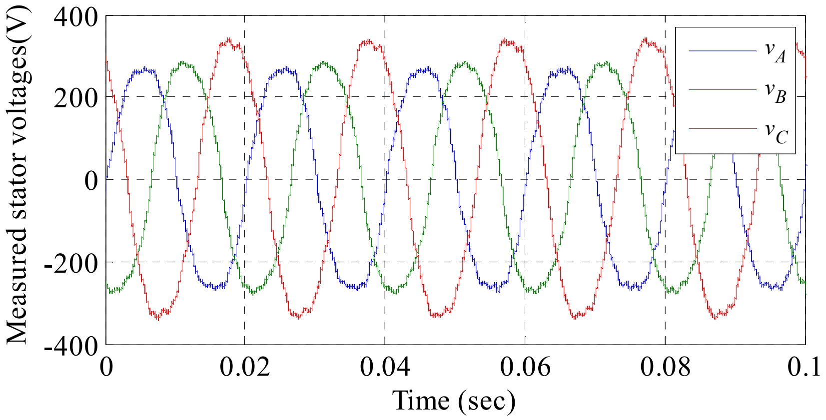

Figure 4.21 Measured stator phase voltage waveforms; developing stator winding combined fault, short-circuit fault in phase A and asymmetry winding-fault in phase B.

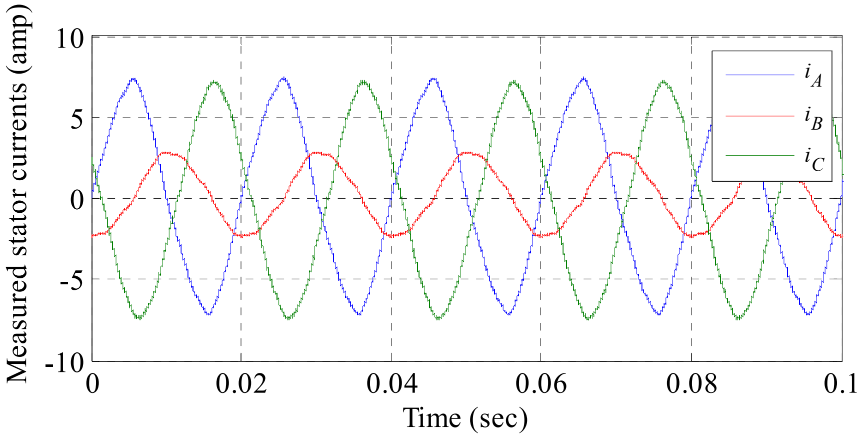

Figure 4.22 Measured stator phase current waveforms; developing stator winding combined fault, short-circuit fault in phase A and asymmetry winding-fault in phase B.

4.3 System simulation

To enable fast analysis and manipulation of the recorded data files, Matlab/Simulink is used to analyse and simulate the IM under both healthy and faulty conditions. The programming was done using M-files that was run along with the simulation to apply proposed approaches and find the solutions.

Figures 4.23 – 4.25 show block diagrams of the Simulink models used in the identifiability analysis, parameter identification and fault diagnosis, respectively.

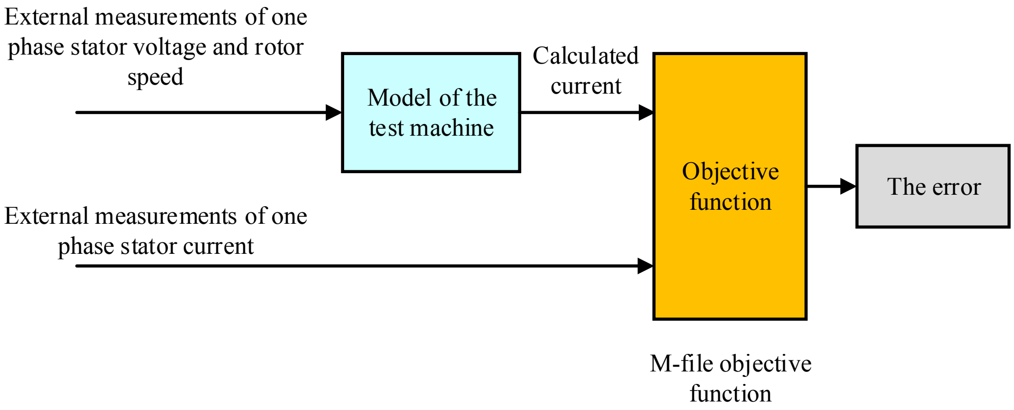

Figure 4.23 Simulink model showing machine mathematical model combined with practical data for identifiability analysis.

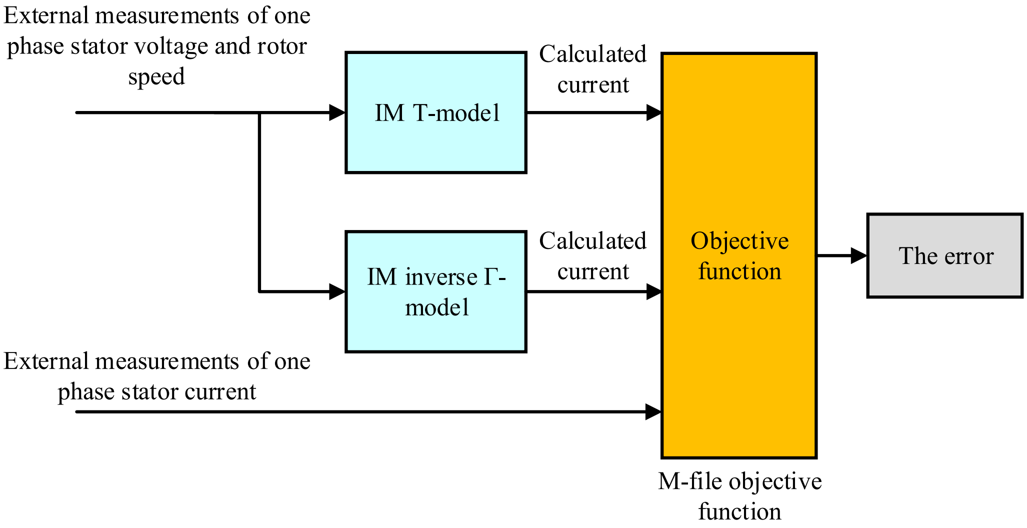

Figure 4.24 Simulink model showing machine mathematical model combined with practical data for IM parameter identification using the proposed integrated steady-state model.

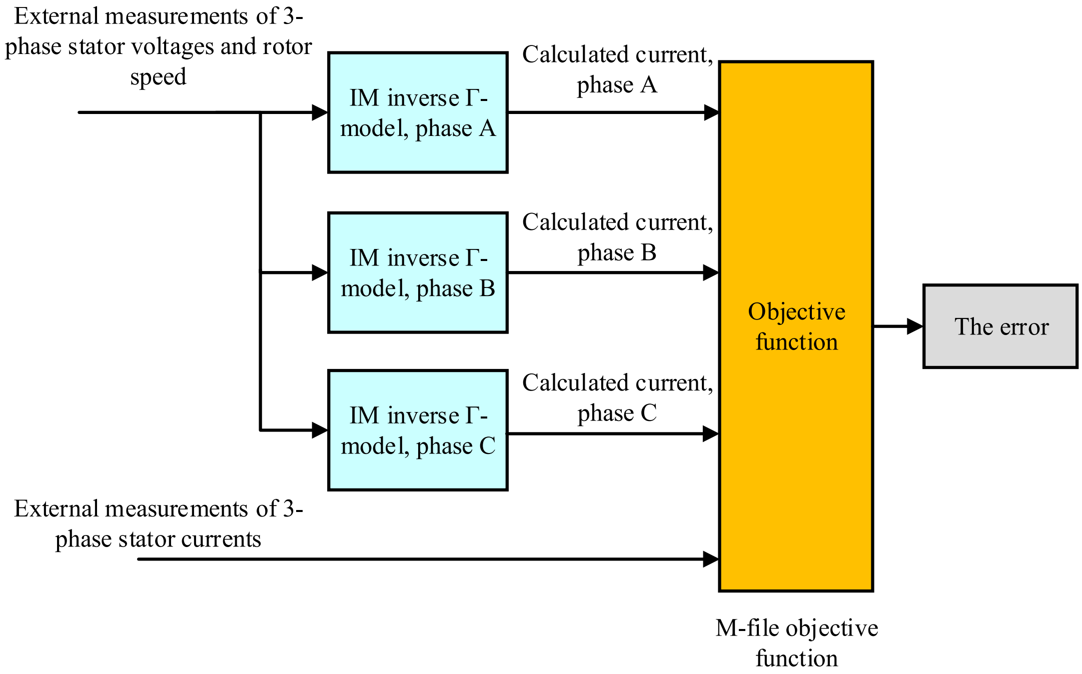

Figure 4.25 Simulink model showing machine mathematical model combined with practical data for the proposed IM fault diagnosis.

4.4 Conclusion

The experimental setup used in the project has been presented in this chapter. The main components of the hardware configuration of experimental system have been described. In addition, measurements of stator voltages, currents, and rotor speed were collected and presented for different operation conditions including healthy and faulty machine to be used in next chapters. Simulation models were presented for the proposed techniques for identifiability analysis, parameter identification and condition monitoring.

Measurements obtained from the healthy IM in conjunction with simulations models will be used to examine the identifiability of the IM models in chapter 5 and for IM parameter identification in chapter 6. Measurements obtained from the faulty machine are used for IM condition monitoring in Chapter 7.

CHAPTER 5

On the identifiability of steady-state induction machine models using external measurements

The identifiability of two commonly used induction machine steady-state models, the T- and the inverse Γ-models is examined using a novel approach based on the Alternating Conditional Expectation (ACE) algorithm. The identifiability analysis results are experimentally verified using external measurements in conjunction with the Levenberg-Marquardt and Particle Swarm Optimization (PSO) algorithm.

5.1 Introduction

A common practice in IM parameter identification techniques is to use external measurements of voltage, current, speed, and/or torque. Using this approach, it is possible to obtain an infinite number of mathematical solutions representing the machine parameters depending on the model employed.

For a healthy IM, the parameters of the T-model (the familiar equivalent circuit of the machine) may be identified by performing the standard no-load, dc and locked rotor tests as detailed in IEEE Standard 112-2004 [48]. This requires the ratio of stator leakage inductance to rotor leakage inductance (l_{ls}/l_{lr}) to be known. When this ratio is unavailable or when the machine in question is in operation and it is not possible to carry out the standard tests, an alternative parameter identification approach is required. One such approach recently proposed in the literature [6, 8, 10], is to try to estimate the IM parameters based on external measurements at stator terminal while the machine is running. Before using a machine model in such a parameter estimation technique, however, it is important to test the identifiability of the model to make sure that its parameters are uniquely identifiable.

This chapter presents an identifiability analysis of two commonly used IM models; the familiar T-Model and the inverse Γ- model (shown in chapter 1) using the techniques described in chapter 2. First, two approaches, the transfer function and the bond graph, which are a priori (structural) identifiability analysis methods are employed. Second, a novel identifiability analysis approach is proposed in which the Alternating Conditional Expectation (ACE) algorithm is used for the first time to test the identifiability of the two IM models.

For verification purposes, an experimental approach based on the use of the Levenberg–Marquardt (L-M) and particle swarm optimization (PSO) algorithms in conjunction with the measured steady-state machine terminal quantities are used to identify the parameters of the test machine, considering both the T- and the inverse Γ-models. These techniques make use of the instantaneous steady-state values of external measurements of only one phase stator voltage and current and rotor speed. These are general schemes that can be utilized with different types of machines under various operating conditions (healthy and faults). They do not require any assumptions and/or a prior knowledge of the IM parameters. Also, they do not need any additional hardware or changes in motor connections to be used for running machines

5.2 Identifiability analysis of IM T-model

In this section, the identifiability of IM T-model is assessed using the aforementioned approaches in chapter 2.

5.2.1 The transfer function approach

Mathematically, the transfer function of the T-model shown in chapter 1 is given by the admittance (*G(s) = I(s)/V(s) = 1/Zeq*). The input impedance of this model given by [160]:

$$Z_{eq}(p,s)=\frac{\rho^2 sa_1+\rho s_1 b_1+\rho c_1+d_1}{\left(\rho sb_1/d_1+1\right)} \tag{5.1}$$

where $\rho = j\omega_S$, and a_1, b_1, c_1 and d_1 are functions of the five electrical parameters that can be obtained from the following expressions:

$$\begin{aligned}
a_1 &= \frac{l_{lr}\left(l_{ls}+L_m\right)+l_{ls}L_m}{R_r},\\
b_1 &= \frac{R_s\left(l_{lr}+L_m\right)}{R_r},\\
c_1 &= l_{ls}+L_m,\\
d_1 &= R_s
\end{aligned} \tag{5.2}$$

Taking Laplace transform, equation (5.1) becomes as:

$$G_T(S)=\frac{1}{Z_{eq}}=\frac{\left(b_1/a_1d_1\right)S+\left(1/sa_1\right)}{S^2+S\left(sb_1+c_1\right)/sa_1+d_1/sa_1} \tag{5.3}$$

Although the T-model has five physical parameters, only four different coefficients (a_1, b_1, c_1 and d_1) can be uniquely determined from the input/output measurements defined by $G_T(s)$. Any parameter can only be expressed by other parameters is not identifiable and vice versa.

5.2.2 Bond graph approach

The different parameter variables of T-model are drawn in the bond graph. All elements are connected to appropriate junctions. Figure 5.1 shows the bond graph of the IM T-model where the half arrows show the direction of power flow. The causal strokes are set in accordance with the procedure discussed in Chapter 2. For example, at 1-junction, the effort (v_s) of source *SE* moves towards its causal stroke while the flow (i_s) moves away from its causal stroke. The inductor element imposes flow, hence can be modelled as a source with a causal stroke at the element side. For a resistive element, causal stroke can go on both directions in such a way to satisfy the junction at the other end of the bond. For a proper causal completion, the causal strokes for R_s and R_r are set on the near of 1-junctions.

As discussed in chapter 2, it is essential that one bond imposes an effort on each 0-junction (i.e. one causal stroke is on the 0-junction). This has not been realized in the bond graph shown in figure 5.1. With such a causality conflict, it is not possible to construct a proper bond-graph for the circuit that can be used in parameter identification.

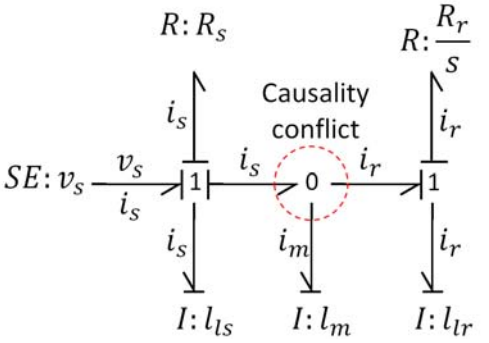

Figure 5.1 T-model causal bond graph.

5.2.3 Alternating conditional expectation algorithm

In this section the ACE algorithm, described in chapter 2, is applied for the first time to test the identifiability of the IM T-Model [10]. The IM T-model is a multivariate model with a response (Z_{eq}) and five predictors (R_s , R_r , x_{ls}, x_{lr}, and x_m). Five hundred tuples of R_s, R_r, x_{ls}, x_{lr} and x_m are independently and randomly drawn from the interval $[0, 1]$ and Z_{eq} was calculated for each tuple. The three inductances have been multiplied by a weighting factor of $(2 \times \pi \times 50)$ to take into account the real contribution of these parameter in the overall impedance.

This was carried out three different times to obtain three different (500×6) matrices $\mathbf{k_i} = [Z_{eq}\ \ R_s\ \ R_r\ \ x_{ls}\ x_{lr}\ x_m]$ (*i*=1, 2 and 3) to serve as inputs to the ACE algorithm.

The optimal transformations of T-model parameters are achieved through minimizing the variance between the transformed response variable $\theta\left(Z_{eq}\right)$ and the summation of transformed predictor variables $\sum_{i=1}^{n} \emptyset_i(\mathbf{k}(p_i))$, where **P**= $[R_s\ \ R_r\ \ x_{ls}\ x_{lr}\ x_m]$.

The optimal transformations of the five predictors R_s, R_r , x_s, x_r, and x_m for the three different estimated matrices are shown in figure 5.2. It is difficult to draw the scatterplot for complex variables (Z_{eq}) because it would require four dimensions (for the real and imaginary parts of Z_{eq} and *θ*). Therefore, a scatterplot of $\left|Z_{eq}\right|$ is plotted to represent Z_{eq}.

For functionally related parameters, almost the same optimal transformations from one sample to another and from one estimate to another will be obtained. Nearly linear transformations are obtained for $\left|Z_{eq}\right|$, x_{ls}, x_{lr} and x_m. These transformations remained stable for all estimates and, thus the parameters are functionally related. However, different transformations are obtained for R_s and R_r.

Optimal transformations of functionally related parameters are invariant under different estimates for each new drawn matrix **k**. A non-identifiable model causes parameters to be functionally related. The maximum correlation between the response and the five predictors is 0.99583. Such a high correlation coefficient between the parameters means that there is a strong dependence between them which is a characteristic of a non-identifiable model. These results obtained from ACE agree with those obtained from the other 2 approaches, the transfer function and the bond graph.

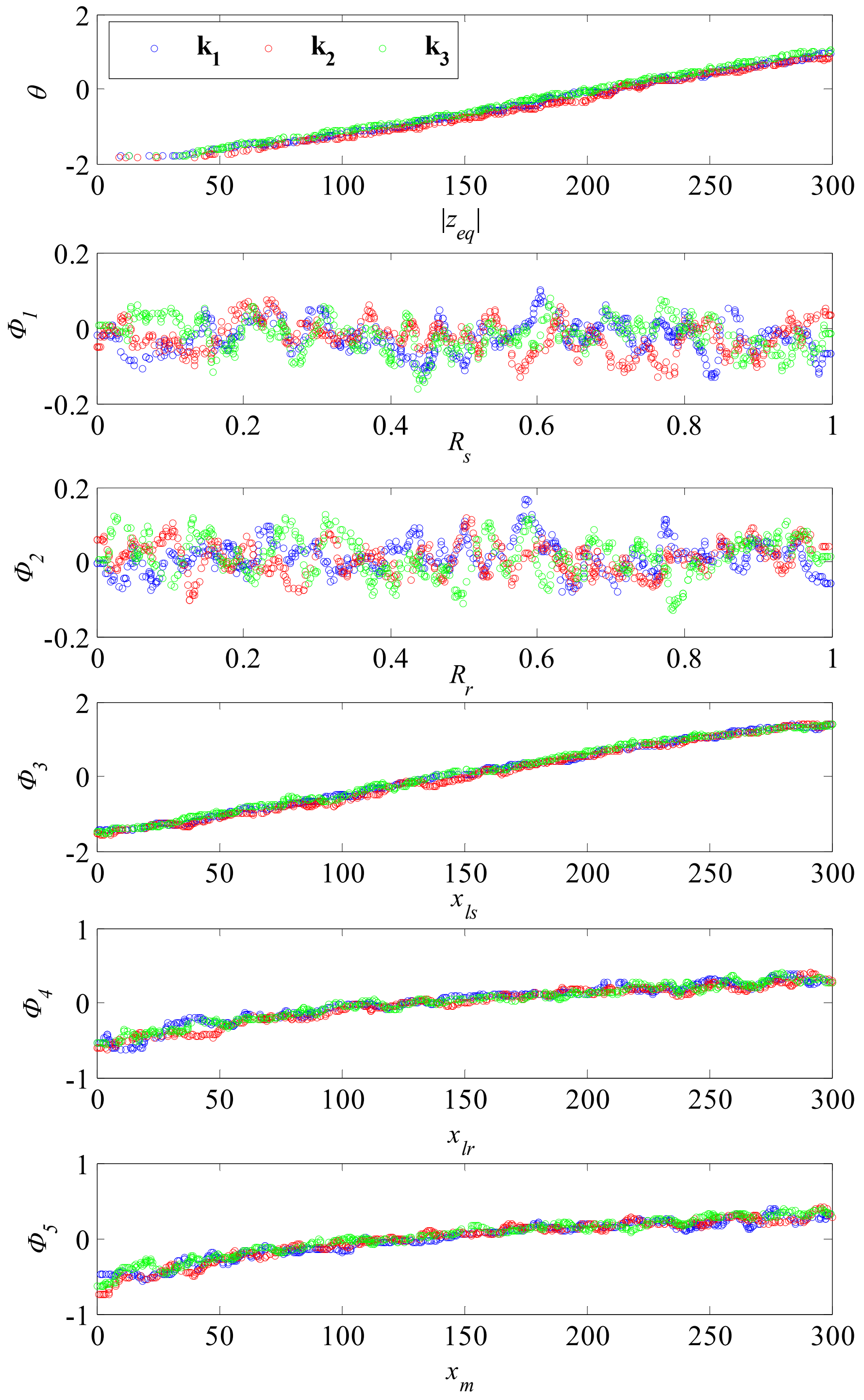

Figure 5.2 ACE optimal transformations plot of the T-model parameters.

5.3 Identifiability analysis of IM inverse Γ-model

Similar to the IM T-model, the identifiability of the inverse Γ-model is tested using the approaches described in chapter 2.

5.3.1 The transfer function approach

The input impedance of the inverse Γ-model as a function of the slip s is given by [18]:

$$Z'_{eq}(p,s)=\frac{\rho^2 s+\rho s a_2/b_2+\rho c_2+a_2 d_2}{\rho s/b_2+d_2} \tag{5.4}$$

where $\rho=j\omega s$, and a_2, b_2, c_2 and d_2 are functions of the four electrical parameters of the model and they can be obtained from the following expressions:

$$\begin{aligned} a_2 &= R_S, \\ b_2 &= l'_{ls}, \\ c_2 &= R'_r(l'_{ls}+L'_m)/l'_{ls}L'_m, \\ d_2 &= R'_r/l'_{ls}L'_m \end{aligned} \tag{5.5}$$

The transfer function of this model is given by [18]:

$$G_\Gamma(s)=1/Z'_{eq}=\frac{Ss/b_2+d_2}{S^2 s+S(sa_2/b_2+c_2)+a_2 d_2} \tag{5.6}$$

There are four coefficients of $G_\Gamma(s)$ that can be uniquely determined if the external measurements are used. Model parameters can then be uniquely identified from these coefficients by using (5.5) [18].

5.3.2 Bond graph Approach

To avoid the causality conflict occurred in the bond graph of the T-model, the stator leakage inductance is combined together with that of the rotor as suggested in [161]. Figure 5.3 shows the bond graph of the inverse Γ-model where the parameter redundancy has been removed and a proper bond graph is obtained [18].

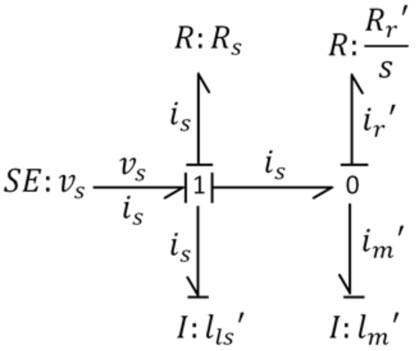

Figure 5.3 Bond graph of IM Inverse Γ-equivalent circuit.

5.3.3 Alternating conditional expectation algorithm

The ACE technique is used to estimate the transformations of a response Z'_{eq} and a set of four predictor variables (R_s, R'_r, L'_{ls} and L'_m) based on the IM inverse Γ-model [10]. R_s , R′r, x'_{ls}, and x'_m are independently drawn and Z'_{eq} was calculated for each estimate. This was repeated three different times and, accordingly, three different matrices $\mathbf{k}_i$ =[Z'_{eq} R_s R'_r x'_{ls} x'_m] (*i*=1, 2 and 3) with dimension of 500×5 are obtained and serve as inputs to the ACE algorithm. The optimal transformations for the response (Z'_{eq}), and the four predictors (R_s, R'_r, L'_{ls} and L'_m) are shown in figure 5.4 [10].

The transformations look different from one estimate to another. This demonstrates the independence of the parameters and thus the identifiable nature of the model. The maximum total correlation between the response Z'_{eq} and the four predictors was calculated at 0.0023038. This very low correlation coefficient between the inverse Γ-model impedance and the four electrical parameters means there is no dependence between the parameters. Thus, the parameters of the inverse Γ-model can be uniquely identified.

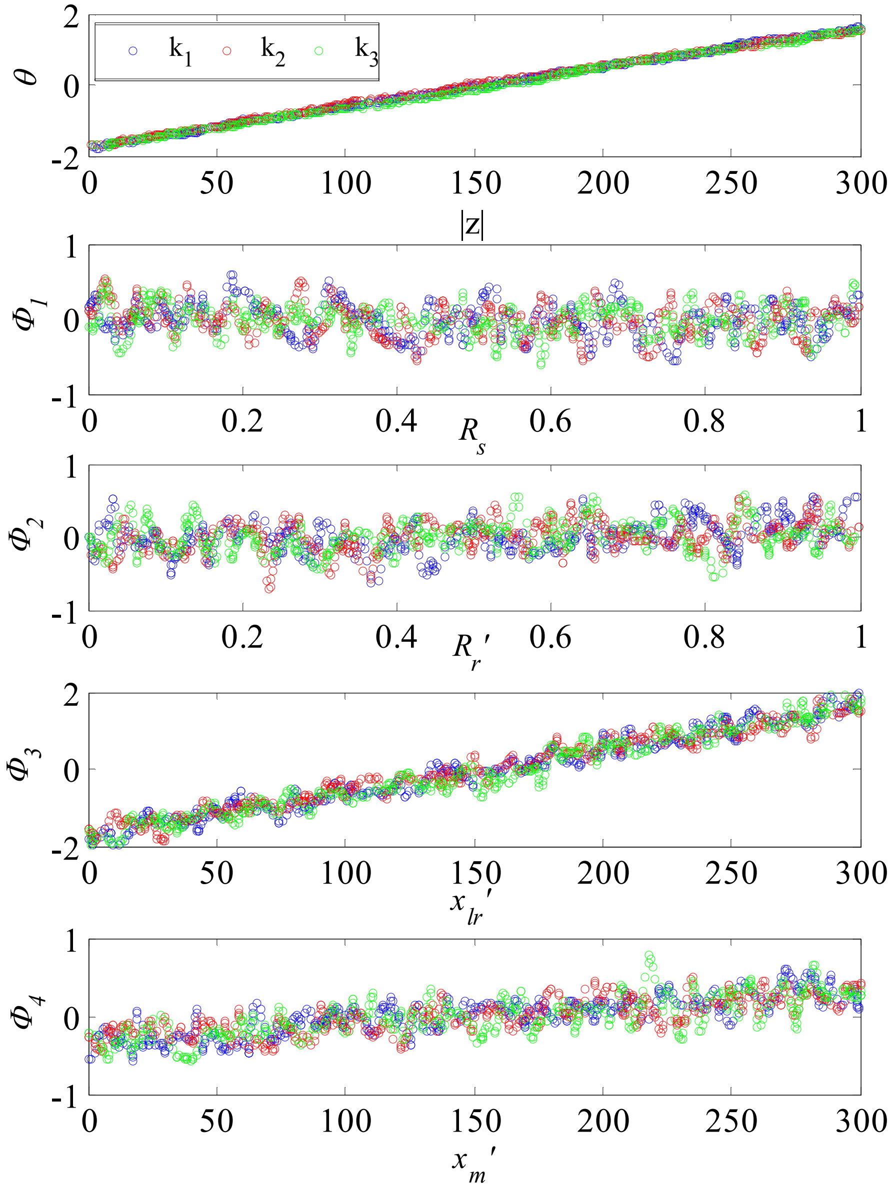

Figure 5.4 ACE optimal transformations plot of IM Inverse Γ-model parameters.

5.4 Experimental verification

In this section, the identifiability analyses presented in Sections 5.2 and 5.3 are verified using the L-M and PSO tools in conjunction with measured data from the test machine described in chapter 4 operating under steady-state conditions. This is verified for both supply-fed and inverter-fed operations of the machine as detailed below.

The L-M and PSO are developed and employed to estimate the parameters of the T- and Inverse Γ-models of the IM. These techniques are based on the use of external measurements of only one phase stator voltage and current and rotor speed. The measured phase A stator current (i_{Am}) is compared with calculated from the simulation model (i_{Ac}) with the model parameters adjusted by the optimization algorithm (L-M or PSO) to minimize the error and to find the model parameters that give the best match between the two current sets. The block diagram of the identification process is shown in figure 5.5.

The IM is modelled using Matlab/Simulink as shown in chapter 4. The optimization algorithms (parameter tuning) were done using M-files that were run along with the simulation to find the solutions (minimum error). This was done for different operating conditions of the test machine.

In the case of an identifiable model, the results should not be affected by the identification algorithm initialization. The algorithm will converge to the same solution (within acceptable limits) regardless of the initial conditions used to initialize the identification search. For a non-identifiable model, different parameter values will be obtained for different initial conditions (*i.e.* for different runs of the algorithm).

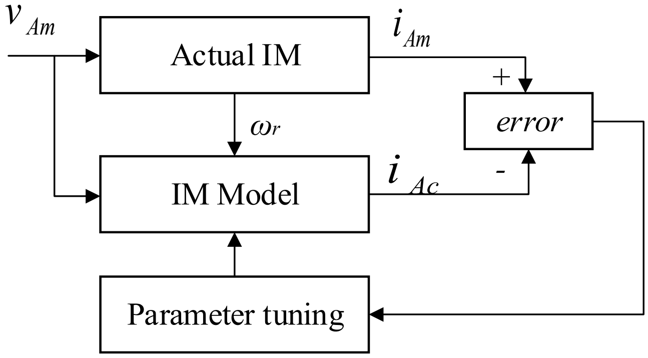

Figure 5.5 General structure of the identification technique.

5.4.1 Levenberg-Marquardt (L-M) algorithm for parameter estimation

The measured current shown in chapter 4 is compared with calculated current obtained from the IM model. The task of the L-M algorithm is to minimize the error and to find the model parameters that give the best match between the two current sets.

A. T-model identifiability analysis using L-M

For the T-model, the L-M algorithm continuously updates the five parameter values (R_s, R_r, l_{ls}, l_{lr}, and L_m) and feeds them to the system model (constructed in Matlab/Simulink) to calculate the phase current until a close agreement between the measured and calculated currents is achieved. The process is then repeated for different initial conditions.

For supply-fed, the current is adjusted by the ac drive of the synchronous machine loading the induction motor. This occurs at a speed of 1418 r/m (i.e. a slip of 0.055) as shown in chapter 4. The parameter identification process using the L-M is repeated many times at different initial conditions achieving completely different results every time, as demonstrated in table 5.1 which shows three such estimates. Figure 5.6 shows the convergence history of the estimated parameters of the T-Model for the three different estimates. Figure 5.7 shows the error function convergence for the 1st estimate.

Figure 5.8 shows the measured current (i_{Am}) and the calculated current (i_{AC}) with one of the parameter sets obtained by L-M parameters (1st estimate). Figure 5.9 shows the squared error (χ^2) as a function of rotor and stator leakage inductances based on the measured data.

Pars.	1st estimate	2nd estimate	3rd estimate
R_s	6.3470 Ω	3.8862 Ω	5.2315 Ω
R_r	2.3655 Ω	2.5006 Ω	3.5782 Ω
l_{ls}	0.1075 H	0.1105 H	0.0418 H
l_{lr}	0.0328 H	0.0344 H	0.0644 H
L_m	1.2383 H	1.5739 H	0.4321 H
$\lvert Z_{eq} \rvert$	67.30 Ω	68.31 Ω	67.77 Ω
$\angle Z_{eq}$	45.76 °	46.12 °	45.61 °

Table 5.1 Parameter Estimation of T-model using L-M; supply-fed at full-load (s= 0.055).

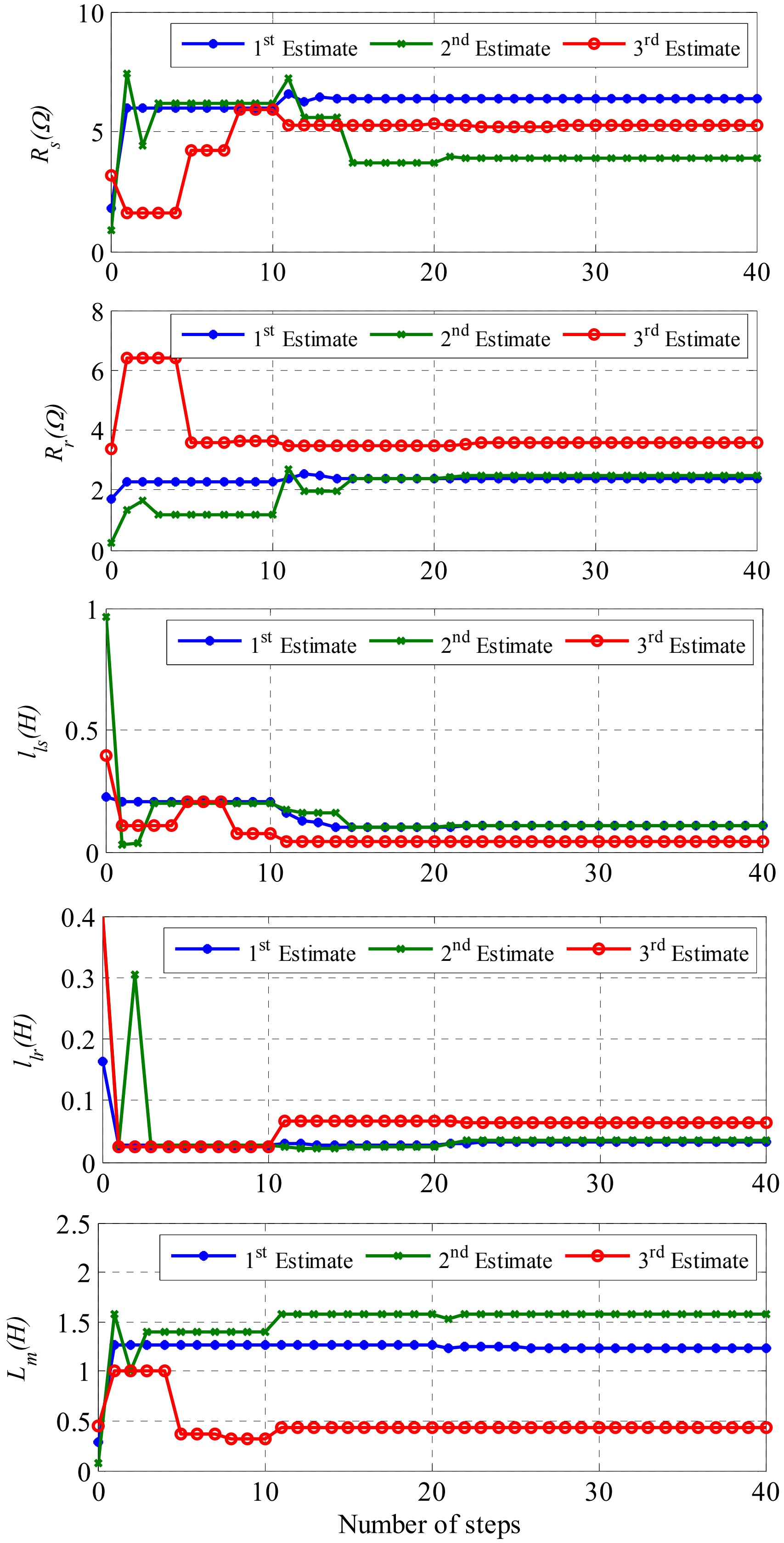

Figure 5.6 Convergence of the estimated parameters of the T-Model for different estimates using L-M; supply-fed at full-load (*s*=0.055).

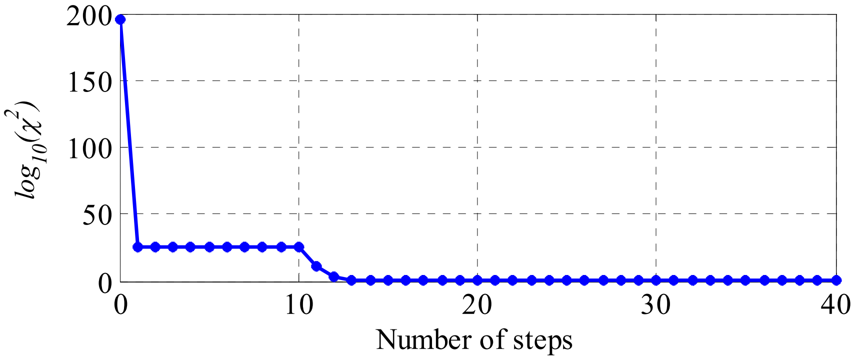

Figure 5.7 The error function convergence for the 1st estimate (T-model) using L-M; supply-fed at load (*s*=0.055).

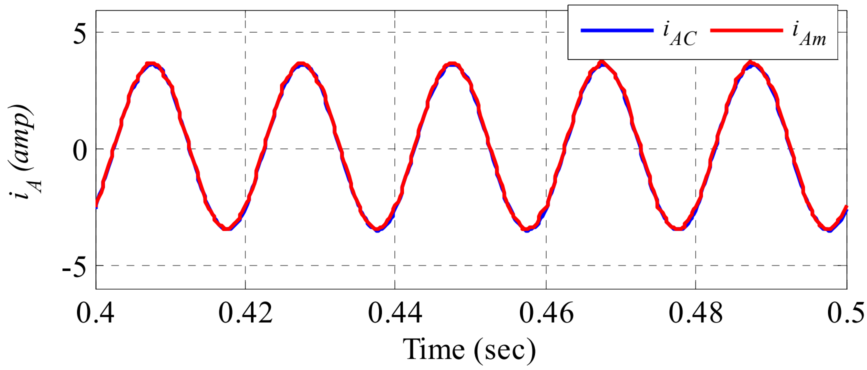

Figure 5.8 Measured (i_{Am}) and calculated (i_{Ac}) stator currents waveforms corresponding to the optimal solution of the 1st estimate (T-Model) using L-M; supply-fed at load (*s*=0.055).

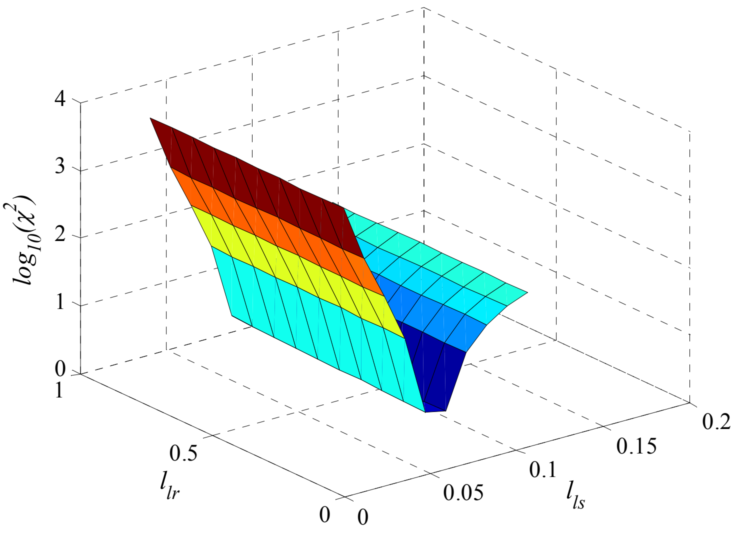

Figure 5.9 The sum of the squared error as a function of l_{ls} and l_{lr} based on the measured data (T-Model).

As shown, infinite combinations of the two inductance values result in the same minimum value of the squared error, i.e. there is no unique global minimum. This confirms that it is not possible to determine l_{ls} and l_{lr} uniquely using external measurements of voltage, current, and speed.

For further validation, parameter identification is also investigated when the machine is driven by the variable frequency inverter described in chapter 4. Simple V/f control was implemented and the parameter identification was investigated at two different frequencies, 50 Hz and 25 Hz.

Similar to the supply-fed case, stator current is adjusted at the full load value using the ac drive of the synchronous machine load. This occurs at a speed of 1417 r/m (i.e. a slip of 0.055) and 694 r/m (i.e. a slip of 0.075) for the 50 Hz and 25 Hz operation, respectively.

Table 5.2 shows three different parameter estimates for 50 Hz inverter-fed operation of the IM at full load with slip of 0.055(1417 r/m). Figure 5.10 shows the convergence history of the estimated parameters of the T-Model for the three different estimates. Figure 5.11 shows the error function convergence for the 1st estimate. Figure 5.12 shows the measured current (i_{Am}) and the calculated current (i_{AC}) with one of the parameter sets obtained by L-M parameters (1st estimate).

Pars	1st estimate	2nd estimate	3rd estimate
R_s	9.5726 Ω	7.8724 Ω	4.2479 Ω
R_r	3.0323 Ω	2.6168 Ω	4.6831 Ω
l_{ls}	0.0656 H	0.0981 H	0.0109 H
l_{lr}	0.0323 H	0.0214 H	0.0206 H
L_m	0.4208 H	0.8366 H	0.2977 H
$\lvert Z_{eq}\rvert$	68.42 Ω	68.41 Ω	66.04 Ω
$\angle Z_{eq}$	42.12 °	41.16 °	44.13 °

Table 5.2 Parameter Estimation of T-model using L-M, inverter-fed, Full-load (*s*= 055 and 50Hz).

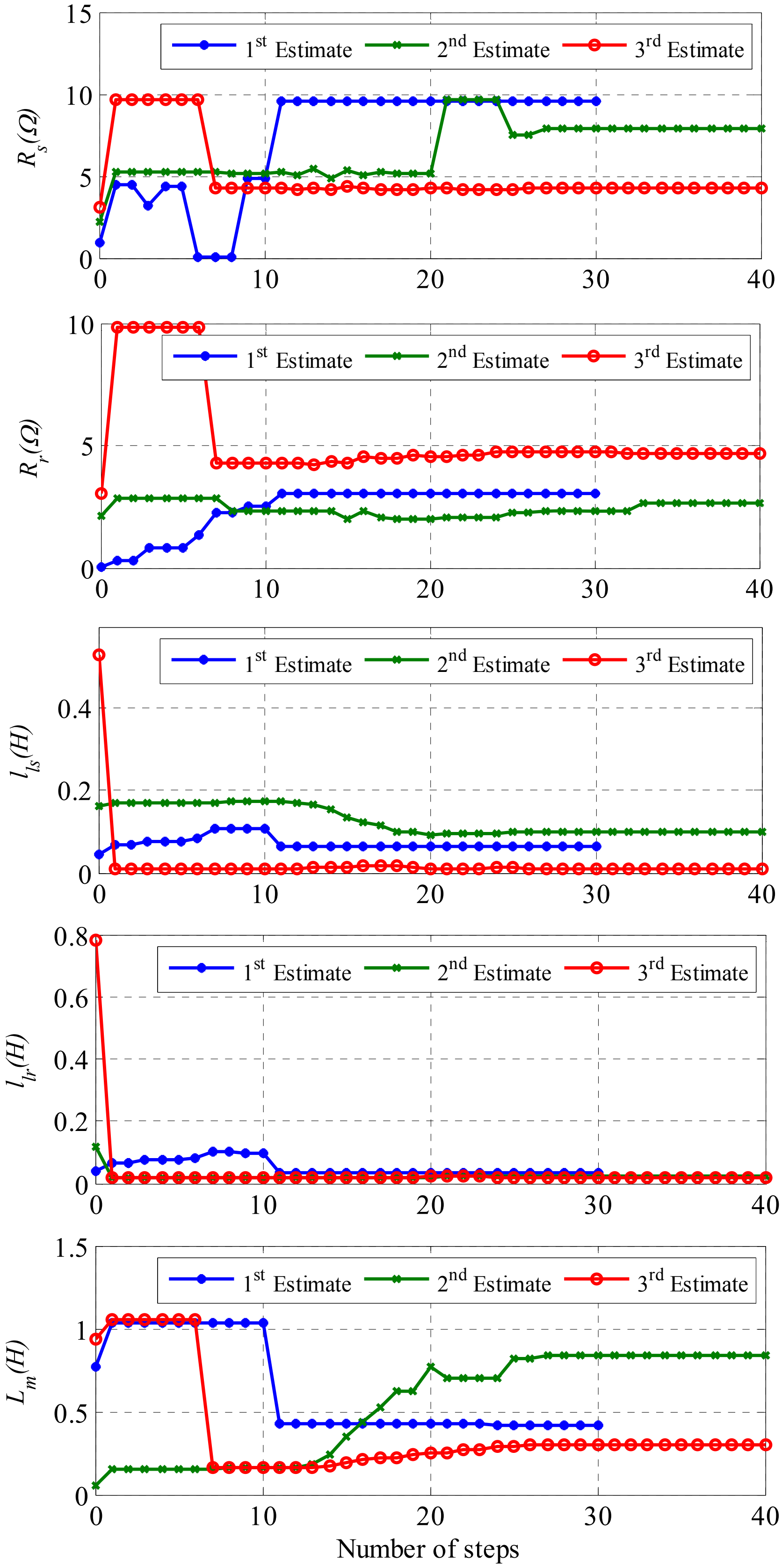

Figure 5.10 Convergence of the estimated parameters of the T-Model for different estimates using L-M, inverter-fed, (s=0.055 and 50 Hz).

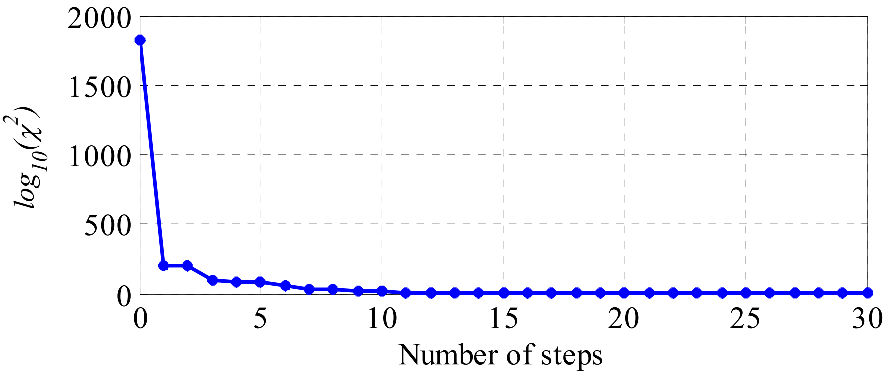

Figure 5.11 The error function convergence for the 1st estimate (T-model) using L-M, inverter-fed, (s=0.055 and 50 Hz).

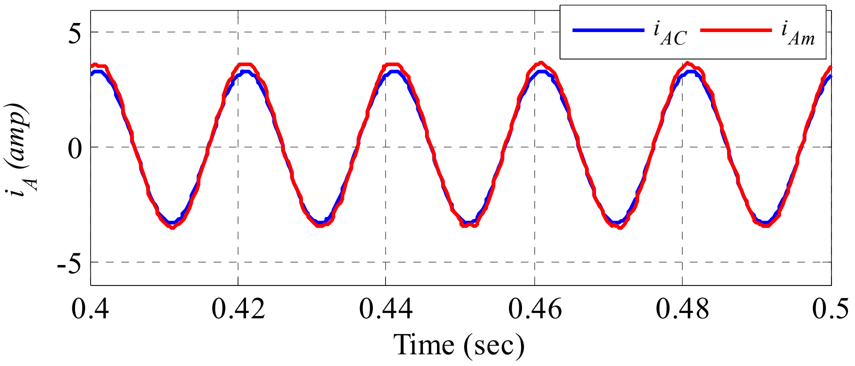

Figure 5.12 Measured (i_{Am}) and calculated (i_{Ac}) stator currents waveforms corresponding to the optimal solution of the 1st estimate using L-M, inverter-fed, (s=0.055 and 50 Hz).

Three different parameter estimates for 25 Hz inverter-fed operation of the IM at full-load with slip of 0.075(694 r/m) are demonstrated in Table 5.3. Figure 5.13 shows the convergence history of the estimated parameters of the T-Model for the three different estimates. Figure 5.14 shows the error function convergence for the 1st estimate. Figure 5.15 shows the measured current (i_{Am}) and the calculated current (i_{AC}) with one of the parameter sets obtained by L-M parameters (1st estimate).

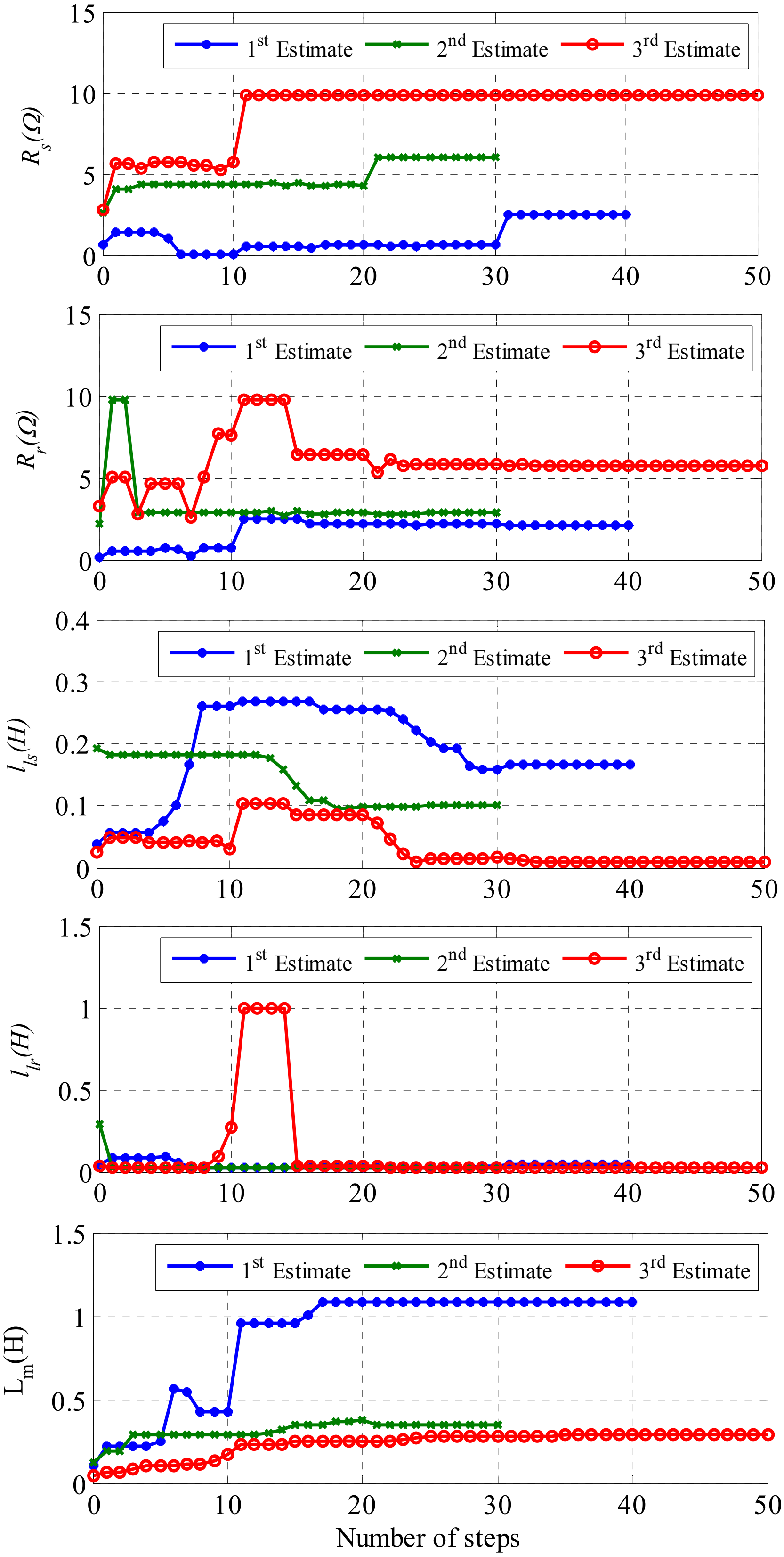

Figure 5.13 Convergence of the estimated parameters of the T-Model for different estimates using L-M, inverter-fed, (s=0.075 and 25 Hz).

Pars	1st estimate	2nd estimate	3rd estimate
R_s	2.4552	5.9963	9.8298
R_r	2.0881	2.8468	5.7151
l_{ls}	0.1665	0.0996	0.0101
l_{lr}	0.0406	0.0279	0.0205
l_m	1.0882	0.3493	0.2880
$\|Z_{eq}\|$	45.74 Ω	54.23 Ω	45.22 Ω
$\angle Z_{eq}$	52.52 °	49.88 °	50.20 °

Table 5.3 Parameter Estimation of T-model using L-M, inverter-fed, Full-load (*s*= 075 and 25 Hz).

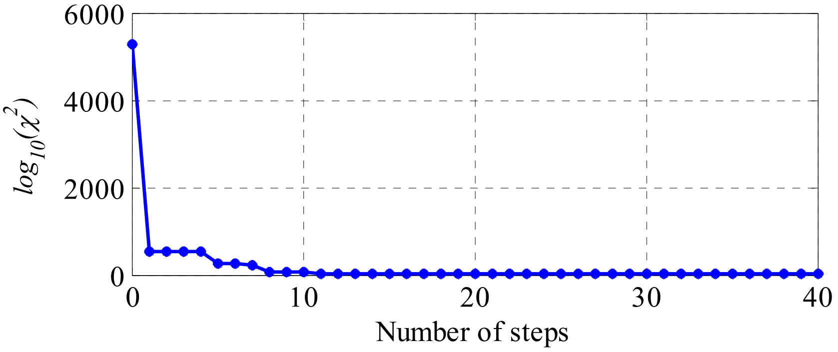

Figure 5.14 The error function convergence for the 1st estimate (T-model) using L-M, inverter-fed, (s=0.075 and 25 Hz).

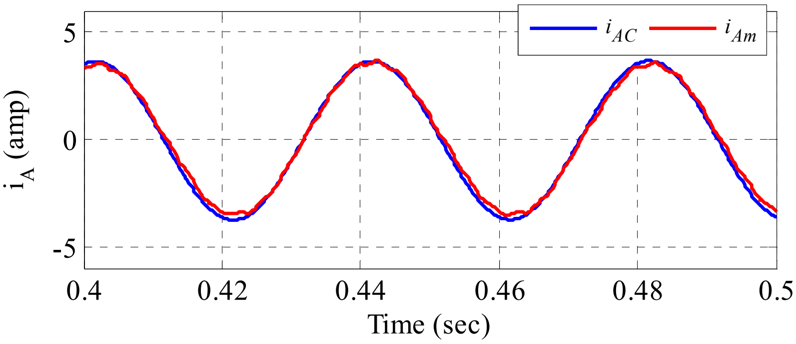

Figure 5.15 Measured (i_{Am}) and calculated (i_{Ac}) stator currents waveforms corresponding to the optimal solution of the 1st estimate using L-M, inverter-fed, (s=0.075 and 25 Hz).

B. Inverse Γ-model identifiability analysis using L-M

In this test, the parameter vector **P** represents a set of the four parameters (R_s, R_r', L_{ls}' and L_m') of the inverse Γ-model. Regardless of the initial conditions, the L-M algorithm successfully estimates the parameter vector of the inverse Γ-model. The same measurements for supply-fed and inverter-fed IM used in previous tests are used here.

Table 5.4 represents three sets of estimated parameter values for different initial conditions at full-load supply-fed IM with slip of 0.055. The total impedance corresponding to each estimate are also calculated and shown in the table. Figure 5.16 shows the convergence history of the estimated parameters of the T-Model for the three different estimates at full-load.

Figure 5.17 shows the error function convergence for the 1st estimate. Figure 5.18 shows the measured current (i_{Am}) and the calculated current (i_{AC}) with one of the parameter sets obtained by L-M parameters (1st estimate).

The squared error (χ^2) as a function of the two inductances (l_{ls}' and L_m') based on the measured data is shown in Figure 5.19. As illustrated, there is only one optimal combination of the two parameter values (l_{ls}'= 0.0912 H, L_m'= 0.366 H) that satisfies the objective function and provides one global minimum.

Pars.	1st estimate	2nd estimate	3rd estimate
R_s	3.4501 Ω	3.6112 Ω	3.5560 Ω
R_r'	2.6900 Ω	2.7045 Ω	2.6181 Ω
l_{ls}'	0.0900 H	0.0998 H	0.0998 H
L_m'	0.3685 H	0.3787 H	0.4103 H
$\lvert Z_{eq}\rvert$	64.46 Ω	66.99 Ω	63.94 Ω
$\angle Z_{eq}$	45.53 °	46.85 °	45.52°

Table 5.4 Parameter Estimation of Inverse Γ-model using L-M; supply-fed at full-load (*s*=0.055).

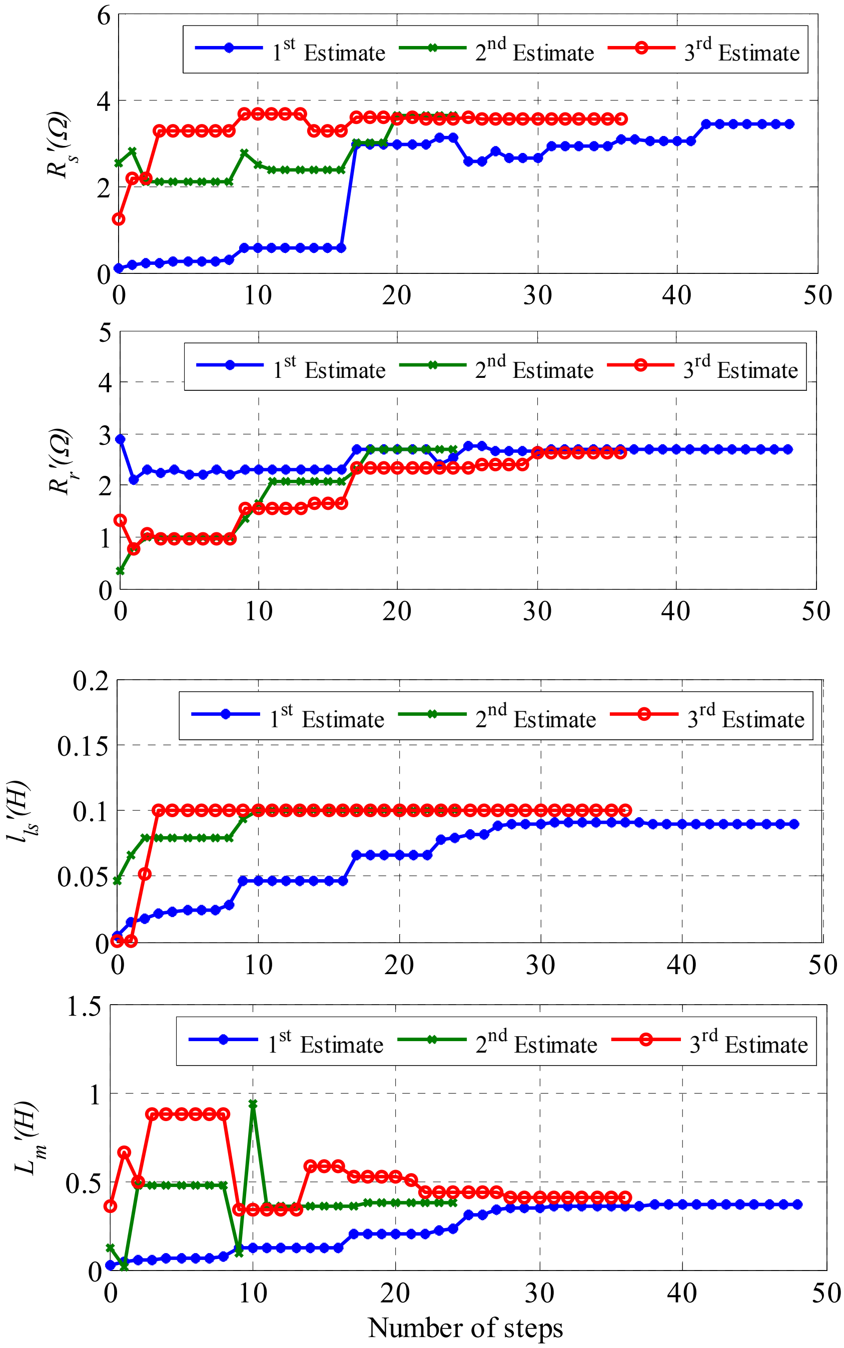

Figure 5.16 Convergence of the estimated parameters of the Inverse Γ-Model for different estimates using L-M at full-load, supply-fed, (s=0.055).

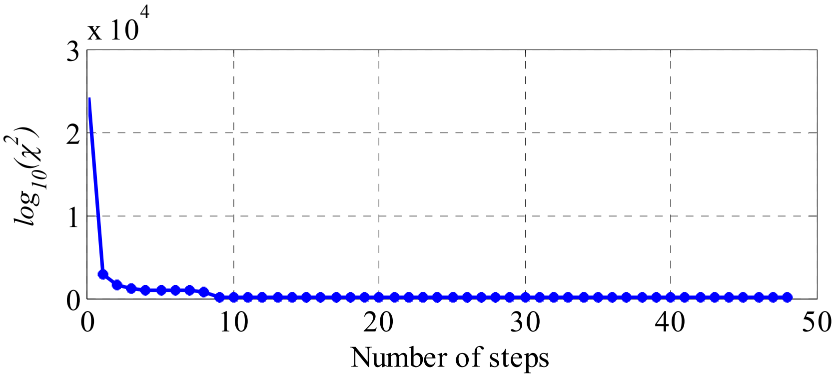

Figure 5.17 **The error function convergence for the 1st estimate (Inverse Γ-Model) using L-M, supply-fed, (s=0.055).**

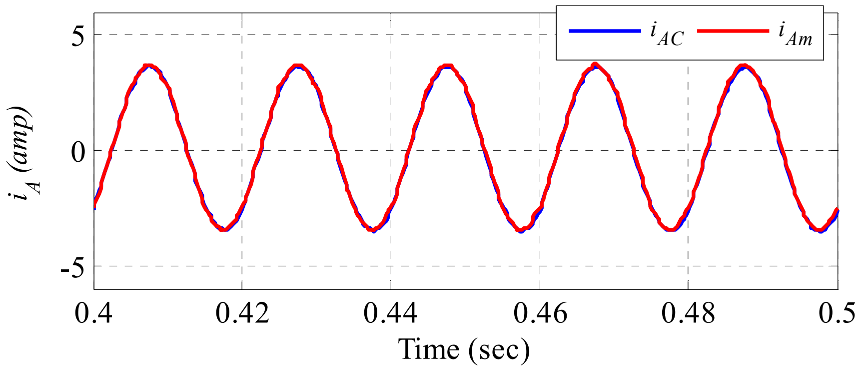

Figure 5.18 **Measured (*i_{Am}*) and calculated (*i_{Ac}*) stator currents waveforms corresponding to the optimal solution of the 1st estimate (Inverse Γ-Model) using L-M, supply-fed, (s=0.055).**

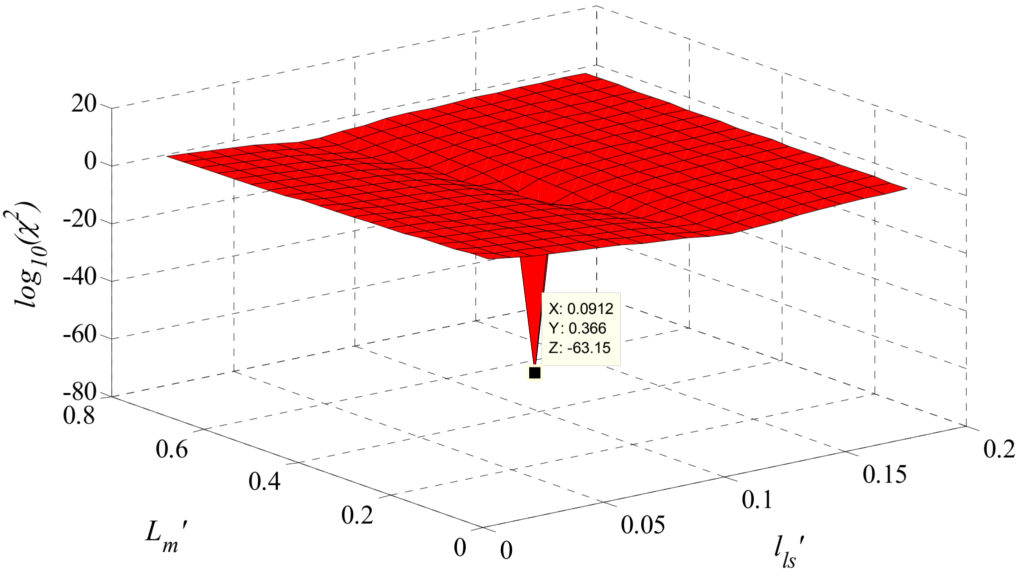

Figure 5.19 **The sum of the squared error as a function of of *l_{ls}'* and *L_m'* based on the measured data (Inverse Γ-model).**

Table 5.5 shows three different parameter estimates for 50 Hz inverter-fed operation of the IM at full-load with slip of 0.055 (1417 r/m). The total impedance corresponding to each estimate are also calculated and shown in the table. Figure 5.20 shows the convergence history of the estimated parameters of the T-Model for the three different estimates.

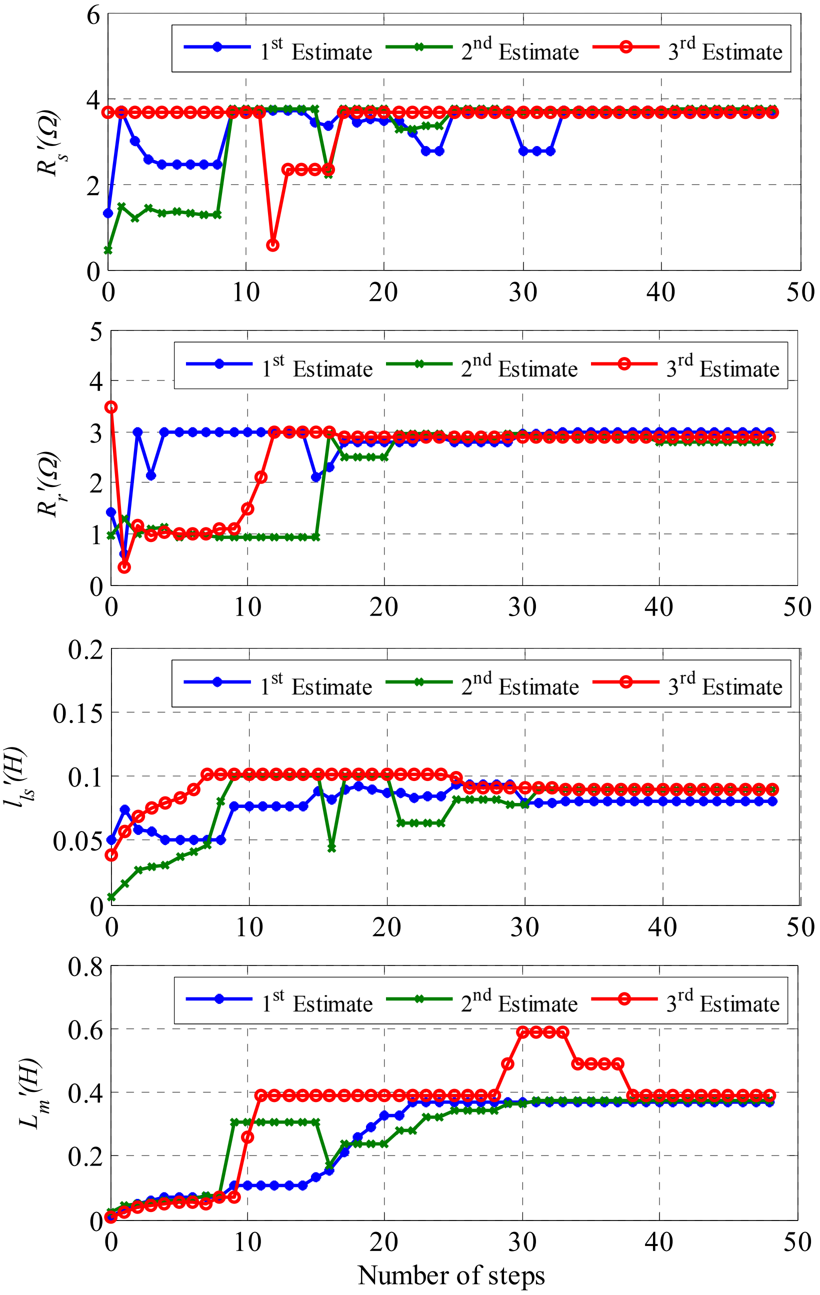

Figure 5.20 Convergence of the estimated parameters of the Inverse Γ-model for different estimates using L-M, inverter-fed, (s=0.055 and 50 Hz).

Figure 5.21 shows the error function convergence for the 1st estimate. Figure 5.22 shows the measured current (i_{Am}) and the calculated current (i_{AC}) with one of the parameter sets obtained by L-M parameters (1st estimate).

Pars.	1st estimate	2nd estimate	3rd estimate
R_s	3.7112 Ω	3.7303 Ω	3.6797 Ω
$R_r{}'$	2.977 Ω	2.8036 Ω	2.8967 Ω
$l_{ls}{}'$	0.0804 H	0.0895 H	0.0890 H
$L_m{}'$	0.3703 H	0.3762 H	0.3893 H
$\lvert Z_{eq}\rvert$	66.36 Ω	66.28 Ω	67.06 Ω
$\angle Z_{eq}$	43.59	44.98	44.91

Table 5.5 Parameter Estimation of Inverse Γ-model using L-M, inverter-fed, (*s*=0.055 and 50Hz).

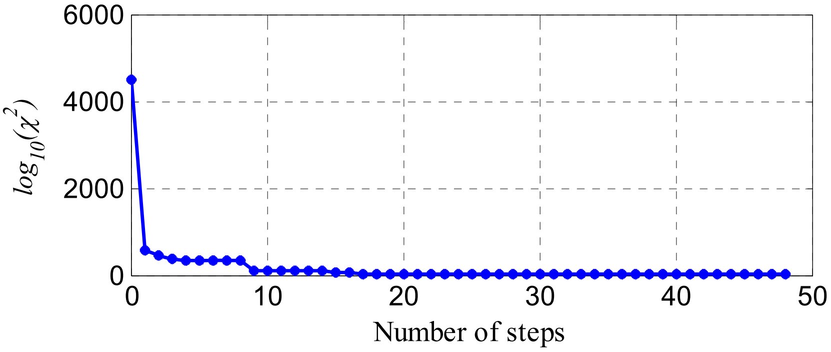

Figure 5.21 The error function convergence for the 1st estimate (Inverse Γ-model) using L-M, inverter-fed, (s=0.055 and 50 Hz).

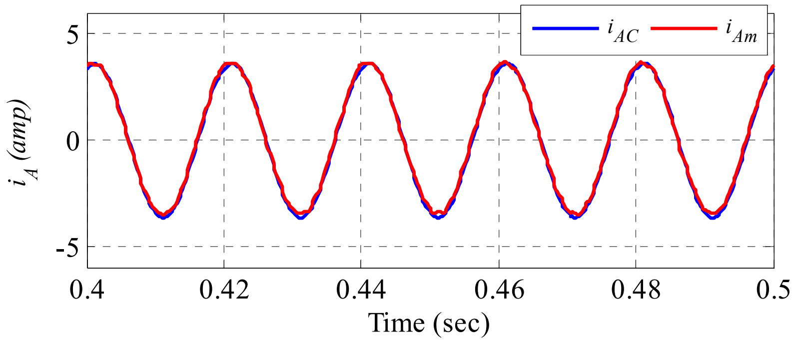

Figure 5.22 Measured (i_{Am}) and calculated (i_{Ac}) stator currents waveforms corresponding to the optimal solution of the 1st estimate using L-M, inverter-fed, (s=0.055 and 50 Hz).

Three different parameter estimates for 25 Hz inverter-fed operation of the IM at full-load with slip of 0.075 (694 r/m) are demonstrated in Table 5.6. Figure 5.23 shows the convergence history of the estimated parameters of the inverse Γ-model for the three different estimates.

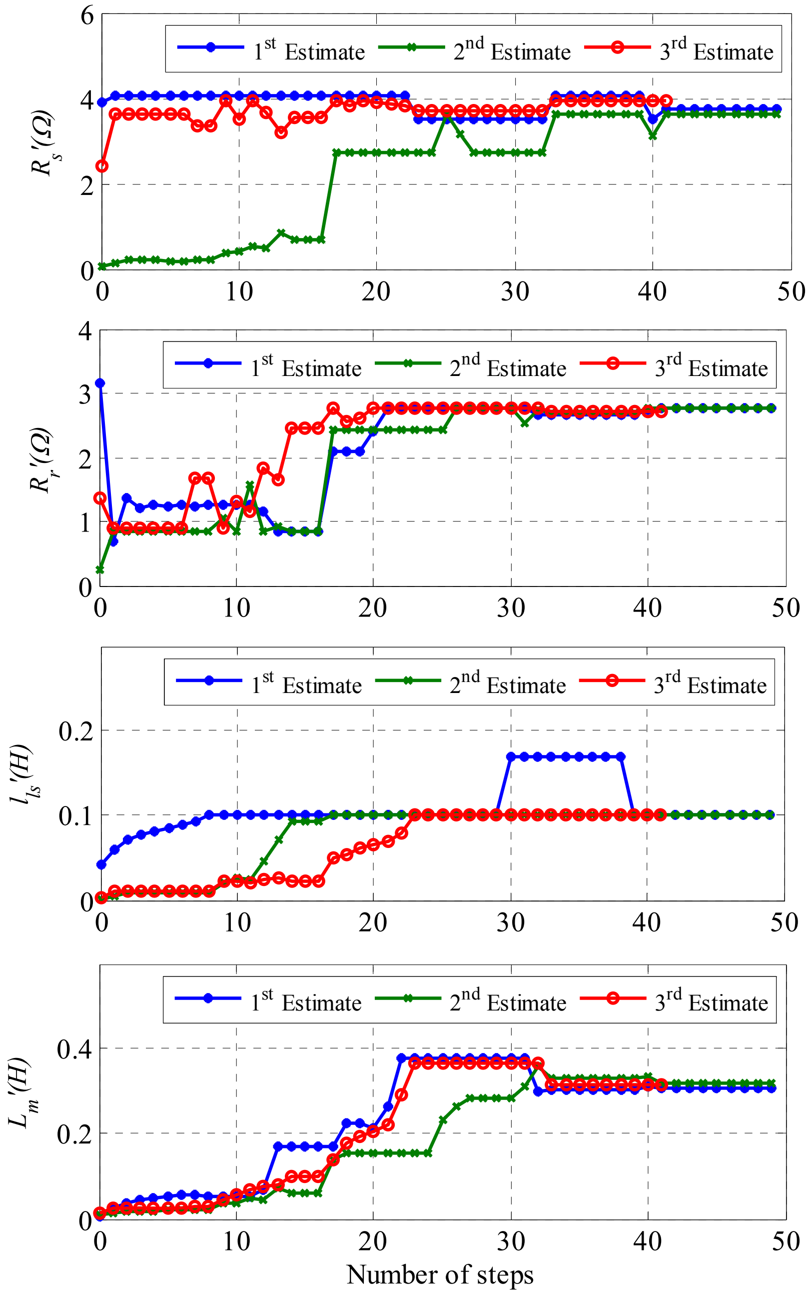

Figure 5.23 The error function convergence for the 1st estimate (Inverse Γ-model) using L-M, inverter-fed, (s=0.075 and 25 Hz).

Figure 5.24 shows the error function convergence for the 1st estimate. Figure 5.25 shows the measured current (i_{Am}) and the calculated current (i_{AC}) with one of the parameter sets obtained by L-M parameters (1st estimate).

Pars.	1st estimate	2nd estimate	3rd estimate
R_s	3.7481 Ω	3.6221 Ω	3.8447 Ω
$R_r{}'$	2.7636 Ω	2.7714 Ω	2.7201 Ω
$l_{ls}{}'$	0.1000 H	0.1005 H	0.1005 H
$L_m{}'$	0.3095 H	0.3201 H	0.3149 H
$\lvert Z_{eq} \rvert$	43.38 Ω	43.46 Ω	43.14 Ω
$\angle Z_{eq}$	50.67	50.46	50.26

Table 5.6 Parameter Estimation of Inverse Γ-model using L-M, inverter-fed (*s*=0.075 and 25Hz).

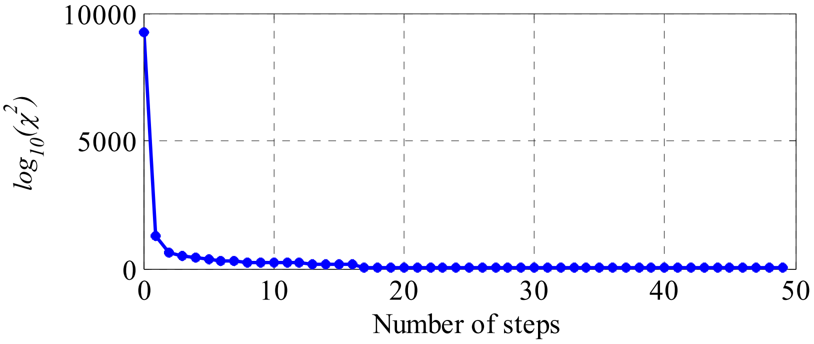

Figure 5.24 The error function convergence for the 1st estimate (Inverse Γ-model) using L-M, inverter-fed, (s=0.075 and 25 Hz).

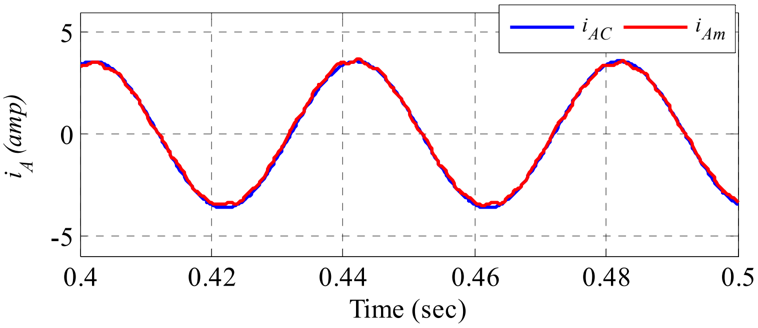

Figure 5.25 Measured (i_{Am}) and calculated (i_{Ac}) stator currents waveforms corresponding to the optimal solution of the 1st estimate using L-M, inverter-fed, (s=0.075 and 25 Hz).

5.4.2 Particle swarm optimization (PSO) algorithm for parameter estimation

The Particle swarm optimization (PSO) tool is developed and employed to estimate the parameters of the T- and Inverse Γ-models of the IM. Herein, the PSO algorithm is used to find the best-fit machine parameters by minimizing an objective function, the integral absolute error (IAE) between the measured phase A stator current (i_{Am}) and that calculated from the simulation model (i_{Ac}):

$$IAE = \sum \left(\left| i_{Am} - i_{Ac} \right| \right) \Delta T \tag{5.7}$$

where ΔT is the sampling period.

This was done for different operating conditions of the test machine. The block diagram of the identification process is shown in figure 5.5. The same previous measurements are used with the PSO. To avoid repetition, only inverter-fed results are included in this chapter, more results can be found in Appendix C.

A. T-model identifiability analysis using PSO

For the T-model, each particle represents one set of the five parameters (R_s, R_r, l_{ls}, l_{lr}, and L_m) of the T-model. The PSO algorithm continuously updates these five parameter values and feeds them to the system model (constructed in Matlab/Simulink) to calculate the phase current until a close agreement between the measured and calculated currents is achieved. The process has been done for different times with different initial conditions. Depending on the initial conditions, completely different sets of parameters can be obtained.

Table 5.7 shows three sets of estimated parameter values (each obtained with different initial conditions) at full-load inverter-fed IM with slip of 0.055. The total impedance corresponding to each estimate are also calculated and shown in the table. Figure 5.26 shows the convergence history of the estimated parameters of the T-Model for the three different estimates. Figure 5.27 shows the error function convergence for the 1st estimate. The 1st parameter sets obtained by PSO is applied using the Matlab model and the calculated (i_{AC}) and measured (i_{Am}) stator currents are showed in figure 5.28.

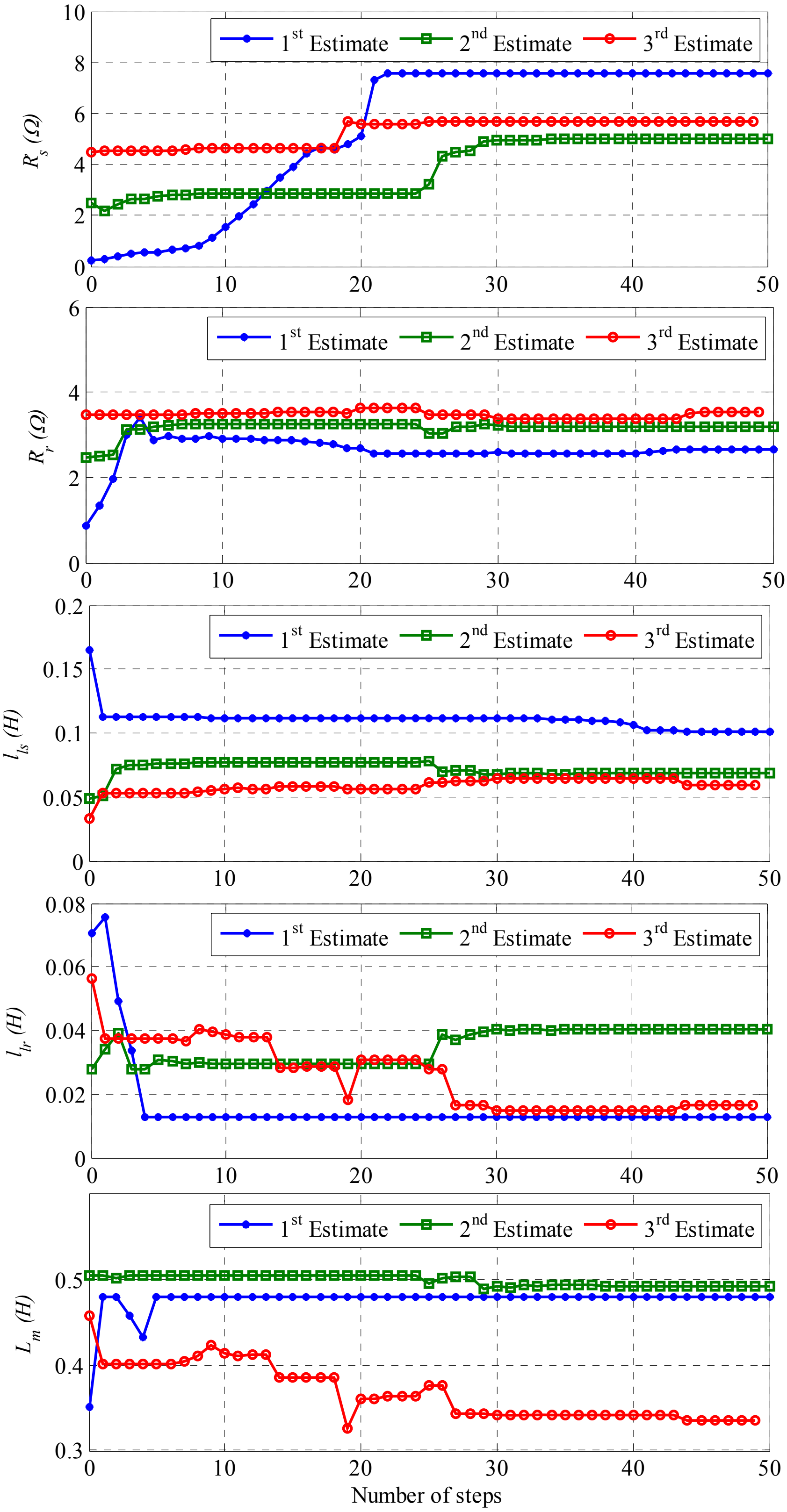

Figure 5.26. Convergence of the estimated parameters of the T-Model for different estimates using PSO; inverter-fed (s=0.055 and 50 Hz).

Pars.	1st estimate	2nd estimate	3rd estimate
R_s	7.5456 Ω	4.9982 Ω	5.6665 Ω
R_r	2.6405 Ω	3.1882 Ω	3.5210 Ω
l_{ls}	0.1001 H	0.0681 H	0.0594 H
l_{lr}	0.0126 H	0.0403 H	0.0167 H
L_m	0.480 H	0.4931 H	0.3350 H
$\|Z_{eq}\|$	68.79 Ω	68.79 Ω	69.04 Ω
$\angle Z_{eq}$	44.66 °	44.52°	44.75°

Table 5.7 Parameter Estimation of T-model using PSO; inverter-fed (s=0.055 and 50 Hz).

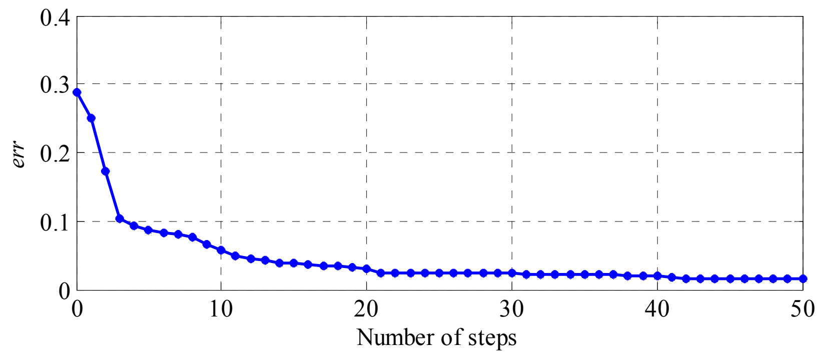

Figure 5.27 The error function convergence for the 1st estimate (T-model) using PSO; inverter-fed (s=0.055 and 50 Hz).

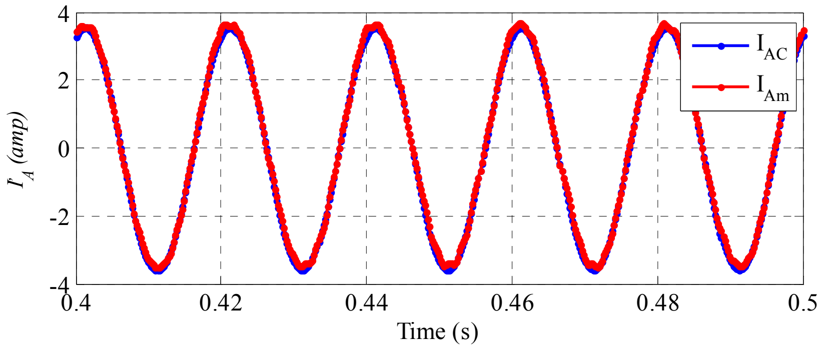

Figure 5.28 Measured (i_{Am}) and calculated (i_{Ac}) stator currents waveforms corresponding to the optimal solution of the 1st estimate (T-Model) using PSO; inverter-fed (s=0.055 and 50 Hz).

Figure 5.29 shows the error (*IAE*) as a function of rotor and stator leakage inductances based on the measured data. As shown, infinite combinations of the two inductance values result in the same minimum value of the error, i.e. there is no unique global minimum. This confirms that it is not possible to determine l_{ls} and l_{lr} uniquely using external measurements of voltage, current, and speed.

Figure 5.30 shows the speed-torque characteristics of the IM for the real (experimental parameters obtained from standard IEEE tests shown in table 4.1) and estimated parameter sets in table 5.7.

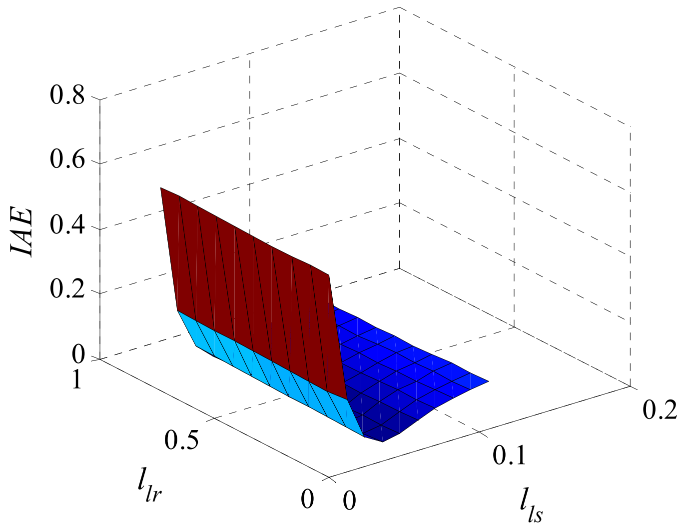

Figure 5.29 The *IAE* error as a function of l_{ls} and l_{lr} based on the measured data (T-Model).

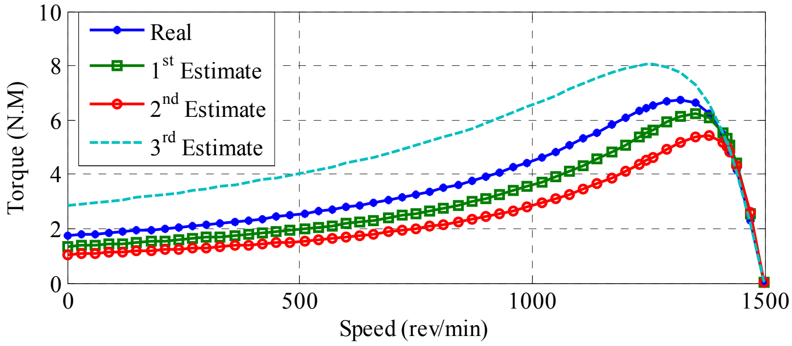

Figure 5.30 Speed vs. Torque for the experimental and the three different parameter sets illustrated in table 5.3

It can be observed from the obtained results that, completely different sets of parameters can be obtained depending on the initial conditions. Three sets of PSO estimated parameter values (each obtained with different initial conditions) for each test are obtained. The total impedance corresponding to each test and estimate are also calculated and shown in the tables. Despite the significant differences between the three sets of parameters, the calculated current closely matches the measured current in each case. In addition, almost the same electromagnetic torque at slip of 0.055 is obtained for the all sets including the real one; 5.1969 N.m, 5.3361 N.m, 5.017 N.m, and 5.2073 N.m respectively. This confirms that the T-model is non-identifiable.

B. Inverse Γ-model identifiability analysis using PSO

Similar to the T-model, identifiability of the inverse Γ-model is investigated using PSO technique. In this test, each particle represents one set of the four parameters (R_s, R_r', L_{ls}' and L_m') of the inverse Γ-model. The task of PSO is to update the four parameter values until a close agreement between the measured and calculated currents is achieved. Again, the process has been done for different times with different initial parameters and operating conditions. Regardless the initial conditions, almost similar sets of parameters with an acceptable error can be obtained. Table 5.8 shows three sets of estimated parameters with different initial conditions at a slip of 0.055 for inverter-fed IM.

The convergence history of the estimated parameters for the three different estimates is demonstrated in figure 5.31. Figure 5.32 shows the error function convergence for the 1st estimate. Figure 5.33 shows the measured current (i_{Am}) and the calculated current (i_{AC}) with one of the parameter sets obtained by PSO parameters (1st estimate).

Pars.	1st estimate	2nd estimate	3rd estimate
R_s	3.7 Ω	3.9907 Ω	3.8969 Ω
$R_r{}'$	2.8565 Ω	2.9679 Ω	2.99768 Ω
$l_{ls}{}'$	0.0978 H	0.0905 H	0.0913 H
$L_m{}'$	0.4292 H	0.3851 H	0.3868 H
$\lvert Z_{eq} \rvert$	68.31 Ω	68.69 Ω	68.94 Ω
$\angle Z_{eq}$	44.59°	44.69°	44.82°

Table 5.8 Parameter estimation of Inverse Γ–model using PSO; inverter-fed (*s*=0.055 and 50Hz).

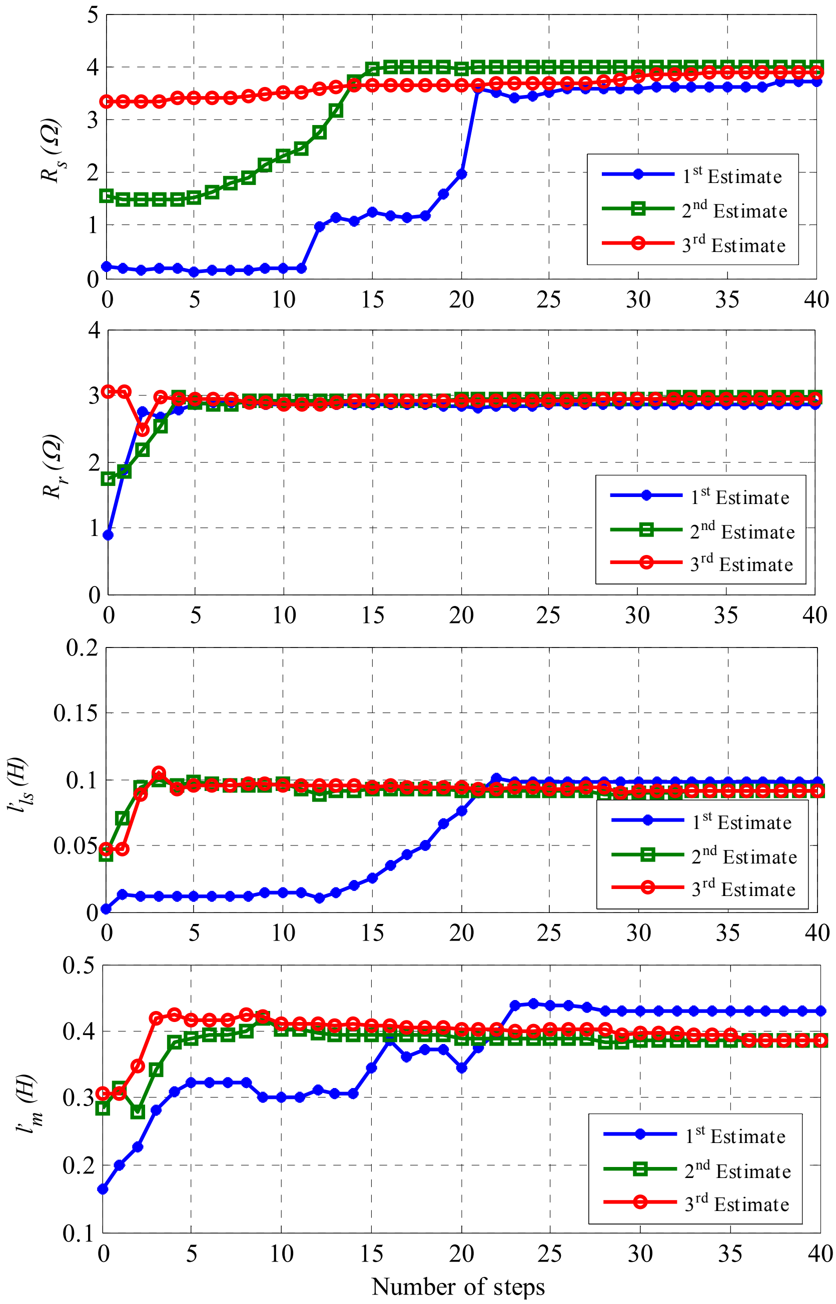

Figure 5.31 Convergence of the estimated parameters of the inverse Γ-model for different estimates; inverter-fed (*s*=0.055 and 50Hz).

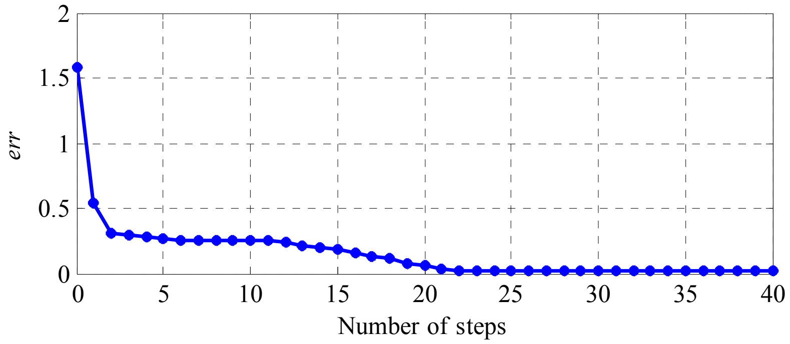

Figure 5.32 The error function convergence for the 1st estimate (inverse Γ -model); inverter-fed (s=0.055 and 50Hz).

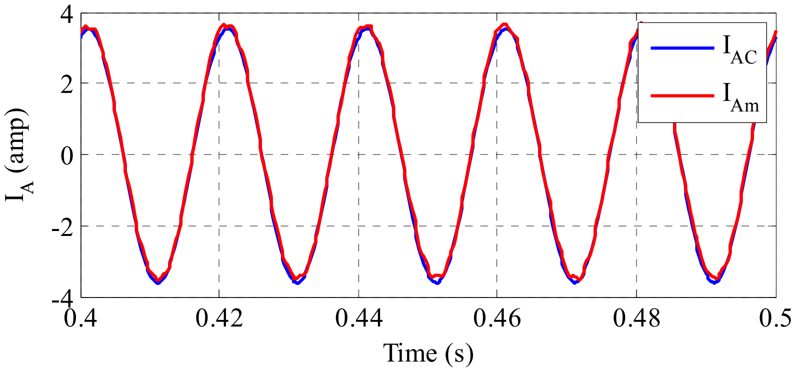

Figure 5.33 Measured (i_{Am}) and calculated (i_{Ac}) stator currents waveforms corresponding to the optimal solution of the 1st estimate (inverse Γ-Model) ; inverter-fed (s=0.055 and 50Hz).

Regardless of the initial conditions, PSO algorithm successfully estimates the parameter vector of the inverse Γ-model with an acceptable error. This small mismatch between the real and estimated parameters is due to measurements noise and unmodeled effects like the skin effect and the heat. As shown, a very good agreement between the measured and calculated current waveforms is realized. Similar agreement between current waveforms is obtained with the other sets of estimated parameters. The parameters of the T-model can be calculated from inverse Γ-model parameters based on equation 5.8.

$$\alpha = L_m / L_r, l_{ls}^{'} = L_s - \alpha L_m, L_m^{'} = \alpha L_m, R_r^{'} = \alpha^2 R_r \qquad (5.8)$$

This requires the ratio of α to be known which is not available in real application and, hence going back from inverse Γ-model to T-model is impossible. For many applications such as high performance control, the knowledge of the real physical parameter values of the T-model is necessary [162, 163].

5.5 Conclusion

This chapter presented a detailed study of the identifiability of the parameters of the T- and inverse Γ-equivalent circuits of the induction motor. The identifiability of both circuits has been investigated by the transfer function and bond graph as a priori identifiability approaches. A novel approach based on the Alternative Conditional Expectation (ACE) algorithm is proposed and applied to assess the identifiability of the two IM models. The analysis shows that, if external measurements are used, the machine T-model is non-identifiable whilst the inverse Γ-model is identifiable.

Using the ACE algorithm, a high correlation coefficient of about 0.996 between the parameters of the T-model is obtained suggesting that the parameters are dependent on each other and cannot be uniquely identified. On the other hand, ACE produces a small maximum correlation coefficient of 0.0023 between the parameters of the inverse Γ-model suggesting that the parameters of the model are identifiable.

These results are experimentally verified using measured machine waveforms, shown in chapter 4, in conjunction with the Levenberg-Marquardt (L-M) and Particle Swarm Optimization (PSO) algorithms. When comparing measured and calculated current waveforms to minimize the sum of the errors, infinite combinations of parameter values produce the same input impedance and torque of the T-model. In contrast, for inverse Γ-model, only one combination of parameter values provides the equivalent impedance and a single global minimum of the objective function is obtained.

It confirms that the T-model parameters are not uniquely identifiable (if the ratio l_{ls}/l_{lr} is unknown). The analysis also confirms that the parameters of the of inverse Γ- model are uniquely identifiable and can then identified from measured steady-state machine data.

CHAPTER 6

Induction Machine Parameter Identification Using Integrated Steady-State Model

A new technique for induction machine parameter identification from external measurements of terminal waveforms is proposed in this chapter. The proposed method uses a combination of the steady-state induction machine conventional equivalent circuit (T-model) and the inverse Γ-model in conjunction with particle swarm optimization and Levenberg-Marquardt as optimization algorithms. This identification technique overcomes the non-identifiability problem associated with the conventional T-model, eliminating the possibility of obtaining incorrect parameter sets that still satisfy the model solution. The transfer function approach is employed to confirm the structural identifiability of the proposed integrated model. The performance of the proposed identification technique is experimentally demonstrated for both supply-fed and inverter-fed operations.

6.1 Introduction

Accurate Parameter identification of Induction machines (IMs) is required for many applications such as condition monitoring [3] and control [4, 5]. In the literature, a number of different IM models have been used in parameter identification studies. The most commonly utilized model is the standard steady-state per phase equivalent circuit (T-model). However, the parameters of this model have been shown not to be uniquely identified from external measurements at the stator terminals (detailed in chapter 5) [10, 161].

The non-identifiability of the T-model is mainly due to the model redundancy where the three dependent inductances (l_{ls}, l_{lr} and L_m) can be described by only two independent inductances. The ratio of l_{ls}/l_{lr} may be available in the datasheet of the IM or can be determined based on motor classification. However, this information is not always available and if available may not always be useful (e.g. for a faulty machine). It has also been shown that, unlike the T-model, the inverse Γ-model is identifiable, i.e. only one unique set of parameter values will be obtained in the identification process [10, 18]. This model includes only four electrical parameters (R_s, R_r', l_{ls}', L_m'). The relationship between the parameters of the T- and inverse Γ- models is given by the following equations [12]:

$$\alpha = L_m / L_r, l_{ls}' = L_s - \alpha L_m, L_m' = \alpha L_m, R_r' = \alpha^2 R_r \tag{6.1}$$

where L_s and L_r are the self-inductances of the stator and rotor given by $L_s = L_m + l_{ls}$ and $L_r = L_m + l_{lr}$, respectively.

The main drawback of using the inverse Γ-model for parameter estimation purposes, however, is that it is not possible to obtain the values of the T-model parameters usually needed in high performance control applications directly from the identified inverse Γ-model parameters.

In this chapter, a new approach based on the use of a combination of the T- and inverse Γ- models is proposed to uniquely estimate the parameters of the standard IM T-equivalent circuit from readily available measured stator waveforms and rotor speed. The transfer function identifiability test approach [18, 34] is used to verify that the parameters of the T-model can be uniquely identified when using the proposed integrated model. The integrated model is then used in parameter identification in conjunction with an optimization technique based on the Levenberg-Marquardt (L-M) and particle swarm optimization (PSO) algorithms.

In the optimization process, the objective function is formulated to minimize the error between the measured current and those obtained from the T- and inverse Γ- models (the two components of the integrated model). This method is suitable for online parameter estimation as no additional hardware or changes in motor connections are required. The proposed identification technique is experimentally verified using the test machine for both supply-fed and inverter-fed operation of the machine. Results confirm the effectiveness of the proposed technique in successfully estimating the machine parameters at different operating conditions.

6.2 Proposed IM Parameter Identification Technique

In the parameter identification technique proposed in this chapter, both the T- and inverse Γ-models are combined as illustrated in figure 6.1, where v_{Am} is the measured stator voltage, i_{Am} is the measured stator current, i_{AT} is the calculated current from the T-model and $i_{A\Gamma}$ is the calculated current from inverse Γ-model.

Only the five parameters of the T-model are considered as the parameter vector to be updated by the optimization algorithm. The parameters of the inverse Γ-model are then calculated using equation (6.1). The two models are solved for the same inputs and the objective function is set to minimize the difference between the measured current and the calculated currents of both models at the same time. A predefined minimum can only be achieved when the calculated currents of both models offer very good agreement with the measured current. Since there is no redundancy in the inverse Γ-model, the parameter vector that satisfies the minimum error is unique.

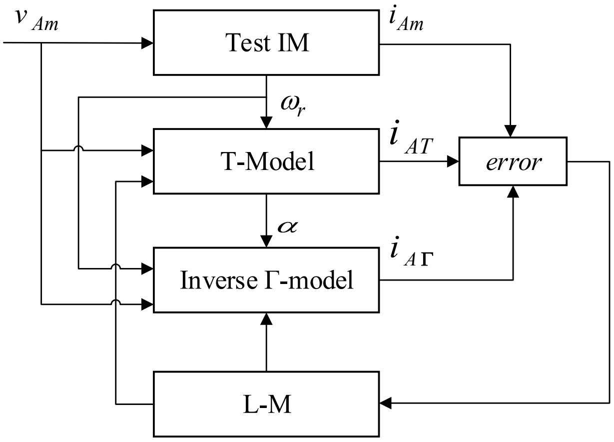

Figure 6.1 Block diagram of the proposed parameter identification technique.

For an identifiable model, good optimization algorithms should be able to detect the global minimum of the objective function and consequently identify the model parameters with a good accuracy. Nearly the same parameter values should be obtained if the identification process is repeated at different initial conditions. The next section will show that this is the case when the L-M and PSO algorithms are employed with the proposed integrated model.

6.3 Identifiability analysis of proposed integrated model

For further verification of the identifiability of the proposed model, an analytical proof is presented in this section. This is achieved by testing the structural identifiability of the model using the transfer function identifiability test approach described in chapter 2 [18, 33, 34].

In this approach, the transfer function is written in a canonical form, common factors in the numerator and denominator are cancelled and the transfer function is simplified so that the coefficients of the higher power of *S* in the denominator is always one. The identifiable parameters are the parameters that can be uniquely deduced from the coefficients of the transfer function matrix.

The transfer function approach has been applied to test the identifiability of both the T- and inverse Γ-models in chapter 5. For both models, the transfer functions as a function of the slip (s) are represented by the input admittance of the circuit (*I(S)/V(S) = 1/Zeq*) as follows [18]:

$$G_T(S) = \frac{c_1 S + d_1}{S^2 + a_1 S + b_1} \tag{6.2}$$

$$G_\Gamma(S) = \frac{c_2 S + d_2}{S^2 + a_2 S + b_2} \tag{6.3}$$

where:

$$
\begin{aligned}
a_1 &= R_s R_r \left(L_s + L_r\right) / l_{lr} L_s + l_{ls} L_m, \\
b_1 &= R_s R_r / s\left(l_{lr} L_s + l_{ls} L_m\right), \\
c_1 &= R_s L_r / L_s l_{lr} \left(L_s + l_{ls} L_m\right), \\
d_1 &= R_r / l_{lr} \left(L_s + l_{ls} L_m\right), \\
a_2 &= \left(s R_s L_m' + R_r' L_s'\right) / l_{ls}' L_m', \\
b_2 &= R_s R_r' / l_{ls}' L_m', \\
c_2 &= s / l_{ls}', \\
d_2 &= R_r' / l_{ls}' L_m',
\end{aligned}
\tag{6.4}
$$

where L_s' is the self-inductances of the stator given by $L_s' = L_m' + l_{ls}'$.

Although the T-model has five physical parameters, only four different coefficients of the transfer function $G_T(S)$ (a_1, b_1, c_1, and d_1) can be uniquely determined from the input/output measurements. On the other hand, the inverse Γ-model has only four parameters which is equal to the number of coefficients of the transfer function $G_\Gamma(S)$ (a_2, b_2, c_2, and d_2). Therefore, the model parameters can be uniquely determined from using equations (6.4), taking into account that the coefficients of the transfer function can be determined from the input/output measurements.

Similarly, the identifiability of the proposed integrated model can be tested using the transfer function approach. The model can be represented by a parallel connection of the T- and inverse Γ-models (figure 6.2) since the two models are solved simultaneously for the same input voltage.

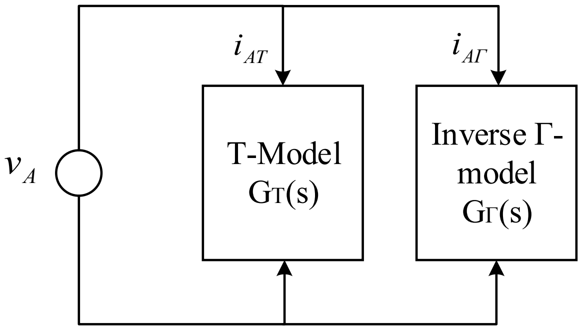

Figure 6.2 Schematic representation of the proposed integrated model.

In this case, the output of the transfer function ($G_I(S)$) can be considered as the total current and the transfer function is given by:

$$G_I(S) = G_T(S) + G_\Gamma(S) \tag{6.5}$$

Inserting equations (6.2), (6.3), and (6.4) into equation (6.5), the transfer function obtained:

$$G_I(s) = \frac{k_5S^3 + k_6S^2 + k_7S + k_8}{S^4 + k_1S^3 + k_2S^2 + k_3S + k_4} \tag{6.6}$$

where:

$$\begin{aligned}
k_1 &= a_1 + a_2, \\
k_2 &= b_1 + b_2 + a_1a_2, \\
k_3 &= a_1b_2 + b_1a_2, \\
k_4 &= b_1b_2, \\
k_5 &= c_1 + c_2, \\
k_6 &= a_2c_1 + d_1 + a_1c_2 + d_2, \\
k_7 &= b_2c_1 + a_2d_1 + c_2b_1 + d_2a_1, \\
k_8 &= d_1b_2 + d_2b_1
\end{aligned} \tag{6.7}$$

With the integrated models, there are eight coefficients of $G_I(s)$ that can be uniquely determined from the input/output measurements. Only the five parameters of the T-model need to be calculated from these eight coefficients using equation (6.7). Therefore, when using the proposed integrated model, the parameters of the T-model can be uniquely identified from external measurements, unlike the case of using the T-model by its own.

6.4 Experimental Verification

To validate the proposed scheme, parameter identification is investigated at two different speeds when the IM is driven by the variable frequency inverter described in chapter 4. The five parameters of the T-model (R_s, R_r, x_{ls}, x_{lr}, and x_m) are considered as the parameter vector **P** to be updated by the optimization algorithm. The parameters of the inverse Γ-model are then calculated using equation (6.1). The two models are solved for the same inputs and the objective function is set to minimize the difference between the measured current and the calculated currents of both models at the same time.

For verification, the proposed method is tested using both the PSO and L-M algorithms in conjunction with the measurements obtained in chapter 4.

6.4.1 Induction machine parameter identification using L-M

The total chi-squared error function (χ^2) of both models is considered as the objective function in this case. The stator current is adjusted at the full load value using the ac drive of the synchronous machine load. This occurs at a speed of 1417 r/m (i.e. a slip of 0.055) and 694 r/m (i.e. a slip of 0.075) for the 50 Hz and 25 Hz operation, respectively.

The parameter identification process using L-M is repeated many times at different initial conditions achieving very similar results every time, as demonstrated in table (6.1) which shows three such estimates for 50 Hz inverter-fed operation of the IM.

The full convergence history for these three estimates is shown in figure 6.3. Figure 6.4 shows the convergence of the error χ^2 for the first estimate. The waveforms of the measured current i_{Am} and the calculated currents i_{AT} and $i_{A\Gamma}$, corresponding to the 1st estimate parameter set in table 6.1, are shown in figure 6.5.

As shown, a very good agreement is obtained between the measured and calculated currents waveforms. Similar results are obtained for the two other estimates.

Pars.	1st estimate	2nd estimate	3rd estimate
R_s	3.8269 Ω	3.8842 Ω	3.9805 Ω
R_r	3.7594 Ω	3.8781 Ω	4.0183 Ω
l_{ls}	0.0358 H	0.0370 H	0.0317 H
l_{lr}	0.0597 H	0.0594 H	0.0573 H
L_m	0.4299 H	0.4307 H	0.4043 H
$\lvert Z_{eq}\rvert$	67.06 Ω	68.70 Ω	68.28 Ω
$\angle Z_{eq}$	44.57 °	44.80 °	44.69 °

Table 6.1 Parameter Estimation of T-model using the proposed integrated model, L-M, Inverter-fed (s = 0.055 and 50 Hz).

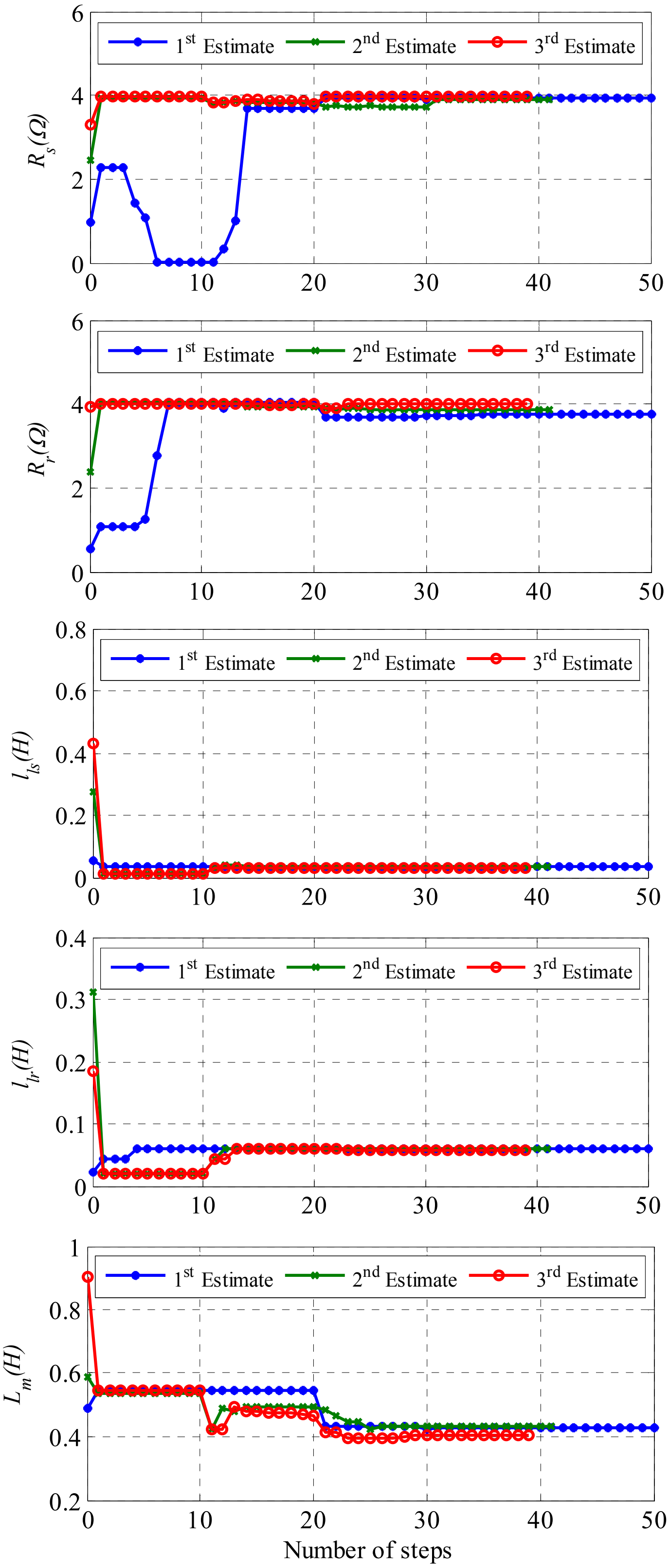

Figure 6.3 Convergence of the estimated parameters for different estimates using the proposed integrated model, L-M, inverter-fed, (s=0.055 and 50 Hz).

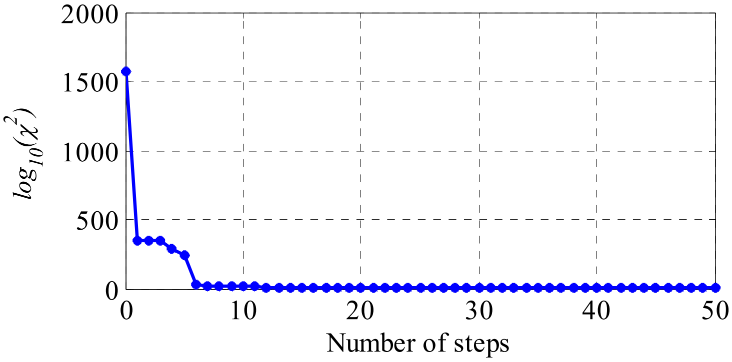

Figure 6.4 The error function convergence for the 1st estimate using the proposed integrated model), L-M, inverter-fed, (*s*=0.055 and 50 Hz).

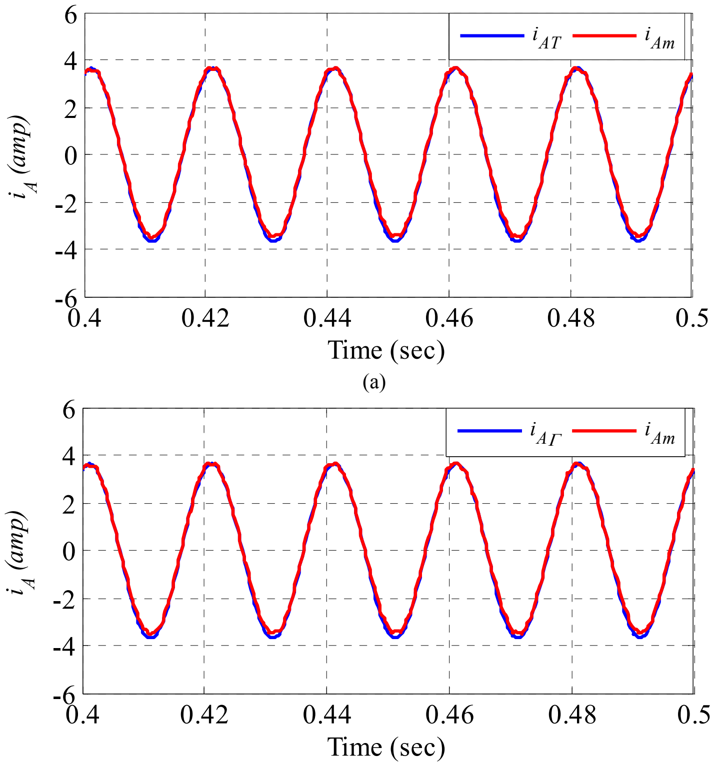

(a)

(b)

Figure 6.5 Stator currents waveforms coresponding to the optimal solution of the 1st estimate (proposed integrated model), L-M, inverter-fed, (s=0.055 and 50 Hz) (a) Measured and T-model calculated currents, i_{Am} and i_{AT} (b) Measured and inverse Γ-model calculated currents, i_{Am} and $i_{A\Gamma}$.

Similar parameter identification results were also obtained for 25 Hz inverter-fed operation at a slip of 0.075 as illustrated in table (6.2). Figure 6.6 shows that the different model parameters converge to the same final values regardless of the initial conditions. The error χ^2 of the first estimate converges to a minimum value, as shown in Figure 6.7.

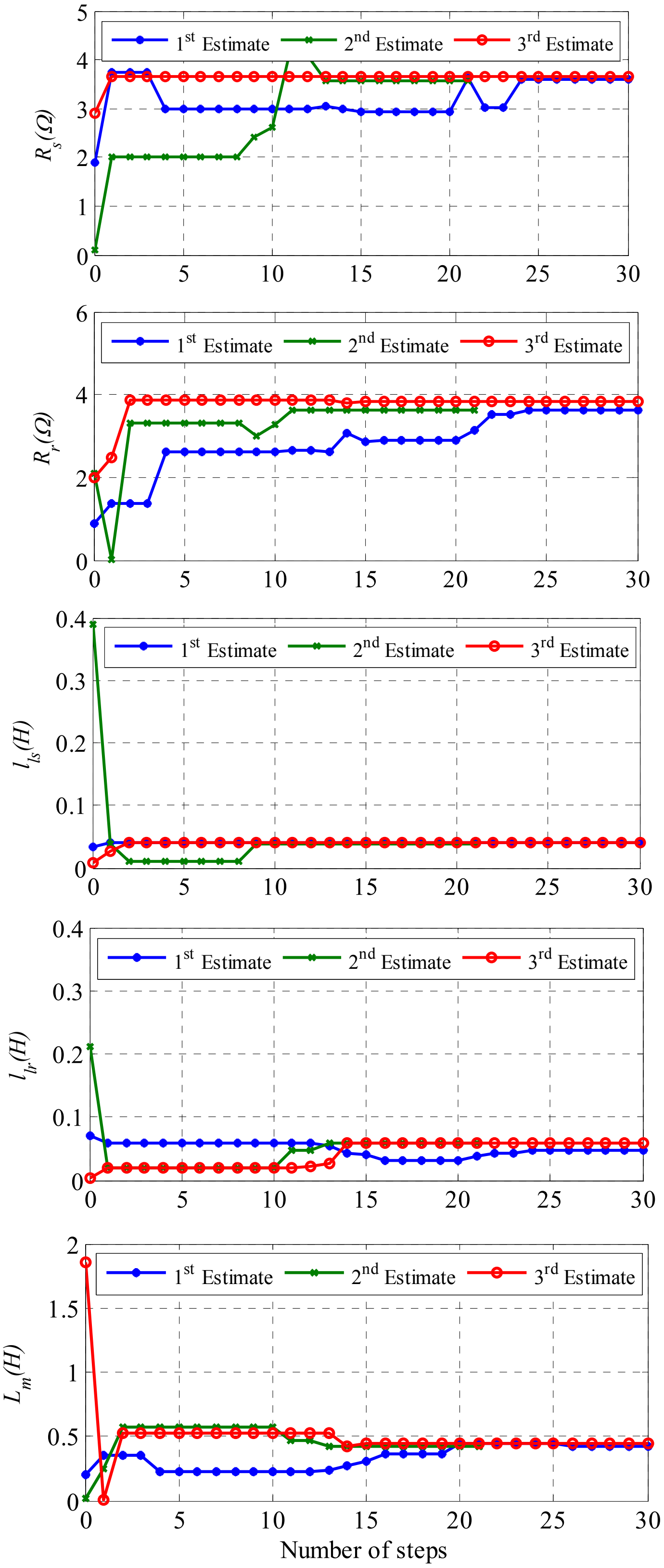

Figure 6.6 Convergence of the estimated parameters for different estimates using the proposed integrated model, L-M, inverter-fed, (s=0.075 and 25 Hz).

Similar to previous cases, a very good agreement between the measured and calculated currents waveforms is also obtained at the 1st estimate parameter set in table 6.2, as shown in figure 6.8. Similar results are also obtained for the other two estimates.

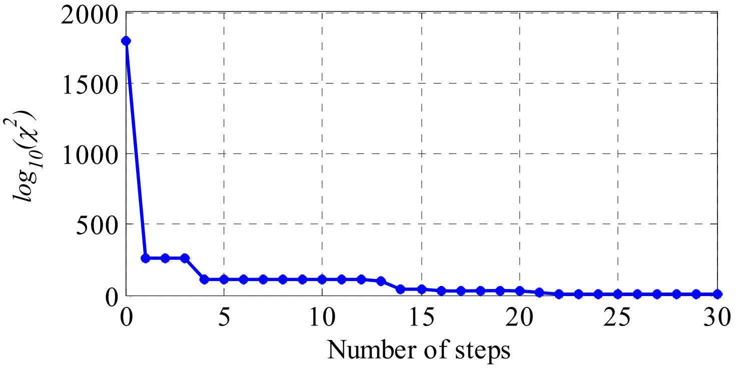

Figure 6.7 The error function convergence for the 1st estimate using the proposed integrated model, L-M, inverter-fed, (*s*=0.075 and 25 Hz).

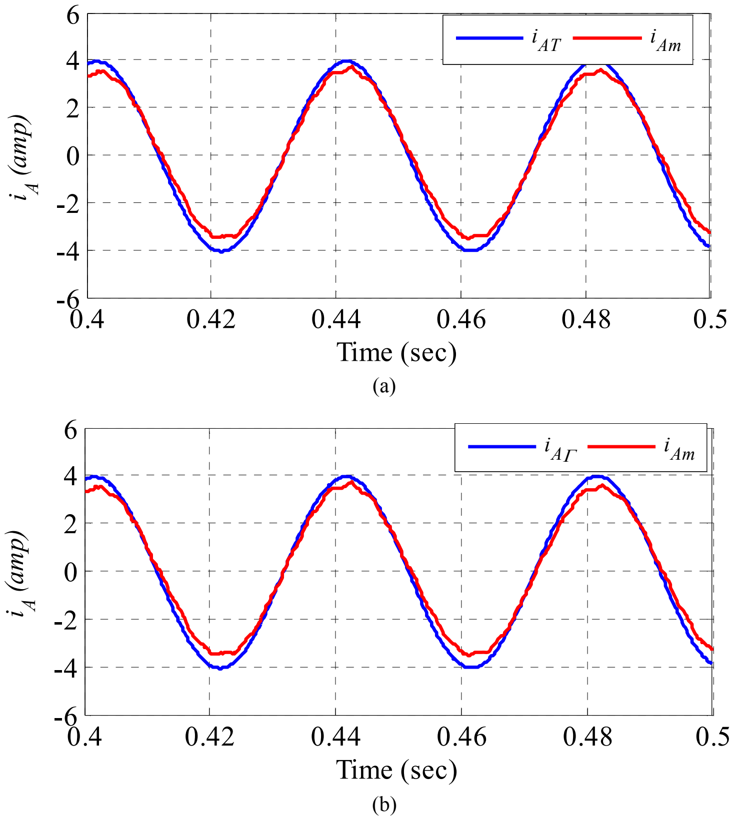

Figure 6.8 Stator currents waveforms corresponding to the optimal solution of the 1st estimate using the proposed integrated model, L-M, inverter-fed, (s=0.075 and 25 Hz) (a) Measured and T-model calculated currents, i_{Am} and i_{AT} (b) Measured and inverse Γ-model calculated currents, i_{Am} and $i_{A\Gamma}$.

Pars.	1st estimate	2nd estimate	3rd estimate
R_s	3.5872 Ω	3.5572	3.6664
R_r	3.6360 Ω	3.6408	3.8405
l_{ls}	0.0395 H	0.0390	0.0394
l_{lr}	0.0470 H	0.0578	0.0593
L_m	0.4231 H	0.4215	0.4395
$\lvert Z_{eq}\rvert$	43.90 Ω	43.46 Ω	45.47 Ω
$\angle Z_{eq}$	44.85 °	46.00 °	45.99 °

Table 6.2 Parameter estimation of T-model using the proposed Technique, L-M, Inverter-fed (s = 0.075 and 25 Hz).

6.4.2 Induction machine parameter identification using PSO

The five parameters of the T- model are considered as the parameter vector to be updated by the PSO algorithm. The two models are solved for the same inputs and the objective function is set to minimize the difference between the measured current and the calculated currents of both models at the same time (figure 6.1). The total integral absolute error (IAE_T) of both models (6.8) is considered as the objective function in this case.

$$IAE_T = \sum\left(\left|i_{Am} - i_{AT}\right| + \left|i_{Am} - i_{A\Gamma}\right|\right) \Delta T \tag{6.8}$$

where i_{Am} is the measured stator current, i_{AT} is the calculated current from the T-model and $i_{A\Gamma}$ is the calculated current from inverse Γ-model.

For supply-fed, the current is adjusted by the ac drive of the synchronous machine loading the IM. This occurs at a speed of 1418 r/m (i.e. a slip of 0.055) as described in chapter 4. The parameter identification process using PSO is repeated many times at different initial conditions achieving very similar results every time, as demonstrated in table 6.3 which shows three such estimates.

The stopping criterion of the optimization algorithm was no significant change in the IAE_T for 10 consecutive iterations. The full convergence history for these three estimates is shown in figure 6.9. Figure 6.10 shows the convergence of the IAE_T for the first estimate.

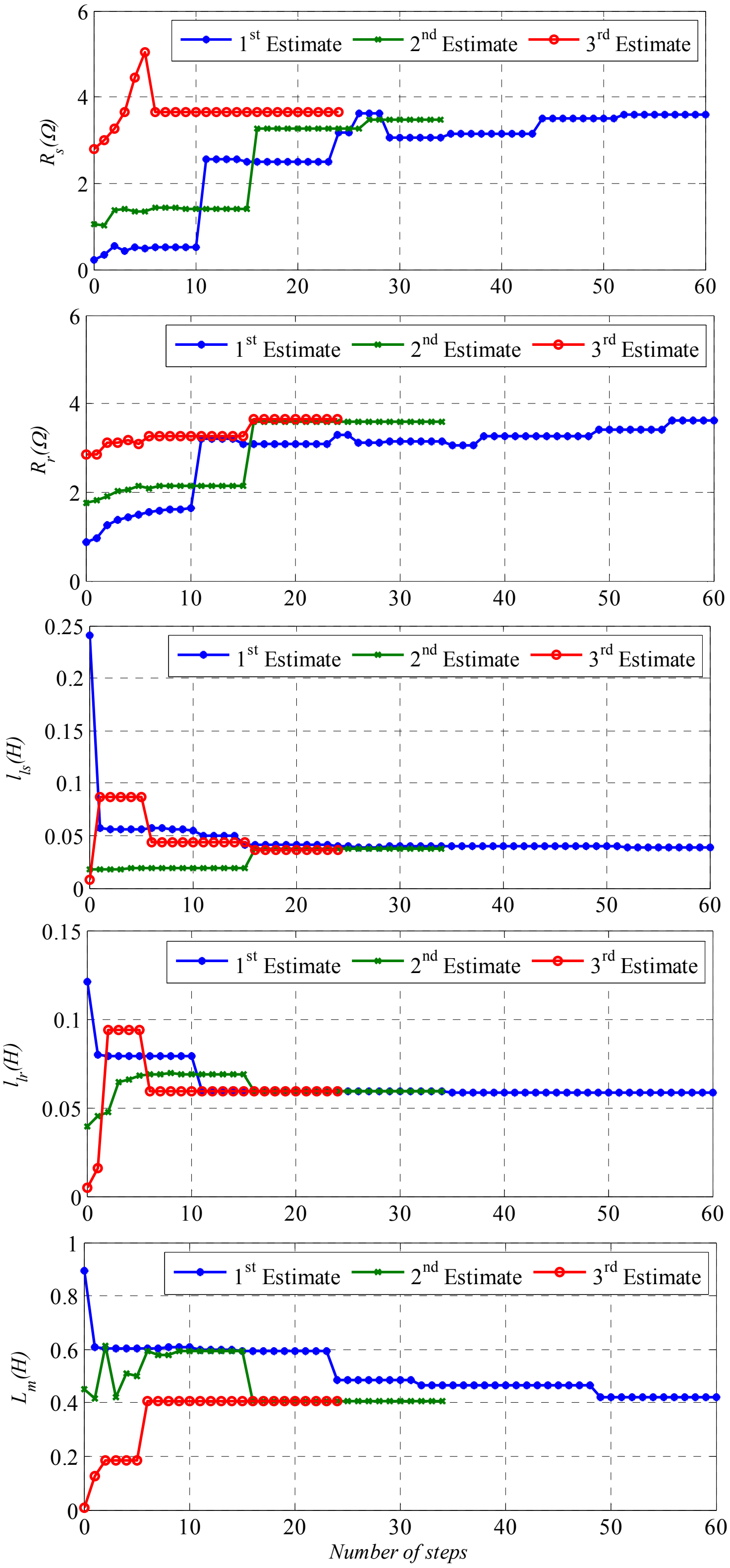

Figure 6.9 Convergence of the estimated parameters for different estimates using the proposed integrated model, PSO, supply-fed (s=0.055).

The waveforms of the measured current i_{Am} and the calculated currents i_{AT} and $i_{A\Gamma}$, corresponding to the 1st estimate parameter set in table 6.3, are shown in figure 6.11. As shown, a very good agreement is obtained between the measured and calculated currents waveforms. Similar results are obtained for the two other estimates.

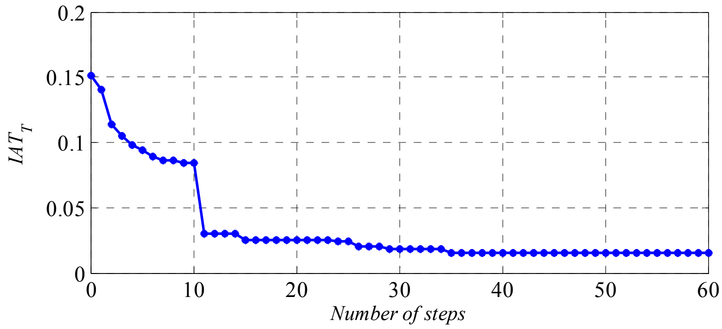

Figure 6.10 The error function convergence for the 1st estimate the proposed integrated model, PSO, supply-fed (s=0.055)

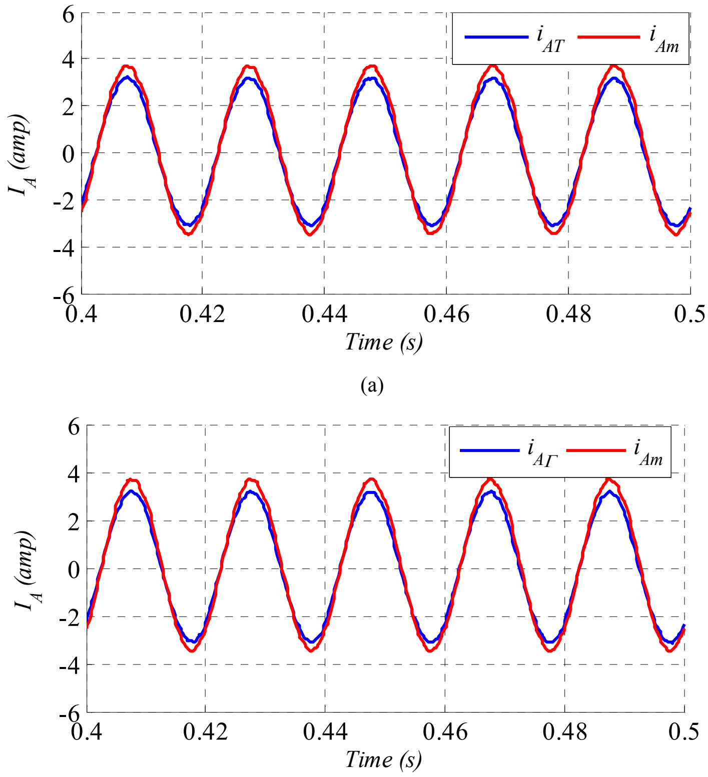

(a)

(b)

Figure 6.11 Stator currents waveforms corresponding to the optimal solution of the 1st estimate using the proposed integrated model, PSO, supply-fed (s=0.055 and 50 Hz) (a) Measured and T-model calculated currents, i_{Am} and i_{AT} (b) Measured and inverse Γ-model calculated currents, i_{Am} and i_{AT}.

Pars.	1st estimate	2nd estimate	3rd estimate
R_s	3.4588 Ω	3.5977 Ω	3.6398 Ω
R_r	3.5781 Ω	3.6069 Ω	3.6646 Ω
l_{ls}	0.0379 H	0.0393 H	0.0368 H
l_{lr}	0.0594 H	0.0590 H	0.0595 H
L_m	0.4070 H	0.4209 H	0.4067 H
$\lvert Z_{eq}\rvert$	64.90 Ω	66.09 Ω	65.77 Ω
$\angle Z_{eq}$	46.66 °	45.64 °	45.81 °

Table 6.3 Parameter estimation of T-model using the proposed technique, PSO, supply-fed (s = 0.055).

To further validate the proposed scheme, parameter identification is also investigated when the machine is driven by the variable frequency inverter described in chapter 4. Simple V/f control was implemented and the proposed technique was investigated at two different frequencies, 50 Hz and 25 Hz.

Similar to the supply-fed case, stator current is adjusted at the full load value using the ac drive of the synchronous machine load. This occurs at a speed of 1417 r/m (i.e. a slip of 0.055) and 694 r/m (i.e. a slip of 0.075) for the 50 Hz and 25 Hz operation, respectively.

The identification process gives very similar results regardless of initial conditions. Three different parameter estimates for 50 Hz inverter-fed operation of the IM are demonstrated in table 6.4. The full convergence history for the three estimates is shown in figure 6.12. The convergence of the absolute integral error IAE_T is shown in figure 6.13. For the parameter set of the 1st estimate in table 6.4, the calculated currents show very good agreement with the measured current as shown in figure 6.14.

Pars.	1st estimate	2nd estimate	3rd estimate
R_s	3.5804 Ω	3.7943 Ω	3.8689 Ω
R_r	3.7767 Ω	3.6251 Ω	3.8816 Ω
l_{ls}	0.0396 H	0.0395 H	0.040 H
l_{lr}	0.0595 H	0.042 H	0.0434 H
L_m	0.4353 H	0.3845 H	0.3900 H
$\lvert Z_{eq}\rvert$	68.5 Ω	68.53 Ω	68.42 Ω
$\angle Z_{eq}$	44.51 °	44.55 °	44.53 °

Table 6.4 Parameter estimation of T-model using the proposed technique, PSO, inverter-fed (s= 0.055 and 50 Hz)

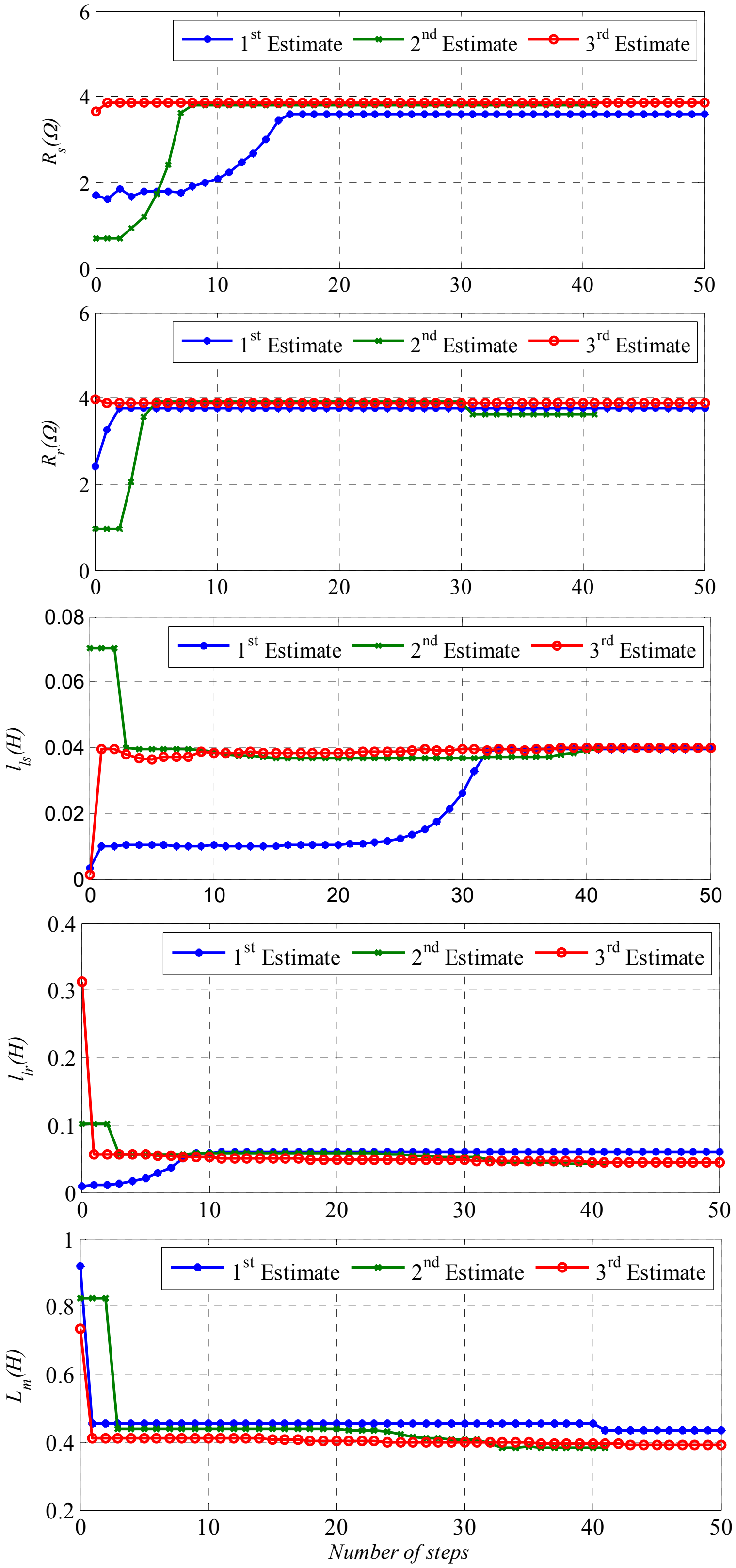

Figure 6.12 Convergence of the estimated parameters for different estimates using the proposed integrated model, PSO, inverter-fed, (s=0.055 and 50 Hz).

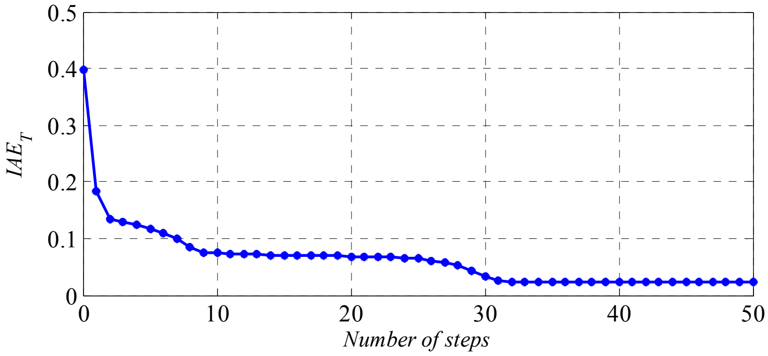

Figure 6.13 The error function convergence for the 1st estimate the proposed integrated model, PSO, inverter-fed, (s=0.055 and 50 Hz).

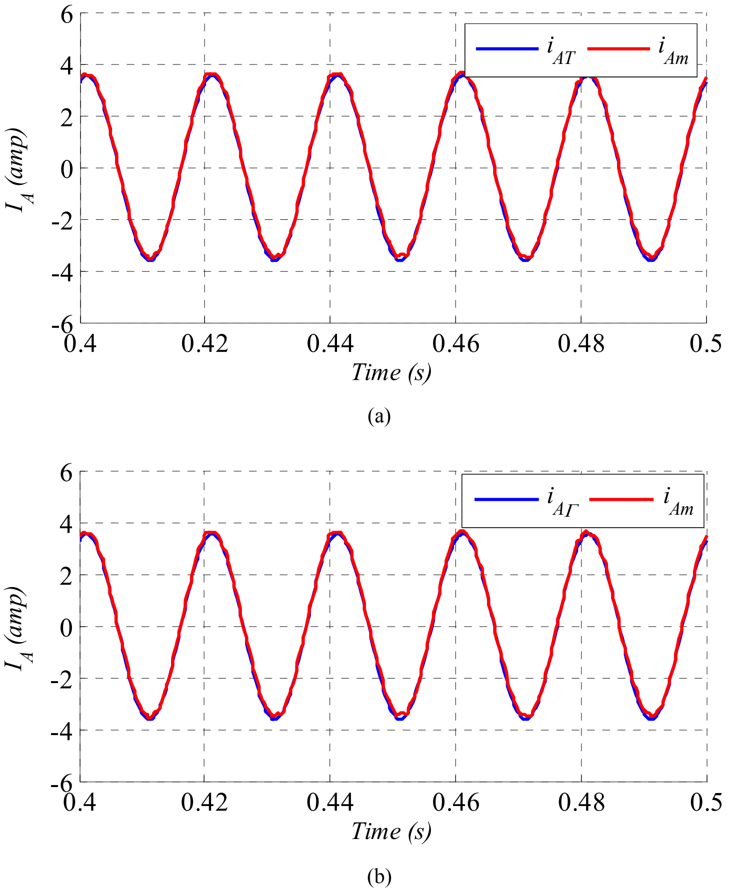

(a)

(b)

Figure 6.14 Stator currents waveforms corresponding to the optimal solution of the 1st estimate the proposed integrated model, PSO, inverter-fed (s=0.055 and 50 Hz) (a) Measured and T-model calculated currents, i_{Am} and i_{AT} (b) Measured and inverse Γ-model calculated currents, i_{Am} and i_{AT}.

Similar parameter identification results were also obtained for 25 Hz inverter-fed operation at a slip of 0.075 as illustrated in table 6.5. Figure 6.15 shows that the different model parameters converge to the same final values regardless of the initial conditions. The IAE_T of the first estimate converges to a minimum value, as shown in figure 6.16. Similar to previous cases, a very good agreement between the measured and calculated currents waveforms is also obtained at the 1st estimate parameter set in Table 6.5, as shown in figure 6.17. Similar results are also obtained for the other two estimates.

Pars.	1st estimate	2nd estimate	3rd estimate
R_s	3.7188 Ω	3.7553 Ω	3.8858 Ω
R_r	3.6495 Ω	3.5470 Ω	3.6429 Ω
l_{ls}	0.0394 H	0.0399 H	0.0399 H
l_{lr}	0.0452 H	0.0517 H	0.0484 H
L_m	0.4547 H	0.4632 H	0.4567 H
$\lvert Z_{eq} \rvert$	44.92 Ω	44.24 Ω	45.00Ω
$\angle Z_{eq}$	43.05°	43.12°	43.22°

Table 6.5 Parameter estimation of T-model using the proposed technique, PSO, inverter-fed; full-load (s = 0.075), 25 Hz.

The results clearly show that successful parameter estimation is achieved when using the integrated steady-state models of the machine with the both L-M and PSO algorithms. This is achieved regardless of the initial conditions and the operating conditions of the machine.

The estimated parameters in tables 6.1 to 6.5 are similar to those obtained from the standard IEEE tests of the machine in chapter 4.

Because of the approximation in the stopping criteria, measurement error and model assumptions, there are always differences between estimated parameters and those obtained from the standard tests. However, the difference is within acceptable limits and the parameter estimation is relatively accurate. For example, the maximum difference in one parameter estimation and the standard test value is less than 7% (for L_m in the 3rd estimate in the table 6.5). This compares favorably with results obtained by other researchers working in the area of parameter identification (for example, a maximum percentage difference of 28.75% was obtained for X_r in [6]).

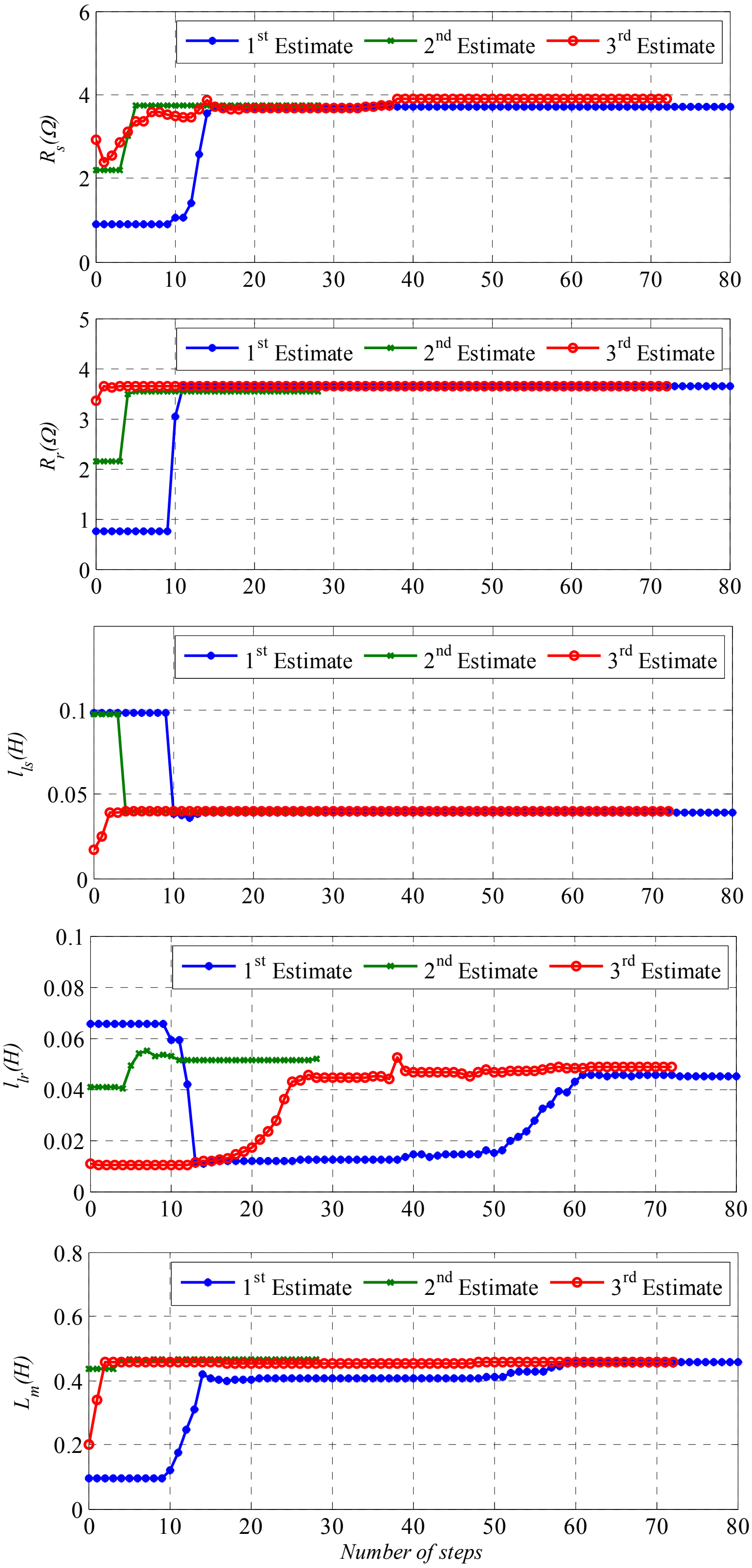

Figure 6.15 Convergence of the estimated parameters for different estimates using the proposed integrated model, PSO, inverter-fed, (s=0.075 and 25 Hz).

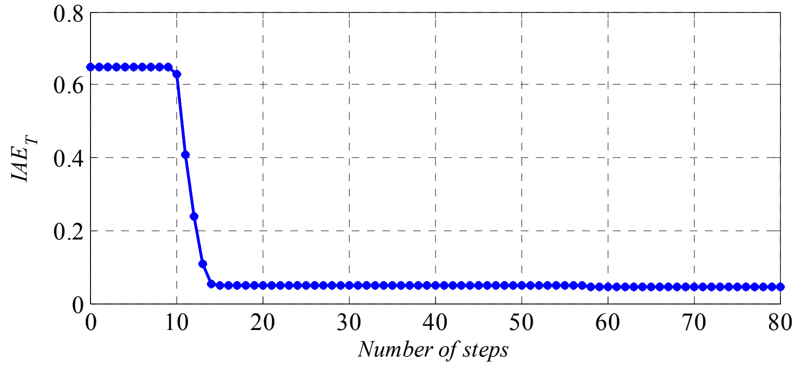

Figure 6.16 The error function convergence for the 1st estimate the proposed integrated model, PSO, inverter-fed, (s=0.075 and 25 Hz).

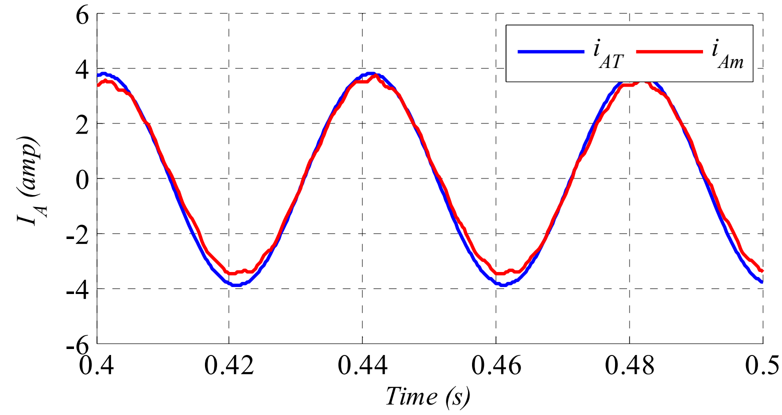

(a)

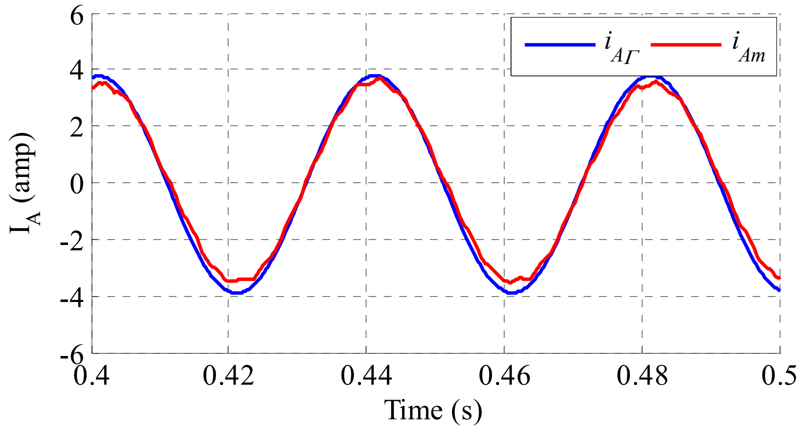

(b)

Figure 6.17 Stator currents waveforms corresponding to the optimal solution of the 1st estimate the proposed integrated model, PSO, inverter-fed, (s=0.075 and 25 Hz) (a) Measured and T-model calculated currents, i_{Am} and i_{AT} (b) Measured and inverse Γ-model calculated currents, i_{Am} and i_{AT}.

6.5 Conclusion

A new model-based parameter identification technique for the electrical parameters of the induction machine T-model equivalent circuit is proposed in this chapter. Steady-state external measurements of motor speed and phase currents are needed for the identification process. The proposed technique uses a combined T- and inverse Γ-steady-state induction machine models. The use of the two models in combination overcomes the problem of the non-identifiability of the T-model that can result in wrong parameter estimation. Using the proposed technique, the redundancy of the T-model is eliminated and only one parameter set that represents the real parameters of the machine is obtained.

Compared with other parameter identification methods (like signal-based), fewer measurements are required to identify model parameters as it only uses the measurements that are normally required for a motor drive. Experimental results based on a 1.1 kW IM have shown that the proposed scheme can successfully estimate induction machine parameters.

CHAPTER 7

Detection of Stator Winding Faults in Induction Machines Based on Parameter Estimation

A novel condition monitoring technique for detecting stator winding faults in induction machines is proposed in this chapter. The scheme uses time domain measurements in conjunction with particle swarm optimization algorithm to estimate the parameters of the simple Inverse Γ-model of the induction machine and detect stator winding faults accordingly. Only stator voltages and currents and rotor speed, which are usually measured in an induction machines, are required for the fault detection process. The proposed technique is robust to supply voltage unbalance and motor loading conditions. The validity and effectiveness of the proposed technique is verified by extensive experimental tests under open circuit, interturn short circuit and combined stator winding faults. The results presented in this chapter show the accuracy of the proposed technique in detection and providing information about type and location the faults.

7.1 Introduction

Induction machines (IMs) are widely used in industrial applications due to their robustness and reliability [59, 164, 165]. They consume around 85% of the generated electrical power produced in the world [65]. However, these machines may face various stresses during operation conditions which might lead to some unavoidable modes of failures/faults.

The key item in the model-based fault diagnosis process is to choose the proper IM model that characterizes the fault. In the literature, intensive work has been done towards deriving different mathematical models of IMs for fault diagnosis. Simple models like classical three phase ABCabc, T-equivalent circuit and space vector models may not be accurate enough for monitoring purposes. For example, it is impractical to use an unbalanced two axis Park's model for fault diagnostic as it is very difficult to distinguish between stator and rotor fault. In addition, it is unsuitable in the case of fault in several phases as the model will translate the defect by anomalous parameter values that satisfy the solution [139]. On other hand, complicated models like finite elements method [166], winding function approach [145], dynamic mesh reluctance approach [151] are complex and take too much computation time. Most of these models require a priori knowledge of the machine design parameters that are usually not available. In fact, these models are useful for scientific purposes to get a deep understanding of the machine behaviour under the fault and, hence they are not suitable for industrial applications [91].

Due to their simplicity and shorter computation time, steady-state IM models have been widely used in the condition monitoring area. Chapter 5 recommended not to use the T- equivalent circuit with external measurements for condition monitoring and parameter identification due to the model non-identifiability [10]. Instead, the inverse Γ-model can be used if it is applicable and suitable for task in hand.

This chapter proposes a new model-based IM condition monitoring technique by means of characteristic parameter estimation using external measurements. The proposed scheme has the advantage of being applicable to IMs condition monitoring under various stator winding failure modes. Only steady-state measurements of three phase stator voltages and currents in addition to rotor speed are required. Unlike the conventional model-based condition monitoring techniques, the proposed technique uses a simple model that can be used to detect different types of stator winding faults. The proposed technique is experimentally verified using the test machine subjected to different stator windings fault conditions as described in chapter 4. Particle Swarm Optimization (PSO) is used in this chapter as an optimization algorithm to minimize the error between measured and calculated currents to obtain the machine characteristic parameters. Results show the effectiveness of the proposed condition monitoring technique and its ability to provide information about the nature and the location of the fault.

7.2 Proposed fault diagnosis technique

The inductances of the induction motors are based on the geometry of the machines and the number of the turns. In both faulty and healthy motor, the mutual inductance of two windings is proportional to the product of the counts of turns in the two windings. When a short circuit between any (stator/rotor) turns arises in a given phase, the corresponding number of winding will decrease [167]. Therefore, both resistances and inductances due to the short-circuit fault are affected and changes in their values have to be taken into account. The open circuit fault causes an asymmetry of the resistance and inductance in the stator phases. This impact can be simply modelled by unbalancing the stator resistances while the inductance changes are negligible due to its insignificant influence compared to the resistance changes [2, 168].

In this chapter, the proposed condition monitoring technique is based on making an approximate relationship between the portion of short-circuit and the change of the stator winding inductances by considering the leakage and magnetizing inductances to be proportional to turns account and the fault has the same effect on both of them. Two characteristic parameters are introduced to define the stator faults. One of these parameters (μ) is linked to both the leakage and the magnetizing inductances and the other (μ_R) is linked to the stator resistances.

Depending on the fault level, the value of μ varies from 1 (where the phase is healthy) and down to zero (where the phase is totally short-circuited) and it is calculated based on:

$$\mu = 1 - \frac{\text{Number of interturns short circuit windings}}{\text{Total number of interturns in healthy windings}} \tag{7.1}$$

The values of μ_R varies from 1 (where the phase is healthy) up to infinity (where the phase is totally open) and down to zero when the phase is totally short-circuited, and it is calculated based on:

$$R_e = \mu_R R_s \tag{7.2}$$

where R_e is the estimated resistance for each phase and R_s is the stator resistance for healthy machine.

Let μ_A, μ_B, and μ_C be the percentage of the remaining un-shorted stator windings in stator phases A, B, and C respectively. The modified stator leakage and magnetizing inductances in the three phase reference frame are given by $\mu_A l_{lA}{}'$, $\mu_B l_{lB}{}'$, $\mu_C l_{lC}{}'$, $\mu_A L_{mA}{}'$, $\mu_B L_{mB}{}'$, $\mu_C L_{mC}{}'$. The modified stator resistances in the stator phases are given by $\mu_{RA} R_A$, $\mu_{RB} R_B$, and $\mu_{RC} R_C$. To improve the accuracy of the proposed techniques and to take the fault effects on the rotor side in account, the rotor resistances have been included in the estimated parameter vector **P**, thus **P**= [μ_A, μ_B, μ_C, μ_{RA}, μ_{RB}, μ_{RC}, R_{ra}, R_{rb}, R_{rc}]. This makes it is possible to detect the presence of any faults or combine faults by monitoring these characteristics parameters values.

The performance of the proposed fault identification technique of the stator windings faults is illustrated by the parameter identification method shown in figure 7.1. The scheme uses three inverse Γ-models and, thus eliminating the effect of the current sequences. It makes use of the instantaneous values of external measurements including stator voltages, currents and rotor slip. The measured stator currents are obtained from the test rig while the calculated currents are obtained computationally from the model constructed in Matlab/Simulink. Measured data of three phase stator voltages v_{Am}, v_{Bm}, v_{Cm} and the rotor slip s are used as an input of the machine model to produce the calculated outputs. The calculated currents are compared with the measured using the objective function:

$$IAE = \sum_{k=1}^{N} \left(\left| i_{Am} - i_{Ac} \right| + \left| i_{Bm} - i_{Bc} \right| + \left| i_{Cm} - i_{Cc} \right| \right) \Delta T \tag{7.3}$$

where N is the number of samples and ΔT is the sampling period.

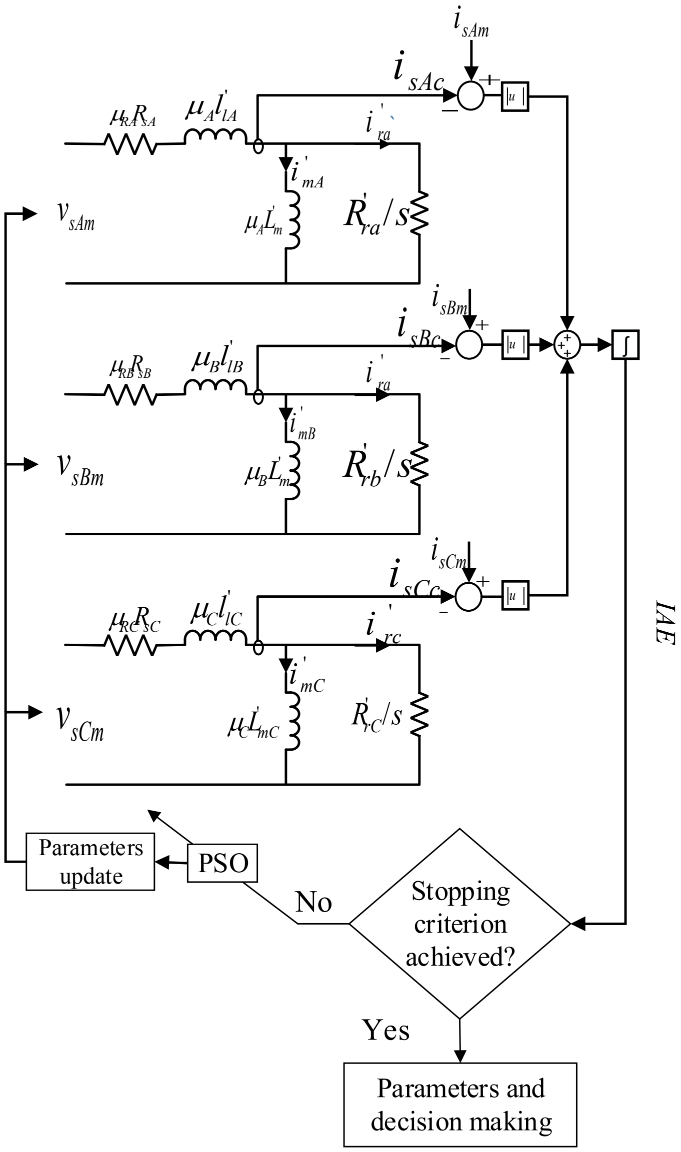

Figure 7.1 General structure of the Model-Based IM fault diagnosis technique.

Since this objective function *IAE* uses time domain quantities, any change in the amplitude of these quantities introduces a change in the *IAE* value. Under healthy condition, both measured and calculated currents are almost symmetrical and the error is close to zero. When a fault occurs, the error will be larger than a predefined threshold, thus it is used as a fault detector. The task of the PSO then is to generate a new set of parameters values and feed them to the IM model to produce the calculated currents and to calculate the error *IAE*. This process iterates until a close agreement between the measured and calculated currents is achieved and, therefore the fault will be localized.

There will always be an error between the machine model and the actual performance of the system regardless of the IM model and the parameter identification technique, because of the assumptions and approximations made in the modelling process.

7.3 Experimental Validation of the Proposed Technique

The proposed technique is experimentally validated using different faults including stator winding asymmetry (open-circuit), inter-turn short circuit and combined fault, i.e. a mixture of open circuit and inter-turn short circuit fault as described in chapter 4.

In this chapter, the particle swarm optimization is used as an optimization technique to minimize the objective function (equation 7.3). The number of the used particles *N*=12, the inertia weight *ω*=1.424, the accelerating coefficients $c_1 = c_2 = 2.2$. To avoid destructive tests, these tests were carried out when the machine is supplied directly from the mains at no-load.

7.3.1 Stator winding asymmetry fault detection

Stator winding asymmetry fault is simply implemented by connecting a 30 Ω resistor in series with phase A imitating an open-circuited fault, as described in chapter 4. This fault leads to an asymmetry in the phase impedance and, consequently produces a large error *IAE* indicating the fault occurrence. The task of the PSO is to minimize the error between the measured (shown in chapter 4) and calculated currents by continuously adjusting the IM model characteristic parameters' values, **P**, until a close agreement between the measured and calculated currents is achieved. Table 7.1 presents the obtained characteristic parameters using PSO. The convergence history of the estimated parameters and the error *IAE* are shown in figures 7.2 and 7.2, respectively. Figure 7.5 shows both the measured currents (i_{Am}, i_{Bm}, i_{Cm}) and calculated currents (i_{Ac}, i_{Bc}, i_{Cc}) obtained from the parameter sets given in table 7.1.

Pars.	Estimated	Pars.	Estimated
μ_A	1.0979	μ_{RC}	1.0237
μ_B	1.0343	R_{ra}	2.9798
μ_C	1.0850	R_{rb}	2.9410
μ_{RA}	9.8564	R_{rc}	2.9511
μ_{RB}	0.8844		

Table 7.1 Parameter Estimation of the IM Model, Open-Circuit Fault in Phase A.

The high value of the characteristic parameter μ_{RA} indicates the presence of an open winding fault in phase A. Based on the equation (7.2), it shows that the estimated stator resistance is equal to 35.58Ω which is almost equal to the simulated one (33.61Ω).

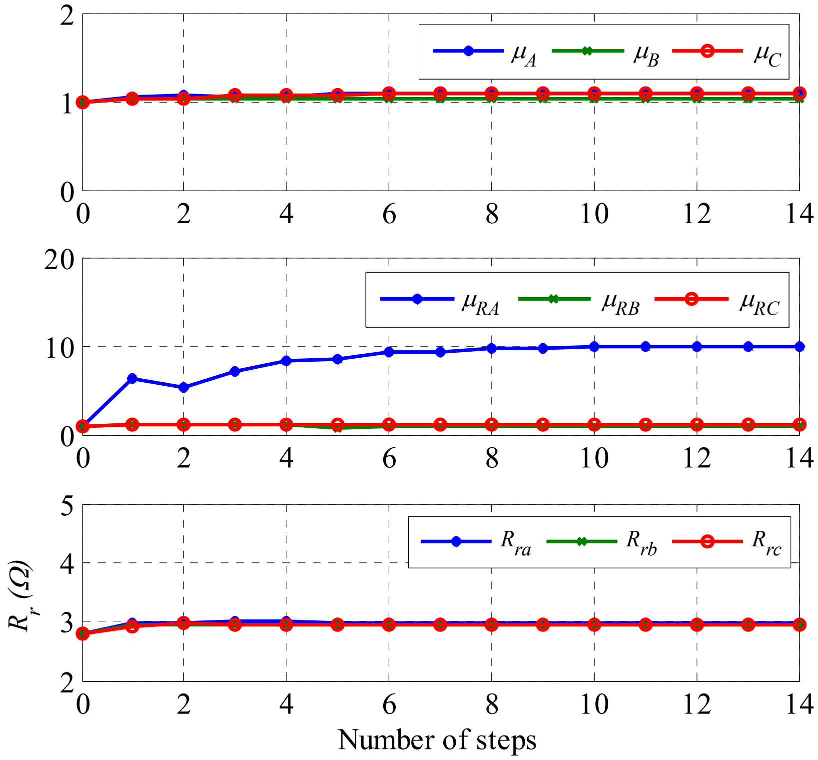

Figure 7.2 Convergence history of the estimated parameters, open-circuit fault in phase A.

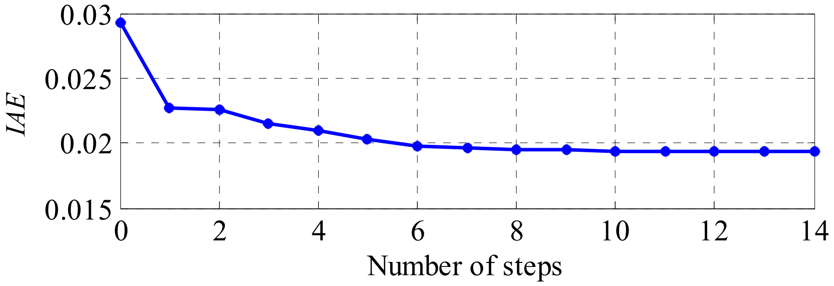

Figure 7.3 The error function convergence for the estimated parameters, open-circuit fault in phase A.

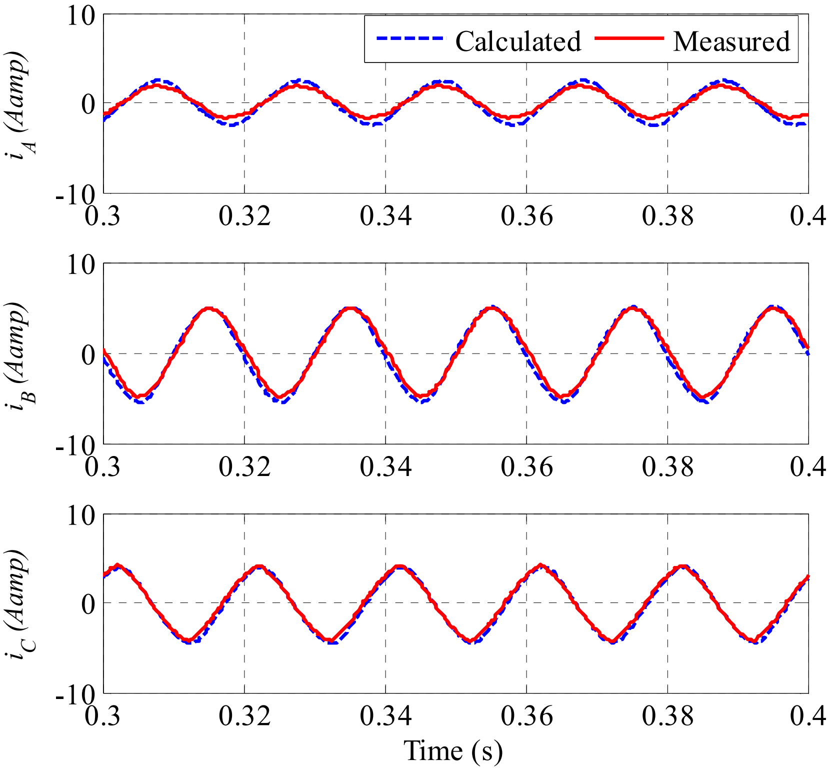

Figure 7.4 Measured and calculated three phase stator currents waveforms coresponding to the optimal obtained solution, open-circuit fault in phase A.

7.3.2 Stator winding interturn short-circuited fault detection

The experimental measurements of about 30% interturn short-circuit fault in phase A have been collected as described in chapter 4. Similar to the previous test, the PSO updated the parameters values of the IM model until a good agreement between the measured and calculated current is obtained.

Table 7.2 shows the parameter values obtained using the PSO. Figures 7.5 and 7.6 show the convergence history of the estimated parameters and the *IAE* convergence, respectively. Figure 7.7 shows a very good agreement between the measured and calculated currents.

The estimated results in table 7.2 indicate that 56.98% of stator winding in phase A are still healthy and about 43.01% are short-circuited (the ratio of the healthy to the total windings μ_A= 0.5652). The value of the parameter associated with the stator resistance μ_{RA} shows the presence of an interturn short-circuit in phase A with a severity of around 27.77%.

Pars.	Estimated	Pars.	Estimated
μ_A	0.5652	μ_{RC}	0.9698
μ_B	0.8919	R_{ra}	2.9775 Ω
μ_C	0.9521	R_{rb}	2.9398 Ω
μ_{RA}	0.7223	R_{rc}	2.9643 Ω
μ_{RB}	0.9902		

Table 7.2 Parameter Estimation of One-Phase Interturn Short-Circuit Fault, Phase A

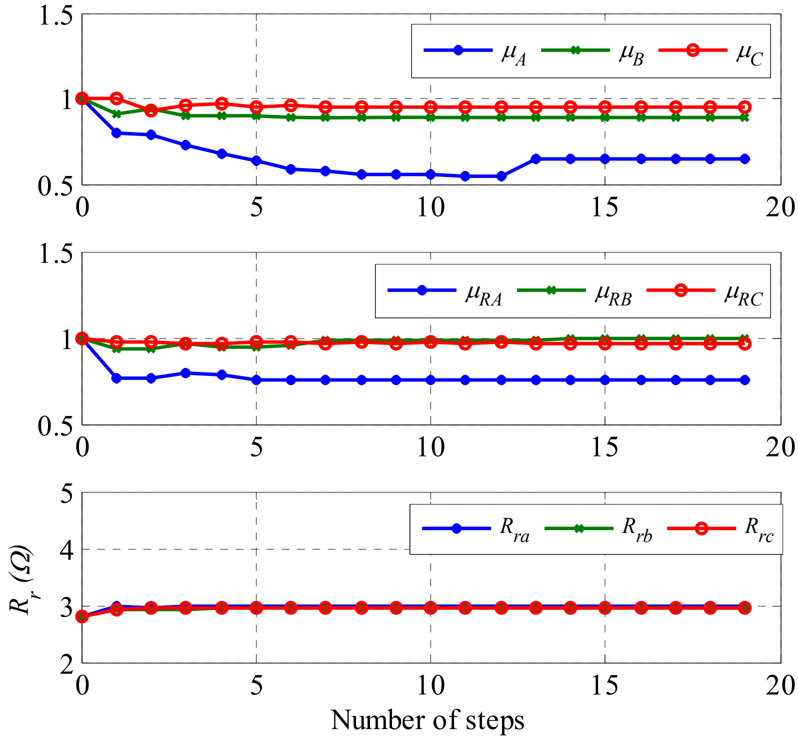

Figure 7.5 Convergence history of the estimated parameters, interturn short circuited fault in phase A.

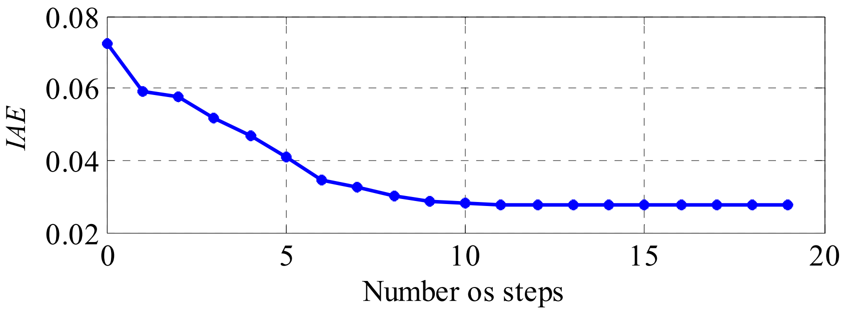

Figure 7.6 The error function convergence for the estimated parameters, interturn short circuit fault in phase A.

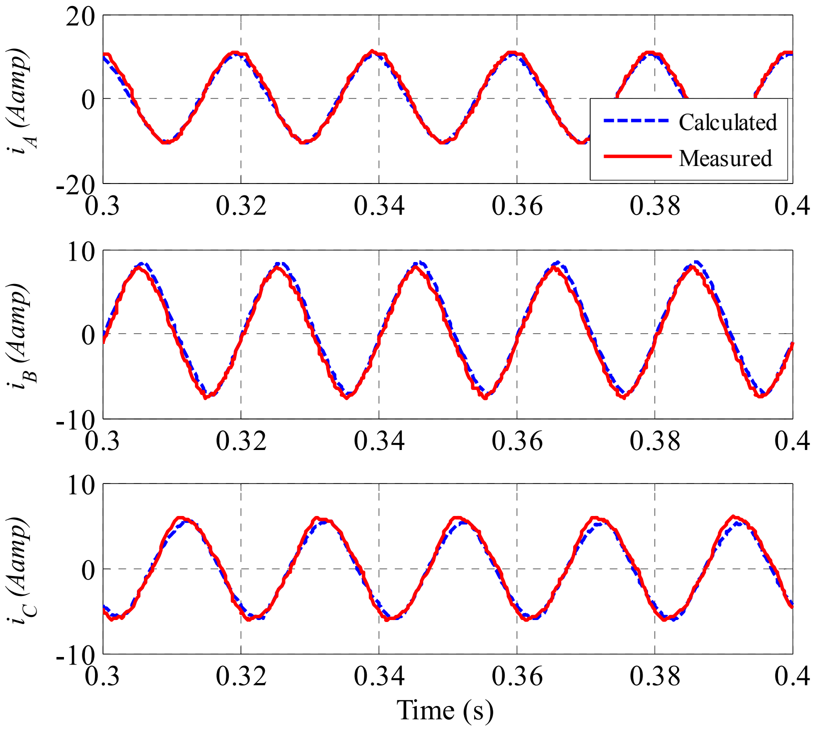

Figure 7.7 Measured and calculated three phase stator currents waveforms coresponding to the optimal obtained solution, interturn short circuit fault in phase A.

7.3.3 Stator winding combined fault detection

The experimental measurements of 30% stator short circuit fault in phase and an open-winding fault in phase B presented in chapter 4 are used in this test. Table 7.3 presents the parameter values obtained using PSO. Figure 7.8 and Figure 7.9 show the convergence history of the estimated parameters and the *IAE* convergence, respectively. A close agreement between the waveforms of the three phase measured currents and that of the calculated current obtained, figure 7.10. The estimated results indicate that an interturn short circuit fault occurs in the phase A (μ_A= 0.5648). The high value of the characteristic parameter μ_{RB} (11.5477) indicates the presence of an open winding fault in phase B. Comparing with other faults, this fault causes the motor to exhibit a high temperature and, thus increasing the resistance in other healthy phases.

Pars.	Estimated	Pars.	Estimated
μ_A	0.5648	μ_{RC}	1.0780
μ_B	1.0278	R_{ra}	3.3139
μ_C	1.0293	R_{rb}	3.5780
μ_{RA}	0.7435	R_{rc}	2.9122
μ_{RB}	11.5477		

Table 7.3 Parameter Estimation of Combined Fault.

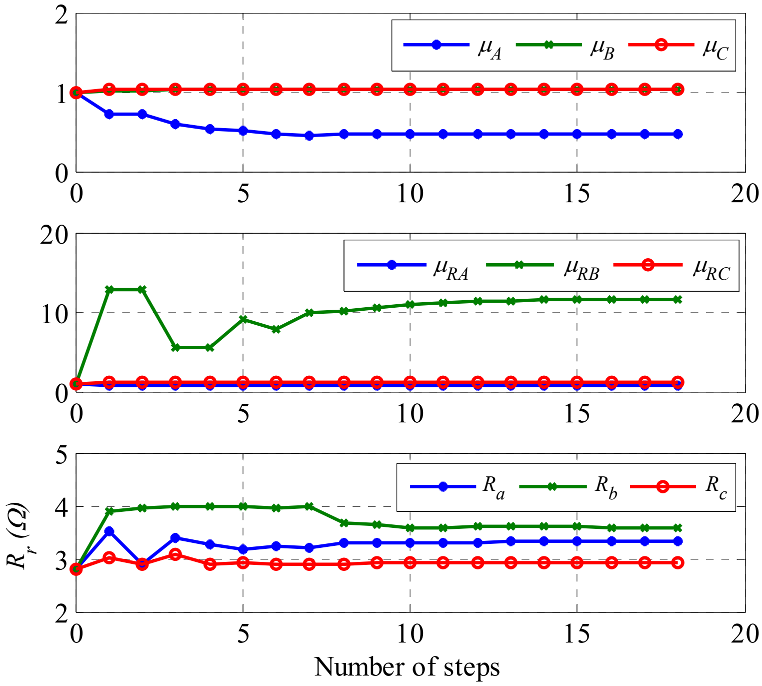

Figure 7.8 Convergence history of the estimated parameters of the combined fault under combined fault.

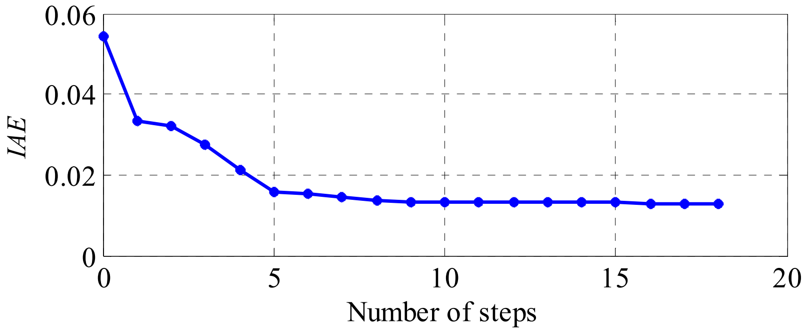

Figure 7.9 The error function convergence for the estimated parameters under combined fault.

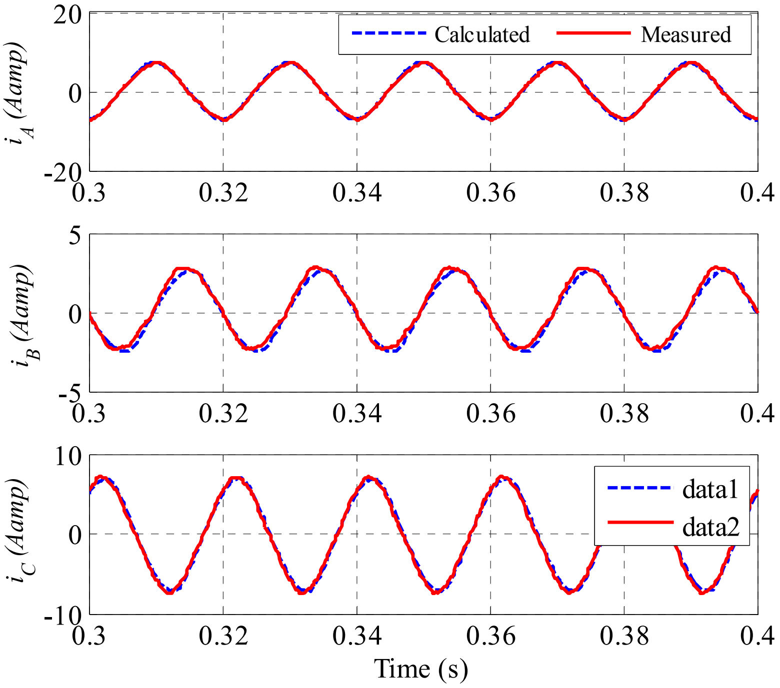

Figure 7.10 Measured and calculated three phase stator currents waveforms coresponding to the optimal obtained solution under combined fault.

7.4 Conclusion

A simple fault diagnosis technique based on parameter estimation is proposed in this paper. The faults were detected by monitoring the characteristic parameters estimated using external measurements including three phase stator voltages and currents and rotor speed. The scheme has been verified using extensive experimental tests under different faults types including interturn short circuit, open circuit, and combined faults. The fault characteristic parameters are estimated using the measured machine waveforms in conjunction with the PSO algorithm. The obtained results show the effectiveness of the proposed on providing good information about the nature and the location of the fault.

CHAPTER 8

Conclusion and future work

8.1 Summary

In this thesis an overall framework has been presented to expand the current state of the art in parameter identification and fault diagnosis of induction machines (IMs). This research has been mainly divided into three major parts: identifiability of IMs' steady-state models (the possibility of obtaining incorrect parameter sets that satisfy model solution), parameter identification of the IMs (the procedure that allows a mathematical representation of the experimental data), and fault diagnosis of the IMs (detecting and localizing the developments of any fault sufficiently).

Commonly, the parameters of the T-equivalent circuit of the IMs are calculated based on measurements at the stator terminals following the standard no-load, dc and locked rotor tests as detailed in IEEE Standard 112-2004 [48]. However, it is not possible to determine both stator and rotor leakage inductances, l_{ls} and l_{lr}, from these tests without making an additional assumption. The ratio of l_{ls}/l_{lr} may be available in the datasheet of the IM or can be assumed depending motor classification. For the motor under consideration, the ratio of l_{ls}/l_{lr} is available (NEMA class B, 40/60). However, this information is not always available and if available may not always be useful (e.g. for a faulty machine). Some researchers assume that l_{ls} and l_{lr} are equal [169], which is not always the case and might lead to incorrect parameter estimation. On the other hand, for the inverse Γ-model, circuit parameters can be independently calculated based on the standard IEEE tests. No assumption is required in this case. The parameters of the inverse Γ-model can also be calculated from those of the T- model (chapter 1) if the l_{ls}/l_{lr} is known.

Usually, motor parameters are identified for the purpose of fault diagnosis of a running motor that is coupled with a load. In this case, performing the standard IEEE tests will not be possible and alternatively the external measurements of voltage, current, speed and/or torque are usually used in parameter identification. Before using a machine model in such a parameter estimation technique, however, it is important to test the identifiability of the model to make sure that its parameters are uniquely identifiable.

The identifiability of T- and inverse Γ-models of the IM are investigated using the transfer function, bond graph and ACE identifiability test techniques. The results of these three techniques are then verified by using the L-M and PSO parameter estimation algorithms that use external measurements of motor's voltage, current and speed. The parameter estimation process has been repeated three times at different initial conditions and the estimated parameters are then compared to the measured parameters (obtained from the standard IEEE tests). For an identifiable model, the difference between the estimated and measured parameters will be always with acceptable limits regardless of the initial conditions. For a non-identifiable model, a big difference between estimated and measured parameter values may be obtained depending on the initial conditions.

The transfer function of the T-model derived in chapter 5 has only four coefficients which are functions of the five unknown electrical parameters of the model. Although the values of the four coefficients can be estimated from the experimental measurements, these four coefficients are not sufficient to mathematically calculate the model parameters (five unknowns). In contrast, the transfer function of the inverse Γ-model derived in chapter 5 has four coefficients which are equal to the number of the unknown parameters. This means that the inverse Γ-model is identifiable while the T-model is non-identifiable according to the transfer function approach.

Causality conflict is observed from the T-model bond graph construction (chapter 5) that shows a redundant energy storage component to be present on the model. This conflict is eliminated by taking the dependent storage element together with an independent storage element leading to the use on the inverse Γ-model.

A novel identifiability analysis approach based on the use of the Alternating Conditional Expectation (ACE) algorithm was developed and applied to test the identifiability of T- and inverse Γ-models. The ACE algorithm confirmed the non-identifiability of the T-model and the identifiability of the inverse Γ-model parameters, in agreement with the results obtained by using transfer function and bong graph approaches. Functionally related parameters provide high correlation coefficient and cause the model to be non-identifiable. A strong correlation coefficient (0.996) between the T-model parameters is observed and, therefore, the T-model in non-identifiable. In contrast, a very low correlation coefficient (0.0023) between the inverse Γ-model parameters is obtained which means the inverse Γ–model is identifiable.

The identifiability analysis is then verified using the Levenberg-Marquardt (L-M) and Particle Swarm Optimization (PSO) as optimization tools in conjunction with measured time-domain data. Although several parameter identification methods have already been proposed including simpler methods that are already in use. However, some of these methods (such as signal based techniques [53] and [170]) require additional external hardware. There are also other model-based methods that require several tests and/or complex statistical operations to be performed (for example [57]).

The algorithms are applied to test the identifiability of both T- and inverse Γ-models using steady-state measured data including stator voltage, stator current and rotor speed. Using these techniques, only steady-state stator phase voltage and current (one phase only) and rotor speed measurements are required to identify the machine parameters. All the tests were carried out while the machine was operating under steady-state conditions with no additional hardware/sensors or changes in motor connections. For comparison, standard IEEE tests are applied and the parameters of the induction motor are determined (chapter 4).

When attempting to identify the parameters of the T-model in this way, a different set of parameter values is obtained at the end of the optimization process every time the algorithm is run with all sets producing results that match the measured data very closely. This is not the case when using the same algorithm and the same data set to identify the parameters of the inverse Γ-model when the same set of parameter values is consistently obtained.

It can be observed from the results given in chapter 5 that, completely different sets of parameters, for T-model, that provide the same impedance Z_{eq} and current can be obtained depending on the initial conditions. Despite the significant differences between the three sets of parameters, the calculated current closely matches the measured current in each case. This confirms that the T-model is non-identifiable.

The squared error (χ^2) as a function of rotor and stator leakage inductances for the T-model based on the measured data is shown in chapter 5. As shown, infinite combinations of the two inductance (l_{ls} and l_{lr}) values result in the same minimum value of squared error, i.e. there is no unique global minimum. This confirms that it is not possible to determine l_{ls} and l_{lr} uniquely using external measurements of voltage, current, and speed. Consequently, the IM T-model is not uniquely determined and there will be an infinite number of T-models of the IM that are theoretically equivalent if the external measurements are used.

In order to solve this problem, an inverse Γ-model that minimizes the parameter number is implemented. The obtained results are satisfactory for different L-M and PSO runs. There will always be an error between the machine model and the actual performance of the system regardless of the IM model and the parameter identification technique, because of the assumptions and approximations made in the modelling process. As shown in chapter 5, a very good agreement between the measured and calculated current waveforms is realized. Similar agreement between current waveforms is obtained with the other sets of estimated parameters for the different tests. The squared error (χ^2) is plotted against different values for l_{ls}' and L_m'). Only one optimal combination of these parameter values that satisfy the error (one global minimum) is realized with the inverse Γ-model (chapter 5).

This study of the identifiability of the parameters of the T- and inverse Γ-equivalent circuits of the induction motor shows that the machine T-model is non-identifiable while the inverse T-model is. Results show that, different sets of parameter values may produce the same input impedance and electromagnetic torque of the T-model while, however, only one combination of parameter values provides the equivalent impedance for inverse Γ-model.

The main drawback, however, of using the inverse Γ-model for parameter identification of the IM is that it is not possible to go back from inverse Γ-model to T-model, as this requires the ratio α to be known. For many applications such as high performance control, knowledge of the real physical parameter values of the T-model is necessary.

To overcome the inverse Γ-model shortcoming and identify the parameter of the T-model, a new technique based on an integrated steady-state model is proposed in this thesis. The model is a combination of the induction machine T- and inverse Γ-steady-state models. The use of this model overcomes the non-identifiability problem of the T-model, eliminating the possibility of obtaining wrong parameter sets that satisfy model solution. The structural identifiability of the integrated model is investigated using the transfer function technique. The obtained results ensure the identifiability of the T-model parameters when the integrated model is use.

Consequently, a new technique for IM parameter estimation using L-M and PSO with the measurements of only one phase stator current and rotor speed is proposed. Results for both supply-fed and inverter-fed operations show the effectiveness of the technique in successfully identifying the parameters of the machine using only readily available measurements without the need for extra hardware.

Due to the critical integration of IMs in enormous industrial applications including nuclear power and petrochemical, fault diagnosis and fault diagnoses has a great importance in enhancing the reliability of the all system. This thesis proposed a fault diagnosis technique that is based on the use of a simple inverse-Γ-model. Unlike other model-based techniques, the proposed can be used to detect different faults and to identify their nature and location. The proposed scheme has been verified by extensive experimental tests under different faults types.

In conclusion, this thesis has achieved the main objectives listed in Chapter 1 which can be summarizes as: assessing the identifiability of two commonly used steady-state IM models, namely the T-model and inverse Γ-model, proposing a technique to improve IM parameter identification, and accurately proposing an IM stator-winding fault diagnosis technique.

8.2 Scope for future work

After achieving the main objectives of this research, there is generally still few key areas are open for further investigation including

- The investigation can be extended to study the identifiability of other induction motor models under different operating condition including healthy and faulty machines.
- L-M and PSO are successfully used to locate the optima of the different objective function throughout the thesis. Further research should be done in order to improve these algorithms in terms of computation time.
- Extend the proposed fault diagnosis techniques by examining different types of faults such as rotor-related faults.
- Study the effects of different faults on the IM parameters.

References

[1] J. Holtz and T. Thimm, "Identification of the machine parameters in a vector-controlled induction motor drive," *IEEE Trans. Ind. Appl.,* vol. 27, pp. 1111-1118, 1991.

[2] A. Bellini, F. Filippetti, G. Franceschini, C. Tassoni, and G. B. Kliman, "Quantitative evaluation of induction motor broken bars by means of electrical signature analysis," *IEEE Trans. Ind. Appl.,* vol. 37, pp. 1248-1255, 2001.

[3] M. E. H. Benbouzid, "H-G diagram based rotor parameters identification for induction motors thermal monitoring," *IEEE Trans. Energy Convers.,* vol. 15, pp. 14-18, 2000.

[4] R. Jiayang and W. Shanming, "A Prediction Error Method-Based Self-Commissioning Scheme for Parameter Identification of Induction Motors in Sensorless Drives," *IEEE Trans. Energy Convers.,* vol. 30, pp. 384-393, 2015.

[5] Y. Zhang and H. Yang, "Model-Predictive Flux Control of Induction Motor Drives With Switching Instant Optimization," *IEEE Trans. Energy Convers.,* vol. PP, pp. 1-10, 2015.

[6] L. Whei-Min, S. Tzu-Jung, and W. Rong-Ching, "Parameter Identification of Induction Machine With a Starting No-Load Low-Voltage Test," *IEEE Trans. Ind. Electron.,* vol. 59, pp. 352-360, 2012.

[7] C. Moons and B. D. Moor, "Parameter identification of induction motor drives," *Automatica,* vol. 31, pp. 1137-1147, 1995.

[8] A. M. N. Lima, C. B. Jacobina, and E. B. de Souza Filho, "Nonlinear parameter estimation of steady-state induction machine models," *IEEE Trans. Ind. Electron.,* vol. 44, pp. 390-397, 1997.

[9] A. Bechouche, H. Sediki, D. O. Abdeslam, and S. Haddad, "A Novel Method for Identifying Parameters of Induction Motors at Standstill Using ADALINE," *IEEE Trans. Energy Convers.,* vol. 27, pp. 105-116, 2012.

[10] A. M. Alturas, S. M. Gadoue, B. Zahawi, and M. A. Elgendy, "On the Identifiability of Steady-State Induction Machine Models Using External Measurements," *IEEE Trans. Energy Convers.,* vol. PP, pp. 1-9, 2015.

[11] V. P. Vas, *Electrical Machines and Drives: A Space-Vector Theory Approach*. Oxford: Clarendon Press, 1988.

[12] S. Yamamura, *AC Motors For High-Performance Applications: Analysis and Control*. New York, USA: Marcel Dekker, Inc, 1986.

[13] E. Hernandez and M. Madrigal, "A Step Forward in the Modeling of the Doubly-fed Induction Machine for Harmonic Analysis," *IEEE Trans. Energy Convers.,* vol. 29, pp. 149-157, 2014.

[14] D. Fang and R. Zivanovic, "Condition Monitoring of an Induction Motor Stator Windings Via Global Optimization Based on the Hyperbolic Cross Points," *IEEE Trans. Ind. Electron.,* vol. 62, pp. 1826-1834, 2015.

[15] S. H. Asgari, M. Jannati, and N. R. N. Idris, "Modeling of three-phase induction motor with two stator phases open-circuit," in *IEEE Conference on Energy Conversion (CENCON)*, 2014, pp. 231-236.

[16] M. Ojaghi and S. Nasiri, "Modeling Eccentric Squirrel-Cage Induction Motors With Slotting Effect and Saturable Teeth Reluctances," *IEEE Trans. Energy Convers.,* vol. 29, pp. 619-627, 2014.

[17] A. Hunghes, *Electric Motors and Drives; Fundaments, Types and Applications*. USA: Elsevier Ltd, 2006.

[18] A. M. Alturas, S. Gadoue, M. M. Elgendy, B. Zahawi, and A. S. Abdel-Khalik, "Structural Identifiability Analysis of Steady-State Induction Machine Models," presented at the IEEE 4th International Conference on Electrical Power and Energy Conversion Systems, EPECS 2015, Sharjah, 2015.

[19] C. Concari, G. Franceschini, and C. Tassoni, "Induction Drive Health Assessment in DSP-Based Self-Commissioning Procedures," *IEEE Trans. Ind. Electron.,* vol. 58, pp. 1490-1500, 2011.

[20] R. Bellman and K. J. Åström, "On structural identifiability," *Mathematical Biosciences,* vol. 7, pp. 329-339, 1970.

[21] R. Bellman and K. J. Astrom, "On Structural Identifiability," *Mathematical Biosciences,* pp. 329-339, 1970.

[22] A. Raue, C. Kreutz, T. Maiwald, J. Bachmann, M. Schilling, U. Klingmüller, and J. Timmer, "Structural and practical identifiability analysis of partially observed dynamical models by exploiting the profile likelihood," *Bioinformatics,* vol. 25, pp. 1923-1929, 2014.

[23] H. P. Boswijk, "Testing Identifiability of Cointegrating Vectors," *Journal of Business & Economic Statistics,* vol. 14, pp. 153-160, 2012.

[24] B. L. S. P. Rao, *Identifiability in Stochastic Models: Characterization of Probability Distributions (Probability & Mathematical Statistics)*: Academic Press Inc, 1992.

[25] M. Milanese and G. P. Molino, "Structural identifiability of compartmental models and pathophysiological information from the kinetics of drugs," *Mathematical Biosciences,* vol. 26, pp. 175-190, 1975.

[26] S. Peilin, T. Jun, W. Shuang, and Z. Ning, "Identifiability Analysis of Local Oscillator Phase Self-Calibration Based on Hybrid Cramér–Rao Bound in MIMO Radar," *IEEE Trans. Signal Process.,* vol. 62, pp. 6016-6031, 2014.

[27] C. Schranz, P. D. Docherty, C. Yeong Shiong, J. G. Chase, Mo, x, and K. ller, "Structural Identifiability and Practical Applicability of an Alveolar Recruitment Model for ARDS Patients," *IEEE Trans. Biomed. Eng.,* vol. 59, pp. 3396-3404, 2012.

[28] E. A. a. M. Catchpole, B. J. T, "Detecting parameter redundancy," *Biometrika,* vol. 84, pp. 187-196, 1997.

[29] B.-K. Choi and H.-D. Chiang, "On the Local Identifiability of Load Model Parameters in Measurement-based Approach," *Journal of Electrical Engineering & Technology,* vol. 4, pp. 149-158, 2009.

[30] A. Raue, C. Kreutz, T. Maiwald, J. Bachmann, M. Schilling, and U. Klingmüller, "Structural and practical identifiability analysis of partially observed dynamical models by exploiting the profile likelihood," *BIOINFORMATICS,* vol. 25, pp. 1923–1929, 2009.

[31] Oana-Teodora Chis, Julio R. Banga, and E. Balsa-Canto, "Structural Identifiability of Systems Biology Models: A Critical Comparison of Methods," *Structural Identifiability in Systems Biology,* vol. 6, 2011.

[32] A. Raue, C. Kreutz, T. Maiwald, Klingmu, x, U. ller, and J. Timmer, "Addressing parameter identifiability by model-based experimentation," *Systems Biology, IET,* vol. 5, pp. 120-130, 2011.

[33] M. Hájek, "A contribution to the parameter estimation of a certain class of dynamical systems," *Kybernetika,* vol. 8, pp. 165-173, 1972.

[34] C. Cobelli and G. Romanin-Jacur, "Controllability, Observability and Structural Identifiability of Multi Input and Multi Output Biological Compartmental Systems," *IEEE Trans. Biomed. Eng.,* vol. BME-23, pp. 93-100, 1976.

[35] J. F. Broenik, " Introduction to physical systems modelling with bond graphs," *SiE Whitebook on Simulation methodologies. University of Twente,* 1999.

[36] P. J. Gawthrop and G. P. Bevan, "Bond-graph modeling," *IEEE Control. Syst. Mag.,* vol. 27, pp. 24-45, 2007.

[37] B. a. J. Friedman, "Estimating optimal transformations for multiple regressions and correlation," *Journal of the American Statistical Association,* vol. 80(19), pp. 580-598, 1985.

[38] D. Wang and M. Murphy, "Estimating Optimal Transformations for Multiple Regression Using the ACE Algorithm," *Journal of Data Science,* vol. 2, pp. 329-346, 2004.

[39] H. Voss and J. Kurths, "Reconstruction of nonlinear time delay models from data by the use of optimal transformations," *Phys. Lett.,* vol. A 234, pp. 336-344, 1997.

[40] J. Kennedy and R. Eberhart, "Particle swarm optimization," in *IEEE International Conference on Neural Networks*, 1995, pp. 1942-1948 vol.4.

[41] R. K. Ursem and P. Vadstrup, "Parameter identification of induction motors using stochastic optimization algorithms," *Applied Soft Computing,* vol. 4, pp. 49-64, 2004.

[42] S. Yuhui and R. Eberhart, "A modified particle swarm optimizer," in *IEEE International Conference on Evolutionary Computation Proceedings*, 1998, pp. 69-73.

[43] Y. Shi, "Particle Swarm Optimization " *IEEE Neural Networks Society,* pp. 8-13, 2004.

[44] J. Kennedy, "Small worlds and mega-minds: effects of neighborhood topology on particle swarm performance," in *Proc. of the 1999 Congress on Evolutionary Computation CEC 99.*, 1999, pp. 1-1938 Vol. 3.

[45] S. Das, A. Abraham, and A. Konar, "Particle Swarm Optimization and Differential Evolution Algorithms: Technical Analysis, Applications and Hybridization Perspectives. Studies in Computational Intelligence," vol. 116, ed: Springer-Verlag Berlin Heidelberg, 2008, pp. 1–38.

[46] M. Clerc, "Standard Particle Swarm Optimization," *HAL open access archive,* 2012.

[47] H. P. Gavin, "The Levenberg-Marquardt method for nonlinear least squares curve-fitting problems," Department of Civil and Environmental Engineering, Duke University2013.

[48] "IEEE Standard Test Procedure for Polyphase Induction Motors and Generators," *IEEE Std 112-2004 (Revision of IEEE Std 112-1996),* pp. 0_1-79, 2004.

[49] M. Carraro and M. Zigliotto, "Automatic Parameter Identification of Inverter-Fed Induction Motors at Standstill," *IEEE Trans. Ind. Electron.,* vol. 61, pp. 4605-4613, 2014.

[50] A. G. Yepes, J. A. Riveros, J. Doval-Gandoy, F. Barrero, O. Lopez, B. Bogado, M. Jones, and E. Levi, "Parameter Identification of Multiphase Induction Machines With Distributed Windings—Part 1: Sinusoidal Excitation Methods," *IEEE Trans. Energy Convers.,* vol. 27, pp. 1056-1066, 2012.

[51] J. A. Riveros, A. G. Yepes, F. Barrero, J. Doval-Gandoy, B. Bogado, O. Lopez, M. Jones, and E. Levi, "Parameter Identification of Multiphase Induction Machines With Distributed Windings—Part 2: Time-Domain Techniques," *IEEE Trans. Energy Convers.,* vol. 27, pp. 1067-1077, 2012.

[52] B. Abdelhadi, A. Benoudjit, and N. Nait-Said, "Application of genetic algorithm with a novel adaptive scheme for the identification of induction machine parameters," *IEEE Trans. Energy Convers.,* vol. 20, pp. 284-291, 2005.

[53] K. Young-Su, L. Jeong-Hum, M. Sang-Ho, K. Byung-Ki, C. Chang-Ho, and S. Jul-Ki, "Standstill Parameter Identification of Vector-Controlled Induction Motors Using the Frequency Characteristics of Rotor Bars," *IEEE Trans. Ind. Appl.,* vol. 45, pp. 1610-1618, 2009.

[54] T. Matsuo and T. A. Lipo, "A Rotor Parameter Identification Scheme for Vector-Controlled Induction Motor Drives," *IEEE Trans. Ind. Appl.,* vol. IA-21, pp. 624-632, 1985.

[55] B. Hua, Z. Pei, and V. Ajjarapu, "A Novel Parameter Identification Approach via Hybrid Learning for Aggregate Load Modeling," *IEEE Trans. Power Syst.,* vol. 24, pp. 1145-1154, 2009.

[56] I. Benlaloui, S. Drid, L. Chrifi-Alaoui, and M. Ouriagli, "Implementation of a New MRAS Speed Sensorless Vector Control of Induction Machine," *IEEE Trans. Energy Convers.,* vol. 30, pp. 588-595, 2015.

[57] A. Lalami, R. Wamkeue, I. Kamwa, M. Saad, and J. J. Beaudoin, "Unscented Kalman filter for non-linear estimation of induction machine parameters," *Electric Power Applications, IET,* vol. 6, pp. 611-620, 2012.

[58] P. P. Harihara, K. Kyusung, and A. G. Parlos, "Signal-based versus model-based fault diagnosis-a trade-off in complexity and performance," in *4th IEEE International Symposium on Diagnostics for Electric Machines, Power Electronics and Drives SDEMPED*, 2003, pp. 277-282.

[59] H. A. Toliyat, E. Levi, and M. Raina, "A review of RFO induction motor parameter estimation techniques," *IEEE Trans. Energy Convers.,* vol. 18, pp. 271-283, 2003.

[60] T. Matsuo and T. A. Lipo, "A Rotor Parameter Identification Scheme for Vector-Controlled Induction Motor Drives," *IEEE Trans. Ind. App.,* vol. IA-21, pp. 624-632, 1985.

[61] H. A. Toliyat and A. A. G. Hosseiny, "Parameter estimation algorithm using spectral analysis for vector controlled induction motor drives," in *IEEE International Symposium on Industrial Electronics*, 1993, pp. 90-95.

[62] H. Sugimoto and S. Tamai, "Secondary Resistance Identification of an Induction-Motor Applied Model Reference Adaptive System and Its Characteristics," *IEEE Trans. Ind. App.,* vol. IA-23, pp. 296-303, 1987.

[63] B. Peischl and F. Wotawa, "Model-based diagnosis or reasoning from first principles," *Intelligent Systems, IEEE,* vol. 18, pp. 32-37, 2003.

[64] E. Sobhani-Tehrani and K. Khorasani, *Fault Diagnosis of Nonlinear Systems Using a Hybrid Approach*. New York: Springer, 2009.

[65] R. J. Romero-Troncoso, R. Saucedo-Gallaga, E. Cabal-Yepez, A. Garcia-Perez, R. A. Osornio-Rios, R. Alvarez-Salas, H. Miranda-Vidales, and N. Huber, "FPGA-Based Online Detection of Multiple Combined Faults in Induction Motors Through Information Entropy and Fuzzy Inference," *IEEE Trans. Ind. Electron.,* vol. 58, pp. 5263-5270, 2011.

[66] R. Isermann, "Model-based fault-detection and diagnosis – status and applications," *Annual Reviews in Control,* vol. 29, pp. 71-85, 2005.

[67] N. Hur, H. Kickul, and N. Kwanghee, "A real-time parameter identification scheme for the sensorless control of induction motors using a reduced order model," in *IEEE Proc. Industrial Electronics, Control, and Instrumentation*, 1996, pp. 1161-1166 vol.2.

[68] D. Vosmik, Z. Sutnar, and Z. Peroutka, "Application of Extended Kalman Filter for parameter identification of electric drives," in *International Conference on Applied Electronics (AE)*, 2010, pp. 1-4.

[69] R. Jaramillo, R. Alvarez, V. Urdenas, and C. Nunez, "Identification of induction motor parameter using an extended Kalman filter," in *1st International Conference on Electrical and Electronics Engineering (ICEEE)*, 2004, pp. 584-588.

[70] T. Du and M. A. Brdys, "Implementation of extended Luenberger observers for joint state and parameter estimation of PWM induction motor drive," in *Fifth European Conference on Power Electronics and Applications, 1993.,* , 1993, pp. 439-444 vol.4.

[71] T. Du, P. Vas, and F. Stronach, "Design and application of extended observers for joint state and parameter estimation in high-performance AC drives," *IEE Proc. Electric Power Applications,* vol. 142, pp. 71-78, 1995.

[72] L. J. Garces, "Parameter Adaption for the Speed-Controlled Static AC Drive with a Squirrel-Cage Induction Motor," *IEEE Trans. Ind. App.,* vol. IA-16, pp. 173-178, 1980.

[73] S. N. Vukosavic and M. R. Stojic, "On-line tuning of the rotor time constant for vector-controlled induction motor in position control applications," *IEEE Trans. Ind. Electron.,* vol. 40, pp. 130-138, 1993.

[74] K. Ohnishi, Y. Ueda, and K. Miyachi, "Model Reference Adaptive System Against Rotor Resistance Variation in Induction Motor Drive," *IEEE Trans. Ind. Electron.,* vol. IE-33, pp. 217-223, 1986.

[75] X. Zhan, G. Zeng, J. Liu, Q. Wang, and S. Ou, "A Review on Parameters Identification Methods for Asynchronous Motor," *(IJACSA) International Journal of Advanced Computer Science and Applications,* vol. 6, 2015.

[76] M. R. Young, "A minimax portfolio selection rule with linear programming solution," *Management Science,* vol. 44, pp. 673–683, 1998.

[77] C. Dong-Hyeok, J. Hyun-Kyo, and L. Cheol-Gyun, "Induction motor design for electric vehicle using a niching genetic algorithm," *IEEE Trans. Ind. App.,* vol. 37, pp. 994-999, 2001.

[78] P. Nangsue, P. Pillay, and S. E. Conry, "Evolutionary algorithms for induction motor parameter determination," *IEEE Trans. Energy Convers.,* vol. 14, pp. 447-453, 1999.

[79] B. Abdelhadi, A. Benoudjit, and N. Nait-Said, "Application of genetic algorithm with a novel adaptive scheme for the identification of induction machine parameters," *IEEE Trans. Energy Convers.,,* vol. 20, pp. 284-291, 2005.

[80] M.-H. Lin, J.-F. Tsai, and C.-S. Yu, "A Review of Deterministic Optimization Methods in Engineering and Management," *Mathematical Problems in Engineering,* vol. 2012, pp. 1-15, 2012.

[81] H. Robbins and S. Monro, "A Stochastic Approximation Method," presented at the The Annals of Mathematical Statistics, 1951.

[82] T. Weise. (2009). *Global Optimization Algorithm – Theory and Application –*.

[83] B. Sendhoff, M. Roberts, and Y. Xin, "Evolutionary computation benchmarking repository [Developmental Tools]," *Computational Intelligence Magazine, IEEE,* vol. 1, pp. 50-60, 2006.

[84] K. Chunki and S. D. Sudhoff, "Genetic algorithm-based induction machine characterization procedure with application to maximum torque per amp control," *IEEE Trans. Energy Convers.,* vol. 21, pp. 405-415, 2006.

[85] S. Buyamin and J. W. Finch, "Comparative Study on Optimising the EKF for Speed Estimation of an Induction Motor using Simulated Annealing and Genetic Algorithm," in *IEEE International Electric Machines & Drives Conference IEMDC*, 2007, pp. 1689-1694.

[86] L. Chun-Feng, H. Chia-Hung, and J. Chia-Feng, "Coordinated Control of Flexible AC Transmission System Devices Using an Evolutionary Fuzzy Lead-Lag Controller With Advanced Continuous Ant Colony Optimization," *IEEE Trans. Power Sys.,* vol. 28, pp. 385-392, 2013.

[87] A. Karaarslan, "The Implementation of Bee Colony Optimization Algorithm to Sheppard-Taylor PFC Converter," *IEEE Trans. Ind. Electron.,* vol. 60, pp. 3711-3719, 2013.

[88] A. A. A. Esmin, G. Lambert-Torres, and A. C. Z. de Souza, "A hybrid particle swarm optimization applied to loss power minimization," *IEEE Trans. Power Sys.,* vol. 20, pp. 859-866, 2005.

[89] Y. Xie, "Investigation of Broken Rotor Bar Faults in Three-Phase Squirrel-Cage Induction Motors," in *Finite Element Analysis - From Biomedical Applications to Industrial Developments, Dr. David Moratal (Ed.), ISBN: 978-953-51-0474-2, InTech, Available from: http://www.intechopen.com/books/finite-element-analysisfrom-biomedical-applications-to-industrial-developments/investigation-of-broken-rotor-bar-faults-in-threephase-squirrel-cage-induction-motors*, ed.

[90] M. Walker, *The Diagnosing of Trouble in Electrical Machines*. London, U.K., 1924.

[91] A. Bellini, F. Filippetti, C. Tassoni, and G. A. Capolino, "Advances in Diagnostic Techniques for Induction Machines," *IEEE Trans. Ind. Electron.,* vol. 55, pp. 4109-4126, 2008.

[92] M. Riera-Guasp, J. A. Antonino-Daviu, and G. A. Capolino, "Advances in Electrical Machine, Power Electronic, and Drive Condition Monitoring and Fault Detection: State of the Art," *IEEE Trans. Ind. Electron.,* vol. 62, pp. 1746-1759, 2015.

[93] A. Sapena-Bano, M. Pineda-Sanchez, R. Puche-Panadero, J. Perez-Cruz, J. Roger-Folch, M. Riera-Guasp, and J. Martinez-Roman, "Harmonic Order Tracking Analysis: A Novel Method for Fault Diagnosis in Induction Machines," *IEEE Trans. Energy Convers.,* vol. PP, pp. 1-9, 2015.

[94] S. Nandi, H. A. Toliyat, and X. Li, "Condition Monitoring and Fault Diagnosis of Electrical Motors—A Review," *IEEE Trans. Energy Convers.,* vol. 20, pp. 719-729, 2005.

[95] S. Grubic, J. M. Aller, L. Bin, and T. G. Habetler, "A Survey on Testing and Monitoring Methods for Stator Insulation Systems of Low-Voltage Induction Machines Focusing on Turn Insulation Problems," *IEEE Trans. Ind. Electron.,* vol. 55, pp. 4127-4136, 2008.

[96] E. Fournier, A. Picot, J. Regnier, M. T. Yamdeu, J. M. Andrejak, and P. Maussion, "Current-Based Detection of Mechanical Unbalance in an Induction Machine Using Spectral Kurtosis With Reference," *IEEE Trans. Ind. Electron.,* vol. 62, pp. 1879-1887, 2015.

[97] D. Z. Li, W. Wang, and F. Ismail, "A Spectrum Synch Technique for Induction Motor Health Condition Monitoring," *IEEE Trans. Energy Convers.,* vol. PP, pp. 1-8, 2015.

[98] Y. Amirat, M. E. H. Benbouzid, B. Bensaker, and R. Wamkeue, "Condition Monitoring and fault Diagnosis in Wind Energy Conversion Systems: A Review," in *Electric Machines & Drives Conference, 2007. IEMDC '07. IEEE International*, 2007, pp. 1434-1439.

[99] N. Mehala, "Condition monitoring and fault diagnosis of induction motor using motor current signature analysis," PhD, electrical engineering department national institute of technology, kurushetra, , india, 2010.

[100] Y. Amirat, M. E. H. Benbouzid, B. Bensaker, and R. Wamkeue, "Condition Monitoring and ault Diagnosis in Wind Energy Conversion Systems: A Review," in *IEEE International Electric Machines & Drives Conference IEMDC '07*, 2007, pp. 1434-1439.

[101] F. Immovilli, C. Bianchini, M. Cocconcelli, A. Bellini, and R. Rubini, "Bearing Fault Model for Induction Motor With Externally Induced Vibration," *IEEE Trans. Ind. Elect.,* vol. 60, pp. 3408-3418, 2013.

[102] M. Amar, I. Gondal, and C. Wilson, "Vibration Spectrum Imaging: A Novel Bearing Fault Classification Approach," *IEEE Trans. Ind. Electron.,* vol. 62, pp. 494-502, 2015.

[103] J. R. Stack, T. G. Habetler, and R. G. Harley, "Bearing fault detection via autoregressive stator current modeling," *IEEE Trans. Ind. Electron.,* vol. 40, pp. 740-747, 2004.

[104] F. Immovilli, M. Cocconcelli, A. Bellini, and R. Rubini, "Detection of Generalized-Roughness Bearing Fault by Spectral-Kurtosis Energy of Vibration or Current Signals," *IEEE Trans. Ind. Electron.,* vol. 56, pp. 4710-4717, 2009.

[105] I. M. Culbert and W. Rhodes, "Notice of Violation of IEEE Publication Principles
Using Current Signature Analysis Technology to Reliably Detect Cage Winding Defects in Squirrel-Cage Induction Motors," *IEEE Trans. Ind. App.,* vol. 43, pp. 422-428, 2007.

[106] M. Riera-Guasp, M. F. Cabanas, J. A. Antonino-Daviu, M. Pineda-Sanchez, and C. H. R. Garcia, "Influence of Nonconsecutive Bar Breakages in Motor Current Signature Analysis for the Diagnosis of Rotor Faults in Induction Motors," *IEEE Trans. Energy Convers.,* vol. 25, pp. 80-89, 2010.

[107] L. Zhenxing, Y. Xianggen, Z. Zhe, C. Deshu, and C. Wei, "Online rotor mixed fault diagnosis way based on spectrum analysis of instantaneous power in squirrel cage induction motors," *IEEE Trans. Energy Convers.,* vol. 19, pp. 485-490, 2004.

[108] J. Cusido, L. Romeral, J. A. Ortega, J. A. Rosero, and A. Garcia Espinosa, "Fault Detection in Induction Machines Using Power Spectral Density in Wavelet Decomposition," *IEEE Trans. Ind. Electron.,* vol. 55, pp. 633-643, 2008.

[109] G. M. Joksimovic, "Dynamic simulation of cage induction machine with air gap eccentricity," *IEE Proc. Electric Power Applications,* vol. 152, pp. 803-811, 2005.

[110] M. Drif and A. J. M. Cardoso, "Airgap-Eccentricity Fault Diagnosis, in Three-Phase Induction Motors, by the Complex Apparent Power Signature Analysis," *IEEE Trans. Ind. Electron.,* vol. 55, pp. 1404-1410, 2008.

[111] J. Faiz, B. M. Ebrahimi, B. Akin, and H. A. Toliyat, "Finite-Element Transient Analysis of Induction Motors Under Mixed Eccentricity Fault," *IEEE Trans. Magn.,* vol. 44, pp. 66-74, 2008.

[112] M. Y. Kaikaa and M. Hadjami, "Effects of the simultaneous presence of static eccentricity and broken rotor bars on the stator current of induction machine," *IEEE Trans. Ind. Electron.,* vol. 61, pp. 2452-2463, 2014.

[113] A. Seghiour, T. Seghier, and B. Zegnini, "Diagnostic of the simultaneous of dynamic eccentricity and broken rotor bars using the magnetic field spectrum of the air-gap for an induction machine," in *3rd International Conference on Control, Engineering & Information Technology (CEIT)*, 2015, pp. 1-6.

[114] L. M. C. Mhango and J. A. Rennie, "Recent developments and benefits of high-speed PWM inverter-fed induction-motor drive for gas filtration in nuclear power plants," in *Sixth International Conference on Electrical Machines and Drives.*, 1993, pp. 564-569.

[115] J. A. Antonino-Daviu, L. Sang Bin, and E. Wiedenbrug, "Reliable detection of rotor bar failures in induction motors operating in petrochemical plants," in *Petroleum and Chemical Industry Conference Europe*, 2014, pp. 1-9.

[116] L. Junyong and M. Weiming, "Research on End Effect of Linear Induction Machine for High-Speed Industrial Transportation," *IEEE Trans. Plasma Science,* vol. 39, pp. 116-120, 2011.

[117] J. S. Hsu, "Monitoring of defects in induction motors through air-gap torque observation," *IEEE Trans. Ind. App.,* vol. 31, pp. 1016-1021, 1995.

[118] R. Maier, "Protection of squirrel-cage induction motor utilizing instantaneous power and phase information," *IEEE Trans. Ind. App.,* vol. 28, pp. 376-380, 1992.

[119] G. M. Joksimovic, J. Riger, T. M. Wolbank, N. Peric, and M. Vasak, "Stator-Current Spectrum Signature of Healthy Cage Rotor Induction Machines," *IEEE Trans. Ind. Electron.,* vol. 60, pp. 4025-4033, 2013.

[120] S. H. Kia, H. Henao, and G. Capolino, "Efficient digital signal processing techniques for induction machines fault diagnosis," in *IEEE Workshop on Electrical Machines Design Control and Diagnosis (WEMDCD)*, 2013, pp. 232-246.

[121] E. H. E. Bouchikhi, V. Choqueuse, and M. Benbouzid, "A Parametric Spectral Estimator for Faults Detection in Induction Machines," presented at the IECON 2013, Vienne, Austria, 2014.

[122] L. Noueddine and O. Tohami, "Application of parametric PSC methods for rotor cage fault detection of induction motors," *Electrical Engineering,* pp. 1-7.

[123] L. A. Pereira, D. Fernandes, D. S. Gazzana, F. B. Libano, and S. Haffher, "Application of the Welch, Burg and MUSIC Methods to the Detection of Rotor Cage Faults of Induction Motors," in *IEEE/PES Transmission & Distribution Conference and Exposition (TDC)*, 2006, pp. 1-6.

[124] F. Cupertino, E. de Vanna, L. Salvatore, and S. Stasi, "Analysis techniques for detection of IM broken rotor bars after supply disconnection," *IEEE Trans. Ind. App.,* vol. 40, pp. 526-533, 2004.

[125] K. Yong-Hwa, Y. Young-Woo, H. Don-Ha, S. Jong-Ho, and K. Dong-Sik, "High-Resolution Parameter Estimation Method to Identify Broken Rotor Bar Faults in Induction Motors," *IEEE Trans. Ind. Electron.,* vol. 60, pp. 4103-4117, 2013.

[126] M. Riera-Guasp, J. Pons-Llinares, V. Climente-Alarcon, F. Vedreno-Santos, M. Pineda-Sanchez, J. Antonino-Daviu, R. Puche-Panadero, J. Perez-Cruz, and J. Roger-Folch, "Diagnosis of induction machines under non-stationary conditions: Concepts and tools," in *IEEE Workshop on Electrical Machines Design Control and Diagnosis (WEMDCD)*, 2013, pp. 220-231.

[127] H. Douglas, P. Pillay, and A. K. Ziarani, "A new algorithm for transient motor current signature analysis using wavelets," *IEEE Trans. Ind. App.,* vol. 40, pp. 1361-1368, 2004.

[128] Z. Wei, T. G. Habetler, and R. G. Harley, "Bearing Fault Detection Via Stator Current Noise Cancellation and Statistical Control," *IEEE Trans. Ind. Electron.,* vol. 55, pp. 4260-4269, 2008.

[129] B. Akin, U. Orguner, H. A. Toliyat, and M. Rayner, "Phase-Sensitive Detection of Motor Fault Signatures in the Presence of Noise," *IEEE Trans. Ind. Electron.,* vol. 55, pp. 2539-2550, 2008.

[130] A. Bellini, G. Franceschini, and C. Tassoni, "Monitoring of induction machines by maximum covariance method for frequency tracking," in *Industry Applications Conference, 2004. 39th IAS Annual Meeting. Conference Record of the 2004 IEEE*, 2004, pp. 743-749 vol.2.

[131] A. Bellini, G. Franceschini, and C. Tassoni, "Monitoring of induction Machines by maximum covariance method for frequency tracking," *IEEE Trans. Ind. App.,* vol. 42, pp. 69-78, 2006.

[132] F. Filippetti, A. Bellini, and G. Capolino, "Condition monitoring and diagnosis of rotor faults in induction machines: State of art and future perspectives," in *IEEE Workshop on Electrical Machines Design Control and Diagnosis (WEMDCD)*, 2013, pp. 196-209.

[133] H. Henao, G. A. Capolino, M. Fernandez-Cabanas, F. Filippetti, C. Bruzzese, E. Strangas, R. Pusca, J. Estima, M. Riera-Guasp, and S. Hedayati-Kia, "Trends in Fault Diagnosis for

Electrical Machines: A Review of Diagnostic Techniques," *IEEE Trans. Ind. Elect. Mag.,* vol. 8, pp. 31-42, 2014.

[134] A. Sapena-Bano, M. Pineda-Sanchez, R. Puche-Panadero, J. Perez-Cruz, J. Roger-Folch, M. Riera-Guasp, and J. Martinez-Roman, "Harmonic Order Tracking Analysis: A Novel Method for Fault Diagnosis in Induction Machines," *IEEE Trans. Energy Convers.,* vol. 30, pp. 833-841, 2015.

[135] A. Soualhi, G. Clerc, and H. Razik, "Detection and Diagnosis of Faults in Induction Motor Using an Improved Artificial Ant Clustering Technique," *Industrial Electronics, IEEE Transactions on,* vol. 60, pp. 4053-4062, 2013.

[136] S. H. Kia, H. Henao, and G. A. Capolino, "A High-Resolution Frequency Estimation Method for Three-Phase Induction Machine Fault Detection," *IEEE Trans. Ind. Electron.,* vol. 54, pp. 2305-2314, 2007.

[137] M. Pineda-Sanchez, M. Riera-Guasp, J. A. Antonino-Daviu, J. Roger-Folch, J. Perez-Cruz, and R. Puche-Panadero, "Diagnosis of Induction Motor Faults in the Fractional Fourier Domain," *IEEE Trans. Instrum. Meas.,* vol. 59, pp. 2065-2075, 2010.

[138] S. X. Ding, *Model-Based Fault Diagnosis Techniques, Second Edition*. London: Springer-Verlag, 2008.

[139] S. Bachir, S. Tnani, J. C. Trigeassou, and G. Champenois, "Diagnosis by parameter estimation of stator and rotor faults occurring in induction machines," *IEEE Trans. Ind. Electron.,* vol. 53, pp. 963-973, 2006.

[140] C. H. De Angelo, G. R. Bossio, S. J. Giaccone, M. I. Valla, J. A. Solsona, and G. O. Garcia, "Online Model-Based Stator-Fault Detection and Identification in Induction Motors," *IEEE Trans. Ind. Electron.,* vol. 56, pp. 4671-4680, 2009.

[141] *Rotating Machinery, Structural Health Monitoring, Shock and Vibration* vol. 5. USA: Springer, 2011.

[142] S. Liming, W. Ke, and L. Yaohua, "On-line parameter identification of linear induction motor based on adaptive observer," in *ICEMS*, 2007, pp. 1606-1609.

[143] Z. Li-Cheng, C. L. DeMarco, and T. A. Lipo, "An extended Kalman filter approach to rotor time constant measurement in PWM induction motor drives," *IEEE Trans. Ind. App.,* vol. 28, pp. 96-104, 1992.

[144] J. Maes and J. A. Melkebeek, "Speed-sensorless direct torque control of induction motors using an adaptive flux observer," *IEEE Trans. Ind. App.,* vol. 36, pp. 778-785, 2000.

[145] S. Nandi, "A detailed model of induction machines with saturation extendable for fault analysis," *IEEE Trans. Ind. App.,* vol. 40, pp. 1302-1309, 2004.

[146] J. C. Moreira and T. A. Lipo, "Modeling of saturated AC machines including air gap flux harmonic components," *IEEE Trans. Ind. App.,* vol. 28, pp. 343-349, 1992.

[147] H. A. Toliyat and M. M. Rahimian, "Transient analysis of cage induction machines under internal faults using winding function," presented at the 3rd Int. Conf. Electrical Rotating Machines — ELROMA, 1992.

[148] H. Hooshmandi, M. Ebrahimi, A. Davoudi, and A. Pouramin, "Analytical Derivation of Induction Motors Inductances under Eccentricity Conditions," *Progress In Electromagnetics Research B,* vol. 60, pp. 95-110, 2014.

[149] N. A. Al-Nuaim and H. A. Toliyat, "A novel method for modeling dynamic air-gap eccentricity in synchronous machines based on modified winding function theory," *IEEE Trans. Energy Convers.,* vol. 13, pp. 156-162, 1998.

[150] J. M. Gojko, D. D. Momir, and O. B. Aleksandar, "Skew and linear rise of MMF across slot modelling-winding function approach," *IEEE Trans. Energy Convers.,* vol. 14, pp. 315-320, 1999.

[151] C. Gerada, K. J. Bradley, M. Sumner, P. Wheeler, S. Pickering, J. Clare, C. Whitley, and G. Towers, "The results do mesh," *IEEE Trans. Ind. App. Mag.,* vol. 13, pp. 62-72, 2007.

[152] V. Ostovic, "A Method for Evaluation of Transient and Steady State Performance in Saturated Squirrel Cage Induction Machines," *IEEE Trans. Energy Convers.,* vol. EC-1, pp. 190-197, 1986.

[153] H. Meshgin-Kelk, J. Milimonfared, and H. A. Toliyat, "Interbar currents and axial fluxes in healthy and faulty induction motors," *IEEE Trans. Ind. App.,* vol. 40, pp. 128-134, 2004.

[154] J. F. Martins, V. F. Pires, and A. J. Pires, "Unsupervised Neural-Network-Based Algorithm for an On-Line Diagnosis of Three-Phase Induction Motor Stator Fault," *IEEE Trans. Ind. Electron.,* vol. 54, pp. 259-264, 2007.

[155] V. N. Ghate and S. V. Dudul., "Induction machine fault detection using support vector machine based classifier," *WSEAS TRANSACTIONS on SYSTEMS* vol. 8, 2009.

[156] F. Filippetti, G. Franceschini, C. Tassoni, and P. Vas, "Recent developments of induction motor drives fault diagnosis using AI techniques," *IEEE Trans. Ind. Electron.,* vol. 47, pp. 994-1004, 2000.

[157] H. S. Goh, "The Effect of Grid Operating Conditions on the Harmonic Performance of Grid-Connected PV Inverters," Doctor of Philosophy, School of Electrical, Electronic & Computer Engineering, Newcastle, 2011.

[158] S. A. Ethni, S. M. Gadoue, and B. Zahawi, "Induction machine winding faults identification using Bacterial Foraging Optimization technique," in *7th IET International Conference on Power Electronics, Machines and Drives (PEMD)*, 2014, pp. 1-6.

[159] M. Alamyal, S. M. Gadoue, and B. Zahawi, "Detection of induction machine winding faults using genetic algorithm," in *9th IEEE International Symposium on Diagnostics for Electric Machines, Power Electronics and Drives (SDEMPED)*, 2013, pp. 157-161.

[160] F. Corcoles, J. Pedra, M. Salichs, and L. Sainz, "Analysis of the induction machine parameter identification," *IEEE Trans. Energy Convers.,* vol. 17, pp. 183-190, 2002.

[161] P. Vaclavek, P. Blaha, and I. Herman, "AC Drive Observability Analysis," *IEEE Trans. Ind. Electron.,* vol. 60, pp. 3047-3059, 2013.

[162] J. F. Brudny, J. Lecointe, F. Morganti, F. Zidat, and R. Romary, "Use of the External Magnetic Field for Induction Machine Leakage Inductance Distinction," *IEEE Trans. Magn.,* vol. 46, pp. 2205-2208, 2010.

[163] D. Chatterjee, "A Simple Leakage Inductance Identification Technique for Three-Phase Induction Machines Under Variable Flux Condition," *IEEE Trans. Ind. Electron.,* vol. 59, pp. 4041-4048, 2012.

[164] C. M. Verrelli, A. Savoia, M. Mengoni, R. Marino, P. Tomei, and L. Zarri, "On-Line Identification of Winding Resistances and Load Torque in Induction Machines," *Control Systems Technology, IEEE Transactions on,* vol. 22, pp. 1629-1637, 2014.

[165] H. Yanhui, W. Yue, F. Yupeng, and W. Zhaoan, "Parameter Identification of an Induction Machine at Standstill Using the Vector Constructing Method," *Power Electronics, IEEE Transactions on,* vol. 27, pp. 905-915, 2012.

[166] J. F. Watson and D. G. Dorrell, "The use of finite element methods to improve techniques for the early detection of faults in 3-phase induction motors," *IEEE Trans. Energy Convers.,* vol. 14, pp. 655-660, 1999.

[167] C. Xianrong, V. Cocquempot, and C. Christophe, "A model of asynchronous machines for stator fault detection and isolation," *IEEE Trans. Ind. Elect.,* vol. 50, pp. 578-584, 2003.

[168] S. Chen and R. Živanović, "Modelling and simulation of stator and rotor fault conditions in induction machines for testing fault diagnostic techniques," *European Transactions on Electrical Power,* vol. 20, pp. 611-629, 2009.

[169] L. Monjo, H. Kojooyan-Jafari, F. Corcoles, and J. Pedra, "Squirrel-Cage Induction Motor Parameter Estimation Using a Variable Frequency Test," *IEEE Trans. Energy Convers.,* vol. PP, pp. 1-8, 2014.

[170] "Report of Large Motor Reliability Survey of Industrial and Commercial Installations, Part I," *IEEE Trans. Ind. App.,* vol. IA-21, pp. 853-864, 1985.

[171] A. Trzynadlowski, "The Field Orientation Principle in Control of Induction Motors," ed: Kluwer Academic, 1994.

[172] M. G. Say, *Alternating Current Machines*, 5 ed.: Pitman Publishing, 1984.

Appendix A

Induction machine dynamic models

The three-phase induction machine with three stator windings and three rotor windings is shown in figure A.1, where *A*, *B*, and *C* referring to stator phases, *a*, *b*, and *c*, referring to rotor phases. The machine is described by three identical stator windings placed on the stator frame with equal separation of 120º in space between each other. The three rotor windings are place with equal distant of 120º around the rotor circumference and rotating at the machine speed ω_r. All these windings have resistances and inductances.

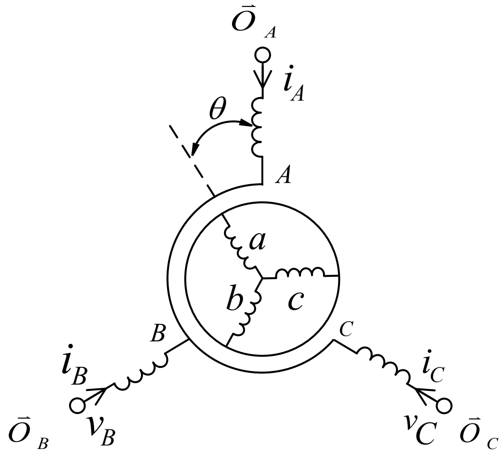

Figure A.1 Three phase machine diagram.

Using Kirchhoff's and Faraday's laws, the voltage relations on rotor and stator sides are given by [11]:

$$\begin{bmatrix} v_A \\ v_B \\ v_C \end{bmatrix} = R_s \begin{bmatrix} i_A \\ i_B \\ i_C \end{bmatrix} + \frac{d}{dt}\begin{bmatrix} \psi_A \\ \psi_B \\ \psi_C \end{bmatrix}, \quad 0 = R_r \begin{bmatrix} i_a \\ i_b \\ i_c \end{bmatrix} + \frac{d}{dt}\begin{bmatrix} \psi_a \\ \psi_b \\ \psi_c \end{bmatrix} \qquad \text{(A.1)}$$

The symbols i and v are for currents and voltages and Ψ for the flux linkages. $R_s = (R_A, R_B, R_C)$ are the stator winding resistances, and $R_r = (R_a, R_b, R_c)$ are the rotor winding resistances and they are assumed to be equal for all phase windings (for healthy machines).

The flux-linkage of a single phase, for example phase A, comprises of both leakage flux path (which thread stator or rotor alone) and mutual flux (which thread both stator and rotor). Therefore, the flux-linkage consists of self-leakage flux due to the current flowing in the winding and the mutual flux due to the current of other windings as given by equation (A.2).

$$\psi_A = L_{AA} i_A + L_{AB} i_B + L_{AC} i_C + L_{Aa} i_a + L_{Ab} i_b + L_{Ac} i_c \qquad \text{(A.2)}$$

where L is the inductance which define the relationship between the machine winding currents and the flux linkage.

Deriving the equations for the flux-linkage of the other windings and substituting it into (A.1) yields:

$$\begin{bmatrix} v_A \\ v_B \\ v_C \\ v_a \\ v_b \\ v_c \end{bmatrix} = [R] \begin{bmatrix} i_A \\ i_B \\ i_C \\ i_a \\ i_b \\ i_c \end{bmatrix} + \frac{d}{dt} \left[[L] \begin{bmatrix} i_A \\ i_B \\ i_C \\ i_a \\ i_b \\ i_c \end{bmatrix} \right] \qquad \text{(A.3)}$$

where:

$$R = \begin{bmatrix} R_A & 0 & 0 & 0 & 0 & 0 \\ 0 & R_B & 0 & 0 & 0 & 0 \\ 0 & 0 & R_C & 0 & 0 & 0 \\ 0 & 0 & 0 & R_a & 0 & 0 \\ 0 & 0 & 0 & 0 & R_b & 0 \\ 0 & 0 & 0 & 0 & 0 & R_c \end{bmatrix} \qquad \text{(A.4)}$$

and

$$L = \begin{bmatrix} L_{AA} & L_{AB} & L_{AC} & L_{Aa} & L_{Ab} & L_{Ac} \\ L_{BA} & L_{BB} & L_{BC} & L_{Ba} & L_{Bb} & L_{Bc} \\ L_{CA} & L_{CB} & L_{CC} & L_{Ca} & L_{Cb} & L_{Cc} \\ L_{aA} & L_{aB} & L_{aC} & L_{aa} & L_{ab} & L_{ac} \\ L_{bA} & L_{bB} & L_{bC} & L_{ba} & L_{bb} & L_{bc} \\ L_{cA} & L_{cB} & L_{cC} & L_{ca} & L_{cb} & L_{cc} \end{bmatrix} \tag{A.5}$$

The mutual inductances between the stator and rotor vary with the relative space position between them as follows:

$$\begin{aligned} M\cos(\vec{O}_A,\vec{O}_a) &= M\cos(\theta) = Ma_1 \\ M\cos(\vec{O}_A,\vec{O}_b) &= M\cos(\theta+\frac{2\pi}{3}) = Ma_2 \\ M\cos(\vec{O}_A,\vec{O}_c) &= M\cos(\theta-\frac{2\pi}{3}) = Ma_3 \end{aligned} \tag{A.6}$$

where θ is the rotor angle, $a_1 = cos(\theta_r)$, $a_2 = cos(\theta_r + \frac{2\pi}{3})$, and $a_3 = \cos(\theta_r - \frac{2\pi}{3})$.

Substituting (A.4), (A.5) and (A.6) in (A.3), the dynamic three phase model (*ABCabc*) model is obtained and represented as following:

$$\begin{bmatrix} v_A \\ v_B \\ v_C \\ v_a \\ v_b \\ v_c \end{bmatrix} = \begin{bmatrix} R_A + \rho L_{ss} & \rho M_{ss} & \rho M_{ss} & \rho M_{sr}a_1 & \rho M_{sr}a_2 & \rho M_{sr}a_3 \\ \rho M_{ss} & R_A + \rho L_{ss} & \rho M_{ss} & \rho M_{sr}a_3 & \rho M_{sr}a_1 & \rho M_{sr}a_2 \\ \rho M_{ss} & \rho M_{ss} & R_A + \rho L_{ss} & \rho M_{sr}a_2 & \rho M_{sr}a_3 & \rho M_{sr}a_1 \\ \rho M_{sr}a_1 & \rho M_{sr}a_3 & \rho M_{sr}a_2 & R_a + \rho L_{rr} & \rho M_{rr} & \rho M_{rr} \\ \rho M_{sr}a_2 & \rho M_{sr}a_1 & \rho M_{sr}a_3 & \rho M_{rr} & R_b + \rho L_{rr} & \rho M_{rr} \\ \rho M_{sr}a_3 & \rho M_{sr}a_2 & \rho M_{sr}a_1 & \rho M_{rr} & \rho M_{rr} & R_c + \rho L_{rr} \end{bmatrix} \begin{bmatrix} i_A \\ i_B \\ i_C \\ i_a \\ i_b \\ i_c \end{bmatrix} \tag{A.7}$$

where L_{ss} and L_{rr} are stator and rotor self-inductances, M_{ss} are the mutual inductance between each pairs of the stator windings, M_{rr} are the mutual inductance between each pairs of the rotor windings, M_{sr} are the peak value of the rotor position dependent mutual inductance between the stator and rotor windings, and θ_r is the rotor angle.

To reduce the computational complexity of the three phase model due to the time-varying mutual inductances, IMs can be described by two equivalent windings rather than three such as $\alpha\beta$ and dq.

The transformation of the stator and rotor variables from *abc* to *αβ* are defined as follows [171]:

$$\begin{aligned} X_{\alpha\beta s} &= T_{\alpha\beta} X_{abcs} \\ X_{\alpha\beta r} &= T_r(\theta) T_{\alpha\beta} X_{abcr} \end{aligned} \tag{A.8}$$

where

$$T_{\alpha\beta} = \sqrt{\frac{2}{3}} \begin{bmatrix} 1 & -1/2 & -1/2 \\ 0 & \sqrt{3}/2 & -\sqrt{3}/2 \end{bmatrix} \tag{A.9}$$

$$T_r(\theta) = \begin{bmatrix} \cos\theta & -\sin\theta \\ \sin\theta & \cos\theta \end{bmatrix} \tag{A.10}$$

Another substantial simplification is made by transforming the three phase quantities into orthogonal two-axis representation known as Park's transformation [172]. This model is commonly referred to as the *dq* model and it has been extensively used in many applications including high performance drive control. This transformation eliminates the effect of time varying inductances by referring the stator and rotor inductances into a fixed or rotating reference frame. This transformation is done using the transformation matrix as follows:

$$X_{dq} = T_{dq} X_{abc} \tag{A.11}$$

where

$$T_{dq} = \begin{bmatrix} 2/3 & -1/3 & -1/3 \\ 0 & 1/\sqrt{3} & -1/\sqrt{3} \end{bmatrix} \tag{A.12}$$

Appendix B

Structural identifiability analysis of IM Γ-model

In this section, the structural identifiability of the Γ-model is tested using the two aforementioned techniques.

B.1 The transfer function approach

The input impedance of the Γ-model in chapter 1 as a function of the slip s is given by:

$$Z''_{eq}(p,s) = \frac{\rho^2 s + \rho s a_2 + b_2 c_2}{\rho d_2 + c_2} \tag{B.1}$$

where $\rho=j\omega_s$, and a_2, b_2, c_2 and d_2 are functions of the four electrical parameters of the model and they can be obtained from the following expressions:

$$\begin{aligned} a_2 &= \frac{R_s L''_m + R''_r R_s + L''_m R''_r / s}{L''_m l''_{lr}}, \\ b_2 &= R_s, \\ c_2 &= R''_r / l''_{lr} L''_m, \\ d_2 &= \left(L''_m + l''_{lr}\right) / l''_{lr} L''_m \end{aligned} \tag{B.2}$$

The transfer function of this model is given by:

$$G_\Gamma(S) = 1 / Z''_{eq} = \frac{S d_2 + c_2}{S^2 s + S s a_2 + b_2 c_2} \tag{B.3}$$

With Γ-model, there are four coefficients of $G_\Gamma(S)$ that can be determined if the external measurements are used. Model parameters can then be uniquely identified from these coefficients by using equation (B.2).

B.2 Bond Graph Approach

In this model, the stator leakage inductance is combined together with that of the rotor as suggested to eliminate the conflict in the T-model in [12]. Figure C.1 shows the bond graph of the Γ-model where the parameter redundancy has been removed and a proper bond graph is obtained.

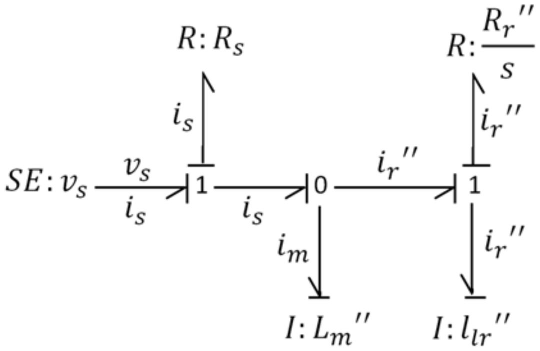

Figure B.1 Bond graph of IM Γ-equivalent circuit.

Appendix C

Extra Results for identifiability analysis

In this section, extra results at different operating conditions from that in the chapter 5 are provided to assess the identifiability of both models (the T and inverse Γ-model).

C.1 T-model identifiability analysis using L-M

Table C.1 represents three sets of estimated parameter values and the total impedance corresponding to each estimate for different initial conditions at supply-fed no-load with slip of 0.0087. Figure C.1 shows the convergence history of the estimated parameters of the T-Model for the three different estimates at no-load. Figure C.2 shows the error function convergence for the 1st estimate. Figure C.3 shows the measured current (i_{Am}) and the calculated current (i_{AC}) with one of the parameter sets obtained by L-M parameters (1st estimate).

As shown in figure C.4, infinite combinations of the two inductance values result in the same minimum value of squared error, i.e. there is no unique global minimum. This confirms that it is not possible to determine l_{ls} and l_{lr} uniquely using external measurements of voltage, current, and speed.

Pars	1st estimate	2nd estimate	3rd estimate
R_s	10.4824 Ω	5.1722 Ω	7.3494 Ω
R_r	7.6361 Ω	2.6230 Ω	4.3881 Ω
l_{ls}	0.0263 H	0.1346 H	0.0696 H
l_{lr}	0.0108 H	0.0199 H	0.0177 H
l_m	0.3387 H	0.2356 H	0.2975 H
$\lvert Z_{eq}\rvert$	115.58 Ω	115.54 Ω	115.37 Ω
$\angle Z_{eq}$	80.35 °	81.34 °	80.45 °

Table C.1 Parameter Estimation of T-model using L-M; supply-fed at no load (s= 0.0087).

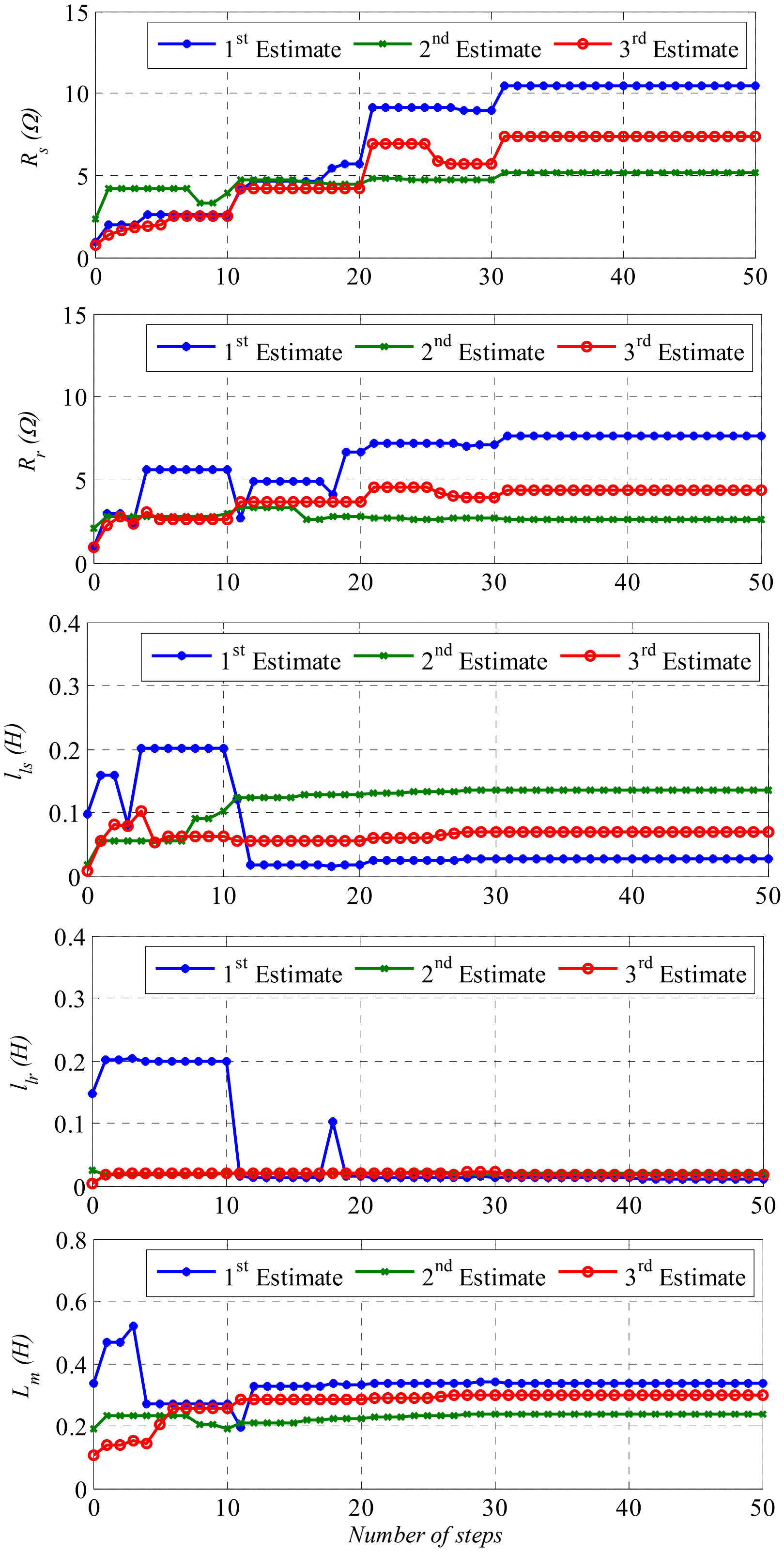

Figure C.1 Convergence of the estimated parameters of the T-Model for different estimates using L-M; supply-fed at no load (s= 0.0087).

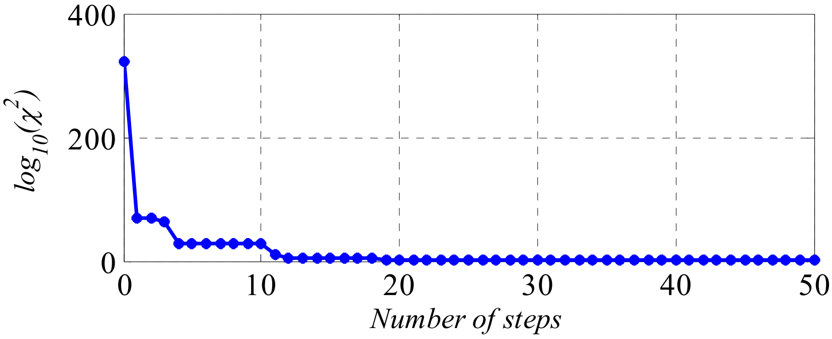

Figure C.2 The error function convergence for the 1st estimate using L-M (T-model); supply-fed at no load (s= 0.0087).

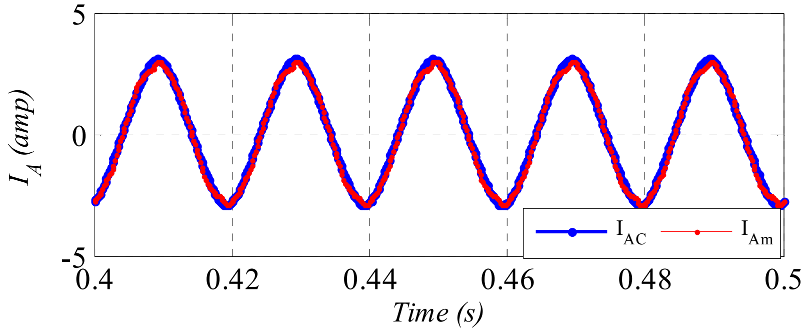

Figure C.3 Measured (i_{Am}) and calculated (i_{Ac}) stator currents waveforms corresponding to the optimal solution of the 1st estimate using L-M (T-Model); supply-fed at no load (s= 0.0087).

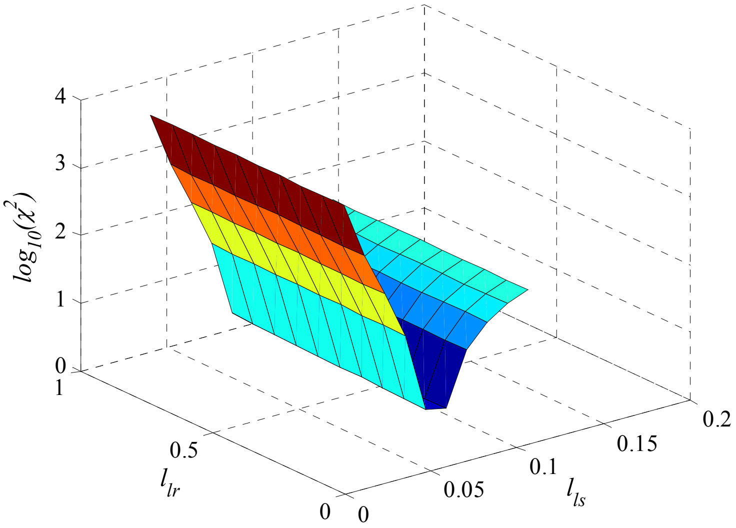

Figure C.4 The sum of the squared error as a function of l_{ls} and l_{lr} based on the measured data (T-Model); supply-fed at no load (s= 0.0087).

Table C.2 represents three sets of estimated parameter values and the total impedance corresponding to each estimate for different initial conditions at full-load with slip of 0.021(1469 r/m). Figure C.5 shows the convergence history of the estimated parameters of the T-Model for the three different estimates at no-load. Figure C.6 shows the error function convergence for the 1st estimate. Figure C.7 shows the measured current (i_{Am}) and the calculated current (i_{AC}) with one of the parameter sets obtained by L-M parameters (1st estimate).

Pars	1st estimate	2nd estimate	3rd estimate
R_s	3.381583 Ω	3.736917	4.921409
R_r	1.329535	2.559239	1.365111
l_{ls}	0.149764	0.075604	0.052693
l_{lr}	0.0042	0.00655	0.0246
l_m	0.328732	0.293377	0.78043
$\lvert Z_{eq} \rvert$	90.59	91.6	92.7
$\angle Z_{eq}$	62.3	63.2	63.33

Table C.2 Parameter Estimation of T-model; supply-fed at full load (*s*= 0.21).

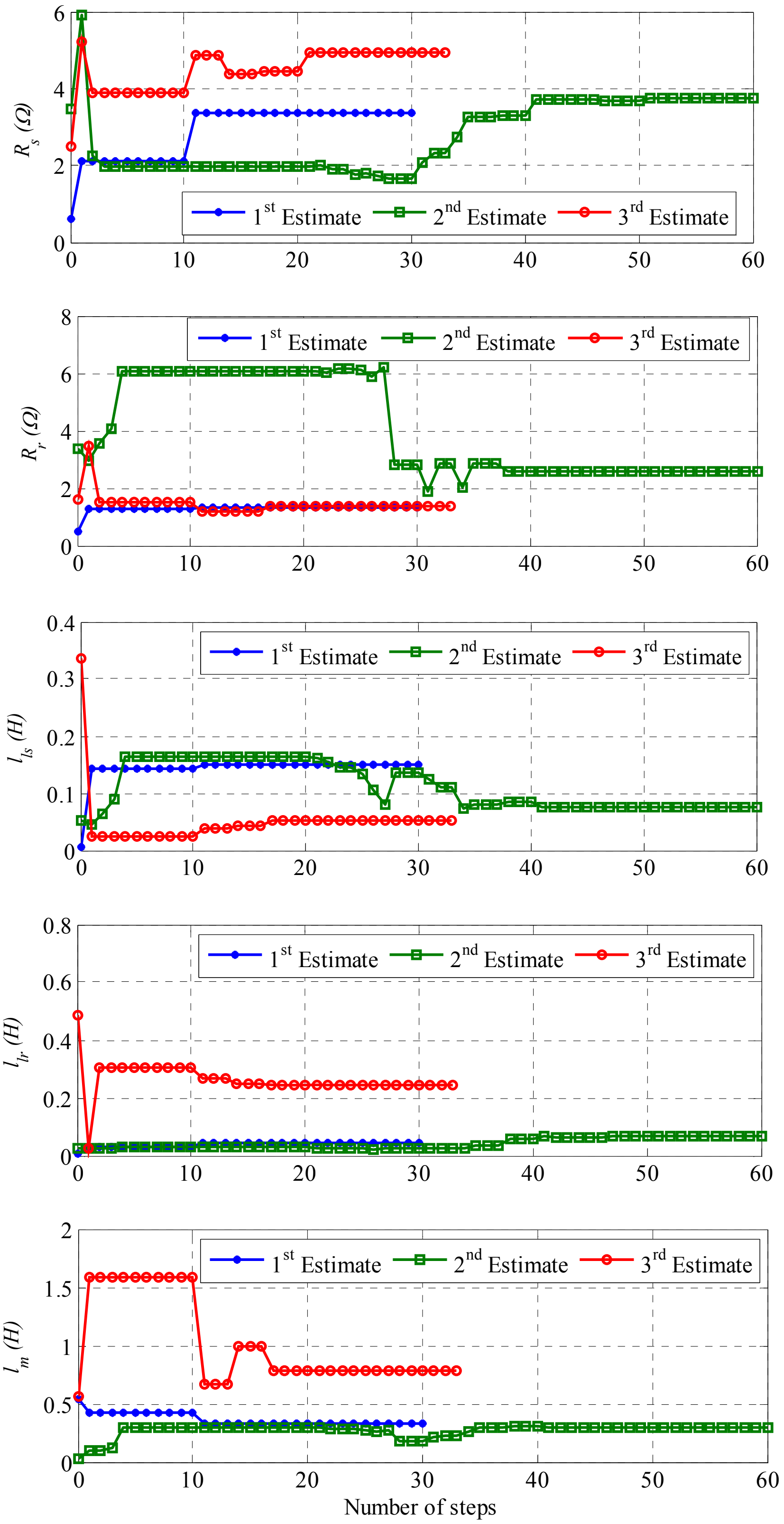

Figure C.5 Convergence of the estimated parameters of the T-Model for different estimates (T-model) using L-M; supply-fed at full load (*s*= 0.21).

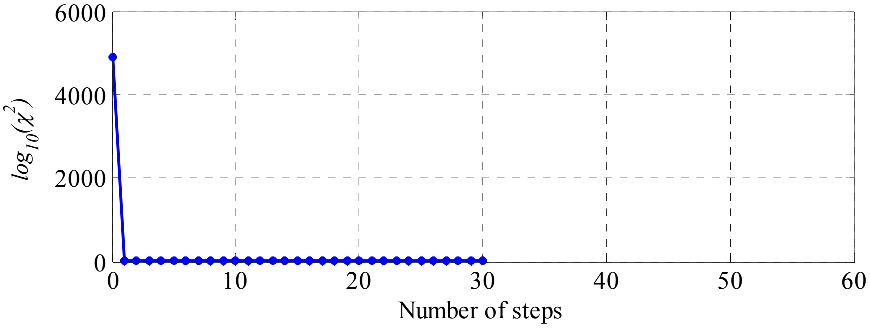

Figure C.6 The error function convergence for the 1st estimate (T-model) using L-M; supply-fed at full load (*s*= 021).

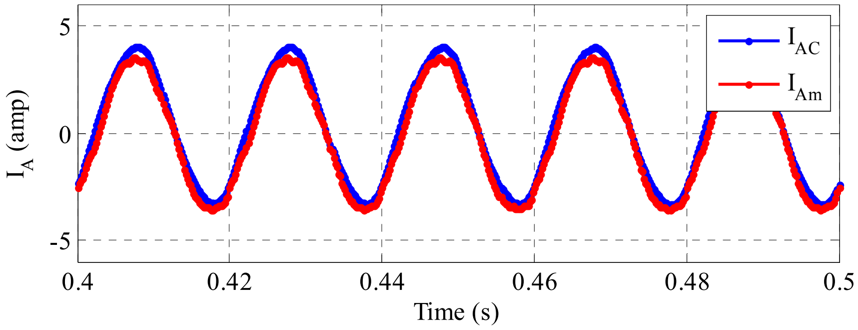

Figure C.7 Measured (i_{Am}) and calculated (i_{Ac}) stator currents waveforms corresponding to the optimal solution of the 1st estimate (T-Model); supply-fed at full load (*s*= 021).

C.2 T-model identifiability analysis using PSO

Table C.3 represents three sets of estimated parameter values and the total impedance corresponding to each estimate for different initial conditions at no-load with slip of 0.0087%. Figure C.8 shows the convergence history of the estimated parameters of the T-Model for the three different estimates at no-load. Figure C.9 shows the error function convergence for the 1st estimate. Figure C.10 shows the measured current (i_{Am}) and the calculated current (i_{AC}) with one of the parameter sets obtained by PSO parameters (1st estimate).

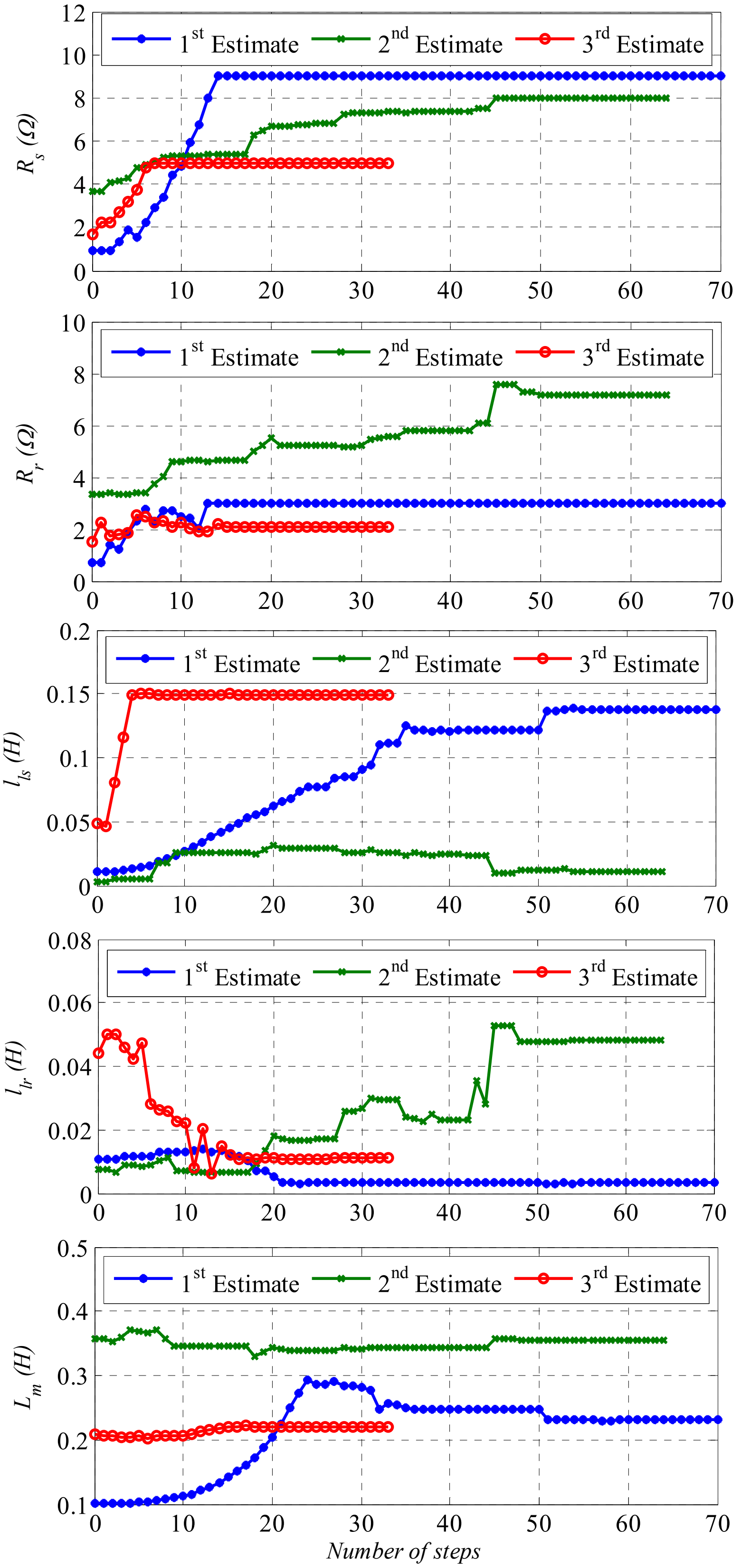

Figure C.8 Convergence of the estimated parameters of the T-Model for different estimates using PSO; supply-fed at no load (s=0.0087).

Pars	1st estimate	2nd estimate	3rd estimate
R_s	8.9998 Ω	7.9880 Ω	4.9982 Ω
R_r	2.9998 Ω	7.1935 Ω	2.0919 Ω
l_{ls}	0.1379 H	0.0114 H	0.1497 H
l_{lr}	0.0032 H	0.0482 H	0.0110 H
L_m	0.2303 H	0.3553 H	0.2211 H
$\lvert Z_{eq} \rvert$	115.82 Ω	115.63 Ω	115.22 Ω
$\angle Z_{eq}$	80.39 °	80.87 °	80.84 °

Table C.3 Parameter Estimation of T-model using PSO; Supply-fed at no load (s= 0.0087).

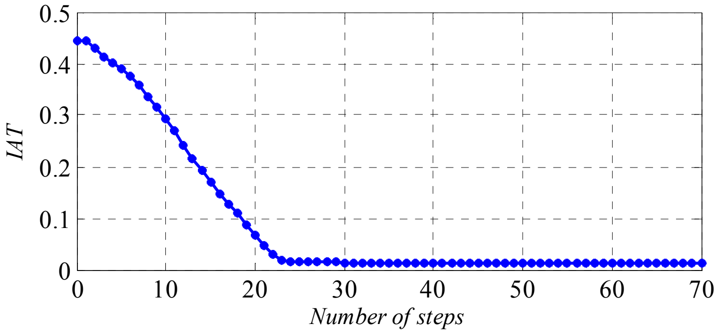

Figure C.9 The error function convergence for the 1st estimate (T-model) using PSO; supply-fed at no-load (s=0.0087).

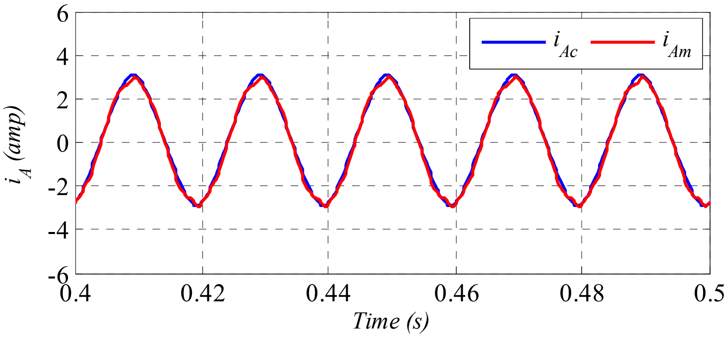

Figure C.10 Measured (i_{Am}) and calculated (i_{Ac}) stator currents waveforms corresponding to the optimal solution of the 1st estimate (T-Model); supply-fed at no-load (s=0.0087).

Table C.4 represents three sets of estimated parameter values and the total impedance corresponding to each estimate for different initial conditions at full-load with slip of 0.021 (1469 r/m). Figure C.11 shows the convergence history of the estimated parameters of the T-Model for the three different estimates at no-load. Figure C.12 shows the error function convergence for the 1st estimate. Figure C.13 shows the measured current (i_{Am}) and the calculated current (i_{AC}) with one of the parameter sets obtained by PSO parameters (1st estimate).

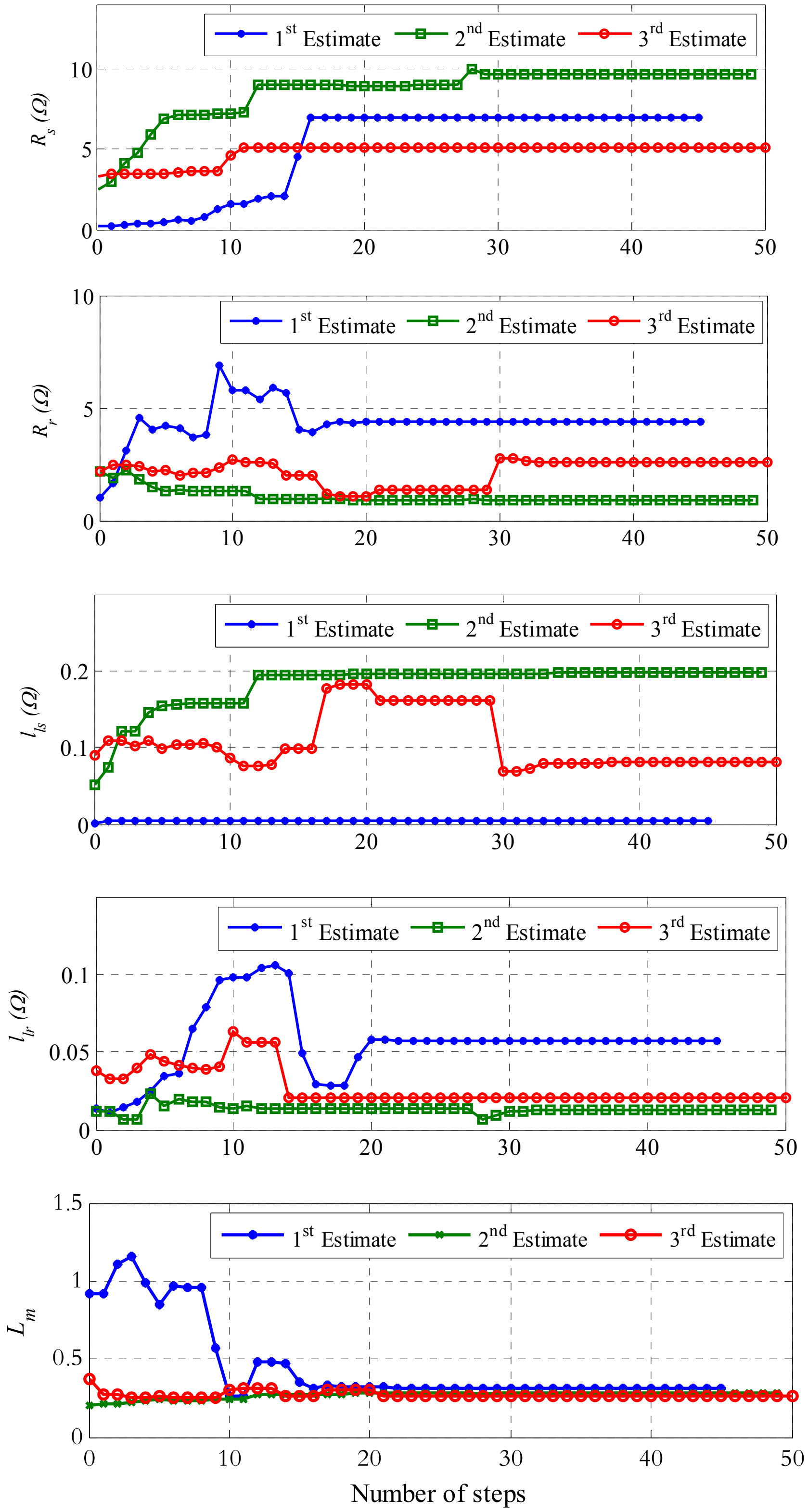

Figure C.11 Convergence of the estimated parameters of the T-Model for different estimates using PSO; supply-fed at full load (s=0.021).

Pars.	1st estimate	2nd estimate	3rd estimate
R_s	6.9999	9.6175	5.0544
R_r	4.3777	0.8972	2.5829
l_{ls}	0.0040	0.1987	0.0806
l_{lr}	0.00571	0.0127	0.0201
L_m	0.3165	0.2850	0.2592
$\lvert Z_{eq}\rvert$	91.51	91.81	91.34
$\angle Z_{eq}$	62.14	62.50	63.58

Table C.4 Parameter Estimation of T-model using PSO, supply-fed at full load (s= 0.021).

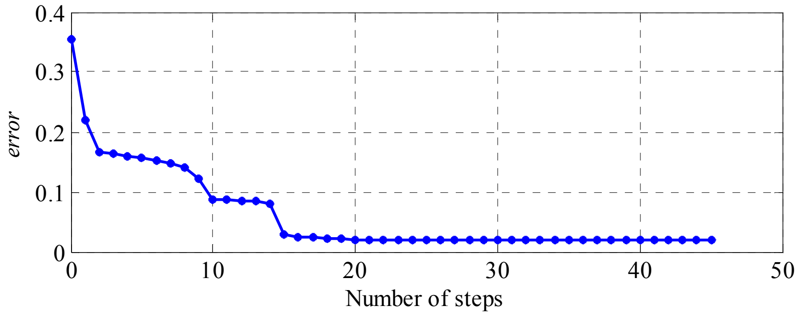

Figure C.12 The error function convergence for the 1st estimate (T-model) using PSO; supply-fed at full load (s=0.021).

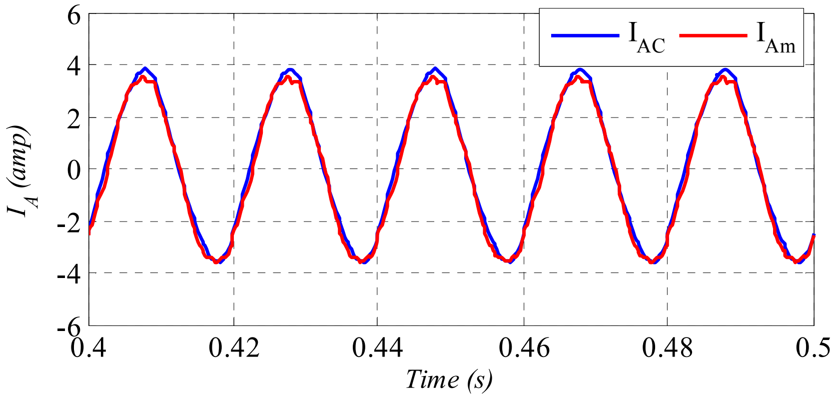

Figure C.13 Measured (i_{Am}) and calculated (i_{Ac}) stator currents waveforms corresponding to the optimal solution of the 1st estimate (T-Model); supply-fed at load (s=0.021).

C.3 Inverse Γ-model identifiability analysis using L-M

Table C.4 represents three sets of estimated parameter values for different initial conditions at no-load with slip of 0.0087. The total impedance corresponding to each estimate are also calculated and shown in the table. Figure C.14 shows the convergence history of the estimated parameters of the T-Model for the three different estimates at no-load. Figure C.15 shows the error function convergence for the 1st estimate. Figure C.16 shows the measured current (i_{Am}) and the calculated current (i_{AC}) with one of the parameter sets obtained by L-M parameters (1st estimate).

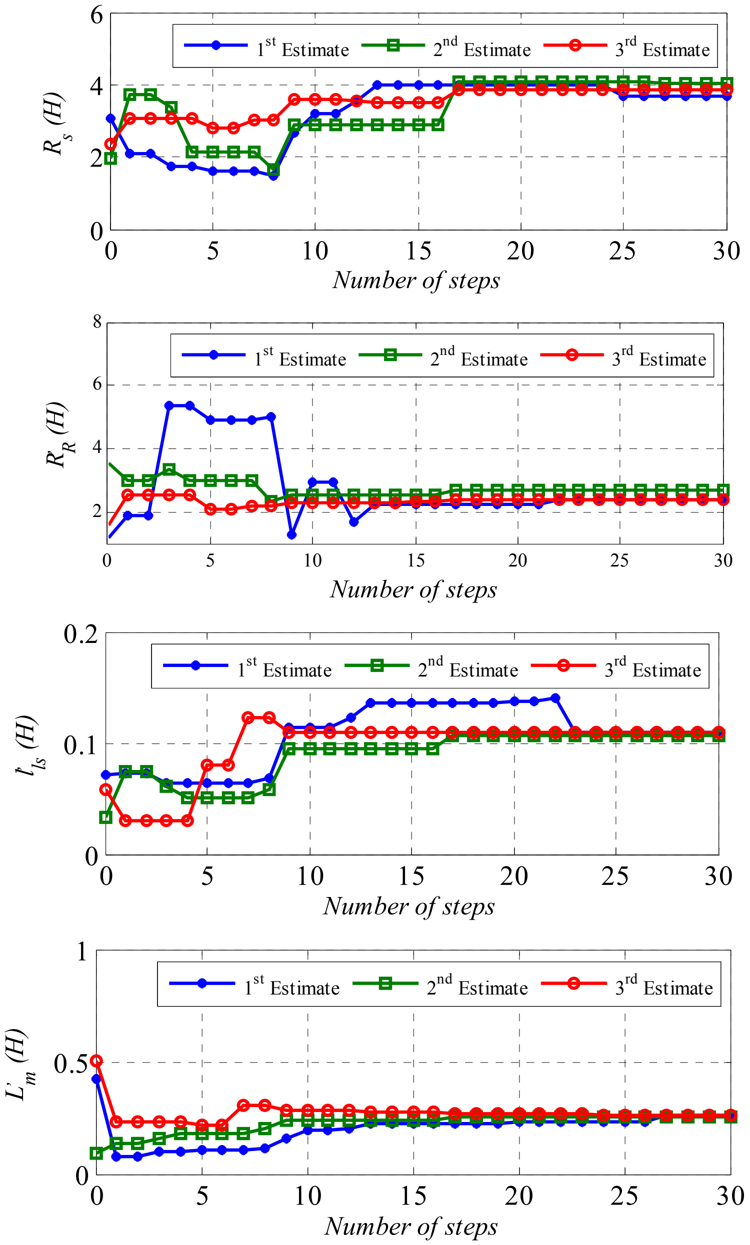

Figure C.14 Convergence of the estimated parameters of the Inverse Γ-Model for different estimates using L-M; supply-fed at no-load (s=0.0087).

Pars.	1^{st} estimate	2^{nd} estimate	3^{rd} estimate
R_s	3.6848 Ω	4.0599 Ω	3.8638 Ω
R_r'	2.368 Ω	2.6858 Ω	2.4024 Ω
l_{ls}'	0.1098 H	0.1118 H	0.1101 H
l_m'	0.2627 H	0.2594 H	0.2616 H
$\lvert Z_{eq} \rvert$	115.4 Ω	115.53 Ω	115.29 Ω
$\angle Z_{eq}$	79.87°	80.79°	79.94°

Table C.5 Parameter Estimation of Inverse Γ-model using L-M; supply-fed at no-load (s=0.0087).

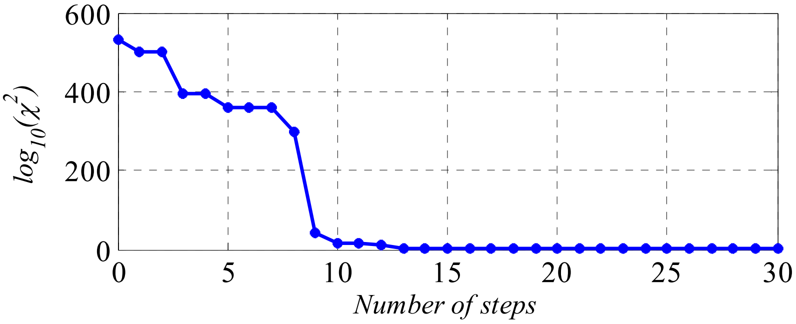

Figure C.15 The error function convergence for the 1st estimate (Inverse Γ-Model using PSO; supply-fed at no-load (s=0.0087).

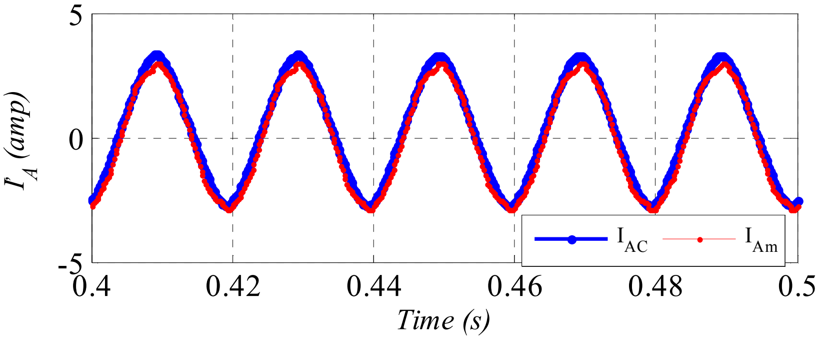

Figure C.16 Measured (i_{Am}) and calculated (i_{Ac}) stator currents waveforms corresponding to the optimal solution of the 1^{st} estimate (Inverse Γ-Model); supply-fed at no-load (s=0.0087).

Table C.6 represents three sets of estimated parameter values for different initial conditions at full-load with slip of 0.021. The total impedance corresponding to each estimate are also calculated and shown in the table. Figure C.17 shows the convergence history of the estimated parameters of the T-Model for the three different estimates at no-load. Figure C.18 shows the error function convergence for the 1st estimate. Figure C.19 shows the measured current (i_{Am}) and the calculated current (i_{AC}) with one of the parameter sets obtained by L-M parameters (1st estimate).

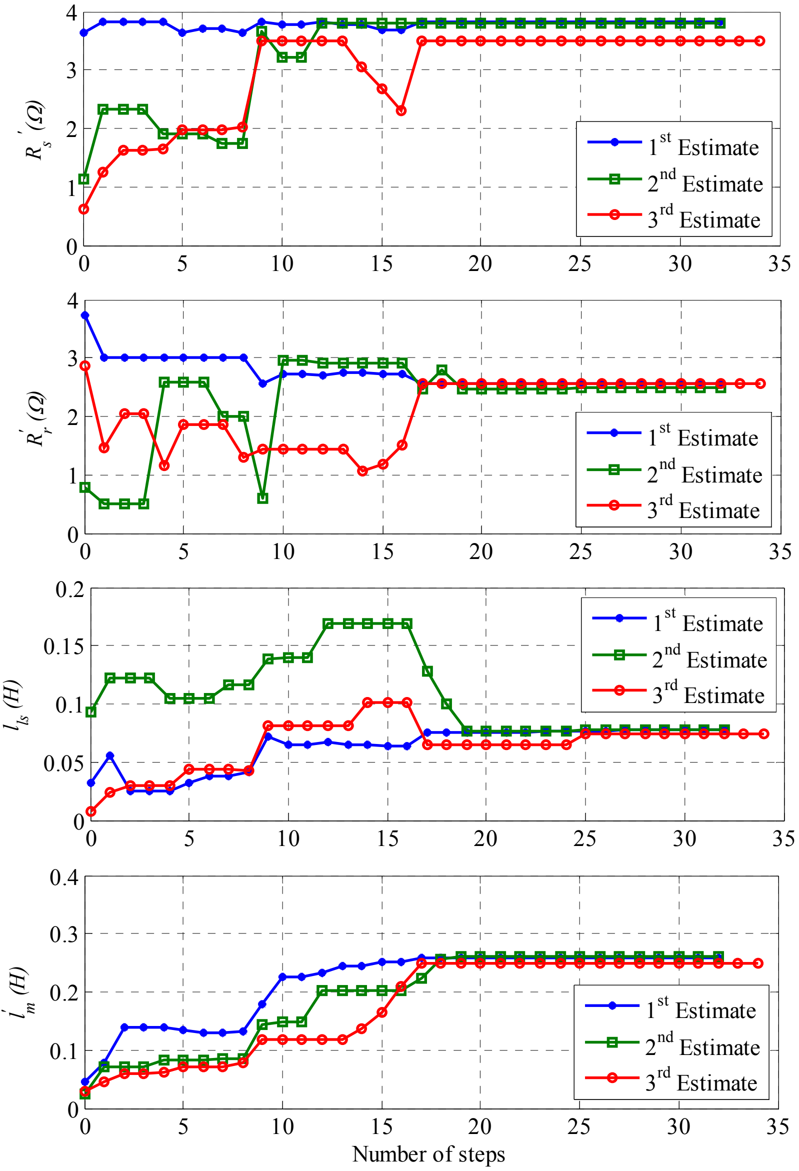

Figure C.17 Convergence of the estimated parameters of the Inverse Γ-Model for different estimates using PSO; supply-fed at full load (s=0.021).

Pars.	1st estimate	2nd estimate	3rd estimate
R_s	3.81987	3.796245	3.500022
R_r'	2.562973	2.480859	2.562602
l_{ls}'	0.077992	0.077504	0.073688
l_m'	0.259485	0.260134	0.250254
$\lvert Z_{eq} \rvert$	91.3	90.46	88.36
$\angle Z_{eq}$	63.1	62.43	63.73

Table C.6 Parameter Estimation of Inverse Γ-model using PSO; supply-fed at full load (s=0.021)

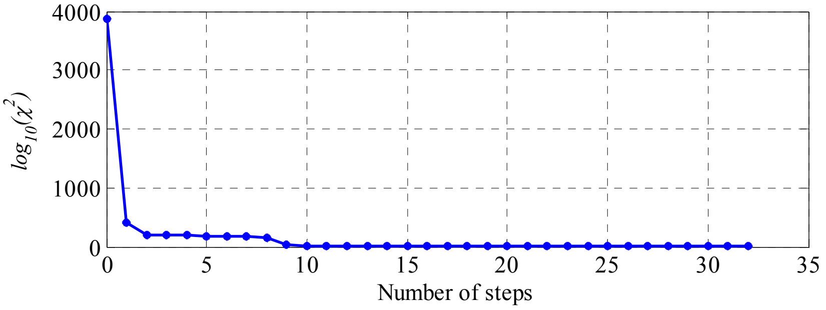

Figure C.18 The error function convergence for the 1st estimate (Inverse Γ-Model) using PSO; supply-fed at full load (s=0.021).

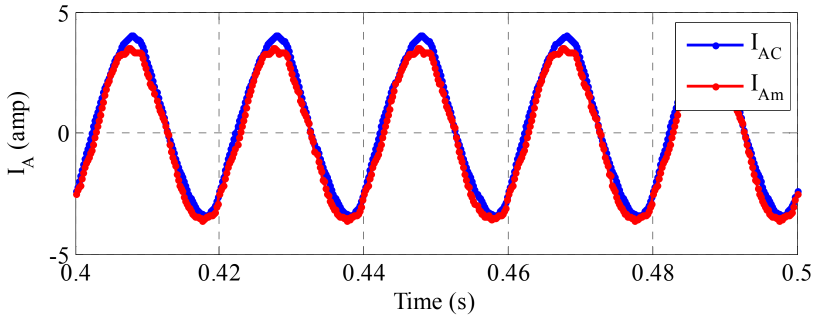

Figure C.19 Measured (i_{Am}) and calculated (i_{Ac}) stator currents waveforms corresponding to the optimal solution of the 1st estimate (Inverse Γ-Model), supply-fed, full-load.